Comparison of turbulent reactive spray characteristics of different renewable fuels using Large Eddy Simulation

Detailed comparison of renewable Diesel fuels
Zur Erlangung des akademischen Grades Doktor-Ingenieur (Dr.-Ing.)
Genehmigte Dissertation von Philip Michael Haspel aus Ludwigsburg
Tag der Einreichung: 30.5.2023, Tag der Prüfung: 17.10.2023

1. Gutachten: Prof. Dr.-Ing. Christian Hasse
2. Gutachten: Prof. Dr.-Ing. Michael Günthner
Darmstadt, Technische Universität Darmstadt

TECHNISCHE
UNIVERSITÄT
DARMSTADT

STFS
Simulation of reactive Thermo-Fluid Systems

Mechanical Engineering
Department

Simulation of reactive
Thermo-Fluid Systems
(STFS)

Comparison of turbulent reactive spray characteristics of different renewable fuels using Large Eddy Simulation
Detailed comparison of renewable Diesel fuels

Accepted doctoral thesis by Philip Michael Haspel

Date of submission: 30.5.2023
Date of thesis defense: 17.10.2023

Darmstadt, Technische Universität Darmstadt

Bitte zitieren Sie dieses Dokument als:
URN: urn:nbn:de:tuda-tuprints-247260
URL: http://tuprints.ulb.tu-darmstadt.de/
Jahr der Veröffentlichung auf TUprints: 2023

Contents

Preface/Vorwort

Die vorliegende Dissertationsschrift entstand im Rahmen meiner Tätigkeit als wissenschaftlicher Mitarbeiter am Fachgebiet "Simulation reaktiver Thermo-Fluid Systeme", Fachbereich Maschinenbau an der Technischen Universität Darmstadt unter der Leitung von Prof. Dr.-Ing. Christian Hasse. Teile dieser Arbeit wurden bereits in folgenden Publikationen veröffentlicht:

[1] Philip Haspel, Sandro Gierth, Sebastian Popp, Sebastian Rieß, Michael Wensing, and Christian Hasse. “Combined experimental and numerical study of OME3 and OME4 spray combustion under heavy-duty conditions” in Fuel (2023) - *under revision*.

[2] Michael H. H. Fechter, Philip Haspel, Christian Hasse, and Andreas S. Braeuer. “Vapor pressures and latent heats of vaporization of Poly(oxymethylene) Dimethyl Ethers (OME3 and OME4) up to the vicinity of the critical temperature”. In: Fuel 303. May (2021).

[3] Sandro Gierth, Philip Haspel, Arne Scholtissek, Zhen Sun, and Sebastian Popp. “Evaluation of the Unsteady Flamelet Progress Variable Approach in Large Eddy Simulations of the ECN Spray A.” In: Science and Technology for Energy Transition (2021).

Der Autor bedankt sich für die ihm zur Verfügung gestellte Rechenzeit auf den Hochleistungsrechnern Lichtenberg an den NHR-Zentren NHR4CES an der TU Darmstadt. Diese werden auf Grundlage der Beschlüsse der GWK zum Nationalen Hochleistungsrechnen an Hochschulen (NHR) durch das Bundesministerium für Bildung und Forschung und die am NHR beteiligten Landesregierungen (www.nhr-verein.de/unsere-partner) gefördert.

Darüber hinaus möchte ich meinen Kollegen: Sandro Gierth, Arne Scholtissek, Matthias Steinhausen, Hannes Böttler, Magnus Kircher und Andrea Pati für die Korrekturen danken. Die Arbeit wurde darüber hinaus auf Grammatik und Rechtschreibung überprüft. Für die Erstellung der Plots wurde das Python tool Matplotlib genutzt [4].

I want to gratefully acknowledge the provision of data and collaboration with Sebastian Rieß & Andreas Peter, Michael Fechter, Tim Beutler, José M. Garcia-Oliver, Prof. Liming Cai, Julien Menin, Kevin Wan, Lyle Pickett, Alessandro Stagni and Matteo Pelucchi.

Für die Fördermittel in den Projekten die ich bearbeiten durfte möchte ich meinen Dank an die Forschungsvereinigung Verbrennungskraftmaschinen, dem Bundesministerium für Wirtschaft und Klimaschutz und der Fachagentur für nachwachsende Rohstoffe aussprechen.

Persönliche Danksagung

Der Weg zur Promotion ist lang und oft steinig, doch mit dem Ziel vor Augen lässt sich auch ein anstrengender Weg bewältigen. Meine Ziele habe ich schon früh abgesteckt, wohl inspiriert von meinem Papa war mein Berufswunsch schon als Stöpsel klar: "Ingenieur für alles". An dieser Stelle möchte ich mich bei meinen Eltern bedanken, die mich auf meinem Weg begleitet und tatkräftig unterstützt haben. Angefangen bei den zahlreichen Bastelprojekten mit Papa, die mein technisches Interesse geweckt haben: Burgen, Klettergerüste, Mohrenkopfschleuder, Armbrust und Co. Auch meiner Mama bin ich sehr dankbar, sie hat mich bei allem unterstützt und mich immer ermutigt, etwas neues auszuprobieren. Sie hat mich von der Schule an bis zur Uni bekräftigt: Du schaffst das! Meinem Opa Rolf habe ich auch viel zu verdanken: du hast mir dein Vertrauen geschenkt als ich noch ein Bub war, das hat Spuren hinterlassen die ich noch heute fährten kann. Schweißen, flexen, Maschinen reparieren, das Traktorfahren und die Jagd in den Ferien haben sicherlich zum Wunschstudium Maschinenbau beigetragen.

Bei meiner Frau Nadja möchte ich mich ganz besonders bedanken! Du hast mir die größten Geschenke gemacht: unsere Söhne Johann und Jakob. Die Promotion mit zwei Kindern ist nicht einfach, da braucht es viel Unterstützung, Verständnis und oft ein offenes Ohr. Danke, dass du mir die Zeit gegeben hast die Promotion zu beenden und mich unterstützt, wo du kannst! Ich freue mich auf die Zeit nach der Promotion mit mehr Familienzeit!

Eine Promotion steht und fällt nicht nur am wissenschaftlichen Thema, ganz wichtig sind die Kollegen und das Umfeld. Die Zeit am Fachgebiet behalte ich in guter Erinnerung, vor allem die Zeit vor Corona war geprägt mit vielen Aktivitäten im Kollegium: Fussball, Merck-Lauf, Doktorwagenbau und viele Promotionsfeiern waren eine willkommene Abwechslung zur Arbeit. Gerade in der Anfangszeit halfen mir die Kollegen (Danny, Andrea, Sandro, Martin, Sebastian, Sandra, Arne, Felix und Steffen) die Arbeit mit einem Lächeln zu verlassen. Wir haben viel gearbeitet, aber auch mindestens so viel gelacht. Auch später habe ich viele nette Kollegen erleben dürfen! Die Liste ist zu lang, ihr dürft euch angesprochen fühlen beim Lesen! Die längste und engste Zusammenarbeit hatte ich mit Sandro, wir haben sehr viel und erfolgreich zusammen gearbeitet. Danke für die zahlreichen Diskussionen und die Unterstützung auch in den späten Abendstunden: wir haben so das ein oder andere Projekttreffen gemeistert!

Für die Möglichkeit zur Promotion und Betreuung meines Promotionsvorhabens möchte ich mich herzlich bei Prof. Christian Hasse bedanken.

Zum Abschluss ein Gedicht von Goethe dass mich schon lange inspiriert:

Bleibe nicht am Boden heften,
Frisch gewagt und frisch hinaus!
Kopf und Arm mit heitern Kräften,
Überall sind sie zu Haus;
Wo wir uns der Sonne freuen,
Sind wir jede Sorge los.
Daß wir uns in ihr zerstreuen,
Darum ist die Welt so groß.

Lorsch im Mai 2023.

Abstract

The human-caused climate change imposes many challenges for future generations. It is commonly agreed to stop the global warming process, and new technologies have to be found to reduce the footprint of greenhouse gases. A high share of greenhouse gas emissions comes from the transport sector. In particular, carbon dioxide CO_2 from the combustion of fossil fuels in engines contributes significantly to global warming. The reduction of emissions in the transport sector can either be achieved by decarbonization, eliminating energy carriers containing carbon, or defossilation, including combustion of carbon-neutral fuels. The defossilation pathway is currently favored, and many fuels from renewable sources are in the focus of research. Two very promising carbon-neutral Diesel fuels are 1-Octanol, which is produced from biogenic feedstock, and the group of Polyoxymethylene ethers (OME) that are synthesized from green hydrogen and ambient carbon dioxide. Both fuels are considered backstop technologies, which makes them very interesting in sustainable energy production. Both fuels exhibit changed thermophysical and chemical kinetic properties compared to conventional fossil fuels. The latent heat of evaporation of 1-Octanol is significantly increased compared to Diesel. Also, OME shows higher latent heat of evaporation and a significantly increased vapor pressure. The reactivity of 1-Octanol is reduced, while OME is considered a high-reactive fuel due to its high level of oxygenation. Both fuels show no soot formation and can be utilized in blends with regular fuels to meet new emission regulations. Furthermore, emissions of CO, CO_2, NO_x and soot can be significantly reduced with 1-Octanol and OME. In the present thesis, the spray flame ignition is examined for the renewable fuels 1-Octanol and OME and compared with the Diesel surrogate n-Dodecane. The investigation utilizes a high-fidelity Large Eddy Simulation framework coupled with a tabulated flamelet-generated manifold combustion model.

In particular, the influence of the changed thermophysical properties on mixture formation is elucidated. Further, the effect of the changed thermophysical properties on ignition is investigated. Also, the influence of the changed chemical kinetic properties on ignition is examined. The impact of the latent heat of evaporation on ignition will be elucidated. The flame structures of 1-Octanol and $\mathrm{OME_{mix}}$ are compared to the Diesel reference fuel n-Dodecane. The analysis is performed in an automotive, heavy-duty and marine injector with increasing nozzle sizes, and the influence of the nozzle size on ignition is discussed.

Excellent agreement of the Large Eddy Simulations under inert conditions with experimental data regarding liquid penetration and vapor penetration length is achieved. The mixture formation analysis of the automotive Engine Combustion Network (ECN) Spray A3 injector shows that 1-Octanol and n-Dodecane exhibit a similar mixture formation process, while $\mathrm{OME_{mix}}$ shows higher values of the scalar dissipation rate and a narrower spray shape. The mixture formation process in the heavy-duty ECN Spray D and marine injector from Woodward L'Orange show delayed mixture formation. The large particle diameter leads to reduced drag and consecutive less momentum exchange and heat transfer to the liquid phase. The temperature distribution of the gas phase clearly shows that the heat loss due to evaporation of 1-Octanol is pronounced. The comparison of the adiabatic mixing line assumed in the combustion model and the temperature distribution in the spray revealed that the higher heat capacity of n-Dodecane inherently leads to a more concave shape of the adiabatic mixing line. This fuel property makes n-Dodecane less sensitive to spray cooling effects on ignition.

The flame structure is first investigated utilizing laminar non-premixed 1D flamelet simulations. OME$_{\mathrm{mix}}$ shows the highest reactivity and the lowest ignition delay times for different scalar dissipation rates at stoichiometry. Furthermore, the highest ignition limit is observed for OME$_{\mathrm{mix}}$. Compared to OME$_{\mathrm{mix}}$, the ignition delay time of n-Dodecane is increased, and its ignition limit is significantly lower. 1-Octanol shows the highest ignition delay times at lower scalar dissipation rates at stoichiometry. In the proximity of the ignition limit of n-Dodecane, the ignition delay time of 1-Octanol is shorter, which is explained by an increased reactivity of 1-Octanol during the high-temperature ignition. A novel flamelet model is derived that incorporates the heat losses due to evaporation based on the results from the analysis of the gas temperature distribution of the spray. In contrast to methods from the literature, the presented model is physically consistent and does not change the spray flame structure.

The novel flamelet model is utilized in the reactive spray simulations for all fuels and injectors investigated. The typical onset of ignition over the spray head in ECN Spray A3 has been confirmed for all fuels. In contrast, the start of ignition at the spray flanks has been observed in the ECN Spray D and the marine injector from Woodward L'Orange. In this thesis, a cause-effect mechanism has been identified that explains the different ignition locations. The onset of ignition in mixture fraction space is similar for each fuel in all injectors. This finding suggests that the mixture formation process dominates the ignition location. The comparison of different-sized nozzles shows that the lowest ignition delay time is found for Spray A3, and the ignition delay time of the larger nozzles is increased. The trend from the flamelet simulation of the lowest ignition delay time for OME$_{\mathrm{mix}}$ is also observed in the spray flame. OME$_{\mathrm{mix}}$ exhibits a significantly different mixture formation and ignition behavior than 1-Octanol and n-Dodecane, due to its high stoichiometric mixture fraction. The mixture formation process of n-Dodecane and 1-Octanol is similar, while the ignition delay time of n-Dodecane is shorter than that of 1-Octanol. The influence of heat loss due to evaporation is very prominent for 1-Octanol. The flamelet model without the heat-loss correction underestimates the ignition delay time by $25\,\%$. The heat-loss corrected model perfectly aligns with the experimental ignition delay time. Overall, this thesis contributes to the understanding of the ignition of spray flames with renewable Diesel fuels. Significant differences in the mixture formation process have been identified and explained with the changed thermophysical properties. A novel flamelet model incorporating heat loss due to latent heat of evaporation is developed and successfully utilized in the simulation of reactive sprays in LES. Perfect agreement by means of ignition delay time and flame structure has been achieved. This thesis significantly contributes to a deeper understanding of renewable fuels in the context of defossilation. The results of this thesis can be utilized to develop new technologies that reduce greenhouse gases in the transport sector and slow down global warming.

1 Introduction

The human-caused climate change is one of the most threatening and challenging problems of the forthcoming generations. Global warming is scientifically proven [5] and already creating environmental changes that are difficult to reverse. The rising sea levels are flooding more and more areas at low sea levels. The number of wildfires is already increasing and is supposed to increase significantly until 2100 [6]. The emissions of greenhouse gases must be reduced drastically to stop global warming and meet the Paris Agreement [7].

As reported in the Annual European Union Greenhouse Gas Inventory [8], in the European Union, the transport sector has been the only key category to increase the CO_2 emissions in the last thirty years. In the future, the transport sector is expected to increase even further [9–11]. Hence, novel technologies are needed to reduce CO_2 emissions. While in the passenger transport sector, Battery Electric Vehicles (BEV) charged with renewable electricity might reduce CO_2 emissions [12], electrification of aviation, marine and heavy-duty applications is cumbersome. Especially in the heavy-duty application, liquid fuels will be needed in the future [9, 13, 14], since the energy density of batteries is still significantly lower than liquid fuels [15, 16]. The reduction of CO_2 in the transport sector can be achieved by two routes [17]:

Decarbonization completely removes carbon from the energy conversion process. In this route, fuels like hydrogen or ammonia may be used due to their molecular structure without carbon atoms.

Defossilation intends to replace fossil fuels with fuels from renewable sources [17].

Currently, the route of Defossilation[1] is favored over Decarbonization due to the retrofit possibilities of renewable Diesel fuels. Biogenic and synthetic fuels are promising candidates to reduce CO_2 emissions in the transport sector [14]. Renewable fuels are usually produced with the Power-to-X concept, which might solve multiple issues in the energy sector. Surplus electricity from peaks in renewable power plants can be stored in, e.g., liquid fuels and stabilize the electricity grid [18]. Especially renewable fuels with Diesel-like properties are the focus of current research [14]. Biogenic and synthetic fuels bind CO_2 from the atmosphere during production and hence, are considered carbon-neutral [19, 20]. The demand for renewable energy sources is higher than ever before and will increase in the future [10]. Recent studies showed [1, 21–23] that the thermophysical and combustion properties of renewable carbon neutral Diesel fuels are significantly different. In order to use renewable fuels in engine applications, the influence of changed thermophysical and chemical kinetic properties on mixture formation and ignition in spray flames under Diesel relevant conditions needs further research.

---

[1] Defossilation is also referred to as Defossilisation. Within this thesis, the term defossilation is used.

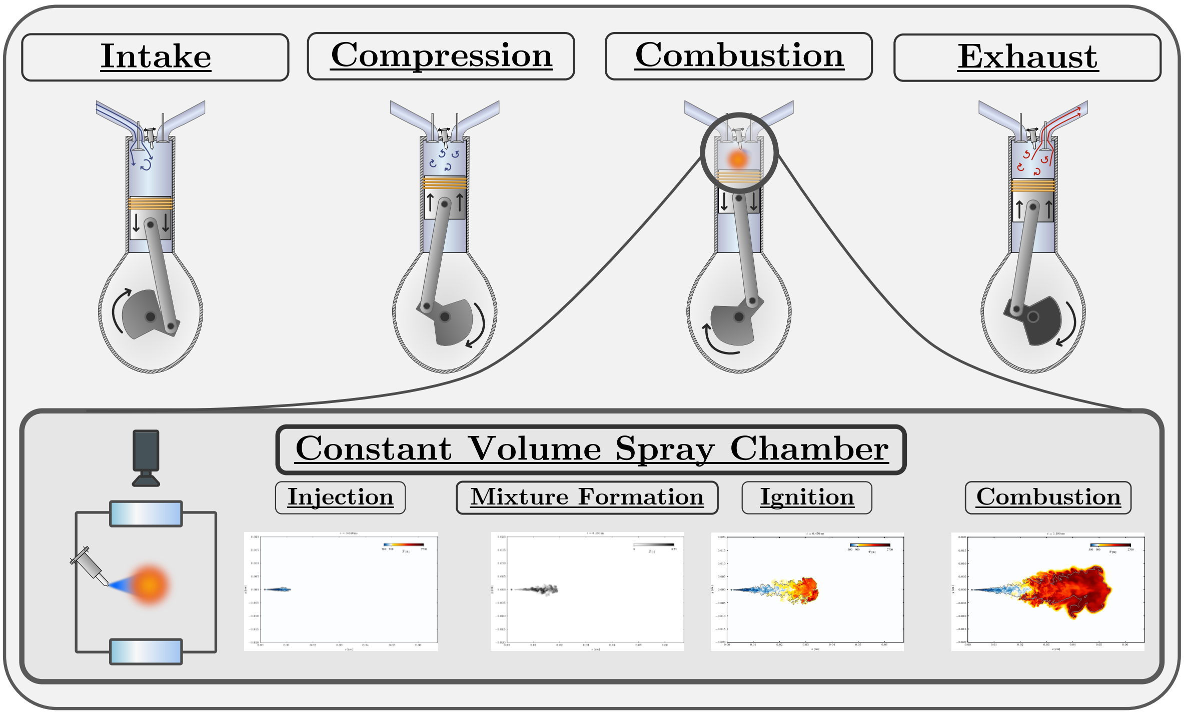

Figure 1.1: Schematic of a four-stroke direct injection Compression Ignition (CI) engine cycle. The spray flame cause-effect chain comprising injection, mixture formation, ignition and combustion is investigated in the simplified Constant Volume Combustion Spray Chamber, reducing the complexity of piston movement and flow in the engine. Even though the high-pressure, high-temperature spray combustion chamber is a simplified geometry, it maintains the full physical complexity.

Modern direct injection Compression Ignition (CI) Diesel engines are complex and constantly under development, optimizing emission reduction to meet new regulations. Besides engine test benches, Computational Fluid Dynamic (CFD) simulations are nowadays an indispensable tool for engine pre-development. With the help of CFD, novel engine designs and combustion process methods can be tested rapidly without manufacturing new parts or expensive time on the test bench. However, numerical models need accurate initial conditions. Hereby, the engine cause-effect chain comprises the spray formation, mixing, combustion and emission production. In particular, combustion models require precise information about mixture formation and temperature distribution in the combustion domain. Regarding the engine, the first steps in the cause-effect chain are spray formation and mixture formation, defining the initial conditions and prediction accuracy of the subsequent simulation of combustion and emission production.

However, as shown in Figure 1.1, the mixture formation process of a four-stroke direct injection Diesel compression ignition engine is very complicated. The moving piston and intake flow in the compression stroke introduce complexity to the system interacting with the combustion process. Hence, it is suitable to investigate combustion in a simplified geometry while maintaining full physical complexity. A common approximation for the ignition process in the engine is a constant volume, high-pressure and high-temperature spray chamber. Especially for novel fuels, the experimental and numerical investigation in constant volume spray chambers is beneficial.

In the context of renewable Diesel fuels, the biogenic fuel 1-Octanol[2] and the E-fuel (Poly-)oxymethylene

---

[2] 1-Octanol: C8H18O

ether (OME_x[3]), are two promising Diesel alternatives. However, due to their chemical composition, the two fuels exhibit significantly different thermophysical and combustion properties compared to reference Diesel fuels, e.g., n-Dodecane[4] [1, 2, 21, 24–28]. The changes from different fuel properties on injection, mixture formation and combustion have not yet been comprehensively examined and understood. Hence, developing new technology with renewable Diesel fuels needs further research. Efficient and accurate models are needed to incorporate the effects introduced by novel renewable fuels on combustion. High-fidelity numerical models, such as the Large Eddy Simulation, are crucial for understanding complex mixing and ignition phenomena in high-pressure spray flames.

In this context, this thesis investigates the influence of thermophysical properties and changed chemical kinetics of 1-Octanol and a mixture of OMEs in high-pressure sprays using Large Eddy Simulations. Furthermore, the influence of increasing nozzle sizes for automotive, heavy-duty and marine injectors is examined. The objectives of this thesis are placed in the context of the archival literature. Subsequently, the aims of this thesis are derived from the literature review.

1.1 Renewable Diesel fuels and spray flames

The following presents a brief but comprehensive overview of the carbon-neutral biogenic Diesel fuel 1-Octanol and the synthetic fuel Polyoxymethylene ether (OME). First, production methods are shown in Sec. 1.1.1, next, emission reduction potentials are discussed in Sec. 1.1.2. In Sec. 1.1.3, the changed thermophysical and chemical kinetic properties are elucidated. Finally, an overview of spray flames with 1-Octanol and OME is presented in Sec. 1.1.5. The literature review reveals open questions regarding modeling and changed combustion properties of renewable Diesel fuels. The aims and questions of this thesis are derived based on the review.

1.1.1 Production routes for the carbon dioxide neutral Diesel fuels 1-Octanol and (Poly-)oxymethylene ethers

The production of 1-Octanol ($C_8H_{18}O$) is not scaled to plant size yet. Though 1-Octanol is already used in the beauty industry for fragrances [29], further research is needed to produce the fatty alcohol on a large scale from biogenic feedstock. In the literature, mainly two pathways are described. One route is the catalytic production of 1-Octanol from biomass [30] via furfural-acetone [31]. The second and main pathway uses genetically modified E-coli bacteria to convert glucose or fatty acids to 1-Octanol [29, 32–34]. The basic chemicals are derived from organic origins, which can be produced from Cyanobacteria/Algae [35]. Further information can be found in the review of Kremer et al. [34]. In Kremer et al. [34], low efficiencies are reported for the pathways described here, while efficiency is assumed to be improved immensely. A considerable advantage of producing 1-Octanol from renewable organic materials is that no hydrogen is used in the production process. Furthermore, the production of 1-Octanol is considered a backstop technology.

The synthesis of OMEs ($H_3C\text{-}O\text{-}(CH_2O)_x\text{-}CH_3$, mainly a mixture of $x \in [3,4,5]$ named OME_{mix}) can be achieved by a manifold of pathways. Most routes start with the basic chemical methanol. Methanol is mainly produced from green hydrogen from electrolysis with renewable energy and carbon dioxide [36, 37]. The CO_2 can be obtained by separation from existing industrial processes, e.g., coal power plants, cement factories, the

---

[3] OME_x: $H_3C{-}O{-}[CH_2{-}O]_x{-}CH_3$, x=1-7
[4] n-Dodecane: n-C12H26

production of ammonia and biogas plants. An alternative is capturing CO_2 from ambient air, which is currently very expensive [20]. Another possible green route for CO_2 production is the anaerobic digestion of biomethane [20]. Some authors also describe methanol production from biomass [38] or from natural gas [39].

An intermediate step in the production of OME is the synthesis of formaldehyde from methanol. From formaldehyde, methylal and trioxane are produced [39, 40]. Methylal and trioxane are further synthesized to OME using catalytic reactions. Different studies conducted a Life Cycle Analysis and cost evaluation [20, 41, 42]. In Rodriguez-Vallejo et al. [20], various pathways of the synthesization of OME are evaluated. Some routes even show a negative CO_2 balance [20]. Due to many unknown cost developments for electricity, hydrogen and CO_2, a price estimation for OME is cumbersome [41]. In 2021, the price for OME was estimated to be 1.5-3.6 times higher than Diesel [20]. Meanwhile, the Diesel cost roughly increased 50% compared to 2021. In Europe, higher taxes for fossil fuels are expected, so OME can be considered competitive with Diesel. In Ueckerdt et al. [42], the possible lack of green hydrogen in Germany is discussed. From a global perspective, the shortage of green hydrogen could be mitigated by producing OMEs in sunny areas internationally. Also, the production of OMEs is considered a backstop technology [42].

1.1.2 Emission reduction potentials

Besides the carbon neutrality of 1-Octanol and OME_{mix}, both fuels are reported to reduce combustion emissions significantly. In the following, the reduction potentials are outlined.

Multiple studies in engines [43–46], observed lower CO emissions for 1-Octanol compared to Diesel. In Graziano et al. [43], also lower CO_2 emissions were reported. Diesel and 1-Octanol blends showed significantly lower formation of NO_x and soot [45–50]. Already small amounts of 1-Octanol reduce soot formation up to 75% [43]. The low sooting tendency of 1-Octanol can be utilized to reduce NO_x emissions (soot-NO_x trade-off). Furthermore, higher Brake Thermal Efficiencies (BTE) are reported [45, 46, 48]. 1-Octanol shows lower exhaust gas temperatures [45, 51], which might cause a negative impact on the exhaust gas after-treatment process.

Also, OME_{mix} is reported to show lower NO_x and CO emissions in engines [52–54]. OME's higher brake thermal efficiency is shown in multiple engine experiments [55–57]. The high degree of bound oxygen in all OMEs inhibits soot formation particularly. Many studies showed the potential to decrease soot formation from neat OME_{mix} and blends with Diesel [28, 38, 52, 57–65]. The soot volume fraction of neat OME_{mix} is so low that it is almost not measurable [58, 66]. Furthermore, Particulate Matter (PM) is also reduced in number and size of particulates [53, 58, 67–69]. In Avolio et al. [68], Real Driving Emission (RDE) measurements revealed that a blend of Diesel and 7 % of OME_{mix} already fulfills the requirements of the Euro 6d regulation.

In summary, 1-Octanol and OME_{mix} are promising candidates to cut emissions, such as CO, net CO_2, NO_x, PM and soot significantly. Both fuels will help to reduce the Green House Gas footprint in the transport sector by defossilation.

1.1.3 Changes in thermophysical properties and chemical kinetics

The changed molecular structure of 1-Octanol and OME due to bound oxygen significantly influences the thermophysical and chemical kinetic properties. This section highlights the most significant changes compared to standard Diesel fuels.

Thermophysical properties Most liquid properties of 1-Octanol are very similar to n-Dodecane as a Diesel surrogate. 1-Octanol exhibits a slightly higher liquid density than n-Dodecane [70]. Vapor-Liquid Equilibria (VLE) measurements in [2, 27] revealed a slightly higher vapor pressure compared to Diesel, which was also reported in Ambrose et al. [71]. A significant difference to n-Dodecane and OME is the high latent heat of evaporation of 1-Octanol [70, 71] that might change the mixture formation process.

Also, the thermophysical properties of OMEs exhibit significant differences to n-Dodecane. In the context of the German publicly funded project "E2Fuels" (funding number: 19|18009|), liquid thermophysical properties of OME_3 and OME_4 have been measured and published [2, 22]. The group of OMEs shows a significantly higher liquid density compared to 1-Octanol and n-Dodecane [22]. The vapor pressure measurements at lower temperatures of Boyd et al. [72] suggested a similar vapor pressure of OMEs compared to n-Dodecane. However, the detailed measurements up to the vicinity of the critical temperature from Fechter et al. [2] revealed that the vapor pressure is significantly higher than n-Dodecane and 1-Octanol. Other recent studies used theoretical models (e.g., force field methods) to derive the thermophysical properties for OME [73, 74] and used the data from Boyd et al. [72] as input. The high-fidelity measurements from Fechter et al. [2] and Beutler et al. [22] are more accurate and therefore used in this thesis. In this work, the influence of the higher vapor pressure of OME on the spray and mixture formation is investigated using Large Eddy Simulations.

Chemical kinetics For the modeling of combustion, detailed chemical kinetic reaction mechanisms are needed. These mechanisms include all relevant reactions and species involved in the combustion reactions. Since 1-Octanol is relatively new in the context of Internal Combustion Engines (ICEs), only a few reaction mechanisms are available. Mainly there are three mechanisms known to the author. The first mechanism was developed by Cai et al. [25] and was reduced by Li et al. [75]. A newer reaction mechanism for 1-Octanol is developed by Pelucchi et al. [76] in the CRECK modeling group (POLIMI). The mechanism of Pelucchi et al. has been utilized in this thesis since it performed best in the reactive spray flame simulations. All kinetic mechanisms show that the chemical ignition delay time of 1-Octanol is higher than n-Dodecane and OME. The ignition delay time of 1-Octanol in engines is also reported to be higher [44, 47]. Further, the bound oxygen atom in 1-Octanol increases the stoichiometric mixture fraction.

OMEs have received more attention recently, and many reaction mechanisms have been developed. The first mechanism from Sun et al. [77] was developed based on laminar flame speed measurements of OME_3. The mechanism by Sun et al. was further reduced in He et al. [78]. The first mechanism, including OME_3 and OME_4, was developed by Cai et al. [24]. This mechanism included experimental data of shock tube measurements and data from Rapid Compression Machine (RCM) experiments that represent the auto-ignition process. A newer reduced mechanism by Niu et al. [79] is based on the mechanism by Cai and includes modeled kinetic data for OME_5 and OME_6. However, no thermophysical data is available for OME_5 and OME_6, which is needed in the CFD. Hence, the detailed mechanism by Cai et al. [24] is used in this thesis. The group of OMEs are reported to be highly reactive fuels, exhibiting short chemical ignition delay times. However, OME's Lower Heating Value (LHV) is significantly lower than n-Dodecane. The LHV for OME_3 is approximately $50\,\%$ lower compared to Diesel [80]. For the equivalent energy of Diesel, the volumetric flow rate has to be increased by a factor of 1.75 [54]. The high level of oxygenation of OMEs increases the stoichiometric mixture fraction significantly. Compared to n-Dodecane, the stoichiometric mixture fraction of OME_3 at the boundary conditions used in this thesis is doubled. The high stoichiometric mixture fraction is a crucial difference from standard hydrocarbons and is essential in the mixture formation process.

Hence, this thesis examines the influence of changed thermophysical properties, e.g., increased vapor pressure and latent heat of evaporation, on the mixture formation. Further, the influence of different chemical kinetic properties on mixture formation and ignition is investigated in this thesis.

1.1.4 ECN: Reference spray flames

The Engine Combustion Network (ECN) is a group of established research institutes examining reference injectors in Constant Volume Combustion Chambers that are representative of Diesel engine combustion. The boundary conditions for each case are standardized and publicly available [81]. The joint effort collected a large database of experimental and numerical reference data that gives a comprehensive insight into Diesel combustion. In particular, ECN Spray A and ECN Spray D represent automotive and heavy-duty Diesel injectors that have been studied by many facilities and at various boundary conditions. In the past, the Diesel surrogate n-Dodecane has been used for investigation. In the last workshops organized by the ECN [81], the focus was set on renewable Diesel fuels. The following section provides an overview of existing reference spray flames.

1.1.5 Reference spray flames of renewable Diesel fuels

In order to be able to better classify this thesis in the context of existing studies, in the following studies on spray flames with the reference fuel n-Dodecane and the renewable fuels 1-Octanol and OME are presented.

The standard surrogate fuel for Diesel, n-Dodecane, has been a focus in the Engine Combustion Network and has been extensively studied experimentally and numerically. Most studies examined spray flames in the Spray A injector, representing light-duty vehicles. Recent studies also investigate spray flames in the heavy-duty injector Spray D. A non-exhaustive list of experimental works is provided here: [82–88]. The mixture formation process of the automotive Spray A and the heavy-duty injector Spray D exhibit remarkable differences. The experimental works show that the liquid penetration length of Spray D is approximately doubled compared to Spray A. The ignition delay time increases with the nozzle size. For n-Dodecane, the ignition delay time in Spray D is increased by approximately $30\,\%$ compared to Spray A. The ignition location in Spray A is reported at the spray head, while in Spray D, the onset of ignition is observed at the spray flanks. The experimental findings are reproduced in reactive CFD simulations. The tabulated chemistry approach has been proven in many studies to reproduce the flame characteristics of the injectors very well [3, 89–95]. Due to low numerical cost and low computation time, the Reynolds Averaged Navier Stokes (RANS) framework is commonly utilized in reactive spray flame simulations. In a RANS framework, inherently, only global combustion characteristics, such as the ignition delay time, can be reproduced. The complex interaction of mixture formation and ignition can only be investigated in high-fidelity Large Eddy Simulation (LES) or Direct Numerical Simulation (DNS) frameworks. The increasing availability of computing resources enabled the detailed examination of spray flames in LES. Recent studies investigated the spray flames of Spray A and Spray D in LES [96–105]. Even though the ignition location at the spray head in Spray A and at the spray flanks for Spray D are reproduced in LES [93, 94, 97, 104], no comprehensive explanation has been found yet and will be addressed in this thesis.

In contrast to n-Dodecane, only limited information about mixture formation and spray flame structure can be found for 1-Octanol. One of the first experimental studies to investigate inert sprays of Di-N-Butyl Ether with 1-Octanol by Palmer et al. [106] highlighted the need for investigations with neat 1-Octanol. Very recently, the study by Strauß et al. [21] examined the mixture formation process of 1-Octanol in the Spray A3 injector[5]. The study revealed that 1-Octanol, with a higher volatility than n-Dodecane, exhibits longer liquid penetration lengths, suggesting differences in mixture formation. In Tian et al. [107], blends of Biodiesel and 1-Octanol showed a changed mixture formation behavior in a constant volume spray chamber under inert conditions. Increased vapor penetration lengths with increasing content of 1-Octanol are reported. Only the study of Ruiz-Rodriguez et al. [51] examines the spray flame structure of 1-Octanol experimentally. The

---

[5] The Spray A3 nozzle is approximate $10\,\%$ larger than Spray A and has a higher conicity factor: K_{SA3}=3 vs. K_{SA}=1.5.

study shows that 1-Octanol produces less soot compared to n-Dodecane. To the author's best knowledge, no numerical study has been published on mixture formation and spray flame ignition for 1-Octanol in the archival literature.

In the literature, the mixture of OME_3, OME_4 and small shares of OME_5 is often referred to as OME_{mix}. Since thermophysical properties are not available for OME_5, OME_{mix} is usually modeled as $60\,\%$ OME_3 and $40\,\%$ OME_4 by volume. Experimental studies investigating OME sprays revealed substantial changes in the mixture formation process. In Dageförde et al. [108], OME_{mix} has been examined in the Spray A injector. The comparison to n-Dodecane using Phase-Doppler-Anemometry (PDA) showed smaller spray velocities for OME_{mix} and less air entrainment. Also, the study of Strauß et al. [21] showed significant differences between n-Dodecane and OME_{mix} in the Spray A3 configuration. Even though OME_{mix} is more volatile, the liquid penetration of OME_{mix} is longer than the less volatile n-Dodecane. The higher liquid penetration length of OME_{mix} suggests a significant change in the mixture formation process. The experimental and numerical study of neat OME_3 and neat OME_4 in a close-to-series heavy-duty injector further suggests that the mixture formation among OMEs exhibits differences [1, 28]. Inner-nozzle flow simulations suggest that cavitation might occur [28]. The tendency for cavitation of OME_{mix} has been confirmed in the ECN Spray C in Singh et al. [109]. The spray flame structure of OME_{mix} has been experimentally studied in Spray A and Spray D in [82, 110, 111]. One key finding is that OME_{mix} does not produce any soot in both injectors. Furthermore, the ignition delay time is significantly shorter than for n-Dodecane. The ignition delay time also increases with the nozzle size, but OME_{mix} is not as sensitive as n-Dodecane. Regarding the flame structure, OME_{mix} shows less formation of the excited OH radical, which has been reported in Ma et al. [66]. The spray flame shape for OME_{mix} is slightly narrower than with n-Dodecane. Chemiluminescence imaging revealed that the formation of OH^* is distributed closer to the spray center line [82].

One of the first simulations of OME_4 has been presented by Goeb et al. [59] and showed significant differences in mixture formation between n-Dodecane and OME_4. However, the Large Eddy Simulation in Goeb et al. [59] underestimated the experimental ignition delay time by approximately $40\,\%$. The spray flame structure of OME_{mix} has been studied in Spray A conditions in an LES framework by Mira et al. [112]. The flame structure of OME_{mix} showed substantial differences from n-Dodecane. The spray flame of OME_{mix} is narrower than n-Dodecane, and the iso-line of the stoichiometric mixture fraction shows separated fuel-rich clouds, while n-Dodecane exhibits an enclosed iso-line of the stoichiometric mixture fraction. Further, the ignition delay time of OME_{mix} is reported to be shorter than n-Dodecane. The RANS simulation of Wiesmann et al. [113] confirmed differences in the mixture formation of OME_{mix} in the Spray A3 injector. As observed in Wiesmann et al. [113], the ignition delay time for OME_{mix} is constantly underestimated by $30\,\%$ for different boundary conditions, raising the question of whether the mixture formation and flamelet models used, need to be extended for changed thermophysical and chemical kinetic properties. Also, the study in RANS by Benjaes et al. [114] of OME_{mix} in Spray A and Spray D conditions underestimated the ignition delay time. Benjaes et al. [114] revealed that the onset of ignition in Spray A for OME_{mix} is located at the spray head and at the spray flanks for Spray D. The study of Haspel et al. [1] was the first to investigate neat OME_3 and neat OME_4 in a close-to-series heavy-duty injector in LES. Significant differences in the mixture formation process among the fuels were observed. While the flame structure analysis in the flamelet simulation revealed an earlier ignition for neat OME_3, the spray flame of OME_4 ignited before OME_3, which is explained with a different mixture formation process in the spray. The study of Haspel et al. [1] revealed that the mixture formation process plays a vital role in the ignition process and the flame structure of OMEs.

1.2 Scientific questions and aims of this thesis

Diesel fuels from renewable sources show great potential to reduce CO_2 emissions. The biogenic aliphatic long-chained alcohol 1-Octanol is produced from organic feedstock. Since the bound carbon comes from photosynthesis, the combustion of 1-Octanol is considered CO_2 neutral. Also, the oxygenated oligomer OME is considered CO_2 neutral when produced from green hydrogen and ambient CO_2. Both fuels have bound oxygen in their molecular structure, which enables the reduction of soot in Diesel blends. Neat 1-Octanol and OME practically show no soot production in engines. However, bound oxygen also substantially changes the thermophysical properties of 1-Octanol and OME. High latent heat of evaporation is reported for 1-Octanol, compared to the reference fuel n-Dodecane. $\mathrm{OME}_{\mathrm{mix}}$, on the other hand, has a significantly increased vapor pressure. Both fuels show a changed mixture formation behavior. Furthermore, the chemical behavior of the renewable fuels is different. While 1-Octanol shows reduced reactivity and higher ignition delay times, OMEs show an increased reactivity and exhibit low ignition delay times.

The literature review elucidated the high potential of 1-Octanol and $\mathrm{OME}_{\mathrm{mix}}$ to reduce greenhouse gas emissions, NO_x and soot. However, the influence of changed thermophysical properties on mixture formation is an unanswered question for 1-Octanol and OME. The complex interplay of mixture formation and chemical kinetics is not comprehensively understood. Moreover, the influence of larger nozzle sizes on mixture formation and ignition is an open question in the literature.

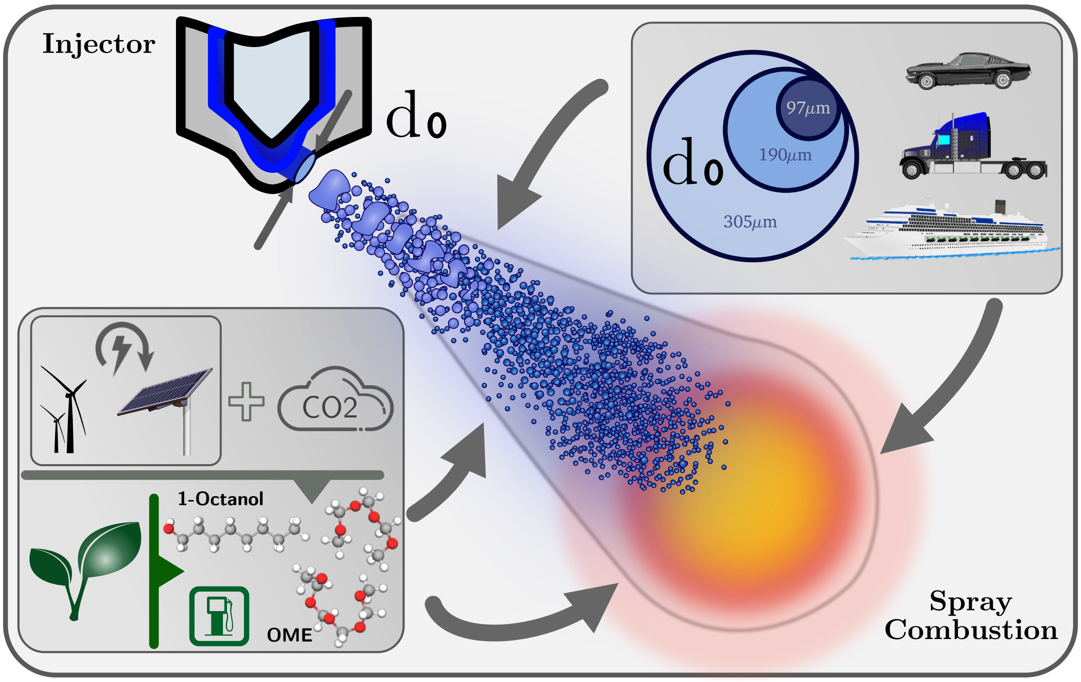

Figure 1.2: Illustration of the aims of this thesis: How do renewable Diesel fuels change the mixture formation process and spray combustion? Which effect does the nozzle size have on mixture formation and spray combustion?

The aim of this thesis is to elucidate the effects of changed thermodynamic and chemical kinetic properties and increased nozzle sizes on mixture formation and ignition. A graphical illustration of the aims of this thesis is shown in Figure 1.2. The aims and questions of this thesis are summarized in bullet points:

Question How do the changed thermophysical properties affect the mixture formation process?

Question How do the changed thermophysical properties, e.g., higher latent heat of evaporation and vapor pressure, change the ignition behavior compared to conventional fuels (e.g., n-Dodecane)?

Question How do the changed chemical kinetic properties influence the spray flame structure?

Question How do the changed chemical kinetic properties influence the ignition of spray flames?

Question How do increasing nozzle sizes (automotive, heavy-duty and marine injector) influence the ignition behavior?

The scientific questions of this thesis are answered in the following. This thesis is structured as follows. First, in Sec. 2, the governing equations, models and numerical models are presented that are used for the inert and reactive Large Eddy Simulations in this thesis. In Sec. 3, the experimental data and methods are briefly explained. Subsequently, the numerical framework of the Large Eddy Simulation is presented in Sec. 4. In particular, the meshes for the different injector setups are presented. The scientific question of how the changed thermophysical properties influence the mixture formation process under inert conditions is investigated in Sec. 5. Further, the influence of increasing nozzle size on mixture formation is examined among the different fuels. The chemical ignition delay times and the spray flame structures are investigated in Sec. 6. The ignition under strained conditions is investigated in the laminar non-premixed flamelet model. A novel flamelet model is derived, which includes the effect of the enthalpy loss due to the latent heat of evaporation. Finally, in Sec. 7, the turbulent spray flame structure of n-Dodecane, 1-Octanol, and $\mathrm{OME}_{\mathrm{mix}}$ is examined in the Large Eddy Simulation. The different mixture formation processes and ignition delay times among the fuels and different injectors are discussed. The thesis is closed in Sec. 8 with a summary and conclusion.

2 Governing equations, Models and Numerical Methods

Spray injection is a dispersed multi-phase problem with complex physical processes: high-pressure injection, breakup, evaporation, mixture formation, turbulence, diffusion and finally, combustion and pollutant formation. All processes are strongly coupled, and each subproblem has a high level of complexity itself. Hence, not all effects are solved by fundamental physical equations but need modeling. In this thesis, a high-fidelity framework is used, trying to minimize the modeling portion. In the following, all equations and models used are briefly presented.

2.1 Gas phase

In the following, the equations for fluid motion used in this thesis are presented. In general, fluid motion can be described by the Navier-Stokes equations. These basic equations describe both inert and reactive conditions in equal measure. In the case of reactive spray simulations, the variable density formulation is applied. For inert simulations, additional transport equations for the species mass fractions for each species Y_k are solved. In this work, additional transport equations for the mixture fraction Z and normalized progress variable Y_C are solved for reactive simulations.[1]

2.1.1 Governing equations

The governing equations used for the inert and reactive spray simulations are presented in the following.

2.1.1.1 Mass conservation equation

Eq. 2.1 denotes the mass conservation equation for spray simulations. Here, ρ represents density, u_j is the velocity in direction j, x_j is the spatial coordinate, and $\dot{S}_m$ is the evaporation source term of evaporated fuel that is further explained in Sec. 2.2.

$$\frac{\partial \rho}{\partial t} + \frac{\partial \rho u_j}{\partial x_j} = \dot{S}_m \tag{2.1}$$

---

[1] In the following, the "Einstein summation convention" is used, where if indices appear twice, the terms are summed.

2.1.1.2 Species mass fraction transport equation

It is common to solve additional transport equations for each species k of the mixture to determine its spatial distribution. These equations are formulated in terms of the species mass fraction Y_k, which is defined as the mass fraction of a single species mass m_k, over the total mass:

$$Y_k = \frac{m_k}{\sum_{k=1}^{N} m_k}. \tag{2.2}$$

The transport equation for each species k is further defined as:

$$\frac{\partial \rho Y_k}{\partial t} + \frac{\partial \rho Y_k \left(u_j + V_{k,j}\right)}{\partial x_j} = \dot{\omega}_k + \dot{S}_k. \tag{2.3}$$

In Eq. 2.3, $V_{k,j}$ is the diffusion velocity of each single species k in direction j. On the right-hand side, $\dot{\omega}_k$ is the so-called chemical source term accounting for production and consumption in chemically reacting flows for each species (see Sec. 2.3.1). In inert simulations, $\dot{\omega}_k$ is set to zero in this thesis. Furthermore, $\dot{S}_k$ denotes the evaporation source term that accounts for the evaporation of liquid fuels in (Diesel) sprays, which is further explained in Sec. 2.2.

Summing up over all species N transport equations, the conservation of mass in Eq. 2.1 may not be violated by definition. It can be shown that the following conditions apply to fulfill mass conservation [115]:

$$\sum_{k=1}^{N} Y_k \overset{!}{=} 1, \tag{2.4}$$

$$\sum_{k=1}^{N} Y_k V_{k,j} \overset{!}{=} 0, \tag{2.5}$$

$$\sum_{k=1}^{N} \dot{\omega}_k \overset{!}{=} 0. \tag{2.6}$$

2.1.1.3 Diffusion velocity

Within this thesis, the Fick diffusion model is employed. The diffusion velocity $V_{k,j}$ is assumed to be proportional to the gradient of the species mass fraction and the diffusion coefficient D_k:

$$V_{k,j} = -D_k \frac{1}{Y_k} \frac{\partial Y_k}{\partial x_j}. \tag{2.7}$$

The measurement of diffusion coefficients and their modeling is not straightforward. For larger molecules like hydrocarbons, in contrast to hydrogen, it is common to assume that the thermal a_k and species diffusivities D_k are equal. The Lewis number Le describes the ratio of thermal and species diffusivity. Within this thesis, the Lewis number of each species k is assumed to be unity $\mathrm{Le}_k = \frac{a_k}{D_k} = 1$, and differential diffusion effects due to high species diffusivity are neglected. Furthermore, each species of the mixture is assumed to have the same diffusion coefficient. The bulk diffusion coefficient D can then be calculated using the mixture mean thermal conductivity λ, the mean heat capacity c_p and mean density ρ:

$$D = \frac{\lambda}{\rho c_p}. \tag{2.8}$$

The modeling of λ and c_p is explained in Sec. 2.1.3.

2.1.1.4 Momentum conservation equation

The momentum conservation equation is given as follows:

$$\frac{\partial \rho u_i}{\partial t} + \frac{\partial \rho u_j u_i}{\partial x_j} = -\frac{\partial p}{\partial x_i} + \frac{\partial \tau_{ij}}{\partial x_j} + \rho g_i + \dot{S}_{u,i}. \tag{2.9}$$

Here, p denotes the pressure, τ_{ij} is the viscous stress tensor that is further described in Eq. 2.10, g_i is the gravitational acceleration in spatial direction i and $\dot{S}_{u,i}$ the momentum source term (see Sec. 2.2.1.2) that represents the coupling of the liquid and gaseous phase.

Applying the Boussinesq hypothesis [116], the viscous stress tensor τ_{ij} reads:

$$\tau_{ij} = \mu \left(\frac{\partial u_i}{\partial x_j} + \frac{\partial u_j}{\partial x_i} - \frac{2}{3}\delta_{ij}\frac{\partial u_p}{\partial x_p} \right). \tag{2.10}$$

In Eq. 2.10, μ is the dynamic viscosity (see also Sec. 2.1.3) and δ_{ij} is the Kronecker delta. The subscript $p = 1, 2, 3$ is used for the Einstein summation.

2.1.1.5 Energy conservation equation

The energy conservation in this work is formulated in terms of the total enthalpy. In Eq. 2.11, the definition of the total enthalpy is presented, where h_t is the total enthalpy, h_a is the absolute enthalpy and u_i the velocity in direction i [115].

$$h_t = h_a + \frac{u_i u_i}{2} \tag{2.11}$$

The absolute enthalpy h_a is composed of the sensible enthalpy h_s and its chemical part, the standard enthalpy of formation $\Delta h^0_{f,k}$ (at reference conditions T_0=298.15 K).

$$h_a = \sum_{k=1}^{n} h_{a,k} Y_k = \sum_{k=1}^{n} \left(\underbrace{\int_{T_0}^{T} c_{p,k} \mathrm{d}T}_{\text{sensible}} + \underbrace{\Delta h^0_{f,k}}_{\text{chemical}} \right) Y_k \tag{2.12}$$

In Eq. 2.12, $h_{a,k}$ is the specific absolute enthalpy (see also Sec. 2.1.3) of species k, Y_k the species mass fraction, $c_{p,k}$ the heat capacity at constant pressure for species k and $\Delta h^0_{f,k}$ represents the standard enthalpy of formation.

A general form of the total enthalpy equation reads [115]:

$$\frac{\partial \rho h_t}{\partial t} + \frac{\partial \rho u_i h_t}{\partial x_i} = \frac{\partial p}{\partial t} - \frac{\partial q_i}{\partial x_i} + \frac{\partial \tau_{ij} u_j}{\partial x_i} + \dot{Q} + \rho \sum_{k=1}^{N} Y_k f_{k,i} (u_i + V_{k,i}) + \dot{S}_{h_t} + \rho u_i g_i. \tag{2.13}$$

The first term on the left-hand side (LHS) resembles the transient change of the total enthalpy h_t, and the second term is the convective part of the enthalpy. On the right-hand side (RHS) of Eq. 2.13, $\frac{\partial p}{\partial t}$ expresses the enthalpy change due to pressure change, and q_i is the energy flux that reads:

$$q_i = -\lambda \frac{\partial T}{\partial x_i} + \rho \sum_{k=1}^{N} h_{a,k} Y_k V_{k,i}. \tag{2.14}$$

In the second term on the RHS of Eq. 2.14, it is commonly assumed that the sensible enthalpy, more precisely the heat capacity, is equal for all species. Furthermore, the enthalpy of formation is zero for elementary molecules, and compound molecules have the same order of magnitude and are assumed constant. Using Eq. 2.5, the second term on the RHS disappears, and it is possible to rewrite Eq. 2.14 as $q_i = -\frac{\lambda}{c_p} \frac{\partial h_a}{\partial x_i}$. Furthermore, it can be shown that for subsonic flows, the viscous heating term $\frac{\partial \tau_{ij} u_j}{\partial x_i}$ in Eq. 2.13 may be neglected [115]. In the present study, $\dot{Q}$ is also set to zero since no external energy sources, e.g., a spark plug, are considered. Also, the volume force $f_{k,i}$ in Eq. 2.14 is neglected. The spray enthalpy source term $\dot{S}_{h_t}$ represents the coupling with the liquid phase, see Eq. 2.56. The final enthalpy equation after reformulation reads:

$$\frac{\partial \rho h_t}{\partial t} + \frac{\partial \rho u_i h_t}{\partial x_i} = \frac{\partial p}{\partial t} - \frac{\partial q_i}{\partial x_i} + \dot{S}_{h_t} + \rho u_i g_i. \tag{2.15}$$

2.1.2 Turbulence modeling

In technical combustion applications, there are many examples of turbulent flows, e.g., power plants, spray and engine flow. In fluid dynamics, a well-known non-dimensional characteristic to distinguish if a flow field is laminar or turbulent is the Reynolds number [117]:

$$\mathrm{Re} = \frac{u L \rho}{\mu}. \tag{2.16}$$

A laminar flow is generally characterized as a layered flow, meaning no eddies occur. However, spatial and temporal changes may be observed. Low Reynolds numbers indicate a laminar flow, and high values of the Reynolds number indicate turbulent flow. From the Reynolds number, it can be derived that low velocities u, small length scales L, and low density flows ρ reduce the Reynolds number. Also, high-viscosity μ fluids dampen instabilities and reduce the Reynolds number leading to laminar flow. On the other hand, turbulent flows are characterized by the presence of eddies and their chaotic or stochastic nature. High velocities and low viscosity fluids allow perturbations to grow and build eddies. Different modeling strategies have been found to simulate turbulent flows. In the following, fully resolved and stochastic turbulence models are presented.

2.1.2.1 Direct Numerical Simulation (DNS)

The equations Eq. 2.1, Eq. 2.3, Eq. 2.9, and Eq. 2.13 comprehensively describe turbulent flows, if the spatial, temporal and chemical scales are discretized well enough. Simulations resolving all physical and chemical scales are called Direct Numerical Simulations (DNS). The dimensions of technical systems are in stark contrast to the discretization requirements of DNS. Hence, reduced complexity models have been developed to describe technical turbulent flows with Computational Fluid Dynamics (CFD) methods.

2.1.2.2 Reynolds-Averaged Navier-Stokes (RANS)

The statistical description of turbulent flows allows the decomposition of different length and time scales. A prevalent turbulence model is the Reynolds-Averaged Navier-Stokes (RANS) model. The basic concept is to decompose a flow quantity ϕ in its time-averaged $\langle\phi\rangle$ and fluctuating $\phi'(t)$ part. The Reynolds average is defined as:

$$\phi(t) = \langle\phi\rangle + \phi'(t). \tag{2.17}$$

After applying the Reynolds averaging on the Navier-Stokes equations, the flow components only depend on their mean values. Only the so-called Reynold stress term, arising from the Reynolds averaging procedure, depends on the fluctuating part. The Reynolds stress tensor cannot be calculated and needs modeling. Hence, the set of RANS equations is unclosed and needs a closure model. Further information can be found in Pope and Fröhlich [118, 119]. The solution of RANS equations represents the mean fields, so no detailed fluctuations are resolved. RANS simulations do not require high mesh resolutions, nor detailed temporal discretization. Due to the lower computational requirements and short simulation times, RANS simulations have a high popularity in pre-development. RANS modeling is mainly used, when only mean quantities are of interest, e.g., drag forces of a specific design or the efficiency of a new engine design. Whenever detailed information about the flow field is required, models of higher complexity have to be employed.

2.1.2.3 Large Eddy Simulation (LES)

A compromise between the very detailed DNS and the RANS simulation is the so-called Large Eddy Simulation (LES). The idea of LES is to resolve as many spatial and temporal fluctuations as possible, reducing the modeling proportion to the unresolved scales. This is accompanied by a higher spatial and temporal resolution, as well as higher computational cost compared to RANS, but significantly lower than DNS. The high fidelity character of LES allows a detailed investigation of the mixture formation of novel fuels with changed thermophysical properties and is the model of choice in this thesis. In contrast to RANS modeling, LES decomposes scales by filtering instead of averaging [120, 121]. All quantities ϕ are spatially filtered to separate the scales into a resolved (grid scale) and unresolved part (sub-grid scale (SGS)). The decomposition of scales reads:

$$\phi = \overline{\phi} + \phi'. \tag{2.18}$$

The filtered quantity $\overline{\phi}$ in Eq. 2.18 can be obtained applying a filter operation ($\bar{\cdot}$):

$$\overline{\phi}(\mathbf{x}) = \int \phi(\mathbf{r},\mathbf{x})G(\mathbf{r},\mathbf{x})\mathrm{d}\mathbf{r}, \tag{2.19}$$

where $G(\mathbf{r}, \mathbf{x})$ is the filter kernel. The filter kernel has its center around $\mathbf{x}$ and is evaluated as a function of the distance to the center $\mathbf{r}$. Besides the explicit filtering (Eq. 2.19), it is prevalent to use implicit spatial filtering in LES [118, 122]. The implicit filtering approach utilizes the grid resolution for scale separation instead of applying a filter operation. The mesh resolution has to be chosen according to the scale decomposition. A general rule is to resolve approximately $80\,\%$ of the turbulent kinetic energy [119]. The unresolved fluctuations are in the sub-grid scale, smaller than the smallest cell size. It has to be noted that choosing the correct cell size in multi-phase, particle-laden flows is not straightforward. Besides the discretization requirements for the gas phase, the liquid phase must also be considered. The spatial expansion of the largest particle size limits the smallest cell size. For spray simulations in particular, the thesis of Wehrfritz [91] proposed a ratio of $\frac{\Delta x}{d_0} \approx 60\,\%$ in LES (d_0 is the nozzle diamter and Δx the cell size) and is used in this thesis. If the cell size is significantly smaller than the largest particle, the results are not necessarily more accurate, but the computational effort increases significantly [123, 124].

The filtered transport equations contain terms of the form $\overline{\rho\phi}$ that cannot be retrieved from the LES. For variable density reactive flows, it is beneficial to apply the Favre-Filter [115, 118, 125]:

$$\widetilde{\phi} = \frac{\overline{\rho\phi}}{\overline{\rho}}, \tag{2.20}$$

and Favre decomposition:

$$\phi = \widetilde{\phi} + \phi''. \tag{2.21}$$

After applying the Favre filter $(\widetilde{\cdot})$ and some rearranging, the filtered transport equations for mass, momentum, enthalpy and species are derived.

$$\frac{\partial \overline{\rho}}{\partial t} + \frac{\partial \overline{\rho}\widetilde{u}_j}{\partial x_j} = \overline{\rho}\widetilde{\dot{S}}_m \tag{2.22}$$

$$\frac{\partial \overline{\rho}\widetilde{u}_i}{\partial t} + \frac{\partial \overline{\rho}\widetilde{u}_j\widetilde{u}_i}{\partial x_j} = -\frac{\partial \overline{p}}{\partial x_i} + \frac{\partial \overline{\tau}_{ij}}{\partial x_j} - \frac{\partial \tau_{ij}^{\mathrm{SGS}}}{\partial x_j} + \overline{\rho} g_i + \overline{\rho}\widetilde{\dot{S}}_{u,i} \tag{2.23}$$

$$\frac{\partial \overline{\rho}\widetilde{h}_t}{\partial t} + \frac{\partial \overline{\rho}\widetilde{u}_j\widetilde{h}_t}{\partial x_j} = \frac{\partial \overline{p}}{\partial t} - \frac{\partial \overline{q}_j}{\partial x_j} - \frac{\partial q_j^{\mathrm{SGS}}}{\partial x_j} + \overline{\rho}\widetilde{u}_j g_j + \overline{\rho}\widetilde{\dot{S}}_{h_t} \tag{2.24}$$

$$\frac{\partial \overline{\rho}\widetilde{Y_k}}{\partial t} + \frac{\partial \overline{\rho}\widetilde{u}_i\widetilde{Y_k}}{\partial x_i} = \frac{\partial}{\partial x_i}\left[\overline{\rho}\left(\widetilde{D} + \frac{\nu_{\mathrm{SGS}}}{\mathrm{Sc}_{\mathrm{SGS}}}\right)\left(\frac{\partial \widetilde{Y_k}}{\partial x_i}\right)\right] + \overline{\rho}\widetilde{\dot{S}}_k \tag{2.25}$$

The viscous stress tensor $\overline{\tau}_{ij}$ in Eq. 2.23 reads:

$$\overline{\tau}_{ij} = \overline{\mu}\left(\frac{\partial \widetilde{u}_i}{\partial x_j} + \frac{\partial \widetilde{u}_j}{\partial x_i} - \frac{2}{3}\delta_{ij}\frac{\partial \widetilde{u}_p}{\partial x_p}\right). \tag{2.26}$$

The new term τ_{ij}^{SGS} in Eq. 2.23 represents the unclosed term $\overline{\rho}(\widetilde{u_i u_j} - \widetilde{u}_i\widetilde{u}_j)$ representing the sub-grid scale viscous stress. The anisotropic part of the sub-grid viscous stress tensor is modeled with the Boussinesq hypothesis [116], similar to the viscous stress tensor, see Eq. 2.27.

$$\tau_{ij}^{\mathrm{SGS}} - \frac{1}{3}\delta_{ij}\tau_{pp}^{\mathrm{SGS}} = \overline{\rho}\nu_{\mathrm{SGS}}\left(\frac{\partial \widetilde{u}_i}{\partial x_j} + \frac{\partial \widetilde{u}_j}{\partial x_i} - \frac{2}{3}\delta_{ij}\frac{\partial \widetilde{u}_p}{\partial x_p}\right) \tag{2.27}$$

The sub-grid scale viscosity ν_{SGS} requires further closure through modeling (see Sec. 2.1.2.4).

Also in the filtered enthalpy transport equation (Eq. 2.24) the unclosed term $q_j^{\mathrm{SGS}} = \overline{\rho}(\widetilde{u_j h_t} - \widetilde{u}_j\widetilde{h}_t)$ arises after Favre-filtering. It is further commonly assumed that small eddies (sub-grid scale) have a diffusive character. Hence, closure for, e.g., q_j^{SGS} is obtained using the gradient assumption and introducing the turbulent thermal diffusivity $a_t = \frac{\nu_{\mathrm{SGS}}}{\mathrm{Pr}_{\mathrm{SGS}}}$, with $\mathrm{Pr}_{\mathrm{SGS}}$ being the turbulent Prandtl number.

$$\overline{q}_j = -\frac{\lambda}{c_p}\frac{\partial \widetilde{h}}{\partial x_j} = -\overline{\rho}\frac{\nu}{\mathrm{Pr}}\frac{\partial \widetilde{h}}{\partial x_j} \tag{2.28}$$

$$q_j^{\mathrm{SGS}} = -\overline{\rho}\frac{\nu_{\mathrm{SGS}}}{\mathrm{Pr}_{\mathrm{SGS}}}\frac{\partial \widetilde{h}_t}{\partial x_j} \tag{2.29}$$

2.1.2.4 LES sub-grid model

As described in Sec. 2.1.2.3, unclosed terms from the filtering procedure arise. In spray simulations, two solution approaches are followed in the literature. As described in Boris et al. [126], the unresolved dissipation can be modeled with high-order numerical schemes that implicitly have a dissipative character. No additional sub-grid model has to be employed. The so-called MILES (Monotonically Integrated LES) has been successfully employed in spray simulation [91]. In this thesis, however, a sub-grid eddy viscosity model is used. With the help of the Boussinesq assumption, the sub-grid scale viscosity ν_{SGS} in Eq. 2.27 is introduced. Nicoud et al. [127] performed an dimensional analysis and showed that ν_{SGS} has the form of:

$$\nu_{\mathrm{SGS}} = (C_m\Delta)^2\,\mathcal{D}_m(\mathbf{u_i}), \tag{2.30}$$

with C_m denoting a grid dependent model constant, Δ the local cell size[2] and $\mathcal{D}_m$ is a differential operator acting on the velocity field $\mathbf{u_i}$. A popular sub-grid LES model is the Smagorinsky model [120], which relies on the strain tensor. However, the original Smagorinsky model is known to produce stresses close to walls, where the operator should vanish. The σ model introduced by Nicoud et al. [127] eliminates this issue. The differential operator $\mathcal{D}_m$ is constructed out of the singular values of the velocity gradient tensor. The operator is presented as:

$$\mathcal{D}_\sigma = \frac{\sigma_3\left(\sigma_1 - \sigma_2\right)\left(\sigma_2 - \sigma_3\right)}{\sigma_1^2}. \tag{2.31}$$

The grid-dependent model constant C_m in Eq. 2.30 is commonly assumed to be $C_\sigma = 1.5$ and the SGS characteristic length scale is evaluated as the grid size $\Delta = V_{\mathrm{cell}}^{\frac{1}{3}}$. The grid constant C_σ can also be evaluated dynamically. Still, Rieth [128] and Gierth [93] showed that the dynamic procedure does not yield significantly better results or is appropriate for particle-laden multi-phase flows, respectively. In the thesis of Gierth [93] it was also shown that a model constant of $C_\sigma = 2.0$ is better suited for the type of meshes used in this

---

[2] for implicit LES filtering

study. Hence, the sigma model with $C_\sigma = 2.0$ is utilized within this thesis. Further information on turbulence modeling can be found in [118, 119].

2.1.3 Thermophysical properties

A widespread approach to determine the heat capacity c_p, absolute enthalpy h_a and entropy s for the gaseous phase is the so-called NASA polynomials [129]. The NASA polynomials consist of seven coefficients a_i used in Eq. 2.32-Eq. 2.34. They are state-of-the-art in many combustion solvers, e.g., CHEMKIN [130], Cantera [131] and others.

$$\frac{c_p^m(T)}{R} = a_0 + a_1 T + a_2 T^2 + a_3 T^3 + a_4 T^4 \tag{2.32}$$

$$\frac{h_a^m(T)}{RT} = a_0 + \frac{a_1}{2} T + \frac{a_2}{3} T^2 + \frac{a_3}{4} T^3 + \frac{a_4}{5} T^4 + \frac{a_5}{T} \tag{2.33}$$

$$\frac{s^m(T)}{R} = a_0 \ln T + a_1 T + \frac{a_2}{2} T^2 + \frac{a_3}{3} T^3 + \frac{a_4}{4} T^4 + a_6 \tag{2.34}$$

Properties like gas viscosity and gas thermal conductivity are computed using the following correlations [132, 133]:

$$\mu_k = \frac{5}{16} \frac{\sqrt{\pi m_k k_B T}}{\pi \sigma_k^2 \Omega_{kk}^{(2,2)*}}, \tag{2.35}$$

$$\lambda_k = \frac{25}{32\pi^{1/2}} \left(\frac{k_B T}{m_k} \right)^{1/2} \frac{C_v}{\sigma_k^2 \mathrm{A} \Omega_{kk}^{(2,2)*}}. \tag{2.36}$$

In Eq. 2.35, μ_k is the viscosity of species k and is calculated using the irrational number π, m_k the mass of species k , the Boltzmann constant k_B, σ_k^2 is the collision diameter of the $k-k$ interaction potential and $\Omega_{kk}^{(2,2)*}$ denotes the collision integral. Further, C_v in Eq. 2.36 denotes the heat capacity at constant volume, and A is the Avogradro number.

As described in Kee et al. [133], using a polynomial fit for the viscosity and thermal conductivity is convenient. The transport properties are computed using Cantera [131] and then fitted with Scipy [134]:

$$\ln \mu_k = \sum_{n=1}^{N} a_{n,k} (\ln T)^{n-1}, \tag{2.37}$$

$$\ln \lambda_k = \sum_{n=1}^{N} b_{n,k} (\ln T)^{n}. \tag{2.38}$$

The properties of mixtures can then be derived from the single species properties. Eq. 2.39 is the so-called Wilke-Bird formula [132, 133, 135], which is used to compute mixture properties and reads:

$$\mu = \sum_{k=1}^{K} \frac{X_k \mu_k}{\sum_{j=1}^{K} X_j \Phi_{kj}}. \tag{2.39}$$

Here, Φ_{kj} is an auxiliary variable that reads:

$$\Phi_{kj} = \frac{1}{\sqrt{8}} \left(1 + \frac{W_k}{W_j}\right)^{-1/2} \left(1 + \left(\frac{\mu_k}{\mu_j}\right)^{1/2} \left(\frac{W_j}{W_k}\right)^{1/4}\right)^2. \tag{2.40}$$

For the mixture averaged thermal conductivity, the following formula is used [133, 136]:

$$\lambda = \frac{1}{2} \left(\sum_{k=1}^{K} X_k \lambda_k + \frac{1}{\sum_{k=1}^{K} X_k / \lambda_k} \right). \tag{2.41}$$

The interested reader is referred to [133] for more detailed information about transport models.

2.2 Liquid phase

In the following, all models and equations that are used to describe the liquid phase are presented. In particular, the spray modeling utilized in this thesis is presented. Furthermore, the liquid thermophysical properties of single and binary fuels are shown.

2.2.1 Spray model

There are several methods to model the multiphase flow in spray simulations. Prevalent are the Euler-Euler methods and Euler-Lagrange methods. In Euler-Euler methods, both the liquid and gas phase are formulated in an Eulerian reference frame. Besides others, one common method in the Euler-Euler approach is the Volume of Fluid (VOF) method. The distinction between the gas and liquid phase is achieved by solving at least one transport equation for the volume fraction of the liquid phase. One advantage of these models is that breakup can be incorporated and simulated. Moreover, it is possible to simulate the inner nozzle flow and spray in one simulation workflow. A big drawback, however, is the high spatial discretization requirement needed to resolve single droplets. In passenger and heavy-duty Diesel engine conditions, droplets have a diameter of approximately $d \in [1 - 300]\ \mu\mathrm{m}$. In VOF, it is essential to discretize the interface very accurately, leading to very fine grids. Otherwise, surface tension forces are not well reproduced. Furthermore, VOF methods are known to be numerically very diffusive with low grid resolutions reducing accuracy. Assuming a resolution of only four cells per diameter of a liquid particle results in very fine meshes with high computational costs. Further information can be found in [137, 138].

Another Euler-Euler approach for high-pressure sprays is the single-fluid Diffuse Interface method or $\Sigma - Y$ model [139]. Most Diesel injections are above the critical pressure but below the critical temperature of the fuel. However, small parts of the spray are supercritical, and no interface between the gas and liquid phase exists. Following this observation, the Diffuse Interface method models the liquid spray as turbulent mixing

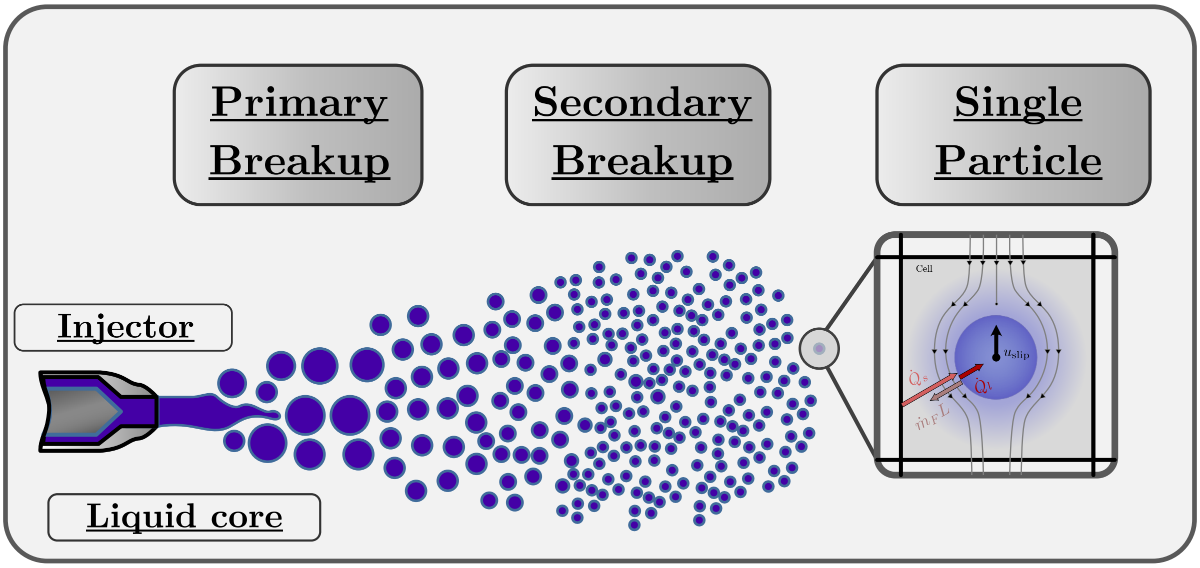

Figure 2.1: Schematic of the spray cause-effect-chain: Liquid core, primary breakup, secondary breakup and single particles.

of a variable density flow [140]. A transport equation for the liquid mass fraction Y and the liquid surface density Σ are solved. With the help of Σ, the liquid surface can be reconstructed. The method has also been applied in LES [50, 140, 141]. However, an equation of state is needed in the Diffuse Interface method for closure. No accurate description is available for renewable fuels, and the Diffuse Interface method cannot be applied.

As described above, the full discretization of the liquid phase is cumbersome and numerically expensive. Hence, Williams [142] proposed a model that reduces the complexity of dispersed flows with many particles. Under the assumption of small spherical droplets and low Weber numbers, the shape and size of a particle can be described by its radius. Hence, it is reasonable to model a spray by a transported probability function that only depends on a few parameters. The probability function describes the number probability of how many particles have a certain radius, location, speed or temperature [142]. The transport function for the particle distribution is called the Williams spray equation [142].

As depicted in Figure 2.1, in Diesel sprays not only small particles occur, which is an assumption in the Williams spray equation. From the liquid core exiting the injector nozzle large droplets are shed. The primary breakup of high-pressure Diesel sprays is usually in the atomization regime, meaning that the liquid core disintegrates catastrophically [143]. After the primary breakup, the large particles further break up into smaller particles, referred to as secondary breakup. Finally, single particles undergo heating and evaporation. In these conditions where the assumptions of the Williams spray equation are not fulfilled, Euler-Lagrange methods, such as the Particle-In-Cell method (PIC), combine the approach of a statistical description of the liquid phase and discrete single particles. The equations for the carrier phase are solved in an Eulerian reference frame, and particles are solved in a Lagrangian reference frame. Since a spray has a high number of particles, particles with the same properties are clustered as parcels. This means that each parcel represents multiple droplets with the same properties, such as velocity, mass, diameter and temperature. This approach maintains a high resolution of the particle distribution while reducing the numerical cost drastically. Even though parcels represent multiple particles they are treated as single discrete droplets. The coupling to the carrier phase in Eulerian coordinates is a two-way coupling (see source terms in Eq. 2.1, Eq. 2.9 and Eq. 2.12). With the help of parcels, the Eulerian mesh does not have high discretization demands compared to VOF methods. The interested reader is referred to [144–146]. Compared to the Euler-Euler methods, the PIC method is numerically less expensive and used within this thesis. In the following, the governing equations and models are presented.

2.2.1.1 Single droplet model

As described above, multiple droplets sharing the same properties are clustered in so-called parcels. These parcels' tracking is formulated as if the parcel is a single particle. The equation of motion for a single parcel reads [123]:

$$\frac{\mathrm{d}}{\mathrm{d}t}\vec{u}_d = \frac{C_D}{\tau_d}\frac{\mathrm{Re}_d}{24}\left(\vec{u}_g - \vec{u}_d\right) = \frac{C_D}{\tau_d}\frac{\mathrm{Re}_d}{24}\vec{u}_{\mathrm{rel}}. \tag{2.42}$$

With Re_d denoting the parcel's[3] Reynolds number:

$$\mathrm{Re}_{\mathrm{d}} = \frac{\rho_g d_d \vec{u}_{\mathrm{rel}}}{\mu_g}, \tag{2.43}$$

and the parcel time scale τ_d is defined as:

$$\tau_d = \frac{\rho_d d_d^2}{18\mu_g}. \tag{2.44}$$

In Eq. 2.42, the subscript $d \in [1, \mathrm{N}_{\mathrm{parcels}}]$ represents the index of the parcel, subscript g denotes the gas phase properties and C_D is the drag coefficient. The drag coefficient is evaluated from the empirical relations [147]:

$$C_D = \begin{cases} \frac{24}{\mathrm{Re}_d}\left(1 + \frac{1}{6}\,\mathrm{Re}_d^{2/3}\right) & \mathrm{Re}_d < 1000 \\ 0.424 & \mathrm{Re}_d \geq 1000. \end{cases} \tag{2.45}$$

As the droplet evaporation model, the model according to Abramzon and Sirignano [148] is used. The mass flux due to evaporation $\dot{m}_{\mathrm{d},i}$ for each species i reads:

$$\dot{m}_{\mathrm{d},i} = 2\pi r_{\mathrm{d}} \frac{\lambda_{g,i}}{c_{p_{g,i}}} \mathrm{Nu} \ln\left(1 + B_{m,i}\right). \tag{2.46}$$

In Eq. 2.46, r_{d} is the representative radius of the parcel, Nu is the Nusselt number and $\mathrm{B}_{m,i}$ the Spalding mass number for species i [149]:

$$\mathrm{B}_{\mathrm{m,i}} = \frac{Y_{f,i}^s - Y_{f,i}^\infty}{1 - Y_{f,i}^s}. \tag{2.47}$$

---

[3] Since equations for single droplets are solved, subscript d is chosen for parcels.

In Eq. 2.47, the subscript f denotes fuel and superscripts s and ∞ indicate the position on the droplet surface and in the gas phase far away, respectively. The mass fraction of fuel at the surface $Y^s_{f,i}$ is computed for each liquid species i from the mole fraction at the surface:

$$X^s_{f,i} = X^l_{f,i}\frac{p_{\mathrm{vap},i}}{p}. \tag{2.48}$$

In Eq. 2.48, $X^l_{f,i}$ is the mole fraction of the fuel species i in the liquid, $p_{\mathrm{vap},i}$ is the vapor pressure of the fuel species i and p is the system pressure. Note that Eq. 2.48 is formulated for the ideal gas assumption, no real-thermodynamic evaporation effects are considered within this thesis. For n-Dodecane and 1-Octanol, Vapor-Liquid Equilibrium measurements are available [27] (see Sec. 2.2.2), and $X^s_{f,i}$ is evaluated directly from the tabulated VLE (see Sec. 2.2.2).

The Nusselt number in Nu Eq. 2.46 is obtained by the Ranz-Marshall correlation [150]:

$$\mathrm{Nu} = 2 + 0.6\,\mathrm{Re}^{1/2}\,\mathrm{Pr}^{1/3}\,. \tag{2.49}$$

The thermophysical properties required in Eq. 2.46 and Eq. 2.49 are evaluated at the position of the so-called one-third rule [151, 152]:

$$Y^{ref}_i = Y^s_i + \frac{1}{3}(Y^\infty_i - Y^s_i), \tag{2.50}$$

$$T^{ref}_i = T^s_i + \frac{1}{3}(T^\infty_i - T^s_i). \tag{2.51}$$

The parcel temperature is calculated by solving an energy balance equation of the form [153]:

$$m_d c_{p,l}\frac{\mathrm{d}T_d}{\mathrm{d}t_l} = \dot{q}_s - \dot{m}_d h_{vap}, \tag{2.52}$$

where $\dot{q}_s$ is the heat flux towards the droplet (surface) and h_{vap} represents the heat of vaporization. Note that in the used numeric framework, a sub-cycling for the liquid phase l is used. Hence the time in Eq. 2.52 is denoted as t_l.

2.2.1.2 LES spray coupling

Closing the two-way coupling with the gaseous phase, the source terms for Eq. 2.22, Eq. 2.25,Eq. 2.23 and Eq. 2.24 are evaluated for the time step Δt_g in the gaseous phase. They are computed as follows [93]:

$$\tilde{\dot{S}}_m = \sum_{q=0}^{Q} N_{d,q}\frac{m^{\mathrm{new}}_{d,q} - m^{\mathrm{old}}_{d,q}}{V_{\mathrm{cell}}\,\Delta t_g}, \tag{2.53}$$

$$\tilde{\dot{S}}_k = \sum_{q=0}^{Q} N_{d,q}\frac{m^{\mathrm{new}}_{d,q,k} - m^{\mathrm{old}}_{d,q,k}}{V_{\mathrm{cell}}\,\Delta t_g}, \tag{2.54}$$

$$\dot{\widetilde{S}}_{u,i} = \sum_{q=0}^{Q} N_{d,q} \frac{\left(u_{d,q,i} m_{d,q}\right)^{\text{new}} - \left(u_{d,q,i} m_{d,q}\right)^{\text{old}}}{V_{\text{cell}} \Delta t_g}, \tag{2.55}$$

$$\dot{\widetilde{S}}_{h_t} = \sum_{q=0}^{Q} N_{d,q} \frac{\left(\left(h_{d,q} + 0.5 u_{d,q,i}^2\right) m_{d,q}\right)^{\text{new}} - \left(\left(h_{d,q} + 0.5 u_{d,q,i}^2\right) m_{d,q}\right)^{\text{old}}}{V_{\text{cell}}\, \Delta t_g}. \tag{2.56}$$

In the definitions for the source terms, the variable q is the parcel index in the cell, $N_{d,q}$ is the number of particles in the parcel with index q and V_{cell} is the volume of the cell where the parcels are located.

In the case of multicomponent fuels, e.g., OME$_{\text{mix}}$, the source terms for mass, momentum and enthalpy are obtained by looping over all fuels.

2.2.1.3 Breakup model

The description of the parcel evolution in Euler-Lagrange methods is manifold. The presumed PDF approach prescribes a probability function of parcel sizes and velocities at a specific location and area. This model assumes that the atomization process and breakup of the liquid jet after the nozzle exit has already occurred. A downside of this approach is that the shape of the distribution is not necessarily known. A standard spray simulation particle size distribution is the Rosin-Rammler distribution [154], which was initially used for coal particles. In contrast to Diesel sprays, gasoline sprays are less dense, and the size and velocity distribution can be measured [155, 156]. Sprays under Diesel-relevant conditions (high pressure, high temperature) have a very dense spray core, where it is challenging to measure size distributions by experimental techniques, e.g., Phase-Doppler-Anemometers.
Another approach that is coupled with the Particle-In-Cell method is a breakup model. Most models assume that breakup is triggered by oscillations on the liquid jet exiting the nozzle, eventually leading to breakup. If a critical frequency on the surface is reached, droplet breakup occurs. One model type is based on the Rayleigh analogy, which assumes that a droplet reacts like a spring and damper system. The most popular model is the Taylor Analogy Breakup model (TAB) [157], and its advancement is the ETAB (Enhanced TAB) model [158]. The class of TAB models solve an additional differential equation of a spring-damper system. A significant downside is that only one eigenmode is considered.

Other models rely on the Kelvin-Helmholtz and Rayleigh-Taylor instabilities that form on the liquid jet and droplet surface (see Figure 2.2). These types of models are also referred to as KH-RT models. One of the first models are the WAVE model [159] and Reitz-Diwakar model [160]. The commonly referred KH-RT breakup model is presented in Beale et al. [161] and is the basis for this work. Note that there are many variants with small differences regarding implementation and details. KH-RT models are used for various sprays, e.g., gasoline and Diesel sprays and different injectors. Large ligaments or the fluid jet undergo the Kelvin-Helmholtz breakup mode, and new droplets with a smaller diameter are formed (see Figure 2.2). Additionally, small droplets may be shed and undergo Rayleigh-Taylor breakup.

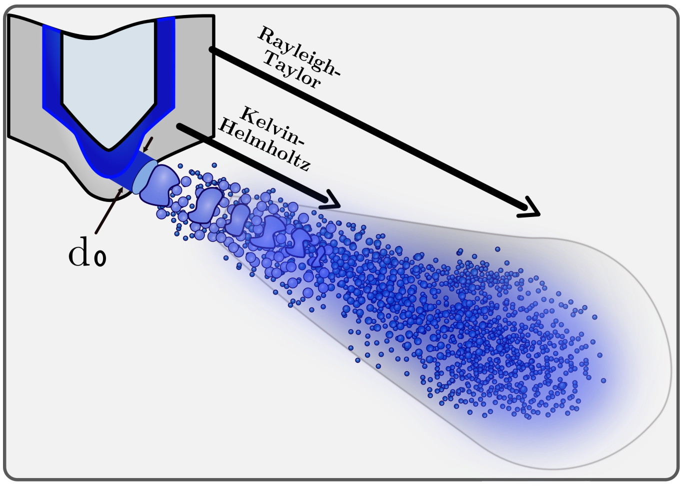

Figure 2.2: Illustration of the spray injection process and the breakup model. The injector with the nozzle diameter d_0 determines the initial parcel diameter (blob method). The liquid ligament close to the nozzle exit is modeled using blobs that undergo Kelvin-Helmholtz breakup. The Rayleigh-Taylor instabilities may also form from the nozzle exit on but are more dominant on smaller parcels (compared to blobs).

The KH-RT model is not predictive and needs adjustment. The fuel and injector-specific model parameters are needed to adjust the spray morphology. The input parameter B_0 scales the new radius of a child parcel after KH breakup and is commonly set to a constant value of B_0=0.61 proposed in [161]. B_1 parametrizes the time after KH breakup is applied and takes values between 1-60. C_τ, which is usually set to unity C_τ=1, scales the time after RT breakup occurs on a droplet. The parameter C_{RT} scales the radius of the droplet after RT breakup and takes the constant value of C_{RT}=0.1 [161]. Note that for the same case, the parameters between RANS and LES simulation might change significantly.

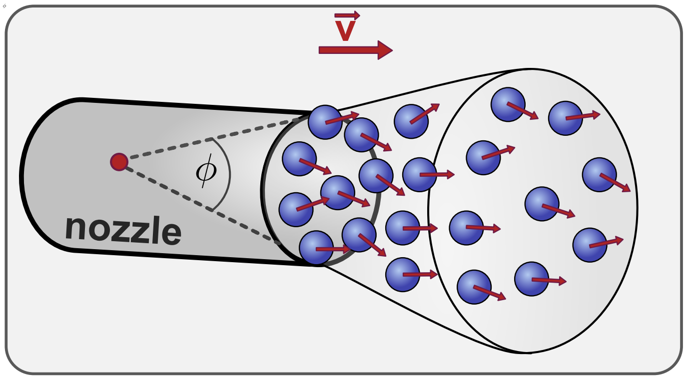

Figure 2.3: Illustration of the spray disk injection method. The blue particles represent blob parcels randomly distributed over the nozzle area. Each blob has its own velocity vector $\vec{v}$ whose absolute velocity matches the injection velocity computed from the rate of injection profile. The velocity vector lies within the cone defined by the spray angle ϕ.

The spray simulation with the KH-RT breakup model in this thesis is conducted by injecting so-called blobs with the size d_0 of the nozzle [159], which can be considered as the primary breakup model (see Figure 2.1).

The velocity and the direction of the injection must be prescribed on the blob. The blob parcel then undergoes the secondary breakup. In this thesis, an advanced method has been implemented. The blobs centers are placed randomly on the nozzle outlet plane, and the velocity vector is also randomly chosen with the constraint to lie in the cone sketched in Figure 2.3. The cone angle ϕ is usually set as the far cone angle measured in experiments as proposed by Naber et al. [162]. The magnitude of the velocity is preserved for all injected parcels to ensure momentum conservation. The aim of this method is an even distribution of the point-modeled parcels in the simulation domain and to achieve better air entrainment in LES.

If available, inner-nozzle flow simulations coupled to the breakup model increase the predictivity. This class of models is able to include transient effects from within the nozzle and can, e.g., incorporate effects of cavitation. The interested reader is referred to [163–166]. Since no inner-nozzle flow simulations are available to the author for the cases in this study, the KH-RT model using measured or modeled Rate of Injection profiles is utilized within this thesis.

2.2.2 Liquid properties

Liquid properties are needed in multiple models, e.g., the breakup and evaporation models. Hence, accurate modeling is crucial for the mixture formation process and subsequent modeling steps. The single-species properties are calculated using temperature-dependent formulas. The n-Dodecane properties provided from OpenFOAM v2012 [167] are used and shown in Figure 2.4. The properties for 1-Octanol are extracted from the VDI-Wärmeatlas [70] and are also displayed in Figure 2.4. The composition for n-Dodecane and 1-Octanol at the surface in Eq. 2.48 are extracted from measured Vapor-Liquid Equilibria (VLE) with nitrogen in Fechter et al. [27]. The VLE measurements have been performed in the context of a project funded by the Fachagentur Nachwachsende Rohstoffe (project ID: 2220NR021B), in which parts of this work have been carried out. The measurements are unique since they have been performed for various pressures relevant to CI engine combustion up to the critical temperature of the fuels. The VLEs are tabulated, and the mole fraction of a species can be uniquely retrieved by the liquid temperature and the system pressure.

The liquid thermophysical properties in Figure 2.4 for neat OME_3 and OME_4 have been measured in the context of the German publicly funded project "E2Fuels" (funding number: 19|18009|) and have been published [2, 22]. The liquid density, heat capacity at constant pressure and thermal conductivity in Figure 2.4 are extracted from [22]. The vapor pressure and latent heat of evaporation for neat OME_3 and OME_4 were measured in Fechter et al. [2]. As shown in Fechter et al. [2], the available vapor pressure curves and latent heat of evaporation from [72, 73] were not accurate, especially close to the critical pressure and temperature. Also, the very detailed measurements of T_{crit} and p_{crit} in Fechter et al. [2] revealed significant differences compared to the available data in the literature. The surface tension for the OMEs has been extrapolated from values at room temperature [168] up to the critical point using a suitable model from [70].

The OME mixture used in the experiments is composed mainly of OME_3 and OME_4, but also has shares of $10.1\,\mathrm{vol\%}$ OME_5 and $1.91\,\mathrm{vol\%}$ OME_6. Since only detailed thermophysical properties and reaction mechanisms were available for OME_3 and OME_4, the mixture was simplified to these components. OME_5 and OME_6 are thermophysically closest to OME_4 (see estimation models in [169]) and are assigned to OME_4. The multicomponent mixture of OME_{mix} is modeled with $57.9\,\mathrm{vol\%}$ OME_3 and $42.1\,\mathrm{vol\%}$ OME_4.

In multicomponent mixtures, the liquid properties in this thesis are computed under ideal mixing assumptions. All mixture quantities ϕ_{mix} (e.g., density, heat capacity, etc.) are evaluated from Eq. 2.57 from their single species properties.

$$\phi_{\text{mix}} = \sum_{i}^{N} X_i \phi_i \tag{2.57}$$

Critical properties of the mixture are also evaluated using the ideal gas law. In Eq. 2.58, $V_{\text{crit,i}}$ is the critical volume for species i. $V_{\text{crit,i}}$ can be measured or estimated with Eq. 2.60. The critical compressibility factor Z_{crit} indicates the influence of the real-thermodynamic effect. For ideal gases, its value is $Z_{\text{crit}} = 1$. The critical pressure of the mixture is evaluated using Eq. 2.59.

$$T_{\text{crit,mix}} = \frac{\sum_i^N X_i T_{\text{crit,i}} V_{\text{crit,i}}}{\sum_i^N X_i V_{\text{crit,i}}} \tag{2.58}$$

$$p_{\text{crit,mix}} = R \frac{\sum_i^N X_i Z_{\text{crit,i}} \sum_i^N X_i T_{\text{crit,i}}}{\sum_i^N X_i V_{\text{crit,i}}} \tag{2.59}$$

$$V_{\text{crit},i} = Z_{\text{crit}} \cdot \frac{R \cdot T_{\text{crit},i}}{p_{\text{crit},i}} \tag{2.60}$$

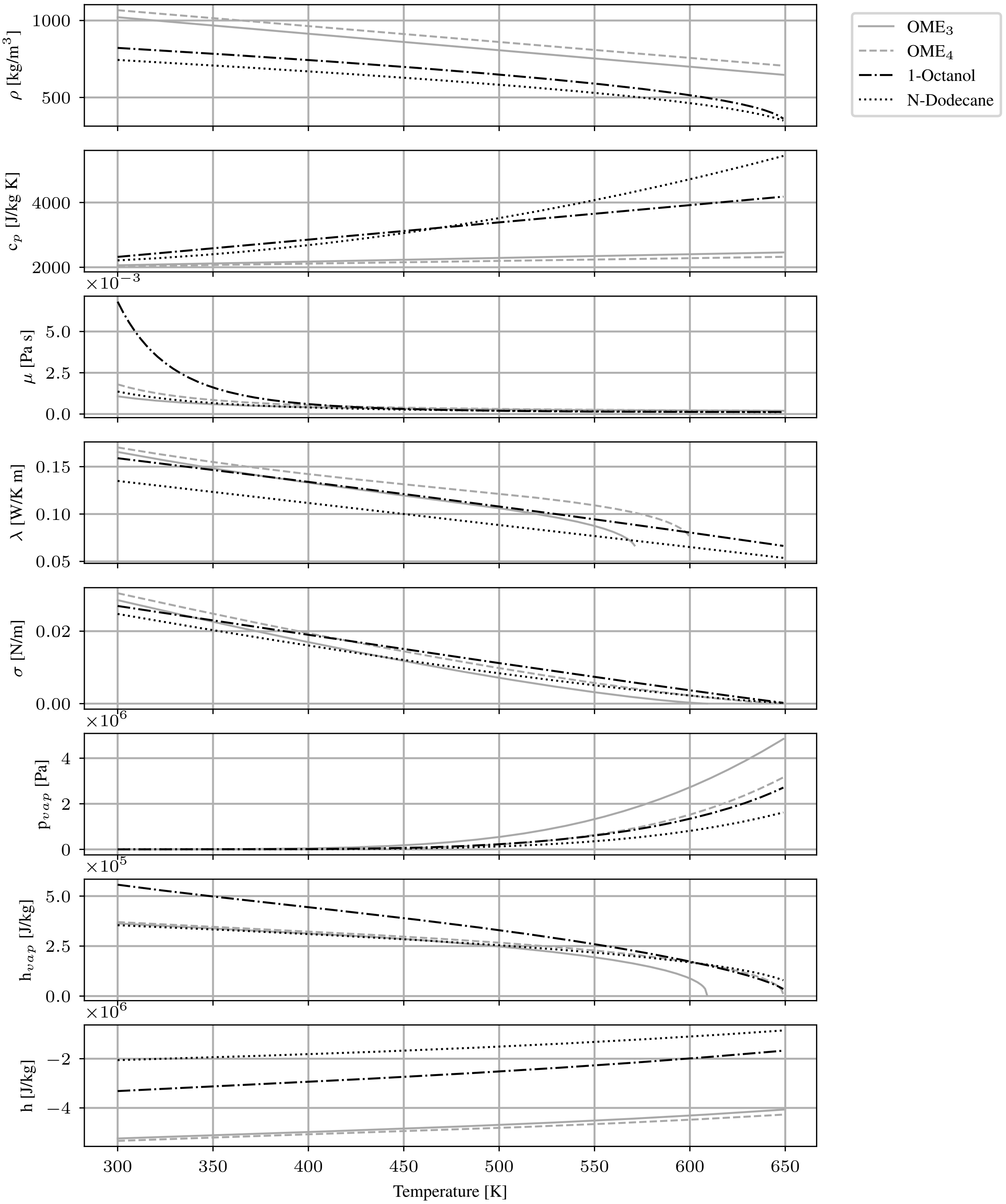

Figure 2.4: The liquid thermophysical properties used in this thesis are partly extracted from [2, 22, 167]. The surface tension is extracted from [168] and extrapolated to the critical point with a formula for surface tension extracted from [70]. The last row denotes the absolute liquid enthalpy (similar to Eq. 2.12).

2.3 Combustion model

This thesis uses multiple combustion models to describe combustion that are presented in the following [115]. First, the description of chemical reactions in numerical simulations is presented. A set of equations for chemical reactions are solved to evaluate the chemical source terms, which are the basis for all upcoming combustion models. Subsequently, the homogeneous reactor model is presented to assess chemical ignition delay times (without transport effects). Next, the laminar non-premixed flamelet model used to describe combustion in spray flames, including transport effects, is presented. Finally, the turbulent combustion model is presented.

2.3.1 Chemical reactions

A chemical system is characterized by M reactions with N molecules. In each reaction, the species $\mathcal{M}_k$ is multiplied by its molar stoichiometric coefficient ν'_{kj} and ν''_{kj} (see Eq. 2.61). Reactions in general, run in forward and reverse directions until equilibrium is achieved. For turbulent spray flames, finite rate chemistry is assumed. The rate of change for each species is defined by the sum of production and consumption $\dot{\omega}_{kj}$ (also denoted as chemical source term) in every reaction, see Eq. 2.62.

$$\sum_{k=1}^{N} \nu'_{kj}\mathcal{M}_k \rightleftharpoons \sum_{k=1}^{N} \nu''_{kj}\mathcal{M}_k \quad \text{for} \quad j = 1, M \tag{2.61}$$

$$\dot{\omega}_k = \sum_{j=1}^{M} \dot{\omega}_{kj} = W_k \sum_{j=1}^{M} \nu_{kj}\mathcal{Q}_j \tag{2.62}$$

The production rate $\dot{\omega}_k$ can be further described by the product of the stoichiometric coefficient ν_{kj} ($\nu_{kj} = \nu''_{kj} - \nu'_{kj}$) and the reaction progress $\mathcal{Q}_j$. The reaction progress depends on the reaction rate K and the product of each reactant/product molar concentration $[X_k]$ with its stoichiometric coefficient as the exponent.

$$\mathcal{Q}_j = K_{fj} \prod_{k=1}^{N} [X_k]^{\nu'_{kj}} - K_{rj} \prod_{k=1}^{N} [X_k]^{\nu''_{kj}} \tag{2.63}$$

In Eq. 2.64, the so-called Arrhenius equation is employed to calculate the forward reaction rate K_{fj}. The reaction rate is defined by the preexponential factor A_{fj}, the temperature T^{β_j} with its temperature coefficient β_j, the activation energy E_j, the universal gas constant R and the temperature T:

$$K_{fj} = A_{fj} T^{\beta_j} \exp\left(-\frac{E_j}{RT}\right). \tag{2.64}$$

For completeness, the reverse reaction rate for equilibrium reactions can be computed using Eq. 2.65. In Eq. 2.65, p_a represents the ambient pressure at $1\,\mathrm{bar}$, ΔS_j^0 and ΔH_j^0 are the entropy and enthalpy changes respectively [115].

$$K_{rj} = \frac{K_{fj}}{\left(\frac{p_a}{RT}\right)^{\sum_{k=1}^{N} \nu_{kj}} \exp\left(\frac{\Delta S_j^0}{R} - \frac{\Delta H_j^0}{RT}\right)} \tag{2.65}$$

2.3.2 Homogeneous reactor model

The homogeneous reactor model is one of the most fundamental combustion models [170]. It assumes perfect mixture homogenization and does not consider any transport effects. The model can be formulated for constant pressure or constant volume conditions. This thesis uses the formulation for constant volume since it most accurately resembles the combustion in a constant volume spray chamber. The change of species i is described by Eq. 2.66 and is equal to the chemical source term from Eq. 2.62.

$$\frac{\mathrm{d}\,[X_i]}{\mathrm{d}t} = \dot{\omega}_i \tag{2.66}$$

The chemical ignition delay time of a fuel can be computed with the homogenous reactor model by neglecting heat fluxes between the system and its environment ($\dot{Q}$=0). The temperature of the reactor is described by Eq. 2.67, where $\bar{h}_i$ and $\bar{c}_{p_i}$ are the molar enthalpy and molar heat capacity, respectively. The index N describes the number of species.

$$\frac{\mathrm{d}T}{\mathrm{d}t} = \frac{(\dot{Q}/V) + RT\sum_{i=1}^{N} \dot{\omega}_i - \sum_{i=1}^{N} \left(\bar{h}_i \dot{\omega}_i\right)}{\sum_{i=1}^{N} [X_i] \left(\bar{c}_{p,i} - R\right)} \tag{2.67}$$

The pressure trace can be either computed using the ideal gas law or solving Eq. 2.68:

$$\frac{\mathrm{d}p}{\mathrm{d}t} = RT\sum_{i=1}^{N} \dot{\omega}_i + \sum_{i=1}^{N} [X_i] \frac{\mathrm{d}T}{\mathrm{d}t}. \tag{2.68}$$

For Diesel fuels, usually, a two-staged ignition behavior is observed. The initial consumption of fuel leads to an increase in temperature, and stable intermediate species are formed. The profile of the Heat Release Rate (HRR) shows its first peak, which is referred to as first stage ignition delay time $\tau_{ign,1}$. During further combustion, the intermediate species are also consumed and form more radicals that accelerate the combustion, referred to as thermal runaway. The main ignition occurs, and the chemical ignition delay time is defined as the main ignition delay time $\tau_{ign,2}$. The main ignition is determined as the second significant peak in the HRR profile. A schematic that visualizes the definition of the ignition delay times is provided in Figure 6.2 (see Sec. 6.2).

2.3.3 Laminar non-premixed flamelet model

Under the assumption of large Damköhler numbers $\mathrm{Da} = \frac{\tau_\mathrm{f}}{\tau_\mathrm{c}}$ (e.g., at high pressures), reaction zones in non-premixed turbulent flames are very thin. High Damköhler numbers represent a state where the flow characteristic flow time τ_f is high compared to the characteristic chemical time scale τ_c. Figuratively speaking, turbulent flow cannot penetrate the flame structure, and reactions are faster compared to the time scales of the surrounding flow. A turbulent flame structure depicted in Figure 2.5 can then be decomposed into an ensemble of so-called flamelets. Thin reaction zones show high gradients in the flame normal direction, and gradients align mainly in this direction. Hence, flamelets can be described with one-dimensional equations for species mass fraction and temperature (or enthalpy). The flamelet modeling approach for non-premixed combustion of technical systems has been mainly influenced and introduced by Peters [171, 172]. Peters presented the element-based, normalized mixture fraction Z as a conserved scalar [171]. The mixture fraction describes the mixing between the oxidizer ($Z = 0$) and the fuel stream ($Z = 1$). The mixture fraction is a conserved scalar, since from an elemental balance, no elements are produced nor consumed during reactions.

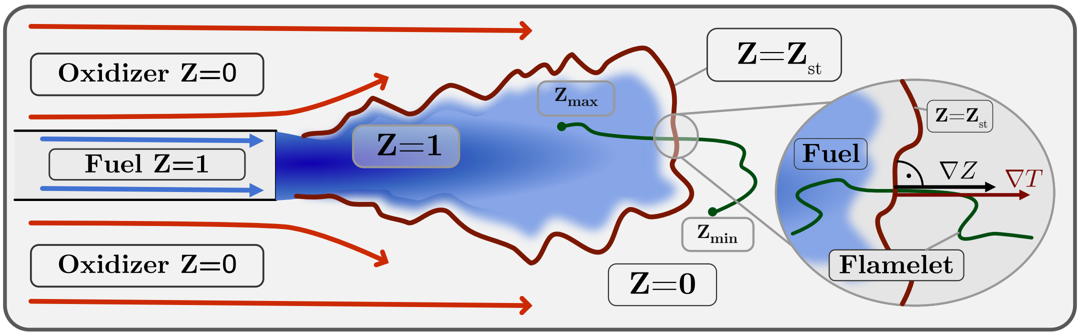

Figure 2.5: Schematic of the laminar non-premixed flamelet model in accordance to [171] and [173]. The diffusion flame is located at Z_st, which is assumed to be a thin flame sheet. The gradients of the mixture fraction ∇Z and the temperature ∇T align along the flame's normal direction.

During the mixing of fuel and oxidizer, the Lewis number $\mathrm{Le}_i = \frac{a_i}{D_i}$ defines the relation between thermal and mass diffusion of species i. In the thesis of Pitsch [174], it was proposed to solve a general transport equation of Z which can be used for unity and non-unity Lewis numbers. For Diesel fuels, it is commonly assumed that the $\mathrm{Le}=1$ assumption is reasonable and is also used within this thesis [3, 59, 91, 93, 94, 101, 112, 123]. The mixture fraction Z is then defined as the ratio of the mass flow rate of fuel $\dot{m}_\mathrm{F}$, normalized by the sum of fuel and oxidizer fuel stream ($\dot{m}_\mathrm{Ox}$):

$$Z = \frac{\dot{m}_\mathrm{F}}{\dot{m}_\mathrm{F} + \dot{m}_\mathrm{Ox}}. \tag{2.69}$$

While flamelet equations can be solved in physical coordinates, the transformation in the so-called mixture fraction space is advantageous. The non-dimensional spatial coordinate after transformation is the mixture fraction Z, and the time in physical space is transformed to the flamelet time τ with the transformation operators given in Eq. 2.70-Eq. 2.72.

$$\frac{\partial}{\partial t} = \frac{\partial}{\partial \tau} + \frac{\partial Z}{\partial t}\frac{\partial}{\partial Z} \tag{2.70}$$

$$\frac{\partial}{\partial x_1} = \frac{\partial Z}{\partial x_1}\frac{\partial}{\partial Z} \tag{2.71}$$

$$\frac{\partial}{\partial x_\alpha} = \frac{\partial}{\partial Z_\alpha} + \frac{\partial Z}{\partial x_\alpha}\frac{\partial}{\partial Z}, \quad \alpha = 2, 3 \tag{2.72}$$

As described above, the gradients of the mixture fraction and the temperature align to the flame normal direction, transport effects in Z_2 and Z_3 direction are neglected in this thesis (see Eq. 2.72). A detailed description of the transformation of the species transport and temperature equation is given in [171, 173–175]. The transformed equation for the mass fraction of species k under the $\mathrm{Le}=1$ assumption now reads:

$$\rho\frac{\partial Y_k}{\partial \tau} = \frac{\rho\chi}{2}\frac{\partial^2 Y_k}{\partial Z^2} + \dot{\omega}_k, \tag{2.73}$$

and the temperature equation is denoted as:

$$\rho\frac{\partial T}{\partial \tau} = \frac{\rho\chi}{2}\frac{\partial^2 T}{\partial Z^2} + \frac{\rho\chi}{2c_p}\frac{\partial c_p}{\partial Z}\frac{\partial T}{\partial Z} + \frac{\rho\chi}{2c_p}\sum_{k=1}^{n_s} c_{p,k}\frac{\partial Y_k}{\partial Z}\frac{\partial T}{\partial Z} - \frac{1}{c_p}\sum_{k=1}^{n_s}\dot{\omega}_k h_k. \tag{2.74}$$

From the transformation, an unclosed term arises, the so-called scalar dissipation rate χ (SDR):

$$\chi = 2D\left(\frac{\partial Z}{\partial x_j}\right)^2. \tag{2.75}$$

The scalar dissipation rate describes mixing effects and the strain effects from the underlying flow field and can be correlated to the physical strain rate a by appropriate correlation. The scalar dissipation rate depends on the spatial gradient of Z and needs closure (model or profile from DNS). Peters proposed an analytical function for the SDR that has been derived from the analysis of a laminar mixing layer (also referred to as the inverse error function complement function) [171, 174]. As shown later in the tabulated chemistry approach, it is reasonable to parameterize the scalar dissipation rate with the value of χ_{st}, which refers to χ at stoichiometric conditions (Z_{st}):

$$\chi(Z) = \chi_{\mathrm{st}}\exp\left(2\left(\left[\mathrm{erfc}^{-1}\left(2Z_{\mathrm{st}}\right)\right]^2 - \left[\mathrm{erfc}^{-1}(2Z)\right]^2\right)\right). \tag{2.76}$$

2.3.4 Tabulated chemistry

As described in Sec. 2.3.3, a turbulent flame can be described as a statistical ensemble of one-dimensional flame structures. This enables pre-computing all thermophysical states Φ in advance and storing them in lookup tables. In the 3D LES, the appropriate thermophysical state can be retrieved by control variables that uniquely define Φ. In this work, the thermo-chemical state is a function of the mixture fraction Z, the scalar dissipation rate at stoichiometry χ_{st} and the flamelet time τ:

$$\Phi = (Z, \chi_{\mathrm{st}}, \tau). \tag{2.77}$$

One parameter that is invariant to pressure, temperature and reaction progress is the mixture fraction at stoichiometry: Z_{st}. Hence, the possible profiles of χ are parameterized at stoichiometric conditions and are defined as $\chi_{\mathrm{st}} = \chi(Z_{\mathrm{st}})$. Furthermore, retrieving the flamelet time τ in the LES is challenging. Hence, Pierce [176, 177] first proposed the concept of the Flamelet Progress Variable (FPV) approach in LES. The progress variable replaces the flamelet time τ and is a non-dimensional parameter that describes the progress of a reaction. A combination of combustion products and intermediates is chosen to define the progress variable Y_C, such that the weighted sum of the species is strictly monotonously increasing over time. It is common to use the mass fractions of combustion products, e.g., CO, CO_2 and H_2O. For the ignition of Diesel fuels with a dominant two-stage ignition behavior, CH_2O as a cool-flame marker is added to the definition of Y_C. Furthermore, since formaldehyde is consumed during ignition, H_2 is used to compensate for the consumption of CH_2O [178], since H_2 is usually monotonically increasing during the main ignition. The definition of the progress variable within this thesis reads:

$$Y_C = \alpha \cdot Y_{\mathrm{CO}} + \beta \cdot Y_{\mathrm{CO2}} + \gamma \cdot Y_{\mathrm{H2O}} + \delta \cdot Y_{\mathrm{CH2O}} + \epsilon \cdot Y_{\mathrm{H2}}. \tag{2.78}$$

In this study, the weights α, β, γ, δ and ϵ have been set to unity because this combination has proven to capture the ignition process very well for all fuels investigated. In general, however, finding the proper weights in Eq. 2.78 can be cumbersome [179] since the combination must ensure monotonicity for all combinations of Z and χ_{st} during the ignition process and at stationary conditions (transport is equal to production).

The progress variable Y_C is a function of each point in mixture fraction space Z. For normalization, the minimum and maximum values at each Z and χ_{st} value are used:

$$C\left(Z, \tau, \chi_{st}\right) = \frac{Y_C\left(Z, \tau, \chi_{st}\right) - Y_{C,\min}\left(Z, \chi_{st}\right)}{Y_{C,\max}\left(Z, \chi_{st}\right) - Y_{C,\min}\left(Z, \chi_{st}\right)}. \tag{2.79}$$

Monotonicity of the progress variable profile ensures unique mapping of the flamelet type time τ on the normalized progress variable C. The thermophysical state after mapping to the progress variable can now be described by:

$$\Phi = (Z, \chi_{\mathrm{st}}, C). \tag{2.80}$$

The original FPV approach was developed for gas-turbine combustors, and only stationary flamelet solutions [176] were incorporated in the ensemble of flamelet solutions, which cannot capture unsteady effects, e.g., auto-ignition. Overcoming this model limitation, this thesis uses unsteady laminar flamelet solutions for tabulation. Unsteady flamelet solutions have first been used in Pitsch et al. [180] in the context of non-premixed methane/air flame in LES. Unsteady Flamelet Progress Variable approaches (UFPV) have the advantage that auto-ignition effects can be incorporated. The full S-shaped curve describing the stable and unstable flamelet solutions of stationary flamelet simulations can be incorporated[4]. Details about the UFPV approach can be found in [3, 181, 182]. Since the original UFPV approach needs the calculation of the S-shaped curve before the simulation of unsteady flamelets, a Reduced Unsteady Flamelet Progress Variable (RUFPV) has been introduced in [3, 93]. The RUFPV approach neglects the igniting solutions of the unstable branch of the S-shaped curve. Only unsteady flamelet solutions that are igniting from the initial solution of the adiabatic mixing line are used as igniting solutions. Solutions with a scalar dissipation rate larger than the stoichiometric scalar dissipation rate at ignition $\chi_{\mathrm{st,ign}}$ are tabulated as not ignited flamelets. Here, $\chi_{\mathrm{st,ign}}$ is defined as

---

[4] Further information about the S-shaped curve and the UFVP approach used in this thesis can be found in Gierth et al. [3].

the first unsteady flamelet solution that undergoes ignition (decreasing the SDR until ignition occurs). The interested reader is referred to Gierth et al. [3], where the suitability of the RUFPV approach in spray flames is shown.

2.3.4.1 Turbulence Chemistry Interaction

As described in Sec. 2.3.3, turbulent flames can be characterized by an ensemble of laminar flamelets. In the concept of the Large Eddy Simulation, sub-grid scale fluctuations are not resolved but modeled. Only mean Favre-filtered quantities $\widetilde{\phi}$ can be retrieved from the LES. The mean Favre-filtered quantity $\widetilde{\phi}$ is represented by the ensemble of corresponding laminar simulations. Since the sub-grid scale distribution is unknown, Turbulence Chemistry Interaction (TCI) models are used to obtain the correct mean values from the lookup table. As described in Peters et al. [171], the statistical distribution in a turbulent flow can be described with a Probability Density Function (PDF). In the case of the RUFPV approach, the thermo-chemical state is defined by Φ $(Z,\, \chi_{\mathrm{st}},\, C)$. A Favre-filtered quantity $\widetilde{\phi}$ $(x_i,$ t) at position x_i and simulation time t can be computed as the integral of the convolution of the value retrieved at the thermo-chemical state $\Phi(Z, \chi_{\mathrm{st}}, C)$ and the joint density weighted Filtered Density Function (FDF) $\widetilde{P}(Z, \chi_{\mathrm{st}}, C)$ as:

$$\widetilde{\phi}\left(x_i, t\right) = \int_0^1 \int_{\chi_{st,\min}}^{\chi_{st,\max}} \int_0^1 \phi\left(Z, \chi_{st}, C\right) \widetilde{P}\left(Z, \chi_{st}, C\right) dZ \mathrm{d}\chi_{st} \mathrm{d}C. \tag{2.81}$$

As presented in Ihme et al. [182], the density-weighted FDF reads:

$$\widetilde{P}\left(Z, \chi_{st}, C\right) = \frac{\rho}{\bar{\rho}} P\left(Z, \chi_{st}, C\right). \tag{2.82}$$

Eq. 2.81 can now be rewritten in the form that the non-density weighted quantities $\bar{\phi}\left(x_i, t\right)$, e.g., the filtered progress variable source term $\bar{\omega}_{Y_C}$, can be computed:

$$\begin{aligned} \bar{\phi}\left(x_i, t\right) &= \int_0^1 \int_{\chi_{st,\min}}^{\chi_{st,\max}} \int_0^1 \phi\left(Z, \chi_{st}, C\right) P\left(Z, \chi_{st}, C\right) \mathrm{d}Z \mathrm{d}\chi_{st} \mathrm{d}C \\ &= \bar{\rho} \int_0^1 \int_{\chi_{st,\min}}^{\chi_{st,\max}} \int_0^1 \phi\left(Z, \chi_{st}, C\right) \frac{1}{\rho} \widetilde{P}\left(Z, \chi_{st}, C\right) \mathrm{d}Z \mathrm{d}\chi_{st} \mathrm{d}C. \end{aligned} \tag{2.83}$$

The relation for the filtered density is presented as [93]:

$$\bar{\rho}\left(x_i, t\right) = \left[\int_0^1 \int_{\chi_{st,\min}}^{\chi_{st,\max}} \int_0^1 \frac{1}{\rho} \widetilde{P}\left(Z, \chi_{st}, C\right) \mathrm{d}Z \mathrm{d}\chi_{st} \mathrm{d}C\right]^{-1}. \tag{2.84}$$

The joint FDF $\widetilde{P}\left(Z, \chi_{st}, C\right)$ can be further decomposed in its marginal and conditioned FDF [182]:

$$\widetilde{P}\left(Z, \chi_{st}, C\right) = \widetilde{P}\left(Z, \chi_{st}\right) P\left(C \mid Z, \chi_{st}\right). \tag{2.85}$$

Statistical independence of the mixture fraction Z and χ_{st} is assumed for the normalized progress variable C in Eq. 2.79. Also, Z and χ_{st} are assumed to be statistical independent [182], the FDF can be further decomposed to:

$$\widetilde{P}\left(Z,\chi_{st},C\right)=\widetilde{P}(Z)P\left(\chi_{\mathrm{st}}\right)P\left(C\right). \tag{2.86}$$

The shape of the presumed FDF is essential for the model quality. The bimodal nature of the sub-grid scale mixing PDF defined by $\widetilde{Z}$ and its variance $\widetilde{Z//^2}$ was discovered in DNS [183]. In Cook et al. [183], a β-PDF was suggested and successfully used in many studies thereafter, e.g., [174–177, 182]. The β PDF is defined as follows:

$$\tilde{P}(Z,\widetilde{Z},\widetilde{Z''^2})=\frac{\Gamma\left(\beta_1+\beta_2\right)}{\Gamma\left(\beta_1\right)\Gamma\left(\beta_2\right)}Z^{\beta_1-1}(1-Z)^{\beta_2-1}. \tag{2.87}$$

The β-PDF is defined by the mean $\widetilde{Z}$ and its sub-grid scale variance $\widetilde{Z''^2}$ (first and second moment of the distribution), where $\widetilde{Z''^2}$ is defined as:

$$\widetilde{Z''^2}=\widetilde{Z^2}-\widetilde{Z}^2. \tag{2.88}$$

In Eq. 2.87, Γ denotes the gamma function:

$$\Gamma(\beta)=\int_0^\infty x^{\beta-1}e^{-x}dx, \tag{2.89}$$

and the parameters β_1 and β_2 are defined as:

$$\beta_1=\widetilde{Z}\left[\frac{\widetilde{Z}(1-\widetilde{Z})}{\widetilde{Z''^2}}-1\right], \tag{2.90}$$

$$\beta_2=(1-\widetilde{Z})\left[\frac{\widetilde{Z}(1-\widetilde{Z})}{\widetilde{Z''^2}}-1\right]. \tag{2.91}$$

The variance of the mixture fraction is further normalized, allowing an efficient table lookup:[5]

$$\widetilde{Z''^2}^N=\left[\frac{\widetilde{Z}(1-\widetilde{Z})}{\widetilde{Z''^2}}\right]^{-1}. \tag{2.92}$$

The entire thermo-chemical state composed of Favre filtered parameters is now defined as $\Phi\left(\widetilde{Z},\widetilde{\chi}_{\mathrm{st}},\widetilde{C},\widetilde{Z''^2}^N\right)$.

In accordance to other works [90, 140, 182, 184], the probability functions for χ_{st} and C are chosen as a dirac δ function.

---

[5] $\widetilde{Z''^2}^N$ is also denoted as the segregation factor [140].

2.3.4.2 RUFPV-LES coupling

The coupling of the combustion model with the Large Eddy Simulation is described in the following and illustrated in Figure 2.6. As presented in Sec. 2.3.4, the Reduced Unsteady Flamelet Progress Variable (RUFPV) approach is used, and the thermo-chemical state is uniquely defined by $\widetilde{\Phi} = \widetilde{\Phi}\left(\widetilde{Z}, \widetilde{\chi}_{\mathrm{st}}, \widetilde{C}, \widetilde{Z''^2}^N\right)$.

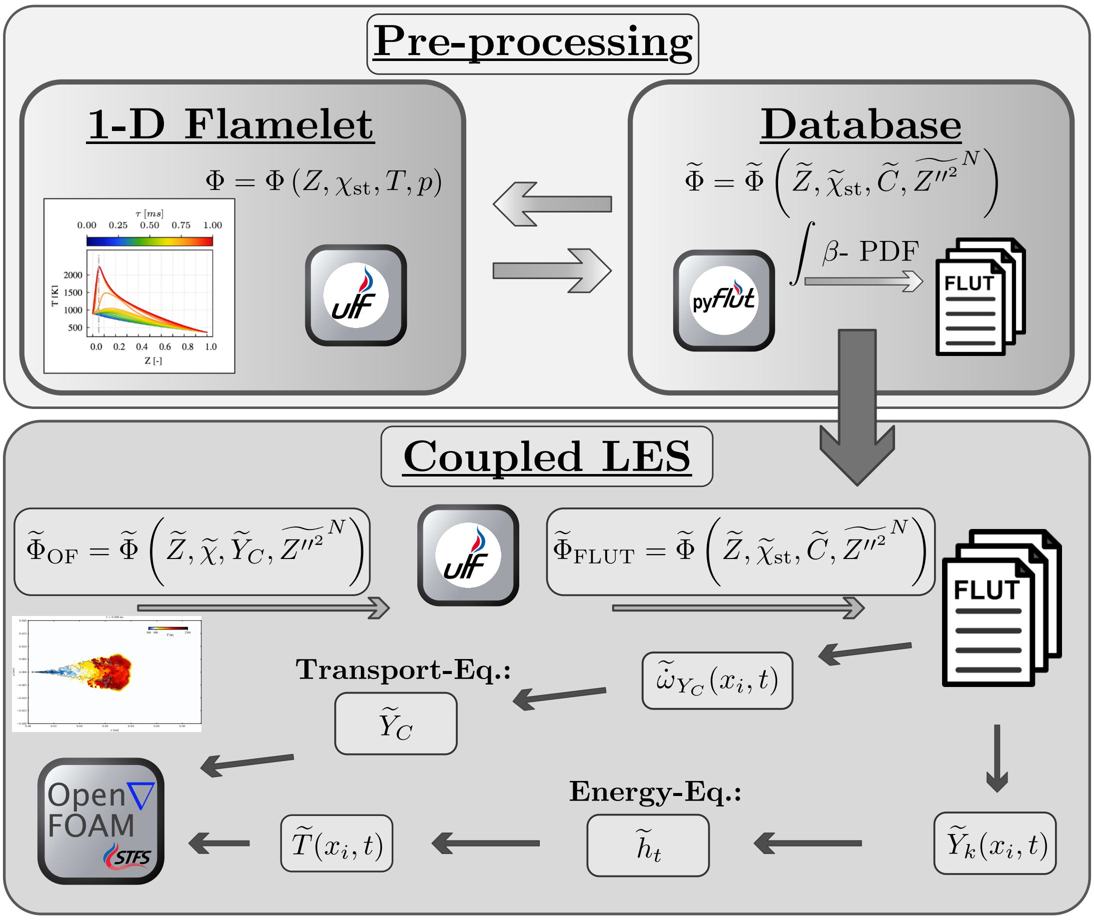

Figure 2.6: Schematic of the RUFPV-LES coupling used in this thesis in the style of [93]. The open-source CFD solver OpenFOAM v2012 [167], the in-house C++ flamelet solver ULF [185], and the in-house Python tool pyFlut are utilized.

In the reactive spray LES, reactive scalar transport equations are solved for $\widetilde{Z}$ and $\widetilde{Y}_C$. The transport equations in Eq. 2.93 and Eq. 2.94 for the filtered mixture fraction $\widetilde{Z}$ and the progress variable $\widetilde{Y}_C$ read:

$$\frac{\partial \bar{\rho} \widetilde{Z}}{\partial t} + \frac{\partial \bar{\rho} \widetilde{u}_i \widetilde{Z}}{\partial x_i} = \frac{\partial}{\partial x_i}\left[\bar{\rho}\left(\widetilde{D}_Z + \frac{\nu_{\mathrm{SGS}}}{\mathrm{Sc}_{\mathrm{SGS}}}\right)\left(\frac{\partial \widetilde{Z}}{\partial x_i}\right)\right] + \bar{\rho}\widetilde{\dot{S}}_m, \tag{2.93}$$

$$\frac{\partial \bar{\rho} \widetilde{Y_C}}{\partial t} + \frac{\partial \bar{\rho} \widetilde{u}_i \widetilde{Y}_c}{\partial x_i} = \frac{\partial}{\partial x_i}\left[\bar{\rho}\left(\widetilde{D}_{Y_C} + \frac{\nu_{\mathrm{SGS}}}{\mathrm{Sc}_{\mathrm{SGS}}}\right)\left(\frac{\partial \widetilde{Y_C}}{\partial x_i}\right)\right] + \bar{\rho}\widetilde{\dot{\omega}}_{Y_C}. \tag{2.94}$$

The diffusion coefficients $\widetilde{D}_Z$ and $\widetilde{D}_{Y_C}$ are evaluated utilizing the Lewis unity number assumption, see Eq. 2.8. The eddy diffusivities are evaluated based on the gradient flux assumption $D_t = \frac{\nu_{\mathrm{SGS}}}{\mathrm{Sc}_{\mathrm{SGS}}}$. Here, $\mathrm{Sc}_{\mathrm{SGS}}$ represents the sub-grid scale Schmidt number. Within this thesis, the turbulent Schmidt and Prandtl numbers are set to $\mathrm{Sc}_{\mathrm{SGS}}{=}\mathrm{Pr}_{\mathrm{SGS}}{=}0.4$ [3, 93]. In contrast to the laminar flamelet transport equations, $\widetilde{Z}$ and $\widetilde{Y_C}$ are reactive scalars due to their source terms $\widetilde{\dot{S}}_m$ and $\widetilde{\dot{\omega}}_{Y_C}$. The spray mass source term $\widetilde{\dot{S}}_m$[6] is evaluated according to Eq. 2.53, and the progress variable source term is defined as the sum of the net production rates of the species composing the progress variable (see Eq. 2.78). The progress variable is normalized for the table lookup according to Eq. 2.79.

The filtered scalar dissipation rate $\widetilde{\chi}_{\mathrm{st}}$ and the variance of the mixture fraction $\widetilde{Z''^2}$ are evaluated from algebraic expressions [177, 186, 187]. The mixture fraction variance is computed using the algebraic expression:

$$\widetilde{Z''^2} = C_{\widetilde{Z''^2}} \Delta^2 \left| \frac{\partial \widetilde{Z}}{\partial x_j} \right|^2 , \tag{2.95}$$

where according to Pierce [177], $C_{\widetilde{Z''^2}}$=0.13. $\widetilde{Z''^2}$ is further normalized using Eq. 2.92.
The Favre-filtered scalar dissipation rate is computed according to [188]:

$$\widetilde{\chi} = 2 \left(\widetilde{D}_Z + \frac{\nu_{\mathrm{SGS}}}{\mathrm{Sc}_{\mathrm{SGS}}} \right) \left| \frac{\partial \widetilde{Z}}{\partial x_j} \right|^2 , \tag{2.96}$$

and the scalar dissipation rate at stoichiometric conditions used for table lookup is evaluated as [188]:

$$\widetilde{\chi}_{st} = \frac{\widetilde{\chi}}{\int_{Z=0}^{Z=1} \frac{f(Z)}{f(Z_{st})} \widetilde{P}(Z) \mathrm{d}Z} . \tag{2.97}$$

As described in further detail in Gierth et al. and the thesis of Gierth [3, 93], mapping the flamelet time on a progress variable results in no ignition without an initial value of the source term at C=0. In this thesis, the progress variable source term at C=0 is replaced with a very small source term according to the following integration:

$$\dot{\omega}^*_{init} \left(Z, \chi_{st} \right) = \frac{\int_0^{t(C=C_{init})} \dot{\omega}_{Y_C} \left(Z, \chi_{st}, t \right) \mathrm{d}t}{\int_0^{t(C=C_{init})} \mathrm{d}t} \quad \forall C \in \left[0, C_{init} \right] . \tag{2.98}$$

The choice of C_{init} has been carefully chosen, so the ignition process is not affected by means of too early ignition. The presented approach has been successfully utilized in [3, 93, 94].

As shown in Figure 2.6, the progress variable source term $\widetilde{\dot{\omega}}_{Y_C}$ and the species mass fraction vector $\widetilde{Y}_k$ are retrieved from the FLUT.

---

[6] In this thesis preferential evaporation effects for multicomponent fuels on combustion are neglected, hence, only one equation for the mixture fraction is solved.

3 Experimental Reference Configurations

Spray simulations, besides other reactive flow simulations, have the strong premise of relying on experimental data due to the non-predictive character of the spray models. The experimental setups and data used within this thesis are briefly described in the following for a deeper understanding of available data. An overview of all available experimental data is provided in Table 3.1.

Table 3.1: Overview of experimental data for the investigated fuels and injectors. The data for the ECN Spray A3 and the Woodward L'Orange injector are provided by the Department of Fluidsystemtechnik (FST) at the University of Erlangen-Nuremberg. For the ECN Spray D, measurement data has been provided by the Sandia National Laboratories (SNL) and by CMT - Motores Térmicos (CMT) at the Universitat Politècnica de València.

Injector:	ECN: Spray A3 ($d=97\,\mu\mathrm{m}$)		ECN Spray D ($d=190\,\mu\mathrm{m}$)		L'Orange Woodward ($305\,\mu\mathrm{m}$)	
Fuel:	Inert	Reactive	Inert	Reactive	Inert	Reactive
$\mathrm{OME}_{\mathrm{mix}}$	FST: Schlieren, Mie	FST: OH^*	SNL: DBI,Rayleigh	CMT: OH^*		
1-Octanol	FST: Schlieren, Mie	FST: OH^*			FST: Schlieren, Mie	FST: OH^*
n-Dodecane	FST: Schlieren, Mie	FST: OH^*	SNL: DBI,Schlieren	CMT: OH^*	FST: Schlieren, Mie	FST: OH^*

3.1 Constant volume chamber diagnostics

The Constant Volume Chamber is utilized to examine Diesel engine combustion since it resembles closest the conditions at the top dead center position when ignition occurs in the engine. The simplified geometry in spray chambers allows the separation of the influence of complex engine flow and piston movement from the mixture formation and combustion process of spray flames while keeping full physical complexity.

In the following, important measurement techniques of integral spray metrics are presented. The liquid penetration lengths defining the furthest distance of the liquid phase from the nozzle are usually measured utilizing the Diffuse Backlight Illumination (DBI) method [189, 190] or Mie-Scattering [191]. The vapor penetration length, denoting the distance of the fuel vapor cloud from the nozzle, is determined by Schlieren imaging or Rayleigh-Scattering [192]. Reactive measurements often utilize imaging of the excited hydroxyl radical OH^*, which is obtained by OH^* chemiluminescence. Another method that can measure the mass fractions of hydroxyl radicals OH and formaldehyde CH_2O is the Planar Laser Induced Fluorescence (PLIF) technique. In Figure 3.1, an image of the high-pressure, high-temperature constant volume chamber from the Department of Fluidsystemtechnik (FST) in Erlangen-Nuremberg is presented.

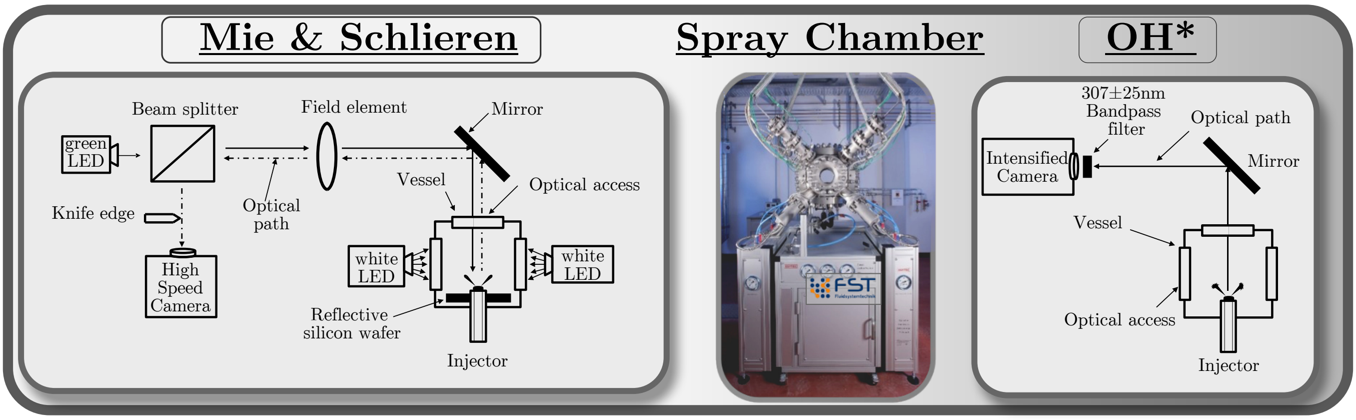

Figure 3.1: Overview of the high-pressure, high-temperature measurements at the Department of "Fluidsystemtechnik" (FST) at the University of Erlangen-Nuremberg. On the left, the combined Mie scattering and Schlieren setup is shown, which is used to evaluate liquid and vapor penetration lengths and to visualize the spray. The image in the center shows the high-pressure, high-temperature spray chamber used at FST. On the right side, the setup is used to measure excited hydroxyl radicals (OH^*) in reactive conditions as a flame marker and evaluate the spray ignition delay time.

3.2 Automotive injector: ECN Spray A3

All fuels investigated in this thesis: n-Dodecane, 1-Octanol and $\mathrm{OME}_{\mathrm{mix}}$, have been measured with the Engine Combustion Network (ECN) Spray A3 single hole injector and have partially been published in Strauß et al. [21]. The nominal nozzle diameter is $d_0 = 90\,\mu\mathrm{m}$. However, each injector in the ECN has a slightly different diameter. In this study, the injector with serial number *02C08028* with an actual $d_0 = 97.48\,\mu\mathrm{m}$ is used. The Spray A class of injectors is representative of automotive applications. The Spray A3 variant has, in contrast to the standard Spray A injector, a higher conicity factor K in the nozzle ($K_{\mathrm{SA3}} = 3$ vs. $K_{\mathrm{SA}} = 1.5$).

The measurements have been performed in the high-pressure, high-temperature spray chamber at the Department of Fluidsystemtechnik (FST) at the University of Erlangen-Nuremberg. The ECN baseline conditions are listed in Table 3.2 and are used for all investigated cases. They also represent the boundary conditions in the LES and flamelet simulations. In Figure 3.1, the measurement techniques are visualized. On the left, in Figure 3.1, the combined Mie-scattering and Schlieren setup is shown. In the center, the spray chamber is displayed and on the right, the setup for the measurements of hydroxyl radicals in its excited state (OH^*) is visualized. The measurements are repeated for 32 injections, the independent injection events are then ensemble averaged. The averaged intensities are then normalized by their respective maximum value. A more detailed explanation of the recording procedures and the equipment is found in Haspel et al. [1] and the thesis of Rieß [191].

Table 3.2: ECN baseline conditions boundary conditions.

Parameter:	$T_{Chamber}$	T_{Fuel}	$p_{Chamber}$	p_{Rail}	X_{Fuel}	X_{O2}	X_{N2}
Inert:	900 K	363 K	60 bar	1500 bar	1	0	1
Reactive:	900 K	363 K	60 bar	1500 bar	1	0.15	0.85

3.3 Heavy duty injector: ECN Spray D

The heavy-duty single-hole injector Spray D from the Engine Combustion network has been put more into focus in the last years. For n-Dodecane, the database of the experimental data is reasonably good, but for OME_{mix}, the data availability is limited. In this thesis, the Spray D nozzle with the serial number *209103* has been utilized, which has an actual diameter of d_0 =190 µm. The data for the inert comparison with n-Dodecane is published on the ECN website [81] and was measured at Sandia National Labs. An overview of the spray chamber at Sandia National Laboratories (SNL) is provided in [190]. Vapor penetration lengths are determined from Schlieren imaging, and liquid penetrations are derived from Diffuse Backlight Illumination (DBI). The data for OME_{mix} has been provided by Sandia National Labs by personal communication (Julien Manin, Kevin Wan and Lyle Pickett). The liquid penetration lengths have been measured using DBI, and the vapor penetration lengths were measured using Rayleigh Scattering. During the measurements of vapor penetration length, Kevin Wan reported particle formation. Similar behavior has been observed during the measurements of vapor pressures in Fechter et al. [2][1]. For Spray D, no Schlieren or Mie imaging data for inert conditions are available for the author.

Ignition delay times are provided by CMT-Motores Térmicos [194]. The chemiluminescence imaging for n-Dodecane and OME_{mix}, which has been published in Pastor et al. [82], has been provided by personal communication (Jose Maria Garcia).

3.4 Marine injector: Woodward L'Orange single hole injector

Since no experimental data is available for 1-Octanol in the Spray D configuration, the technical single-hole injector from Woodward L'Orange with a nozzle diameter of d_0=305 µm is used for the comparison in a large injector setup. The nozzle size is typical for marine engines and off-road stationary engines. The applied measurement techniques are the same as described in Sec. 3.2. In the marine injector, n-Dodecane and 1-Octanol have been examined.

---

[1] The author assumes that at high temperatures and under inert conditions, formaldehyde is produced [193]. Since formaldehyde is the basic chemical for the polymer polyoxyethylene, a polymerization reaction under inert conditions is likely.

4 Numerical Setup

The settings of the numerical framework used in this study are briefly presented in this chapter. An overview of the used meshes and their design is given. Furthermore, the parameters for the spray breakup model are provided. Finally, the used numerical schemes and discretization methods are presented.

4.1 Mesh generation

In this thesis, multiple meshes are used that are optimized toward each injector size. Since Large Eddy Simulations are always grid-dependent, and spatial discretization is crucial to the simulation accuracy. In the Euler-Lagrange approach, the spatial expansion of the parcels is neglected. In the Eulerian field, they can be regarded as a point source. Only in the two-way coupling the diameter is taken into account for momentum exchange. This represents a limitation to the grid resolution since the parcel diameter is supposed to be smaller than the cell size (far field assumption). In contrast, in LES, a high grid resolution is needed. The parcels are the largest near the nozzle, and their diameter decreases significantly due to breakup and evaporation downstream. The far-field assumption can be violated in the near nozzle region using the blob method and a too-fine mesh resolution. Note that the influence of parcels larger than the grid size is regarded as negligible since the high-pressure injection leads to a fast primary breakup. In the region where the far field assumption is violated, a common approach is to limit the evaporation source term to the cell volume, which is also applied in this thesis [195, 196].

Table 4.1: Mesh dimensions of the meshes for ECN Spray A3, ECN Spray D and Woodward L'Orange single hole injector.

	d_0	Δx_{min}	X	Y	Z
ECN Spray A3	$97\,\mu\text{m}$	$62.5\,\mu\text{m}$	$(-0.03\,\text{m},0.03\,\text{m})$	$(0\,\text{m},0.1\,\text{m})$	$(-0.03\,\text{m},0.03\,\text{m})$
ECN Spray D	$190\,\mu\text{m}$	$125\,\mu\text{m}$	$(-0.04\,\text{m},0.04\,\text{m})$	$(0\,\text{m},0.15\,\text{m})$	$(-0.04\,\text{m},0.04\,\text{m})$
Woodward L'Orange	$305\,\mu\text{m}$	$183\,\mu\text{m}$	$(-0.03\,\text{m},0.03\,\text{m})$	$(0\,\text{m},0.14\,\text{m})$	$(-0.03\,\text{m},0.03\,\text{m})$

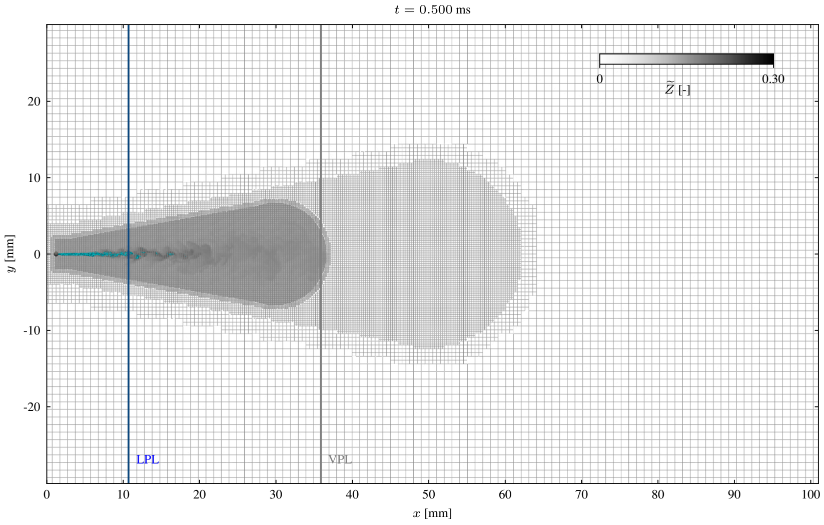

(a) ECN Spray A3 mesh.

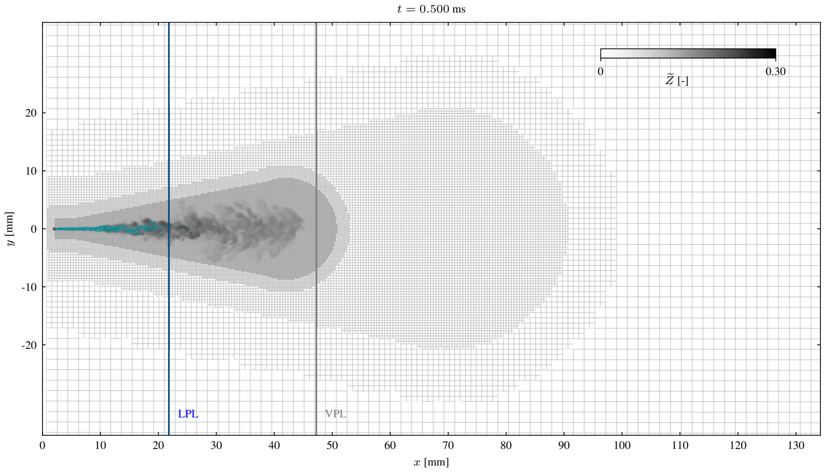

(b) ECN Spray D mesh.

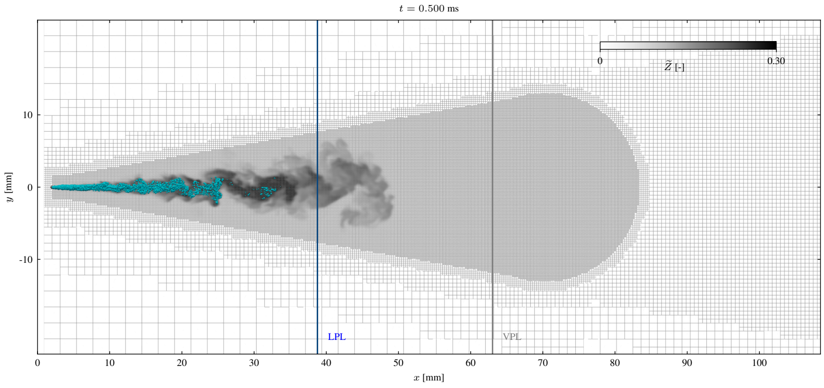

(c) Woodward L'Orange single hole injector mesh.

Figure 4.1: Overview of the meshes used in this study. The vapor penetration length at the according time step is marked as a vertical gray line, and the liquid penetration length is shown as a blue line to illustrate the dimensions of the spray. The mesh for Spray A3 (a) has approximately $11.6\,\mathrm{xe6}$ cells, the mesh of Spray D (b) has $4.8\,\mathrm{xe6}$ cells, and the Woodward L'Orange mesh (c) has $7.4\,\mathrm{xe6}$ cells. The meshes only use hexahedral cells.

In the study of Wehrfritz et al. [123], a mesh study has been performed for the ECN Spray A configuration ($d_0 = 90\,\mu\mathrm{m}$). The key finding here is that a cell size close to the nozzle of $\Delta x \approx \frac{2}{3} \cdot d_0 = 64.5\,\mu\mathrm{m}$ is a good compromise in terms of liquid and vapor penetration lengths and grid resolution of the gas phase in LES. In this study, the ratio of $\frac{2}{3}$ has also been applied to the larger injectors. Good agreement has been achieved using this ratio.

In Figure 4.1, the meshes used in this study are displayed. In order to reduce the overall number of cells, while maintaining the same simulation quality, a refinement strategy is applied. From an initial mesh, four refinement levels are applied. The shape of the refinement is adapted to the spray and has the shape of a cone. The meshes only use hexahedral cells and have been created using the OpenFOAM tool snappHexMesh [167].

4.2 Solver settings and discretization

The 3D-CFD simulations have been performed with the open-source C++ software OpenFOAM v2012 (ESE branch) [167]. The solver used in this thesis is based on the OpenFOAM solver sprayFoam. This solver has been extended with a coupling to the in-house *C++* code Universal Laminar Flame (ULF) solver [185] and the interface flameletConfig [197] for the efficient retrieval of data in precomputed tables. The coupling with ULF enables the usage of the tabulated chemistry approach in OpenFOAM. Several models in OpenFOAM have been modified, e.g., the evaporation model, breakup model and liquid properties have been added to the standard version (see Sec. 2.2.2). The adapted transient low-Mach number transient Euler-Lagrange solver used in this thesis was developed together with Sandro Gierth [93] and is named sprayFlameletFoam. The solver uses the Finite Volume Method (FVM) [198] as the discretization method. For the pressure velocity coupling, the PISO algorithm is used [199]. The discretization order in time is 1$^{\mathrm{st}}$ order due to robustness reasons. Very small maximum time steps of $\Delta t_{\mathrm{max}} = 150\,\mathrm{ns}$ ensure small numerical integration errors. Spatial discretization schemes are 2$^{\mathrm{nd}}$ order schemes.

Table 4.2: Overview of the breakup model parameters used in this thesis. The settings shown in this table have been used for inert and reactive simulations equally.

Fuel:	Injector:	B_0	B_1	C_τ	C_{RT}	ms_{Limit}	We_{Limit}	Spray angle [°]	m_{inj} [kg]	t_{inj} [s]
n-Dodecane	ECN Spray A3 ($d_0 = 97\,\mu\mathrm{m}$)	0.61	5	1	0.1	0.05	6	20	3.77e-06	0.00151
	ECN Spray D ($d_0 = 190\,\mu\mathrm{m}$)	0.61	5	1	0.1	0.05	6	19.7	50.56e-06	0.0045
	Woodward L'Orange ($d_0 = 305\,\mu\mathrm{m}$)	0.61	5	1	0.1	0.05	6	20	74.36e-06	0.0028
1-Octanol	ECN Spray A3 ($d_0 = 97\,\mu\mathrm{m}$)	0.61	5	1	0.1	0.05	6	20	3.97e-6	0.00151
	Woodward L'Orange ($d_0 = 305\,\mu\mathrm{m}$)	0.61	5	1	0.1	0.05	6	19	80.43e-06	0.0028
OME_{mix}	ECN Spray A3 ($d_0 = 97\,\mu\mathrm{m}$)	0.61	5	1	0.1	0.05	6	20	4.22e-06	0.00151
	ECN Spray D ($d_0 = 190\,\mu\mathrm{m}$)	0.61	5	1	0.1	0.05	6	21.5	59.60e-06	0.0045

The breakup model implemented in this thesis is presented in Sec. 2.2.1.3. During the simulation of the transient injection in Haspel et al. [1] many breakup models have been studied and examined. The KH-RT model has been proven to be a robust and trustworthy semi-empirical model. Towards predictive spray modeling a strong influence has been identified on the fuel mass flux (ROI) and spray angle. In Haspel et al. [1], the highly transient rate of the injection profile has been extracted from inner-nozzle flow simulations

[28], improving the liquid penetration lengths significantly. The simulations highlighted the importance of proper inflow conditions. As described in Pickett et al. [200], the rate of injection measurement techniques are often not reliable for the simulation and hence, modeling is needed to find the correct shape of the injection profile. Furthermore, the experimental far cone angle with the definition of Naber et al. [162] should be used in the KH-RT model as a boundary condition. All other parameters in the KH-RT model were determined for the used LES framework[1] at ECN baseline conditions. The parameters are constant for all injectors used, only the spray angle and ROI profiles change for each injector. The breakup parameter and spray angles are provided in Table 4.2.

---

[1] The author wants to emphasize that the settings should be adjusted to the numerical framework. Even in the same simulation framework, different parameters are expected in a RANS model.

5 Spray Mixture Formation Analysis

In the compression ignition engine cause-effect chain, the first step is the mixture formation. As mixture formation defines the boundary conditions for the following steps, it is crucial to the ignition process. Within this thesis, novel synthetic and biogenic Diesel fuels are under investigation. The mixture formation process is examined in sprays of increasing complexity. An automotive-sized injector (ECN Spray A3, in Sec. 5.1), a heavy-duty injector (ECN Spray D, in Sec. 5.2) and a marine-sized injector (Woodward L'Orange, in Sec. 5.3) is employed in this thesis. In the following, the effects of different thermophysical properties are investigated. As a first step, the modeling framework is validated utilizing experimental data. Experimental Schlieren and Mie images are compared to LES results providing a visual impression of the sprays. Vapor and liquid penetration lengths are further used for a quantitative comparison. Differences in thermophysical fuel properties that influence the mixture formation are discussed in detail. In Sec. 5.4.1, global mixture characteristics, such as averaged mixture fraction and scalar dissipation rates, are derived from the Large Eddy Simulations and compared between the sprays. Finally, the temperature distribution of the gas phase is analyzed in mixture fraction space in Sec. 5.4.2. This analysis elucidates the differences between the assumptions made in the combustion model and the actual conditions in the spray.

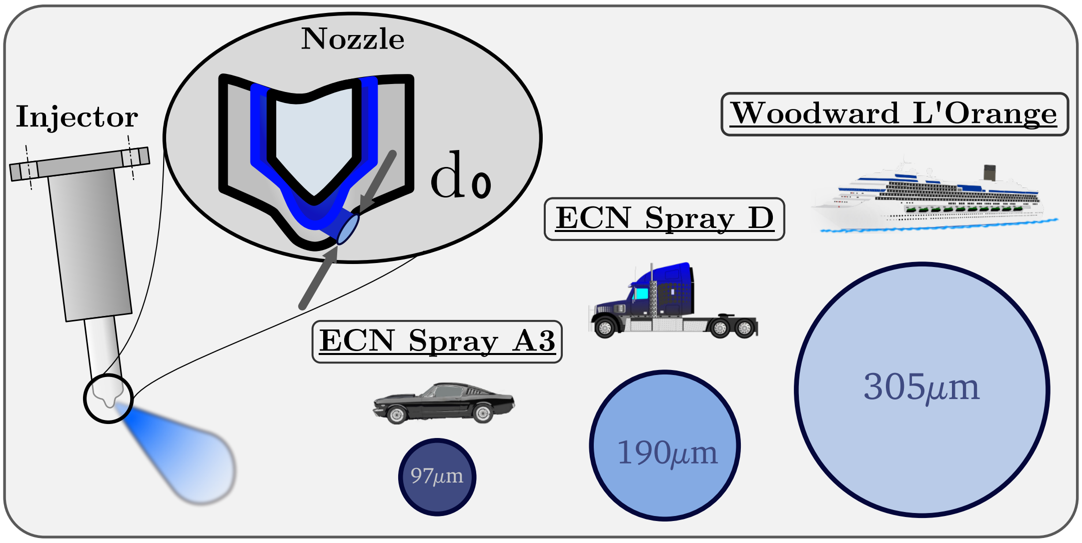

Figure 5.1: Overview of the injectors used in this thesis. A representative injector for the automotive sector is available with the Engine Combustion Network (ECN) Spray A3 injector with a nozzle diameter of d_0=97 µm. The heavy-duty sector is represented by the ECN Spray D injector with a nozzle diameter of d_0=190 µm. The representative Woodward L'Orange marine injector with a nozzle diameter of d_0=305 µm, can also be utilized in off-road power generators.

5.1 Automotive injector

The ECN Spray A3 injector introduced in Sec. 3.2 has a nozzle diameter of $d_0 = 97\,\mu\mathrm{m}$ and is typical for automotive applications. N-Dodecane is used as a surrogate for Diesel and serves as a reference case. Further, 1-Octanol and OME$_{\mathrm{mix}}$ are investigated as biogenic and synthetic fuels. In the following, the LES framework is validated, and differences between the fuels in the ECN Spray A3 injector at baseline conditions are elucidated.

5.1.1 Visual inspection of ECN Spray A3

In Figure 5.2, a visual impression is presented for all fuels in Spray A3. A time series is shown for the period relevant to mixture formation and ignition (t=$0.1\,\mathrm{ms}$-$0.4\,\mathrm{ms}$). In the top rows of each subfigure, the experimental averaged, normalized Schlieren signal I (gray) from FST (see Sec. 3.2) is overlayed by the Mie scattering signal (cyan). In the bottom rows, the Favre-filtered mixture fraction field $\widetilde{Z}$ from the LES is used for comparison. An iso-line with $\widetilde{Z}$ = 0.001 encloses the spray. According to Naber et al. [162], the value of $\widetilde{Z}$ = 0.001 is also used to determine the vapor penetration lengths within this thesis. For a comparison to the experimental Mie scattering signal, the parcel cloud is colored in cyan.

The comparison between the experiment and simulation shows overall good agreement for all fuels. Vapor and liquid penetration are matched qualitatively very well. Also, the spray shapes from the instantaneous LES align well with the experimental averaged counterpart. A closer examination shows that the spray shapes are similar for n-Dodecane and 1-Octanol. The shape with a broad spray head and a narrow spray area close to the injector is typical for automotive-sized injectors and has been reported in many studies for n-Dodecane [59, 91, 96, 99]. Also, for 1-Octanol, the shape from the LES aligns with existing experimental studies [21, 107]. The OME$_{\mathrm{mix}}$ spray shows a smaller spray far cone angle of approximately $19°$ than n-Dodecane with $21°$ in the experiment. Also, the LES shows that the OME$_{\mathrm{mix}}$ spray is narrower, and the spray pattern shows a more elongated shape. This behavior is also observed in experimental Raman-Rayleigh measurements in Wiesmann et al. [113]. The iso-contour of $\widetilde{Z}$=0.001 suggests that the spray is continuous. However, as shown in Figure 7.5 (reactive simulation), the iso-line of Z_{st} is not continuous. A detached region of smaller clouds with an enclosed iso-Z_{st} contour is observed, which is not found for n-Dodecane or 1-Octanol (see also Figure 7.3 and Figure 7.4). The spray separation has also been observed in the study by Mira et al. [112] for the Spray A injector (nominal nozzle diameter d_0=$90\,\mu\mathrm{m}$). As shown in Figure 5.2 (c), the $\widetilde{Z}$ = 0.001 iso-line of OME$_{\mathrm{mix}}$ does not show a disjointed spray visually. However, considering the high Z_{st}=0.1083 of OME$_{\mathrm{mix}}$, it becomes clear that the iso-line of Z_{st} may be separated from the spray core. This complex mixture formation phenomenon is only visible in LES (or DNS). Hence, other studies [82, 113, 114] in a RANS context, cannot deliver this in-depth information.

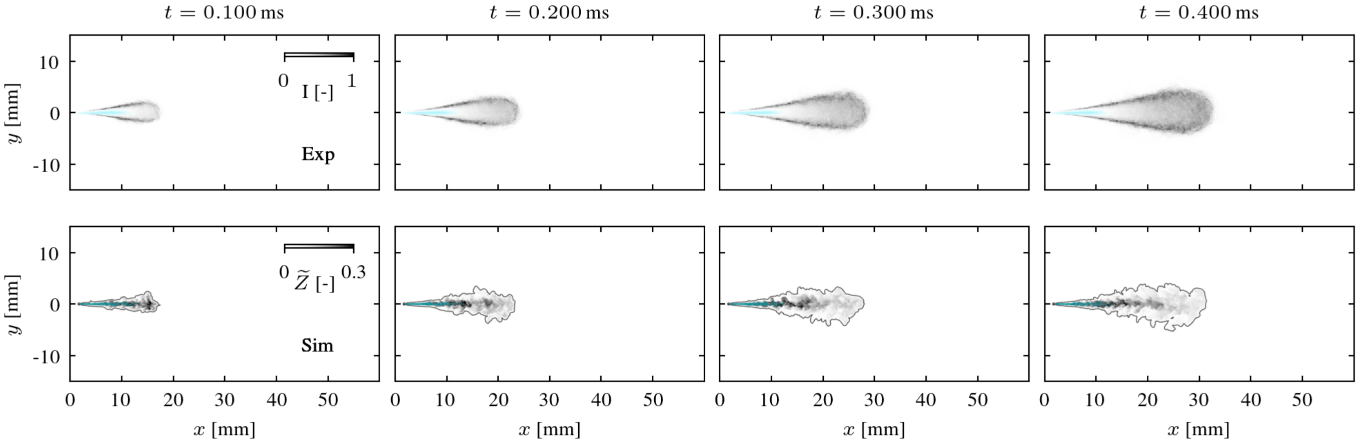

(a) n-Dodecane.

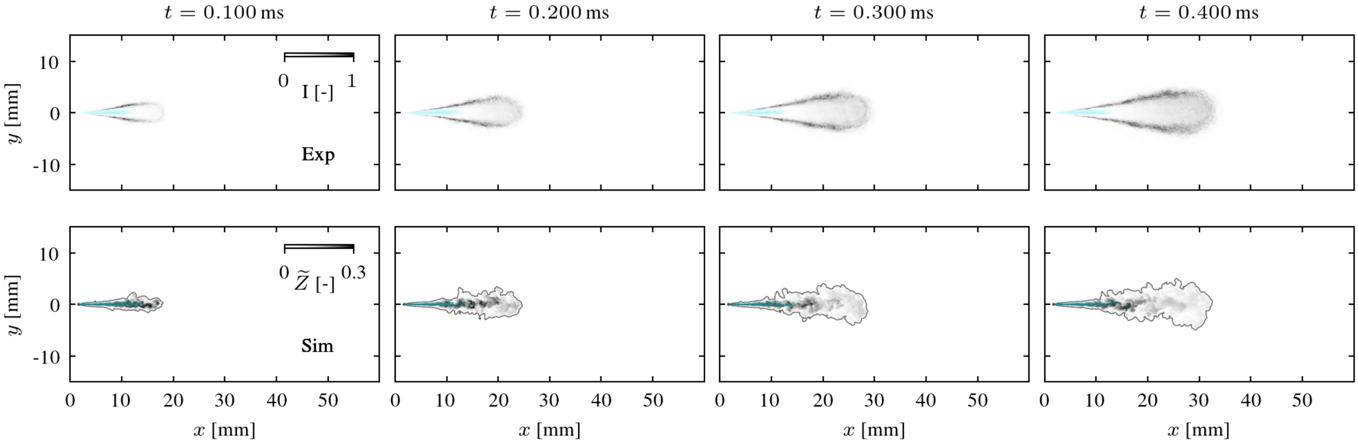

(b) 1-Octanol.

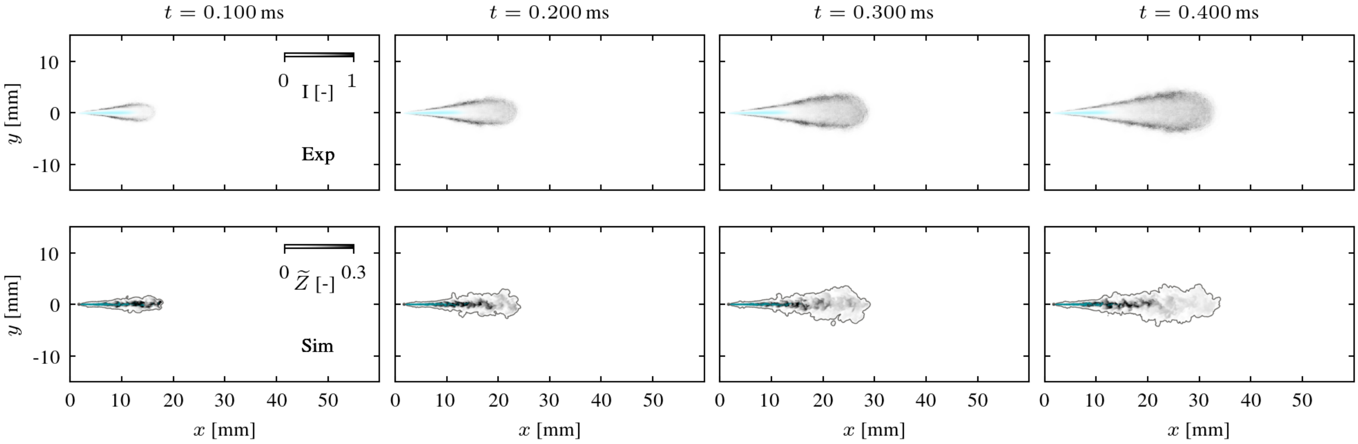

(c) $\mathrm{OME_{mix}}$.

Figure 5.2: Comparison of non-reactive Large Eddy Simulation results towards experimental data for ECN Spray A3. The results of n-Dodecane are shown in (a), 1-Octanol in (b) and $\mathrm{OME_{mix}}$ in (c). In the top rows of each subfigure, the overlayed averaged Schlieren (grayscale) and Mie (cyan) signals are displayed (normalized signal intensity I). The mixture fraction field $\widetilde{Z}$ and the parcels (cyan) are displayed in the bottom row. The iso-line around the spray corresponds to $\widetilde{Z}= 0.001$, which represents the spray contour as in the Schlieren image.

5.1.2 Quantitative comparison: Vapor and liquid penetration of ECN Spray A3

For a quantitative comparison, the vapor and the liquid penetration lengths are shown for the ECN Spray A3 injector in Figure 5.3. As described above, the vapor penetration in the LES is determined by the furthest distance of the $\widetilde{Z}=0.001$ iso-line to the nozzle. The liquid penetration in the LES is defined as the distance from the nozzle, where $99\,\%$ of the liquid mass is incorporated. In Figure 5.3, also the rate of injection (ROI) profile is presented with the dash-dotted line. The experimental ROI is determined with the "hydraulic pressure rise analyzer" ("Hydraulischer Druckanstiegs-Analysator" (HDA)); further details on the measurement technique are found in [201]. In modern high-pressure injectors, the ROI profiles usually follow a top-hat profile. As shown in Figure 5.3, the experimental ROI shows a flatter ramp-up compared to the modeled ROI used in the LES. The HDA measurement principle reacts slowly to rapid changes due to inertia effects in the pressure recordings. The slower ramp-up leads to higher liquid penetration lengths in the initial phase. Circumventing this issue, a rate of injection profile generator with physically more accurate profiles has been developed and provided by CMT and SNL [200].

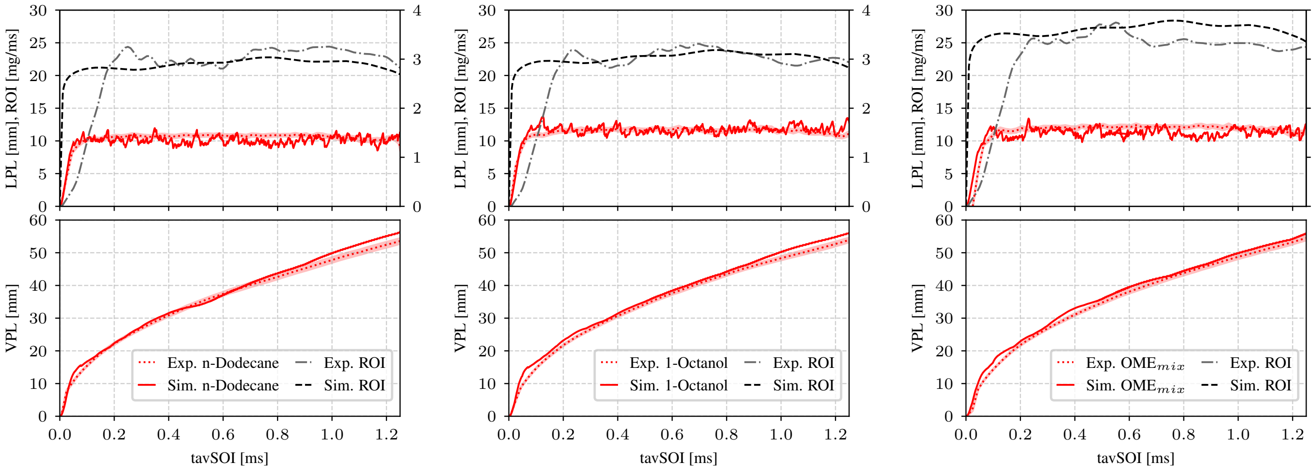

(a) n-Dodecane. (b) 1-Octanol. (c) $\mathrm{OME}_{\mathrm{mix}}$.

Figure 5.3: Comparison of the liquid and the vapor penetration length of n-Dodecane (a), 1-Octanol (b) and $\mathrm{OME}_{\mathrm{mix}}$ (c) under inert conditions for the ECN Spray A3. Experimental liquid and vapor penetration are plotted as a dotted line, LES results are represented by solid lines. The experimentally measured rate of injection profile is displayed using dash-dotted lines, and the modeled ROI [200] used in the LES is shown as a dashed line. While the vapor penetration lengths are similar, the liquid penetrations of 1-Octanol and $\mathrm{OME}_{\mathrm{mix}}$ are longer than that of n-Dodecane.

All fuels align quantitatively very well with the experimental data. Only minor deviations are observed at the start of the injection. The LES slightly overestimates the VPL at around $t=0.05\,\mathrm{ms}$ after the visible start of injection (tavSOI). This is found for all fuels, suggesting that the modeled ROI profile is not accurate in this region. However, deviations are small, and in comparison to other studies in the literature [97, 98, 101, 202], the results align very well. For n-Dodecane and 1-Octanol at around tavSOI$=1.0\,\mathrm{ms}$, again, a small overestimation of the VPL is observed, which is most likely attributed to the modeled ROI profile used. Also, the liquid penetration aligns very well with the experimental results for all fuels. For $\mathrm{OME}_{\mathrm{mix}}$, the LPL is partially underestimated, but overall the LES matches the experimental results well. The LES framework has been visually and quantitatively validated with experimental data for Spray A3, and results produced by the simulation are found to align very well.

5.1.3 Influence of thermophysical properties on mixture formation in ECN Spray A3

After successful validation of the used LES framework, mixture formation phenomena are elucidated. In Strauß et al. [21], it has been found for Spray A3 that the liquid penetration lengths of 1-Octanol ($\approx\langle 11.7\,\mathrm{mm}\rangle$) and OME$_{\text{mix}}$ ($\approx\langle 12.2\,\mathrm{mm}\rangle$) are longer than n-Dodecane ($\approx\langle 10.8\,\mathrm{mm}\rangle$). Considering the liquid thermophysical properties in Figure 2.4, the shorter LPL of n-Dodecane is counterintuitive. N-Dodecane has the lowest vapor pressure over a wide temperature range, indicating that it has the lowest volatility of all fuels. This raises the question, of how the fuel (n-Dodecane) with the lowest volatility can have the shortest liquid penetration length.

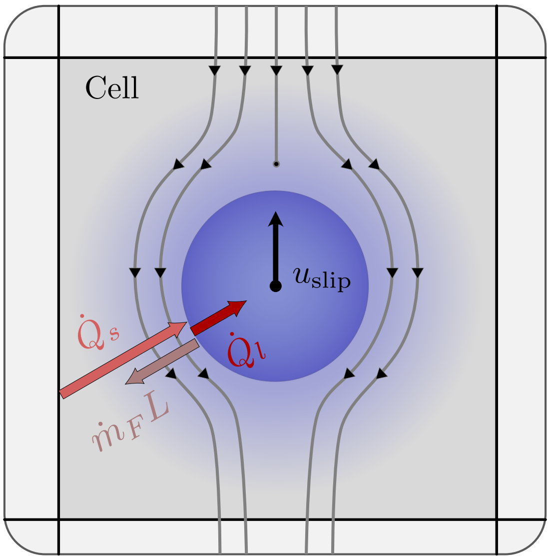

Figure 5.4: Illustration of the heat balance for a parcel in a cell shown in Eq. 2.52. The heat flux provided by the gas phase is denoted as $\dot{Q}_s$, the heat flux heating the droplet is represented by $\dot{Q}_l$ and the heat flux withdrawn from the parcel is calculated by the mass flux $\dot{m}_F$ times the latent heat of evaporation L. The parcel has the relative velocity u_{slip} in the gas phase.

In general, evaporation is dominated by the underlying thermophysical properties (vapor pressure and latent heat of evaporation) and the heat provided by the ambient (see Eq. 2.52). The amount of evaporated fuel is mainly depending on the temperature-dependent vapor pressure of the fuel. This means that heat from the surrounding is needed to heat up the droplet for evaporation. As shown in Figure 5.4, the amount of heat delivered from the gas phase ($\dot{Q}_s$) limits the evaporation process. If this consideration is followed further, a fuel with high vapor pressure and high heat of evaporation would withdraw more heat from the ambient. Consequently, the temperature in the gas phase would decrease. Since heat transfer is proportional to the temperature difference between the gas and liquid phase, less heat can be transferred from the ambient to the liquid phase and the evaporation rate decreases. Finally, longer liquid penetration lengths can be observed for fuels with high vapor pressure and high latent heat of evaporation. Please note that in high-pressure sprays, the heat provided to the spray is strongly linked to the air-entrainment process. Hence, thermophysical properties are not the only cause of longer liquid penetration lengths. In order to better quantify the complex interaction between air entrainment, heat exchange and thermophysical properties, a non-dimensional number for the particle heat transfer is derived with the help of dimensional analysis [203]. In Table 5.1, all thermophysical and physical quantities that supposedly contribute to evaporation and heat transfer are listed. Following the Buckingham Π-Theorem [203], eight quantities $N = 8$ are found with four dimensions $M = 4$, that result in $N - M = 4$ independent non-dimensional numbers. The quantities are the parcel slip velocity $u_{\text{slip}} = u_{\text{parcel}} - u_{\text{gas}}$, the liquid heat capacity at constant pressure $c_{p,l}$, the latent heat of evaporation h_{vap}, the cell gas temperature T_g, the gas thermal conductivity λ_g, the parcel diamter d, the liquid density ρ_l and the fuel vapor pressure p_{vap}. They have the dimensions length L [m], mass M [kg], time T [s] and temperature Q [K].

Table 5.1: Dimensional analysis to derive a non-dimensional number that describes the parcel heat transfer as a ratio of heat provided by the ambient and the required heat of the liquid phase to evaporate.

	u_{slip}	$c_{p,l}$	h_{vap}	T_g	λ_g	d	ρ_l	p_{vap}
L	1	2	2	0	1	1	-3	-1
M	0	0	0	0	1	0	1	1
T	-1	-2	-2	0	-3	0	0	-2
Q	0	-1	0	1	-1	0	0	0

Table 5.2: Non-dimensional numbers according to Π-Theorem that are derived from the dimensional analysis.

	$\frac{h_{\text{vap}}}{c_{p,l} \cdot T_g}$	$\frac{p_{\text{vap}} \cdot u_{\text{slip}} \cdot d}{\lambda_g \cdot T_g}$	$\frac{T_g \cdot \lambda_g}{\rho_l \cdot d \cdot u_{\text{slip}} \cdot h_{\text{vap}}}$	$\frac{\lambda_g \cdot T_g \cdot u_{\text{slip}}}{p_{\text{vap}} \cdot d \cdot h_{\text{vap}}}$
L	0	0	0	0
M	0	0	0	0
T	0	0	0	0
Q	0	0	0	0

The smart combination of variables gives the four independent non-dimensional variables $\Pi_i, i \in [1, 4]$ (see Table 5.2):

$$\Pi_1 = \frac{h_{\text{vap}}}{c_{p,l} \cdot T_g} \qquad \Pi_2 = \frac{p_{\text{vap}} \cdot u_{\text{slip}} \cdot d}{\lambda_g \cdot T_g}$$

$$\Pi_3 = \frac{T_g \cdot \lambda_g}{\rho_l \cdot d \cdot u_{\text{slip}} \cdot h_{\text{vap}}} \qquad \Pi_4 = \frac{\lambda_g \cdot T_g \cdot u_{\text{slip}}}{p_{\text{vap}} \cdot d \cdot h_{\text{vap}}}.$$

From the variables, Π_4 is selected for the analysis of longer liquid penetration lengths in the ECN Spray A3 for 1-Octanol and OME$_{\text{mix}}$ than n-Dodecane, since it incorporates the effect of changed vapor pressure and latent heat of evaporation of renewable fuels. The Parcel Heat index (PH index) in Eq. 5.1 can be interpreted as the ratio of heat that can be provided by the gas phase for evaporation, to the heat flux needed for evaporation in the liquid phase. Returning to the previous idea above, the PH index describes the cooling of the gas phase by evaporation and its influence on evaporation and the liquid penetration length. Hence, the PH index provides deeper insight into the mixture formation process.

$$\mathrm{PH} = \Pi_4 = \frac{\lambda_g \cdot T_g \cdot u_{\text{slip}}}{p_{\text{vap}} \cdot d \cdot h_{\text{vap}}} = \frac{\lambda_g(T_{g,\text{cell}_i}) \cdot T_{g,\text{cell}_i} \cdot u_{\text{slip,cell}_i}}{p_{\text{vap}}(T_{\text{parcel,cell}_i}) \cdot d \cdot |h_{\text{vap}}(T_{\text{parcel,cell}_i})|} \approx \frac{\text{"Heat flux from the gas phase"}}{\text{"Heat flux needed for evaporation"}} \tag{5.1}$$

The analysis of the PH index in the sprays has been performed in the following methodology. Liquid properties have been extracted from the Lagrangian phase. In the OpenFOAM implementation, the evaluation of affiliated gas properties is not straightforward. For each parcel, the corresponding cell in the Eulerian frame of reference has to be found by the cartesian coordinates of the parcel. With LES meshes of approximately 10 million cells, the iterative process for each parcel is computationally expensive. Hence, the parallelization technique of multithreading is applied to determine the gas properties of the parcels. In Figure 5.5, the conditional, parcel mass-weighted PDF of the parcel heat index for all parcels with an LPL over $10\,\mathrm{mm}$ is shown at tavSOI=$0.3\,\mathrm{ms}$ (liquid penetration is at steady state).

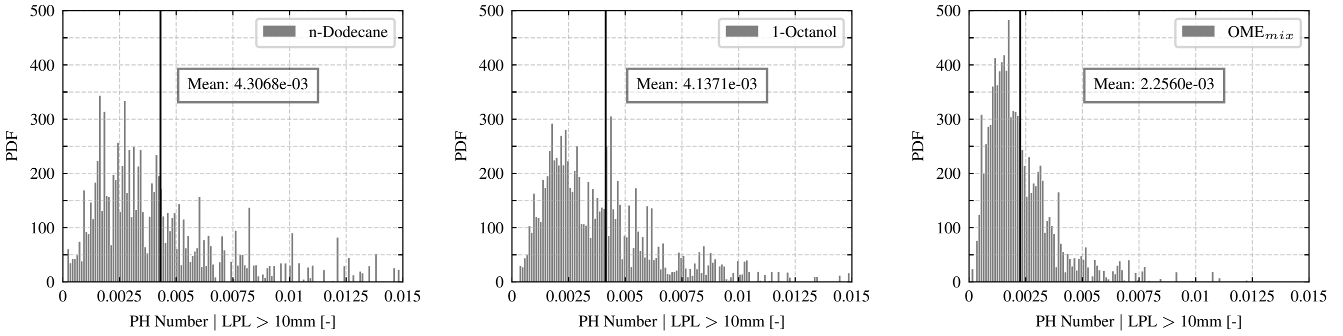

(a) n-Dodecane.

(b) 1-Octanol.

(c) OME$_{\text{mix}}$.

Figure 5.5: Comparison of the conditional, parcel mass-weighted distribution of the non-dimensional number PH at tavSOI=$0.3\,\mathrm{ms}$ for n-Dodecane (a), 1-Octanol (b) and OME$_{\text{mix}}$ (c) in ECN Spray A3. The PH number describes the ratio of available heat flux from the gas phase and the required heat for the evaporation of the fuel. The conditional mean of the PH of parcels shows lower values of PH for 1-Octanol and OME$_{\text{mix}}$, indicating higher liquid penetration lengths.

In Figure 5.5 (a), the PDF of n-Dodecane shows a higher variance compared to the other fuels. Higher values up to PH=0.0015 are reached[1]. N-Dodecane also has the highest mean value of PH=4.3068e-03. In regard to the smallest vapor pressure of all fuels investigated, but the lowest LPL, it is assumed that the spray of n-Dodecane can transfer more heat from the gas phase to the liquid phase, and hence, evaporation is increased. Consequently, the liquid penetration length of n-Dodecane is lower. While the shape of the PDF for 1-Octanol is very similar to n-Dodecane, overall lower values of the parcel heat index PH are observed. The lower mean value of PH= 4.1371e-03 for 1-Octanol (b) means that the parcels received less heat during their lifetime and exhibit a longer LPL. OME$_{\text{mix}}$ (c) shows a significantly different distribution and has the lowest mean of PH=2.2560e-03. Further, the distribution exhibits a lower variance. The mean value of PH for OME$_{\text{mix}}$ is considerably lower compared to n-Dodecane and 1-Octanol, which is reflected in the highest value of the liquid penetration length. The low values of PH suggest that the gas phase transferred less heat, and evaporation was

---

[1] Please note that also values PH $\gg$ 1 are observed at different parcel locations and time after visible start of injection.

limited. In summary, lower mean values of the PH number align well with the increasing liquid penetration lengths observed.

This analysis of the newly introduced Parcel Heat transfer number clearly shows, that thermophysical properties alone, e.g., the vapor pressure, are not sufficient to predict liquid penetration lengths in sprays. The mixture formation process plays a significant role in the evaporation of complex and novel renewable Diesel fuels. Since non-dimensional numbers like the PH index reduce complex phenomena into a single scalar, an interpretation of the observed phenomena is needed. In Sec. 5.4, more analysis is performed on the mixture formation process, allowing for a better understanding of the mixture formation process.

5.1.4 Interim conclusion for Spray A3

In the following, the most significant findings are summarized in bullet points:

- The LES framework has been successfully validated for renewable Diesel fuels under ECN Spray A3 inert baseline conditions.
- Significant differences have been identified in the mixture formation among n-Dodecane, 1-Octanol and $\mathrm{OME_{mix}}$. In regard to the thermophysical properties, the most volatile species $\mathrm{OME_{mix}}$ showed the longest liquid penetration length.
- The non-dimensional parcel heat transfer number (PH) has been derived with the help of dimensional analysis.
- The conditional PDF of the parcel heat transfer number showed that less heat is transferred from the gas phase for 1-Octanol and $\mathrm{OME_{mix}}$ during the parcel lifetime. This analysis explains the higher liquid penetrations of the renewable Diesel fuels 1-Octanol and $\mathrm{OME_{mix}}$ compared to the less volatile n-Dodecane.

5.2 Heavy-duty injector

The ECN Spray D injector presented in Sec. 3.3 represents a heavy-duty application, e.g., truck engines. In contrast to the nominal nozzle diameter of $d_0{=}180\,\mathrm{\mu m}$, the injector used in this thesis exhibits a slightly larger $d_0{=}190\,\mathrm{\mu m}$ (see Sec. 3). Unfortunately, no experimental data exists for 1-Octanol, but n-Dodecane and $\mathrm{OME_{mix}}$ are investigated in the following.

5.2.1 Visual inspection of ECN Spray D

As described in Sec. 3.3, no Schlieren and Mie image data is available for the ECN Spray D. Nevertheless, a visual impression of Spray D is given in Figure 5.6 showing a time series of the Favre-filtered mixture fraction field $\widetilde{Z}$ (gray) and the parcel cloud (cyan). The iso-line of $\widetilde{Z}{=}0.001$ represents the contour of the spray and is also used for the determination of the vapor penetration length.

The visual inspection of Figure 5.6 at t$=0.1\,\mathrm{ms}$ shows, that the parcel cloud of n-Dodecane (a) and $\mathrm{OME_{mix}}$ (b) is in the range of the vapor penetration ($\widetilde{Z}{=}0.001$ iso-line). This is a significant difference from the ECN Spray A3 injector, at the same time step, the liquid phase approximately penetrated half the distance compared to

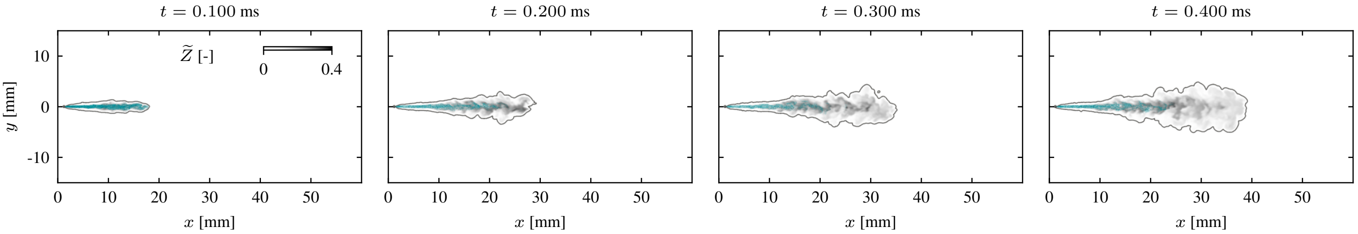

(a) n-Dodecane.

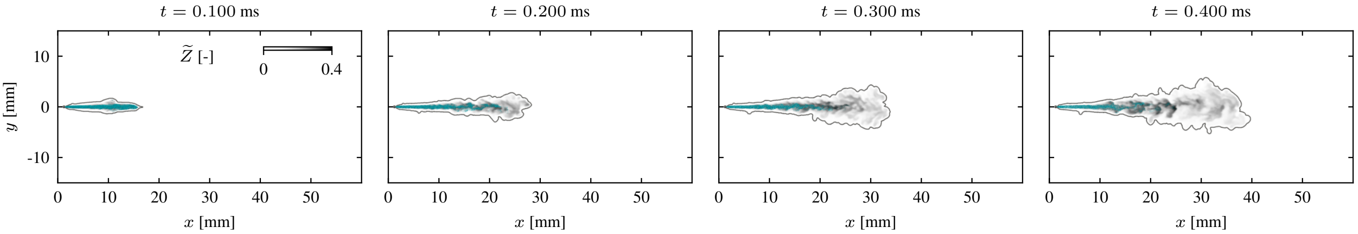

(b) $\mathrm{OME_{mix}}$.

Figure 5.6: Comparison of non-reactive Large Eddy Simulation results for n-Dodecane (a) and $\mathrm{OME_{mix}}$ (b) in the ECN Spray D. The mixture fraction field $\widetilde{Z}$ is displayed in gray, and the parcels are represented in cyan. The iso-line around the spray corresponds to $\widetilde{Z}$= 0.001, which represents the spray contour used to determine the vapor penetration lengths.

its vapor phase. As expected for a larger nozzle with the same injection duration, higher values of the mixture fraction are observed[2]. The shape of both sprays is more elongated compared to the ECN Spray A3. This might be attributed to the fact, that the liquid penetration length is doubled. After the visual inspection, a quantitative comparison of the experiment and LES is conducted.

5.2.2 Quantitative comparison: Vapor and liquid penetration of ECN Spray D

There are not many studies [140, 204, 205] numerically investigating the ECN Spray D under inert conditions. While there is a comprehensive dataset for n-Dodecane, data for $\mathrm{OME_{mix}}$ is very limited. While the ROI is used from CMT for n-Dodecane and $\mathrm{OME_{mix}}$, liquid and vapor penetration data is obtained from the ECN database [81] for n-Dodecane and for $\mathrm{OME_{mix}}$ from SNL by personal communication (Julien Menin, Kevin Wan, Lyle Pickett). The vapor penetration measurements for $\mathrm{OME_{mix}}$ at SNL do have some uncertainty. During the measurements, the formation of a white substance has been reported, that might disturb the Raman-Rayleigh signal. The field of view is limited from $30\,\mathrm{mm}$ to $70\,\mathrm{mm}$ (horizontal line) for $\mathrm{OME_{mix}}$.

---

[2] In comparison to Figure 5.3, the maximum in the color bar of the Favre-filtered mixture fraction is $\widetilde{Z}$=0.4.

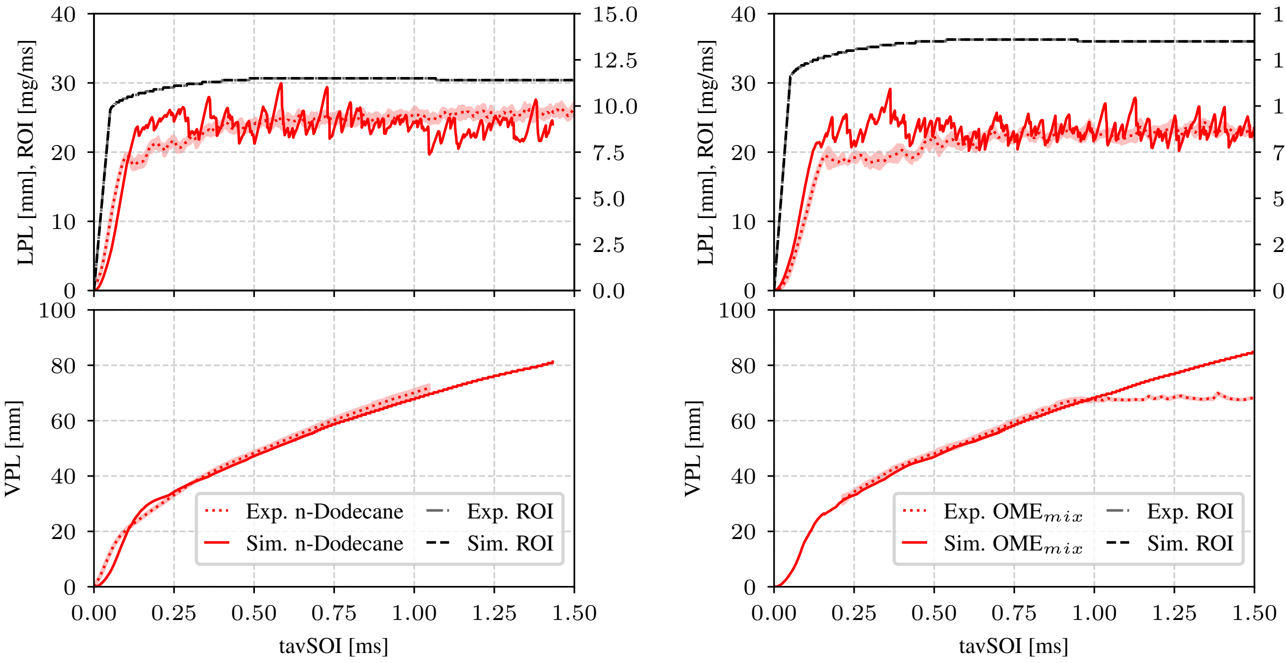

(a) n-Dodecane.

(b) OME$_{\text{mix}}$.

Figure 5.7: Comparison of liquid penetration and vapor penetration length of n-Dodecane (a) and OME$_{\text{mix}}$ (b) under inert conditions for the ECN Spray D injector. Experimental liquid and vapor penetration are plotted as a dotted line, and LES results are represented by solid lines. The experimentally measured rate of injection profile is displayed using dash-dotted lines, and the ROI used in the LES is shown as a dashed line (identical in this configuration). The experimental vapor penetration data for OME$_{\text{mix}}$ in (b) starts at $30\,\text{mm}$, and the field of view in the experiment is limited to $70\,\text{mm}$ (horizontal line). The LES results align very well with the experimental data.

The vapor penetrations derived from the LES in Figure 5.7 align with the experimental measurements for both fuels. Small deviations are observed for n-Dodecane (a) in the initial phase until tavSOI$=0.25\,\text{ms}$. These small deviations are most likely linked to the different ROI profile used in the simulation (ROI from CMT), while the vapor penetration has been measured at SNL. The vapor penetration length of OME$_{\text{mix}}$ (b) aligns perfectly with the experimental results. At larger nozzle diameters, it has been observed by the author, that in contrast to Spray A3, $95\,\%$ of the liquid mass in the LES should be used to determine the liquid penetration length[3]. The liquid penetration lengths for both fuels are slightly overestimated by the LES in the initial injection phase, the quasi-stationary liquid penetration lengths align excellently. The initial overprediction is observed by other groups as well [140, 205], and is most likely attributed to inaccuracies in the ROI measurement. As described in Sec. 5.1 the measurement of the transient increase at the beginning of injection is cumbersome and error-prone. In Spray D, n-Dodecane exhibits a higher liquid penetration length than OME$_{\text{mixt}}$.

Overall excellent alignment is found for both fuels between LES and the experiment. The LES framework is considered validated for the ECN Spray D setup.

---

[3] A comparison between computed [206] and experimental Mie signal in a heavy-duty injector [1] showed best alignment for $95\,\%$ of the liquid mass.

5.2.3 Influence of thermophysical properties on mixture formation in ECN Spray D

The vapor penetration lengths in Spray D for both fuels are almost identical. Following the studies of [191, 207, 208], the vapor penetration is strongly dominated by the momentum introduced by the liquid spray. It can be concluded that similar momentum is introduced. But a significant difference in the ROI profiles between the fuels is observed. The ROI of OME_mix in Figure 5.7 (b) shows higher values compared to n-Dodecane. The higher ROI values can be explained with the higher liquid density of OME_mix $\rho(T{=}363\,\mathrm{K}){=}974\,\mathrm{kg/m^3}$, than n-Dodecane $\rho(T{=}363\,\mathrm{K}){=}698\,\mathrm{kg/m^3}$ (see Figure 2.4). Consequently, n-Dodecane must exhibit higher parcel velocities to have the same momentum. Following this thought, the velocity distribution in the spray direction U_y is examined in Figure 5.8 for both fuels at tavSOI$=0.55\,\mathrm{s}$, where the quasi-steady state for the LPL is reached. It is visible that n-Dodecane has a higher mean value of the velocity $\langle U_y \rangle$ $=316.688\,\mathrm{m/s}$ and reaches higher maximum velocities. OME_mix has a lower mean value of $\langle U_y \rangle$ $=298.739\,\mathrm{m/s}$ and has lower maximum velocities. A study by Dageförde et al. [108] supports the results from the LES, where OME_mix has been reported to have lower nozzle exit velocities compared to the reference Diesel fuel. Generally, the injection rate in Spray D is four times higher than in Spray A3. The liquid penetration is approximately doubled.

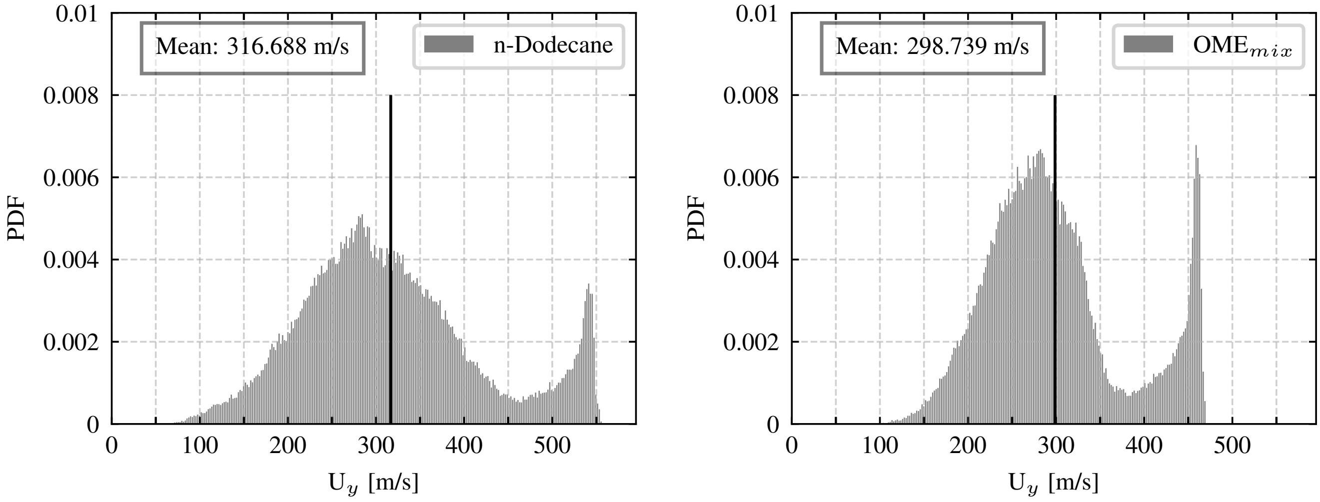

(a) n-Dodecane.

(b) OME_mix.

Figure 5.8: Comparison of the parcel velocity in spray axis U_y (y-direction) of n-Dodecane (a) and OME_mix (b) under inert conditions for the ECN Spray D injector at tavSOI$=0.55\,\mathrm{ms}$. The maximum and mean velocity (black vertical line) of n-Dodecane is significantly higher than for OME_mix.

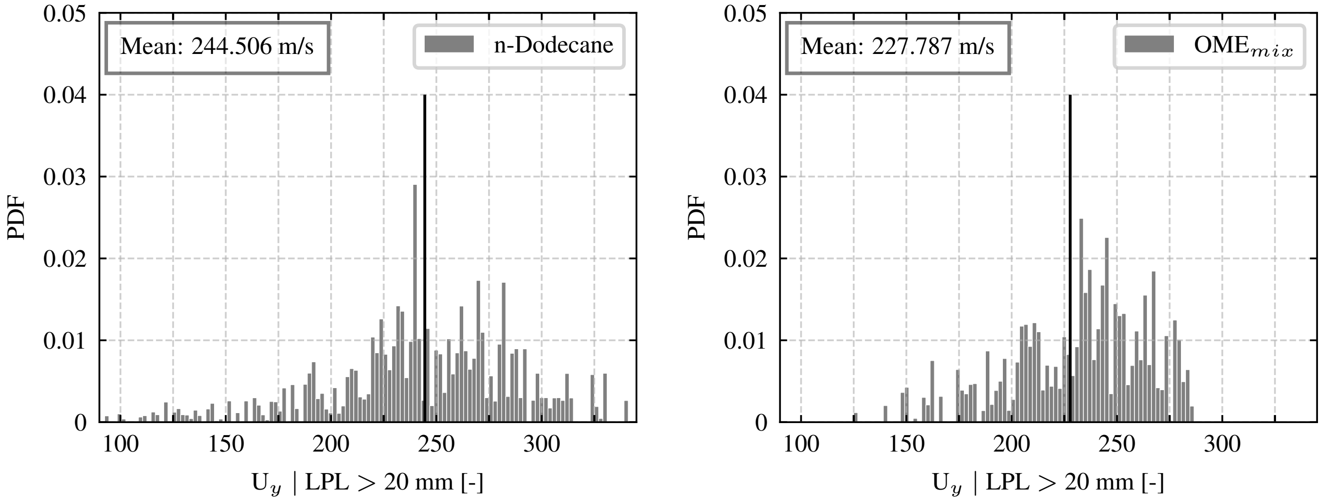

(a) n-Dodecane.

(b) OME_{mix}.

Figure 5.9: Comparison of the conditional parcel velocity in spray axis U_y (y-direction) for parcels whose liquid penetration length is larger than $20\,\mathrm{mm}$. N-Dodecane (a) and OME_{mix} (b) are compared under inert conditions for the ECN Spray D injector at tavSOI=$0.55\,\mathrm{ms}$. Also, at the tip of the liquid spray, the maximum and mean velocity (black vertical line) of n-Dodecane is significantly higher than for OME_{mix}.

In contrast to the results in Spray A3 (Sec. 5.1.2), n-Dodecane has a longer liquid penetration length in Spray D than OME_{mix}. The influence of the higher parcel velocity on the liquid penetration length is examined using the conditional parcel velocity distribution, which is presented in Figure 5.9. The parcel velocity is evaluated for all parcels that exceed the liquid penetration length of $20\,\mathrm{mm}$, representing the parcel cloud's tip. Again, n-Dodecane (a) reaches higher maximum velocities and a mean of $\langle U_y \rangle = 244.506\,\mathrm{m/s}$. OME_{mix} (b) has a mean of $\langle U_y \rangle = 227.787\,\mathrm{m/s}$ and parcel velocites do not exceed $275\,\mathrm{m/s}$. The higher velocity of n-Dodecane suggests that the momentum exchange is different, and the parcels do have more inertia left. The analysis using the parcel heat index shows higher values of n-Dodecane compared to OME_{mix}[4], indicating that in contrast to Spray A3, the longer LPL of n-Dodecane is not only an effect of thermophysical properties but also an effect of reduced momentum exchange. It can be concluded that the mixture formation process of n-Dodecane is significantly different, leading to higher parcel velocities and a higher liquid penetration length.

5.2.4 Interim conclusion for Spray D

The most important findings are summarized in bullet points:

- Good agreement with experimental data is observed in terms of liquid and vapor penetration length.
- The vapor penetration lengths are similar for both fuels. Hence, the same momentum is introduced to the spray.
- The rate of injection for OME_{mix} is significantly higher due to its higher liquid density of $\rho(T=363\,\mathrm{K})=974\,\mathrm{kg/m^3}$ (n-Dodecane: $\rho(T=363\,\mathrm{K})=698\,\mathrm{kg/m^3}$).

---

[4] Results of the PH distribution of Spray D are not shown here for brevity reasons.

- To meet the momentum balance, n-Dodecane must have higher injection velocities. This finding is also observed in the LES and aligns with experimental observations.
- The parcel cloud's tip of n-Dodecane has significantly higher velocities than $\mathrm{OME_{mix}}$.
- Consequently, n-Dodecane shows a longer liquid penetration length than $\mathrm{OME_{mix}}$. This is a significant difference from ECN Spray A3.
- The liquid penetration length is approximately doubled in Spray D compared to Spray A3.

5.3 Marine injector

The third injector investigated in this thesis is the Woodward L'Orange single-hole marine injector with a nozzle size of $d_0 = 305\,\mu\mathrm{m}$. With this injector, the influence of larger nozzle diameters on mixture formation is examined for n-Dodecane and 1-Octanol. As described in Sec. 3, the ECN baseline conditions are used for the inert spray simulation. It has to be mentioned that this study is the first of its kind to investigate n-Dodecane and 1-Octanol in an injector this size. To the author's best knowledge, injectors with nozzle sizes above $d_0 = 200\,\mu\mathrm{m}$ are not frequently studied in LES. The inert mixture formation analysis in LES of a large marine injector for n-Dodecane and 1-Octanol is a novelty presented in this work. In the following, a validation of the LES setup is performed, and differences to the other spray setups are elucidated.

5.3.1 Visual inspection of the Woodward L'Orange spray

The visual inspection of the large injector for marine applications is presented in Figure 5.11. In this configuration, in each subfigure, the experimental Schlieren and Mie images (top row) are available for comparison to the simulation (bottom row). The examined fuels are n-Dodecane (a) and 1-Octanol (b). The same time steps as for the other injectors were chosen for the comparison in Figure 5.11 to ensure comparability.

In the initial injection phase at $t = 0.1\,\mathrm{ms}$, the LES slightly overpredicts the vapor and liquid penetration length for n-Dodecane (a) and 1-Octanol (b). As observed for the heavy-duty Spray D injector in Sec. 5.2, the liquid spray cloud in Figure 5.11 is close to the vapor tip until $t = 0.2\,\mathrm{ms}$ for both fuels. This behavior seems to be typical for injectors with large nozzles and is observed in the experimental data (top row) and LES (bottom) for n-Dodecane (a) and 1-Octanol (b). It is assumed that the droplets after primary breakup are significantly larger compared to smaller injectors and exhibit more mass. More time is needed to heat up the parcels with a higher mass until they start to evaporate and the fuel vapor cloud lifts off the liquid spray. Furthermore, the spray morphology of the marine injector is more elongated compared to the automotive Spray A3. This might be attributed to the fact that the larger particle diameters exhibit reduced momentum exchange with hot ambient gases. The reduced momentum exchange of large particles can be explained by their reduced drag coefficient. In Figure 5.10, it is shown that the drag coefficient C_D decreases significantly for increasing droplet diameters. Hence, momentum exchange and, consequently also, air entrainment is reduced.

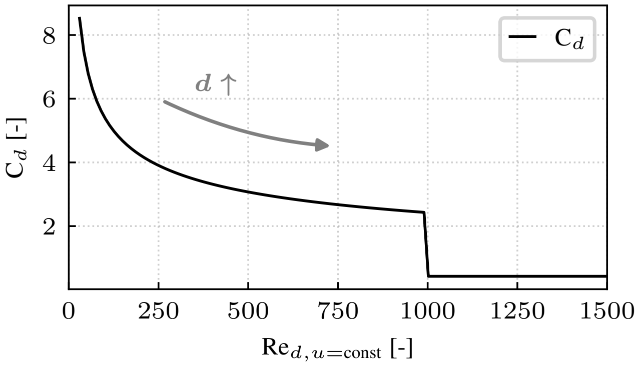

Figure 5.10: Drag law from Eq. 2.45 for a constant slip velocity and increasing droplet diameter d=0.1-$400\,\mu\mathrm{m}$. The drag is exponentially reduced for larger parcel diameters, indicating less momentum exchange with the gas phase.

The separation of the liquid and vapor cloud becomes more obvious at t=$0.3\,\mathrm{ms}$ for both fuels. In contrast to Spray A3 in Figure 5.2, where lower values at the spray tip are observed, high values of the mixture fraction $\widetilde{Z}$ are observed on the center line up to the $\widetilde{Z}= 0.001$ iso-line for the marine injector. This spray morphology has also been observed for Spray D in Figure 5.6 and is most likely attributed to the reduced momentum exchange in the initial injection phase.

At t=$0.4\,\mathrm{ms}$, it becomes more obvious, that the experimental Schlieren image at the spray tip is not visible, which can be explained by the experimental methodology of how the normalized Schlieren image is processed. The postprocessing of the Schlieren signal is explained in detail in the thesis of Rieß [191]. The author comes to the conclusion, that very high absolute intensities at the spray flanks cause the lower signal at the tip to disappear in the grayscale used in this thesis. The LES of both fuels slightly overestimates the experimental vapor penetration at t=$0.4\,\mathrm{ms}$, which is likely attributed to the rate of injection profile (see Sec. 5.3.2). The liquid penetration of the LES, which is represented by the parcel cloud (blue) in Figure 5.11 (a) and (b), however, align very well with the experimental Mie signal. Overall good agreement between the experiment and simulation is observed.

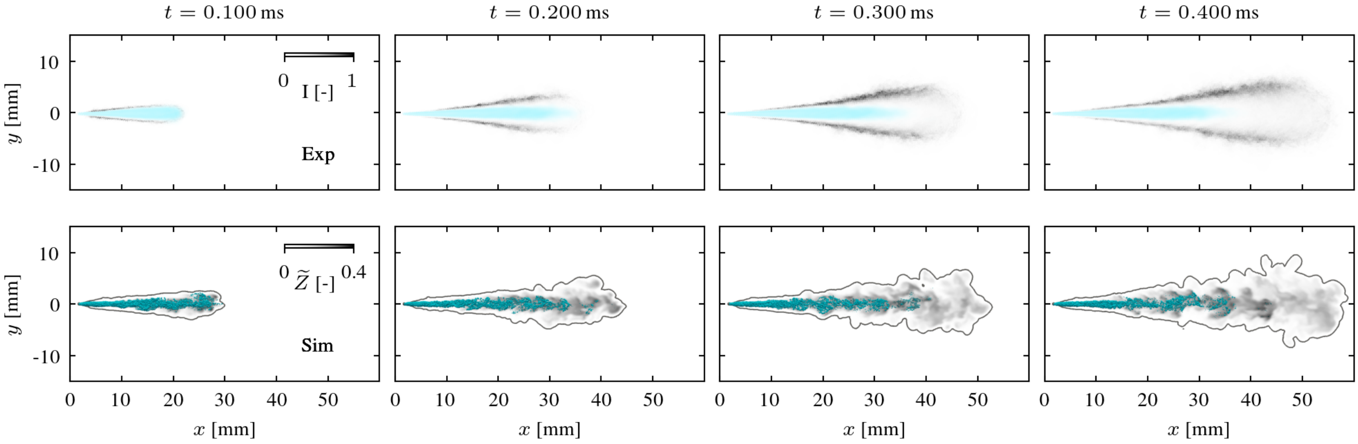

(a) n-Dodecane.

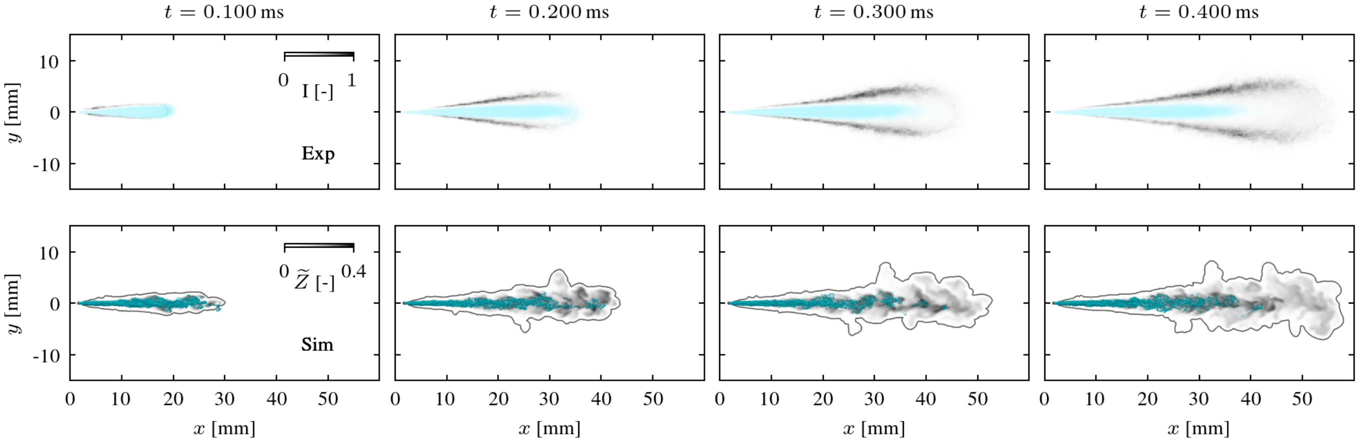

(b) 1-Octanol.

Figure 5.11: Comparison of non-reactive Large Eddy Simulation results towards experimental data for n-Dodecane (a) and 1-Octanol (b) in the marine Woodward L'Orange injector. In the top rows of each subfigure, the overlayed averaged Schlieren (grayscale) and Mie (cyan) signals are displayed (normalized signal intensity I). In the bottom row, the mixture fraction field $\widetilde{Z}$ and the parcels (cyan) are displayed. The iso-line around the spray corresponds to $\widetilde{Z}$= 0.001, which represents the spray contour as in the Schlieren image.

5.3.2 Quantitative comparison: Vapor and liquid penetration of the Woodward L'Orange injector

In the simulation of the Woodward L'Orange injector, the rate of injection profile has been measured with the pressure rise method (HDA). As explained in Sec. 5.1, this measurement technique is not suitable to use without modification in the LES. Since the tool from [200] is not designed for nozzles this size, the ROI profile has been modified based on experience from similar injectors. As shown in Figure 5.12, the experimental ROI profile is shifted for better comparison with the modified ROI profile used in the simulation. The experimental ROI profile exhibits a slow ramp-up in the ROI profile, which is not visible in Figure 5.12.

In the profile used for the LES (dashed line) in Figure 5.12 (a) and (b), the experimental profile is cut off, obtaining a more realistic increase in ROI. In the preliminary simulations, a pronounced overprediction of the vapor penetration length shortly after the visible start of injection has been observed. The overshoot soon subsided, indicating that the initial phase of the experimental ROI profile is not accurate. Hence, the original experimental ROI signal was adapted in the time range tavSOI=0-$0.25\,\mathrm{ms}$ with a weight function to maintain the shape of the ROI but reduce its value. The final ROI used in the LES improved the overprediction of the vapor penetration significantly, while still, small deviations are visible that could not be compensated for. In comparison to the automotive and heavy-duty injectors above, the Woodward L'Orange injector exhibits the highest ROI values of approximately $30\,\mathrm{mg/ms}$. This is about ten times higher than Spray A3 and three times higher than Spray D.

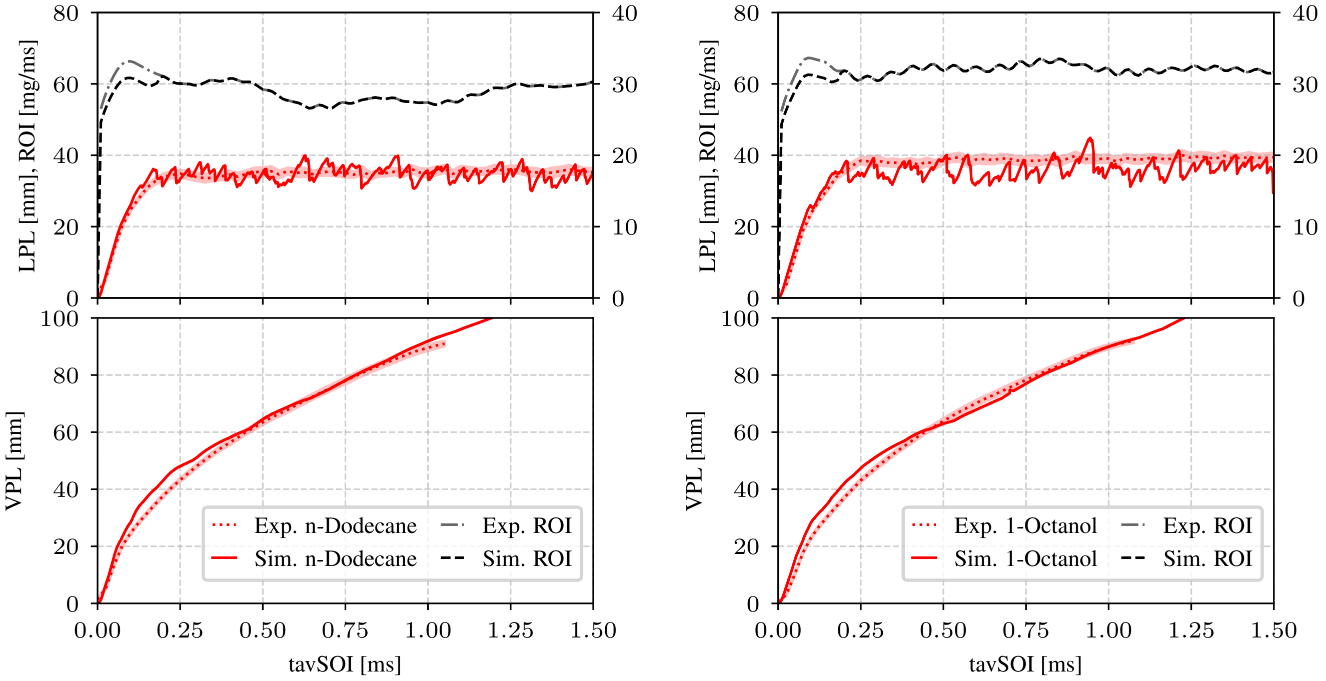

(a) n-Dodecane.

(b) 1-Octanol.

Figure 5.12: Comparison of the liquid and vapor penetration length of n-Dodecane (a) and 1-Octanol (b) under inert conditions for the Woodward L'Orange injector. Experimental liquid and vapor penetration are plotted as a dotted line, LES results are represented by solid lines. The experimentally measured rate of injection profile is displayed using dash-dotted lines, and the modeled ROI used in the LES is shown as a dashed line.

As mentioned above, the first peak of the experimental ROI induces a slight overestimation in the vapor penetration length of the LES for both fuels. Since this deviation is only present in a limited time frame, the author assumes that this slight overprediction is not affecting the mixture formation process. The liquid penetration for n-Dodecane (a) aligns perfectly with the experimental data. For 1-Octanol (b), the LES captures the liquid penetration length well. However, on average, the LES seems to underestimate the LPL for 1-Octanol slightly. As reported in Li et al. [209], the breakup and mixture formation process for large nozzles is very complex and cumbersome. Considering the increased scales, e.g., nozzle diameter and flow rates, compared to other sprays in the archival literature, the vapor and liquid penetration lengths align perfectly with experimental data.

While the vapor penetration lengths are similar for both fuels, the liquid penetration length for 1-Octanol is slightly higher compared to n-Dodecane. The difference is marginal but visible in the experiment and follows the trend observed in Spray A3. Further analysis on this behalf is not reasonable because the LES only predicts very slight differences that are too small to be assessed with the methodology developed in Sec. 5.1.3.

5.3.3 Influence of thermophysical properties on mixture formation in the Woodward L'Orange injector

The liquid penetration length of 1-Octanol in the experiment and the simulation in Figure 5.12 is slightly higher than n-Dodecane. This trend has also been observed in Spray A3. While the LES reproduces this trend, the difference in LPL is not distinct enough for conclusive results. It is assumed that a similar mode of action as observed in Spray A3 in Sec. 5.1.3 is present.

5.3.4 Interim conclusion for the Woodward L'Orange injector

The following most important findings are summarized in bullet points:

- First study of its kind to investigate a spray in such a big nozzle in LES for n-Dodecane and 1-Octanol.
- Excellent agreement of the vapor and the liquid penetration length with the experiment is obtained.
- Comparable spray shapes and structures have been identified compared to Spray D.
- The experimental rate of injection profile has successfully been modified for the LES. The modeled rate of injection profile yields significantly better alignment in the vapor penetration.
- The liquid penetration is almost four times higher than in Spray A3.
- Slightly higher liquid penetration of 1-Octanol than n-Dodecane is observed in the experiment. The LES reproduces this trend, but the differences are too small for further investigation.
- The Large Eddy Simulation framework presented in this work can successfully reproduce sprays with different scales.

5.4 Comparison of combustion relevant mixture formation metrics

After the LES framework has been successfully validated for all sprays (ECN Spray A3, ECN Spray D and Woodward L'Orange single hole) and fuels (n-Dodecane, 1-Octanol and OME_{mix}) investigated, the mixture formation process can be examined using LES results. The LES shows its full potential to provide in-depth information about the mixture formation process relevant to the ignition, complementing the experiment. Quantities that are not accessible in the experiment, such as 3D fields of mixture fraction, scalar dissipation rates and temperature, can be analyzed in the LES. A detailed analysis of the mixture formation process under inert conditions is provided in the following.

5.4.1 Analysis of the averaged mixture fraction and the averaged conditional scalar dissipation rates

In the study by Dahms et al. [210], the ignition process of spray flames has been elucidated in great detail. Dahms et al. report that the first stage ignition of the spray starts around the stoichiometric mixture fraction Z_{st} and propagates into fuel-rich regions. It can be concluded that ignition occurs when enough fuel-rich mixtures ($\widetilde{Z} > \widetilde{Z}_{\mathrm{st}}$) are available. Additionally, the scalar dissipation rate at stoichiometry (inverse residence time) is below the ignition limit ($\chi_{\mathrm{st}} < \chi_{\mathrm{st,ign}}$). Assessing this interplay of ignitable mixture fraction and residence time locally in three dimensions is cumbersome. Hence, volume-averaged values of the mixture fraction and conditional scalar dissipation rates at stoichiometry are derived from the LES and are used to compare the differences in mixture formation observed between the sprays and among the fuels. This analysis will later be utilized in the examination of reactive sprays, explaining differences in the ignition delay time.

The conditional domain average of the Favre-filtered mixture fraction is evaluated for all cells, where fuel is present ($\widetilde{Z} > 0.0001$). The conditional domain average of $\widetilde{\chi}_{\mathrm{st}}$ is evaluated for all cells that are ignitable ($\langle \widetilde{\chi}_{\mathrm{st}} | \widetilde{Z} \in [Z_{\mathrm{st}}, 0.3] \rangle$).

The analysis for the ECN Spray A3 is shown in Figure 5.13. All fuels have in common that the average of the mixture fraction and scalar dissipation rate at stoichiometry show a steep increase and then a falloff behavior[5]. The peak values of $\langle \widetilde{Z} \rangle \approx 0.11$ are reached at approximately tavSOI=$0.1\,\mathrm{ms}$ for all fuels (Figure 5.13). The mixing process is similar for all fuels. The average mixture fraction approaches $\langle \widetilde{Z} \rangle \approx 0.04$ asymptotically at tavSOI=$1.0\,\mathrm{ms}$.

While the $\widetilde{\chi}_{\mathrm{st}}$ profiles for n-Dodecane (a) and 1-Octanol (b) are similar in Figure 5.13, reaching a peak value of $\widetilde{\chi}_{\mathrm{st}} \approx 100\,1/\mathrm{s}$ and then fall off to almost zero, OME$_{\mathrm{mix}}$ (c) has a peak value of $\widetilde{\chi}_{\mathrm{st}} \approx 250\,1/\mathrm{s}$ and then approaches $\widetilde{\chi}_{\mathrm{st}} \approx 75\,1/\mathrm{s}$ asymptotically. OME$_{\mathrm{mix}}$ in Spray A3 has the highest peak value of $\widetilde{\chi}_{\mathrm{st}}$ for all fuels and injectors investigated. Also in Spray D with OME$_{\mathrm{mix}}$ (Figure 5.14 (b)), lower peak values of $\widetilde{\chi}_{\mathrm{st}}$ are found. An explanation of this observation can be found in the simulation results in Figure 5.2 (c). In the Favre-filtered mixture fraction field in Figure 5.2 (c), locally, significantly higher values of $\widetilde{Z}$ are found for OME$_{\mathrm{mix}}$ than for n-Dodecane (a) and 1-Octanol (b) on the spray center axis. Consecutively, higher gradients of $\widetilde{Z}$ and $\widetilde{\chi}_{\mathrm{st}}$ are expected (see Eq. 2.97).

---

[5] The write out frequency of the cases in Figure 5.13, Figure 5.14 and Figure 5.15 unfortunately differ. For some cases the time span from tavSOI=0-$0.05\,\mathrm{ms}$ has not been written out. Due to limited computational and storage resources, the cases could not be repeated with higher write-out frequency. Despite this, the profile after tavSOI=$0.05\,\mathrm{ms}$ is considered to be important for ignition [210].

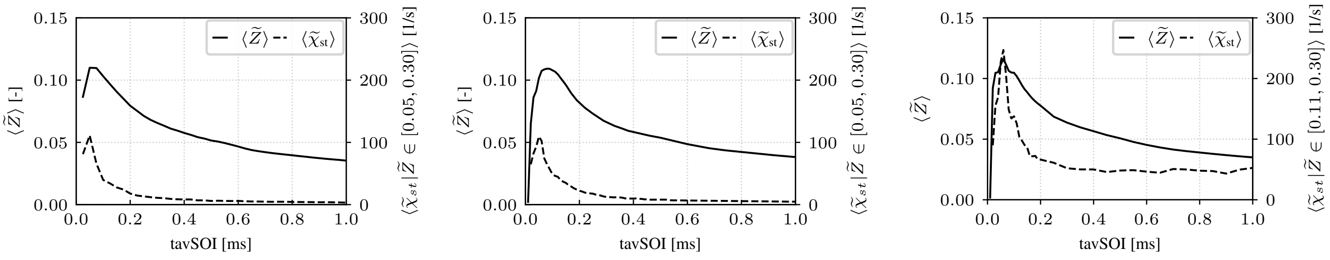

(a) n-Dodecane.

(b) 1-Octanol.

(c) OME$_{\mathrm{mix}}$.

Figure 5.13: Comparison of the conditional mean of the mixture fraction field $\langle \widetilde{Z} \rangle$ ($\widetilde{Z} > 0.0001$) and the scalar dissipation rate $\langle \widetilde{\chi}_{\mathrm{st}} | \widetilde{Z} \in [Z_{\mathrm{st}}, 0.3] \rangle$ in the ECN Spray A3 for n-Dodecane (a), 1-Octanol (b) and OME$_{\mathrm{mix}}$ (c). The volume-averaged mixture fraction is represented by a solid line, and the conditional scalar dissipation rate at stoichiometry is shown as a dashed line.

Only slightly higher peak values of the averaged mixture fraction are observed for n-Dodecane (a) and OME$_{\mathrm{mix}}$ (b) in Figure 5.14 for Spray D. OME$_{\mathrm{mix}}$'s peak value is higher than n-Dodecane at $\langle \widetilde{Z} \rangle \approx 0.125$. Compared to Spray A3, the peaks of the mixture fraction and scalar dissipation rate are shifted towards approximately tavSOI$=0.2\,\mathrm{ms}$. The peak shift indicates that the evaporation process is slower than for the smaller nozzle in Spray A3. This finding can also be observed in Figure 5.6, where the parcel cloud and the vapor cloud at tavSOI$=0.1\,\mathrm{ms}$ are head to head. The peak of the $\widetilde{\chi}_{\mathrm{st}}$ profile is also shifted later in time. Further, OME$_{\mathrm{mix}}$ has double the peak value than n-Dodecane of $\widetilde{\chi}_{\mathrm{st}} \approx 100\,1/\mathrm{s}$ and asymptotically reaches values of $\widetilde{\chi}_{\mathrm{st}} \approx 25\,1/\mathrm{s}$, while n-Dodecane falls off to zero. In contrast to Spray A3, n-Dodecane has a significantly lower peak of $\widetilde{\chi}_{\mathrm{st}} \approx 50\,1/\mathrm{s}$.

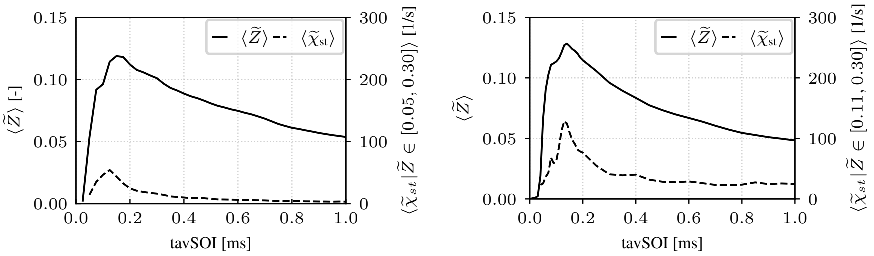

(a) n-Dodecane.

(b) OME$_{\mathrm{mix}}$.

Figure 5.14: Comparison of the conditional mean of the mixture fraction field $\langle \widetilde{Z} \rangle$ ($\widetilde{Z} > 0.0001$) and the scalar dissipation rate $\langle \widetilde{\chi}_{\mathrm{st}} | \widetilde{Z} \in [Z_{\mathrm{st}}, 0.3] \rangle$ in the ECN Spray D for n-Dodecane (a) and OME$_{\mathrm{mix}}$ (b). The volume-averaged mixture fraction is represented by a solid line, and the conditional scalar dissipation rate at stoichiometry is shown as a dashed line.

The profiles for the Woodward L'Orange injector in Figure 5.14 of n-Dodecane (a) and 1-Octanol (b) follow the shift in time observed for Spray D. As explained in Sec. 5.3, the reduced drag and momentum exchange delays evaporation due to less air entrainment. Further, larger particle diameters need more time to heat up until evaporation occurs.

As observed in Spray A3, n-Dodecane and 1-Octanol have very similar mixing characteristics. The peak values of the scalar dissipation rate at stoichiometry are reduced $\widetilde{\chi}_{\mathrm{st}} \approx 50\,1/\mathrm{s}$ compared to Spray A3, and are similar to Spray D in Figure 5.14. The lower values of the scalar dissipation rate than in Spray A3 are explained by the prolonged mixing time (shift of peak values), leading to lower gradients of the mixture fraction (see Eq. 2.96). The longer mixing times for large nozzles (Spray D and Woodward L'Orange) injectors are a significant difference compared to Spray A3.

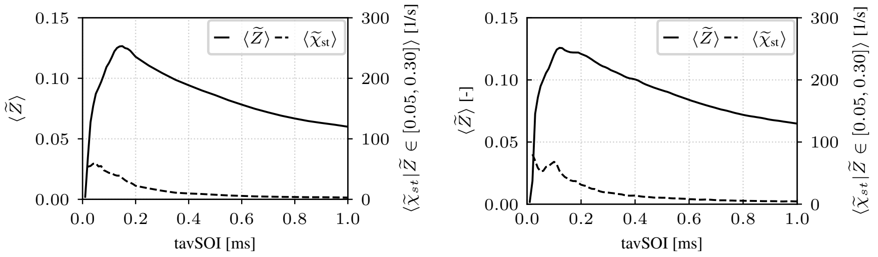

(a) n-Dodecane.

(b) 1-Octanol.

Figure 5.15: Comparison of the conditional mean of the mixture fraction field $\langle\widetilde{Z}\rangle$ ($\widetilde{Z} > 0.0001$) and the scalar dissipation rate $\langle\widetilde{\chi}_{\mathrm{st}}|\widetilde{Z} \in [Z_{\mathrm{st}}, 0.3]\rangle$ in the Woodward L'Orange injector for n-Dodecane (a) and 1-Octanol (b). The volume-averaged mixture fraction is represented by a solid line, and the conditional scalar dissipation rate at stoichiometry is shown as a dashed line.

The following bullet points summarize the main findings of the analysis of the domain averaged mixture fraction and scalar dissipation rate at stoichiometry:

Spray A3 :

- Peak values of the domain averaged mixture fraction and scalar dissipation rate at stoichiometry are found at approximately tavSOI=$0.1\,\mathrm{ms}$, suggesting the faster onset of evaporation.
- Highest peak values of the scalar dissipation rate at stoichiometry are observed among all injectors.

Spray D :

- Same trends for $\mathrm{OME_{mix}}$ are observed as in Spray A3: higher peak values of the mixture fraction and the scalar dissipation rate compared to n-Dodecane.
- Similar minimum and maximum values of the averaged mixture fraction are found as in Spray A3.
- The peaks of the distributions are shifted towards approximately tavSOI=$0.2\,\mathrm{ms}$.
- Significantly lower peak values of the scalar dissipation rate are observed that are explained by longer mixing times.

Woodward L'Orange single hole :

- N-Dodecane and 1-Octanol show the same mixing characteristics and peak values.
- The peaks of the distributions are shifted towards tavSOI=$0.2\,\mathrm{ms}$ as observed in Spray D.
- As observed in Spray D, lower averaged scalar dissipation rates have been shown.

Conclusions :

- In the domain averaged mixture fraction and scalar dissipation rate at stoichiometry profiles, all fuels show distinct mixing characteristics among all injectors.

- The heavy-duty and marine injectors show longer mixing times and reduced scalar dissipation rates.
- The volume averaged mixture fraction values increase only slightly for larger nozzle sizes.
- For the larger nozzle sizes (Spray D and Woodward L'Orange), the onset of evaporation is delayed compared to Spray A3, suggesting that ignitible mixtures occur later than in Spray A3.

5.4.2 Temperature distribution in the spray relevant for ignition

As described in Sec. 5.4.1, the spray's ignition strongly depends on the ignitable mixture fraction and the strain rate. The mixture's temperature is another crucial parameter for ignition and strongly influences the ignition delay time. Due to the significant differences observed in the thermophysical properties in Figure 2.4, e.g., in the vapor pressure and latent heat of evaporation, the question arises of how the changed properties affect ignition in the spray. Since it is challenging for experimental techniques to determine the spray temperature, the Large Eddy Simulation is crucial to examine the temperature distribution in the spray. In the following, the gas temperature distribution for each spray and fuel in mixture fraction space is examined. The scatters in Figure 5.16, Figure 5.18 and Figure 5.19 are colored with their respective value of the scalar dissipation rate at stoichiometry, giving further information on the strain the corresponding fluid element is encountering. The marginal PDFs of the mixture fraction and the temperature are shown at the edges. The adiabatic mixing line, which is assumed in the flamelet model (see Sec. 6), is represented by the red solid line.

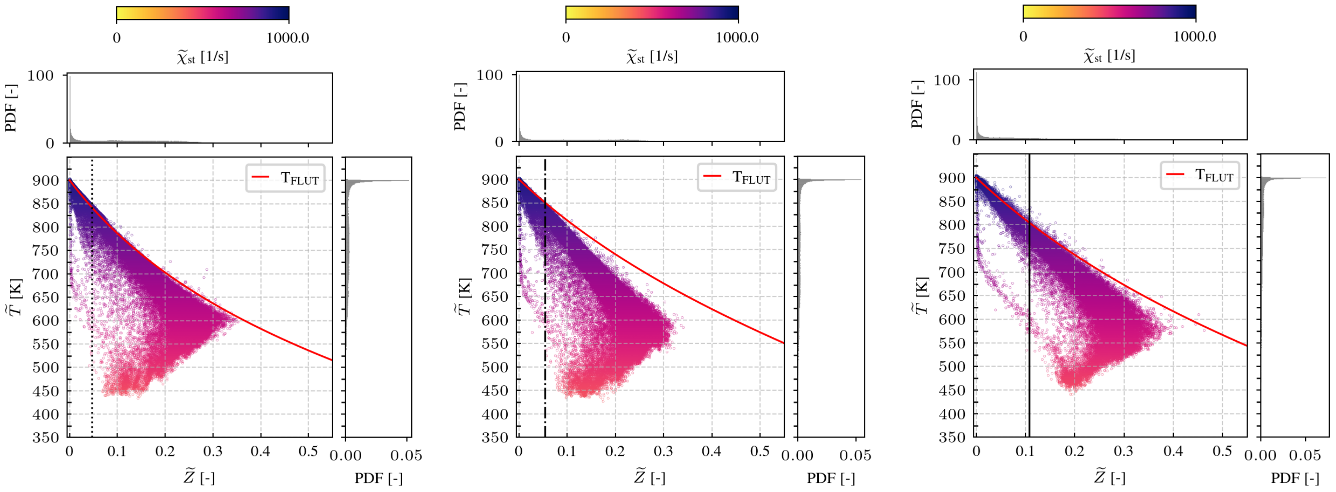

(a) n-Dodecane.

(b) 1-Octanol.

(c) OME$_{\text{mix}}$.

Figure 5.16: Comparison of the gas temperature distribution over the according mixture fraction at tavSOI= $0.1\,\mathrm{ms}$ for n-Dodecane (a), 1-Octanol (b) and OME$_{\text{mix}}$ (c) in the ECN Spray A3 injector. The scatters are colored with their respective value of the scalar dissipation rate at stoichiometry, indicating whether the mixture is ignitible. The red line represents the adiabatic mixing line that is used as the initial profile in the flamelet simulations. The vertical lines represent the value of the stoichiometric mixture fraction $\widetilde{Z}_{\text{st}}$ of each fuel. The marginal PDF of the mixture fraction (top) and the temperature (right) are mass-weighted.

All fuels in Figure 5.16 for the ECN Spray A3 injector show undercooling introduced due to latent heat of evaporation of the liquid phase. The evaporation process cools the gas phase down to $\widetilde{T}=450\,\mathrm{K}$, which is also reported in other studies in LES [90, 101, 112]. Considering the marginal PDFs of mixture fraction and temperature, it is visible that the probability of low temperatures of $\widetilde{T}=450\,\mathrm{K}$ is small.

The maximum value of the mixture fraction for n-Dodecane (a) is $\widetilde{Z}\approx 0.35$, 1-Octanol (b) has a slightly lower maximum value of $\widetilde{Z}\approx 0.30$ and $\mathrm{OME_{mix}}$ (c) reaches values up to $\widetilde{Z}\approx 0.4$. The high values for $\mathrm{OME_{mix}}$ have also been observed in Figure 5.2. All fuels have in common that leaner mixtures show higher values of the scalar dissipation rate at stoichiometry, which would inhibit ignition.

A significant difference between the fuels is the temperature difference between the adiabatic mixing line, which is prescribed as an initial condition in the combustion model, and the temperature distribution in the spray. For n-Dodecane (a), the adiabatic mixing line aligns with the highest values of the temperature distribution of the spray simulation. 1-Octanol (b) and $\mathrm{OME_{mix}}$ (c) exhibit a significant gap between the adiabatic mixing line and the temperature distribution from the spray. The highest deviation from the adiabatic mixing line is observed for 1-Otanol (b) at $\widetilde{Z}\approx 0.30$ with an indicated difference of $\Delta\widetilde{T}=75\,\mathrm{K}$. For $\mathrm{OME_{mix}}$ (c), the highest deviation to the adiabatic mixing line shifts to $\widetilde{Z}\approx 0.40$, the undercooling for $\mathrm{OME_{mix}}$ is approximately $\Delta\widetilde{T}=50\,\mathrm{K}$. The undercooling effect of the spray in comparison to the adiabatic mixing line used in the combustion model scales with the latent heat of evaporation (see Figure 2.4). 1-Octanol shows the highest undercooling effect and also exhibits the highest latent heat of evaporation h_{vap} of all fuels. Overall, the temperature distributions of 1-Octanol and $\mathrm{OME_{mix}}$ are shifted towards lower temperatures than n-Dodecane in Spray A3. Revisiting the results of the parcel heat transfer number of Sec. 5.1.3, the temperature distribution analysis confirms the assumption that the gas phase provides less heat for evaporation for 1-Octanol and $\mathrm{OME_{mix}}$ than n-Dodecane.

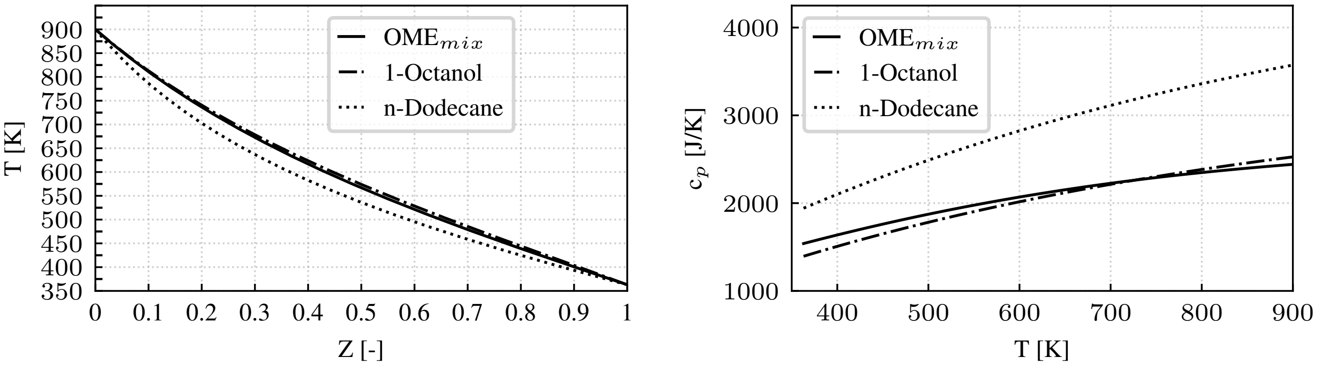

(a) Adiabatic mixing line for all fuels over Z.

(b) Heat capacities over the temperature.

Figure 5.17: The influence of gas properties on the modeling of spray undercooling is examined by comparing the adiabatic mixing lines for all fuels in (a) and their heat capacities in (b). N-Dodecane has the highest heat capacity of all fuels, and hence the adiabatic mixing line exhibits a more concave shape.

Furthermore, comparing the adiabatic mixing lines of all fuels shown in Figure 5.17 (a) reveals, that n-Dodecane shows a more concave shape than the other fuels. This means that in the ignition-relevant regions, the spray undercooling effect is less significant for n-Dodecane than for the other fuels. The more concave shape of the adiabatic mixing line for n-Dodecane is explained by a significantly higher heat capacity than for 1-Octanol and $\mathrm{OME_{mix}}$, which leads to lower temperatures of the mixture of oxidizer and fuel for n-Dodecane. In Figure 5.17 (b), the heat capacity at constant pressure clearly shows the higher values of n-Dodecane. This finding is a novelty discovered in this thesis. It explains differences of sensitivities on ignition delay in the spray in Sec. 7 and will be used in Sec. 6.4 for optimization of the flamelet model.

For Spray D in Figure 5.18, the temperature distributions for n-Dodecane (a) and OME$_{\text{mix}}$ (b) show a similar distribution as observed in Spray A3. Again, the adiabatic mixing line of n-Dodecane (a) is closest to the temperature distribution, but in Spray D, a gap between the adiabatic mixing line and the temperature distribution at $\widetilde{Z}=0.25$ is exhibited. While the maximum values of $\widetilde{Z}$ shifted to lower values compared to Spray A3, $\widetilde{Z}=0.275$ for n-Dodecane and to $\widetilde{Z}=0.3$ for OME$_{\text{mix}}$, the marginal PDFs of the mixture fraction shifted towards higher values of the mixture fraction. The marginal PDF of the temperature is shifted towards lower temperatures for both fuels. This is a significant difference between the Spray A3 and Spray D. For OME$_{\text{mix}}$, the maximum distance to the adiabatic mixing line increased to approximately $\Delta\widetilde{T}=75\,\text{K}$ at $\widetilde{Z}\approx0.30$. At the same $\widetilde{Z}$ position in Spray A3, the temperature difference was only $\Delta\widetilde{T}=25\,\text{K}$. This means that fluid elements exhibit substantially lower temperatures in Spray D compared to Spray A3.

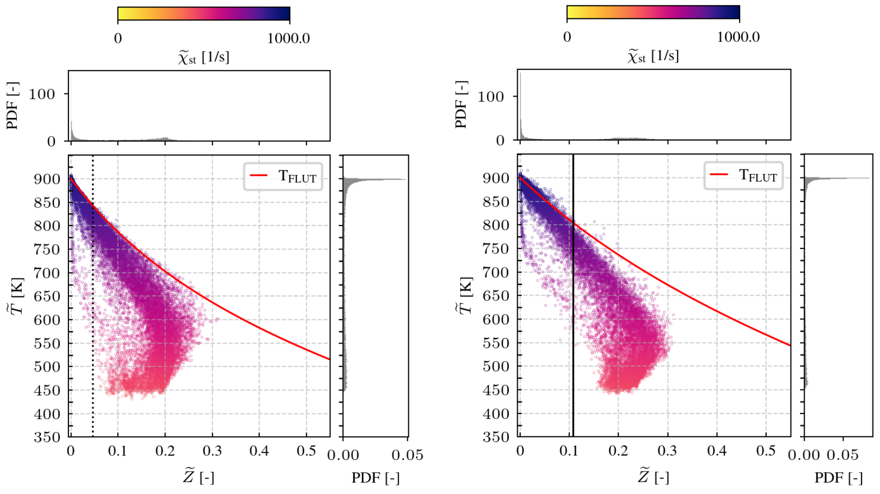

(a) n-Dodecane.

(b) OME$_{\text{mix}}$.

Figure 5.18: Comparison of the gas temperature distribution over the according mixture fraction at tavSOI= $0.1\,\text{ms}$ for n-Dodecane (a) and OME$_{\text{mix}}$ (b) in the ECN Spray D injector. The scatters are colored with their respective value of the scalar dissipation rate at stoichiometry, indicating whether the mixture is ignitible. The red line represents the adiabatic mixing line that is used as the initial profile in the flamelet simulations. The vertical lines represent the value of the stoichiometric mixture fraction $\widetilde{Z}_{\text{st}}$. The PDF of the mixture fraction (top) and the temperature (right) are mass-weighted.

In the Woodward L'Orange injector in Figure 5.19, the minimum temperatures of $\widetilde{T}\approx450\,\text{K}$ remain. But the distribution of the marginal temperature PDF shifts significantly towards lower temperatures for both fuels. The shift is more pronounced than in Spray D. Also the maximal mixture fraction for n-Dodecane (a) and 1-Octanol (b) shifts towards fuel-richer mixtures ($\widetilde{Z}\approx0.4$), similar to Spray A3 in Figure 5.16. As observed in Spray A3, the distribution for n-Dodecane fits very well to the spray temperature distribution, while 1-Octanol exhibits a significant temperature difference to the adiabatic mixing line. However, the shape of the distribution for both fuels is similar. The similarity in mixture formation for n-Dodecane and 1-Octanol has also been observed in Figure 5.2 and Figure 5.11. The marginal temperature distribution reveals, that the gas temperatures of 1-Octanol are lower compared to n-Dodecane. The lower temperature distribution of 1-Octanol also confirms the slightly higher liquid penetration length exhibited in 5.12 (b).

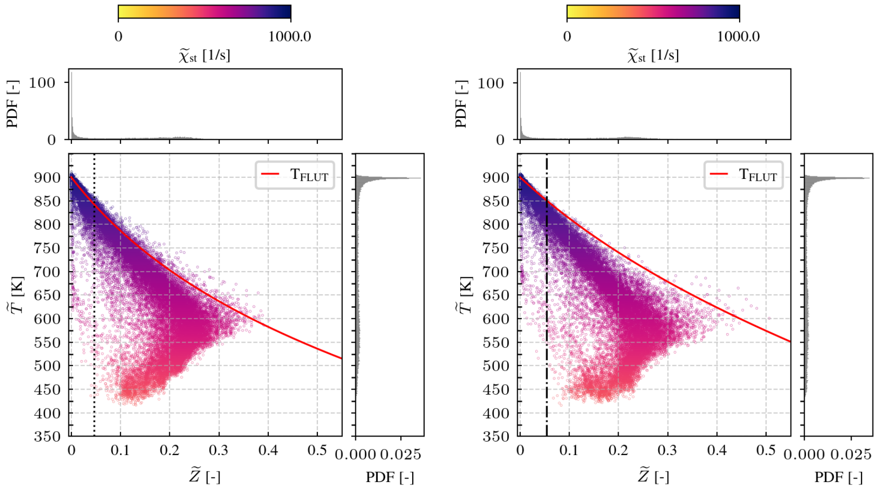

(a) n-Dodecane.

(b) 1-Octanol.

Figure 5.19: Comparison of the gas temperature distribution over the according mixture fraction at tavSOI= $0.1\,\mathrm{ms}$ for n-Dodecane (a) and 1-Octanol (b) in the Woodward L'Orange single hole injector. The scatters are colored with their respective value of the scalar dissipation rate at stoichiometry, indicating whether the mixture is ignitible. The red line represents the adiabatic mixing line that is used as the initial profile in the flamelet simulations. The vertical lines represent the value of the stoichiometric mixture fraction $\widetilde{Z}_{\mathrm{st}}$. The PDF of the mixture fraction (top) and the temperature (right) are mass-weighted.

The following bullet points summarize the most significant findings:

- 1-Octanol and $\mathrm{OME}_{\mathrm{mix}}$ exhibit a lower temperature distribution than n-Dodecane in all injector sizes investigated. The spray cooling effect scales with the latent heat of evaporation.
- The temperature distribution of n-Dodecane is closest to the adiabatic mixing line in all spray configurations. An explanation is found in the lower latent heat of evaporation. Furthermore, for the first time, it is shown that the higher heat capacity at constant pressure of n-Dodecane compared to other fuels leads to a more concave adiabatic mixing line that fits the shape of the temperature distribution of the spray.
- 1-Octanol and $\mathrm{OME}_{\mathrm{mix}}$ exhibit a higher sensitivity for heat loss due to evaporation than n-Dodecane.
- The outcome of the parcel heat transfer number analysis in Sec. 5.1.3 for Spray A3, that longer liquid penetration lengths of 1-Octanol and $\mathrm{OME}_{\mathrm{mix}}$ are attributed to lower temperature in the gas phase, are confirmed.
- Increasing nozzle sizes lead to similar temperature distributions, but the marginal PDFs are shifted towards lower temperatures and higher values of the mixture fraction.

5.5 Conclusion on the mixture formation analysis

First, the used Large Eddy Simulation framework has been validated under inert conditions. The results of the LES and the experiment for the inert sprays are in perfect alignment. For the first time, 1-Octanol has been successfully investigated in a high-fidelity LES framework. The LES as a diagnostic tool is utilized to complement experimental findings. Complex mixture formation processes which cannot be explained with experimental measurements have been investigated in-depth. The mixture formation analysis for increasing nozzle sizes with n-Dodecane, 1-Octanol, and $\mathrm{OME_{mix}}$ revealed significant differences due to distinct thermophysical properties. In Spray A3, higher liquid penetration lengths have been observed in the experiment and the simulation for 1-Octanol and $\mathrm{OME_{mix}}$, compared to n-Dodecane. The newly derived non-dimensional parcel heat transfer number PH suggested that even though 1-Octanol and $\mathrm{OME_{mix}}$ are more volatile, the gas phase cannot deliver enough heat for evaporation. This finding is supported by the analysis of the temperature distribution in Sec. 5.4.2.

A comprehensive investigation of the domain averaged mixture fraction and scalar dissipation rate at stoichiometry showed distinct mixing characteristics for the different fuels and injectors. While n-Dodecane and 1-Octanol show similar profiles and maximum values of the scalar dissipation rate, $\mathrm{OME_{mix}}$ exhibits higher peak values and falls off faster. With increasing nozzle size, the maximum values of the conditional domain averaged scalar dissipation rate at stoichiometry at fuel-rich mixtures decrease for all fuels. The heavy-duty and marine injectors showed a shift of the peak of the domain averaged mixture fraction to later times, suggesting slower evaporation rates in the initial phase. Compared to smaller particles, e.g., in Spray A3, reduced momentum exchange or air entrainment is observed in the initial phase of injection due to lower drag coefficients of larger parcels (see Figure 5.10). Consecutively, less heat is transferred to the liquid phase, limiting evaporation. Hence, also mixing is shifted back in time.

Finally, the gas phase temperature distribution in mixture fraction space showed that the thermophysical properties of the fuels have a significant impact on mixture formation. The gas phase temperature scales with the latent heat of evaporation of the fuel. The temperature distribution of 1-Octanol exhibited the largest difference to the adiabatic mixing line. The fuel with the highest vapor pressure ($\mathrm{OME_{mix}}$) showed the highest value of the mixture fraction. With increasing nozzle size (injected mass), the marginal probability density function for the mixture fraction shifts towards higher values, while the marginal temperature PDF shifts towards lower temperatures. For the first time, the influence of a higher heat capacity of n-Dodcane on the adiabatic mixing line has been shown. The higher gas heat capacity at constant pressure of n-Dodcane implies a more concave shape of the adiabatic mixing line. The steeper curve at lower mixture fractions fits better with the temperature distribution of the spray.

6 Spray Flame Structure Analysis

This chapter aims to elucidate the combustion behavior of n-Dodecane, 1-Octanol and $\mathrm{OME}_{\mathrm{mix}}$. The analysis is structured by models of increasing complexity. First, chemical kinetic mechanisms are identified (Sec. 6.1), and the chemical ignition delay times are investigated in the 0-D homogenous reactor model (Sec. 6.2). All fuels show significant differences in their reaction kinetics and chemical ignition delay times. Furthermore, the influence of strain on 1-D flame structures is investigated in the laminar non-premixed flamelet model in Sec. 6.3. This detailed analysis is vital for flame characterization of novel Diesel fuels. Next, the results from the mixture formation analysis are transferred to derive a realistic spray heat-loss corrected temperature profile for the flamelet simulations in Sec. 6.4. The methodology of deriving the initial temperature profile from inert spray simulations is introduced, and effects on the spray flame and ignition are elucidated. Finally, the methodology of assembling the flamelet manifold into a table for look-up is briefly described in Sec. 6.5 and the results from the flame structure analysis are concluded in Sec. 6.6.

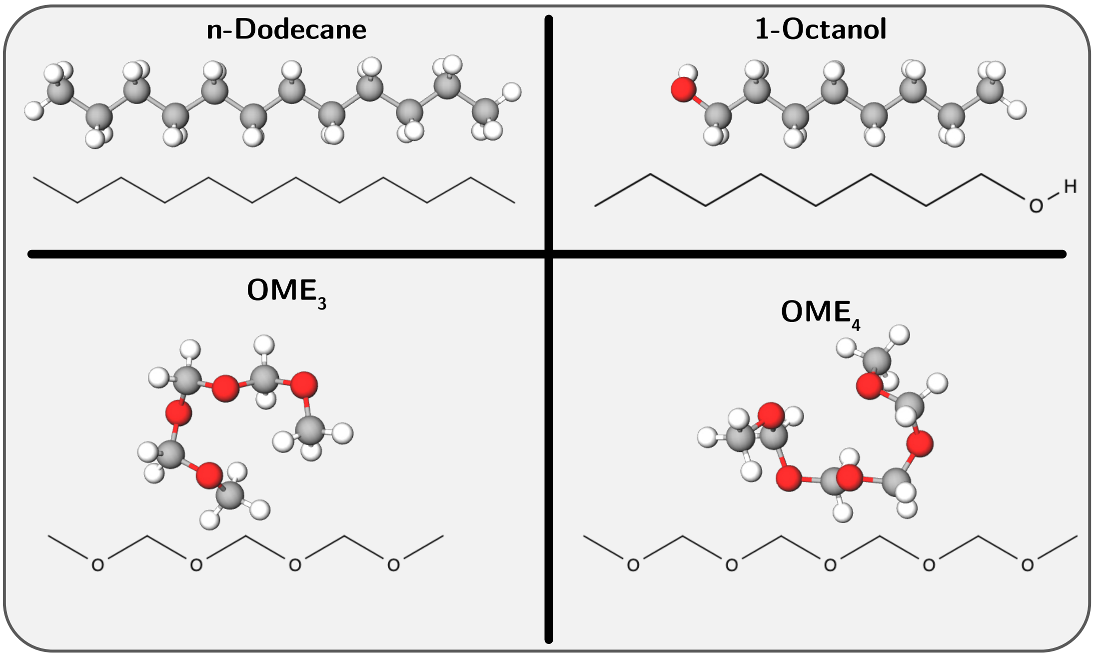

Figure 6.1: Molecular structure of n-Dodecane, 1-Octanol and the main components of $\mathrm{OME}_{\mathrm{mix}}$: OME_3 and OME_4. The overview shows the distinct differences between the fuels. N-Dodecane and 1-Octanol show a linear structure, and the OME-type fuels are non-linear. The lack of carbon-carbon bonds is visible for OME_3 and OME_4. Molecule images are produced using Molview [211].

6.1 Kinetic reaction mechanism selection

As a first step, suitable kinetic reaction mechanisms that reproduce the combustion properties under homogenous and strained conditions must be identified.

For n-Dodecane as a standard surrogate fuel for Diesel (EN 590), many reaction mechanisms are available, which span all levels of detail (skeletal, lumped, reduced and detailed). In the spray combustion community, the reduced mechanisms of Yao, Standford University and POLIMI (CRECK modeling group) are commonly used [212–214]. In this thesis, a detailed POLIMI mechanism is used. The modular concept of POLIMI allows for generating highly flexible reaction kinetics. The detailed mechanism from POLIMI provided by personal communication (Alessandro Stagni) [215] includes kinetic pathways for NO and PAH formation and has been successfully used in [3, 93, 94].

Since 1-Octanol has only recently raised interest in the combustion community, fewer mechanisms are available. The author has found two detailed mechanisms by Cai et al. [25] and Pelucchi et al. [26, 216] (POLMI). Both mechanisms are very detailed, meaning they have a high number of species and reactions included. Both mechanisms have been tested in reactive spray LES. The mechanism of Cai significantly overestimated the spray ignition delay time, while the mechanism of Pelucchi slightly underestimated the ignition delay time (IDT). As described later in Sec. 6.4, an underestimation of the UFPV approach for a fuel with increased vapor pressure and latent heat of evaporation is more reasonable. Hence, this study uses the mechanism of Pelucchi et al. [216].

The multicomponent fuel $\mathrm{OME_{mix}}$ is mainly composed of $\mathrm{OME_3}$ and $\mathrm{OME_4}$. The group of Polyoxymethylenethers is also relatively new in the context of combustion. The first mechanism available by Sun et al. [77] only considered $\mathrm{OME_3}$ and hence was not suitable for $\mathrm{OME_{mix}}$. Besides that, only laminar flame speed measurements were used to optimize the mechanism. In the context of self-igniting Diesel spray combustion, chemical ignition delay times are more relevant as input for mechanism optimization. Based on Sun et al. [77], He et al. [78] improved the kinetics using additional experimental chemical ignition delay times measured in the Rapid Compression Machine and reduced the number of species. The mechanism by Cai et al. [24] was the first mechanism that also contained $\mathrm{OME_4}$. In comparison to Sun et al. [77] and He et al. [78], the chemical ignition delay times for the Cai mechanism are slightly shorter and match very well with the experimental data (shock tube). Recently also, the mechanism by Niu et al. [79] extended the mechanism by Cai with $\mathrm{OME_5}$ and $\mathrm{OME_6}$. Since no experimental data for the chemical ignition delay time of neat $\mathrm{OME_5}$ and $\mathrm{OME_6}$ are present, reaction rates are extrapolated using data of lower chain lengthed OMEs. In Wiesmann et al. [113], the mechanism of Niu underestimated the spray ignition delay time of $\mathrm{OME_{mix}}$ compared to the Cai mechanism. This behavior is also observed in homogenous reactor simulations (not shown here for brevity reasons). Another mechanism of POLIMI, which is not published yet and retrieved by personal communication (Alessandro Stagni) [215], slightly overestimates the chemical ignition delay times compared to Cai et al. [24]. The POLIMI mechanism is also based on the Cai mechanism. Further, the Niu and the POLIMI mechanism are reduced mechanisms. The extension of Niu of $\mathrm{OME_5}$ and $\mathrm{OME_6}$ is only modeled; hence, no validation is possible. Hence, in this study, the detailed mechanism of Cai is used.

An overview of the used mechanisms utilized in this thesis is provided in Table 6.1. It has to be noted that the level of detail of the used mechanisms in this thesis (number of species and reactions) is notable, even for a tabulated chemistry approach.

Table 6.1: Overview of the used mechanisms for flamelet simulations and chemical ignition delay times. Further, the discretization of the flamelet lookup tables is shown.

Fuel	Mechanism	Number of species	Number of reactions	Resolution $\widetilde{Z}$	Resolution $\widetilde{C}$	Resolution $\widetilde{\chi}_{\mathrm{st}}$	Resolution $\widetilde{Z''^2}^N$	Z_{st}	$\chi_{\mathrm{st,ign}}$
$\mathrm{OME}_{\mathrm{mix}}$	[24]	322	1611	101	151	16	7	0.1083	370 $\frac{1}{s}$
1-Octanol	[26, 216]	524	18940	101	151	24	7	0.0538	84 $\frac{1}{s}$
n-Dodecane	[214, 217]	405	10481	101	151	32	7	0.0460	55.3 $\frac{1}{s}$

6.2 Ignition under homogeneous conditions

The Homogenous Reactor Model (HRM) is considered one of the most fundamental combustion models (see Sec. 2.3.2). The HRM includes only the reaction kinetics and no transport effects. Fuels for compression ignition combustion engines are commonly characterized by their ignition delay curves, which can be determined from a manifold of homogenous reactor simulations with different initial temperatures and equivalence ratios. The first stage and main ignition delay times are derived from the Heat Release Rate (HRR) profiles of the simulations.

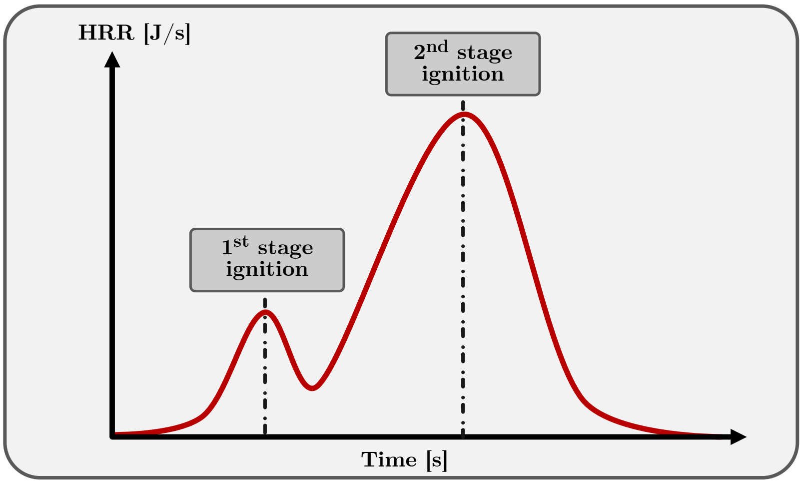

Figure 6.2: Schematic of a representative Heat Release Rate profile. The definition of the first and second stage ignition is visualized.

As shown in Figure 6.2, the first-stage ignition is defined as the first significant peak in the HRR profile. The main ignition is defined as the second peak with the global maximum. The main ignition ($\tau_{ign,2}$) is regarded as the chemical ignition delay time. The chemical ignition delay times are then plotted over their respective initial temperature, which denotes the ignition delay curve (see Figure 6.3).

In Figure 6.3, the ignition delay curves are displayed for different equivalence ratios. The equivalence ratios are chosen according to relevant mixture fractions present in the sprays investigated in this thesis: $\widetilde{Z} \in$ [0.025-0.4], which corresponds to $\Phi \in$ [0.5-4] or $\lambda \in$ [0.25-2].

It is common to define the abscissa of ignition delay curves as the inverse temperature: $1000/T$. Since the chemical ignition delay time has a multiscale character, it is convenient to use a logarithmic scale. The gray box in Figure 6.3 represents the temperature range $T \in [730\mathrm{K} - 900\mathrm{K}]$ where auto-ignition typically occurs in spray combustion.

From Figure 6.3, it is evident that $\mathrm{OME_{mix}}$ has the shortest chemical ignition delay time over the whole range of initial temperatures and equivalence ratios investigated. In the relevant temperature range for ignition (gray box), the ignition delay time is approximately three times lower than for the other fuels. In the high-temperature ignition region, $\mathrm{OME_{mix}}$ ignites about six times faster. Compared to n-Dodecane and 1-Octanol, $\mathrm{OME_{mix}}$ does not show a pronounced two-stage ignition behavior typical for Diesel fuels, while n-Dodecane and 1-Octanol do show a Negative Temperature Coefficient (NTC) regime at $T \in [833\,\mathrm{K}$ - $1000\,\mathrm{K}]$. This regime is typical for fuels with a two-stage ignition behavior. In the NTC regime, stable intermediate species form, which is an endothermic process that withdraws enthalpy from combustion. The formation of intermediate species increases the main ignition delay time.

There is no clear opinion in the literature if $\mathrm{OME_{mix}}$ exhibits a two-stage ignition behavior without the presence of an NTC regime. The author follows the opinion that $\mathrm{OME_{mix}}$ also has a two-stage ignition behavior since a short first-stage ignition regime is visible, as shown in Sec. 6.3.

All fuels have in common that the ignition delay times decrease for increasing equivalence ratios. While n-Dodecane ignites faster than 1-Octanol in a wide temperature range, there is a turning point in the high-temperature region where 1-Octanol ignites faster. This means that the low-temperature chemistry of 1-Octanol is slower than n-Dodecane, but the high-temperature chemistry above $T{\approx}1100\,\mathrm{K}$ is faster than n-Dodecane. This effect gets more pronounced for higher equivalence ratios.

In summary, it can be stated that:

- $\mathrm{OME_{mix}}$ has the shortest chemical ignition delay time (factor 3-6).
- In the relevant temperature range for auto-ignition, n-Dodecane has a shorter chemical ignition delay time compared to 1-Octanol.
- N-Dodecane and 1-Octanol clearly show a two-stage ignition behavior, while $\mathrm{OME_{mix}}$ does not show a distinct NTC regime.
- 1-Octanol has a shorter chemical ignition delay time compared to n-Dodecane in the high-temperature ignition regime ($T \geq 1100\,\mathrm{K}$).

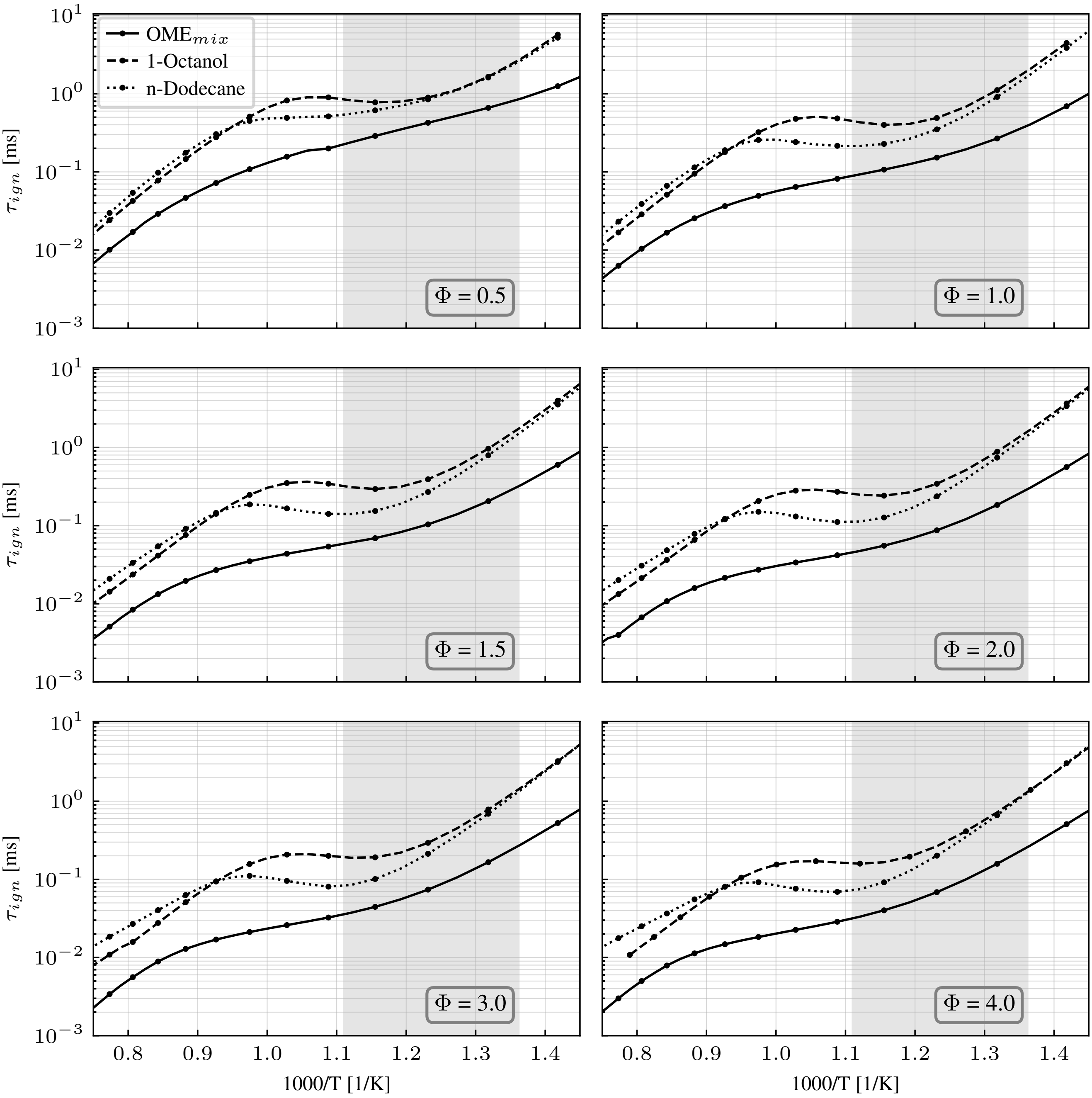

Figure 6.3: Comparison of chemical ignition delay times for: OME$_{\text{mix}}$, 1-Octanol and n-Dodecane at ECN baseline conditions ($X_{\mathrm{O}_2} = 0.15$, p= $60\,\mathrm{bar}$). The equivalence ratios relevant for ignition $\Phi \in [0.5, 1.0, 1.5, 2.0, 3.0, 4.0]$ are displayed. The gray box represents the temperature range where auto-ignition typically occurs $T \in [730\mathrm{K} - 900\mathrm{K}]$. The homogenous reactor simulations have been conducted with the chemistry solver Cantera [131].

6.3 Ignition under strained conditions

After examining the ignition behavior without transport effects in the homogeneous reactor model (0D), the fuels investigated in this thesis are now examined under strained conditions (1D). Within this work, the non-premixed flamelet model described in Sec. 2.3.3 is utilized. First, n-Dodecane, 1-Octanol and OME$_{\mathrm{mix}}$ are compared for identical profiles of the scalar dissipation rate. Then the ignition delay times are compared for different scalar dissipation rates at stoichiometry. The flamelet simulations have been conducted using the in-house code ULF [185].

6.3.1 Strained ignition with the identical scalar dissipation rate profile

The following compares the flame structures under strained conditions for n-Dodecane, 1-Octanol and OME$_{\mathrm{mix}}$. Since the mixture fractions at stoichiometry Z_{st} (see Table 3.2) are significantly different for all fuels at the ECN baseline conditions ($X_{\mathrm{O2}}{=}15\,\%$, n-Dodecane: $Z_{\mathrm{st}}{=}0.0460$, 1-Octanol: $Z_{\mathrm{st}}{=}0.0538$ and OME$_{\mathrm{mix}}$: $Z_{\mathrm{st}}{=}0.1083$)[1], a comparison at the same scalar dissipation rate at stoichiometry χ_{st} would lead to different underlying scalar dissipation rate profiles (see also Eq. 2.76). Hence, in Figure 6.4, 1-D flamelet simulations with the identical underlying χ profile are shown for the flamelet time $\tau \in$ [0,1] ms. For n-Dodecane (left column), this gives a value of $\chi_{\mathrm{st}}{=}40\,1/\mathrm{s}$ for parametrization of the scalar dissipation profile in Eq. 2.76, for 1-Octanol (center) a value of $\chi_{\mathrm{st}}{=}51.32\,1/\mathrm{s}$ and $\chi_{\mathrm{st}}{=}146.08\,1/\mathrm{s}$ for OME$_{\mathrm{mix}}$ (right). The temperature profiles are shown in the first row of Figure 6.4. In the second row, the mass fraction of the low-temperature marker formaldehyde Y_{CH2O} is shown, in the third row, the mass fraction of the high-temperature ignition marker Y_{OH} is displayed and in the following rows the mass fractions of the major combustion species Y_{CO}, Y_{CO2} and Y_{H2O} are presented. Enabling the comparison of temporal changes during ignition, the identical time steps were used for all lines in the plot among all fuels (time steps between all lines are constant ($\Delta\tau{=}50\,\mathrm{\mu s}$) for all fuels). This means that conclusions about the ignition delay times and ignition behavior can be drawn using the color code in Figure 6.4.

Low-temperature chemistry

While the maximum temperatures at the flamelet time $\tau{=}1\,\mathrm{ms}$ for all fuels are very similar (around T$=2200\,\mathrm{K}$), the course of ignition is very different. OME$_{\mathrm{mix}}$ exhibits notably higher temperatures in fuel-rich regions until approximately $\tau{=}0.25\,\mathrm{ms}$. This is also visible in the mass fraction of formaldehyde Y_{CH2O} as the marker for low-temperature ignition. The formation of CH_2O in slightly fuel-lean mixtures is observed for all fuels investigated. The formed CH_2O is then transported towards fuel-rich mixtures, and a first increase in temperature is known as *cool flame propagation* described in detail by Dahms et al. [210]. At an initial stage of ignition, the formation of Y_{CH2O} for OME$_{\mathrm{mix}}$ is observed to reach more fuel-rich mixtures ($Z{\approx}$0.4-0.5) compared to n-Dodecane and 1-Octanol. An explanation is found in the approximately doubled value of the stoichiometric mixture fraction $Z_{\mathrm{st}}{=}0.1083$ for OME$_{\mathrm{mix}}$, shifting the regions of CH_2O formation to fuel-richer regions. 1-Octanol has slightly lower values of Y_{CH2O} in the low-temperature chemistry (until $\tau{=}0.75\,\mathrm{ms}$) compared to n-Dodecane.

---

[1] While all fuels have similar chain lengths, the bound oxygen in 1-Octanol and OME$_{\mathrm{mix}}$ increase the stoichiometric mixture fraction. The atom-based balance of the combustion reaction (Bilger's mixture fraction) allows for higher fuel concentrations under stoichiometric conditions due to the bound oxygen.

High-temperature chemistry/ Main ignition

At the simulated χ profile, OME$_{\text{mix}}$ has the shortest IDT of $\tau_{\text{ign}}{\approx}0.45\,\text{ms}$, followed by n-Dodecane at $\tau_{\text{ign}}{\approx}0.65\,\text{ms}$ and 1-Octanol at $\tau_{\text{ign}}{\approx}0.75\,\text{ms}$. These findings align with the chemical IDT shown in Figure 6.3. As discussed in Sec. 6.2, n-Dodecane and 1-Octanol show a pronounced NTC behavior, meaning that the formation of stable intermediate species in the low-temperature ignition slows down the ignition process. As described above, this behavior is visible in a prolonged low-temperature/first-stage ignition and formation of Y_{CH2O}, delaying the second-stage ignition for 1-Octanol and n-Dodecane. While n-Dodecane has a shorter IDT than 1-Octanol, the transition from low to high-temperature ignition is faster for 1-Octanol. This is visible by the line density between low and high temperatures. N-Dodecane shows two (yellow) lines between the first and main ignition ($\Delta\tau \approx 0.15\,\text{ms}$), 1-Octanol and OME$_{\text{mix}}$ only show one line during main ignition ($\Delta\tau{\approx}0.1\,\text{ms}$). During the main ignition, Y_{CH2O} is consumed, while Y_{OH} is formed around stoichiometry (vertical lines denote Z_{st} in Figure 6.4). This behavior is observed for all fuels.

N-Dodecane and 1-Octanol have similar peak values of Y_{OH}, while slightly higher values for OME$_{\text{mix}}$ are observed. The higher OH mass fraction of OME$_{\text{mix}}$ is most likely linked to the higher Z_{st} value. At higher values of the mixture fraction Z, more fuel is present for combustion, increasing the quantity of products. Also for the major species (Y_{CO},Y_{CO2},Y_{H2O}) higher maximum values are observed for OME$_{\text{mix}}$. 1-Octanol shows a slight increase in the maximum values for the major species, which can be explained by the higher stoichiometric mixture fraction compared to n-Dodecane.

In contrast to the flamelet analysis presented here, 1-Octanol and OME$_{\text{mix}}$ are reported to show less Y_{CO} in engine experiments [43, 53, 54, 218]. Especially for lean operating conditions, the Y_{CO} and Y_{CO2} could be reduced compared to a regular Diesel fuel for OME$_{\text{mix}}$ and 1-Octanol. This finding is notable because the flamelet analysis shows a doubled maximum Y_{CO} value for OME$_{\text{mix}}$ and a slight increase for 1-Octanol compared to n-Dodecane. However, the maximum of Y_{CO} for OME$_{\text{mix}}$ is located at around $Z{=}0.4$, while n-Dodecane and 1-Octanol peak at $Z{=}0.15$ and $Z{=}0.2$ respectively. All fuels show significant amounts of Y_{CO} in regions from stoichiometry to fuel-rich mixtures. Comparing the Y_{CO} values for all fuels at, the stoichiometric mixture fraction of n-Dodecane at $Z_{\text{st}}{=}0.0460$ ($\lambda{=}1$ operating condition), significantly reduced formation of Y_{CO} for OME$_{\text{mix}}$ is observed.

For Y_{CO2}, the peak values are all located at Z_{st} (location of the non-premixed flame). A significant difference is observed for OME$_{\text{mix}}$. In fuel-rich mixtures, the shape of the Y_{CO2} profile for OME$_{\text{mix}}$ is convex, while n-Dodecane and 1-Octanol are concave. The convex shape of OME$_{\text{mix}}$[2] indicates that in fuel-rich operating conditions (fuel-air ratio $\lambda < 1$ or $\Phi{>}1$) OME$_{\text{mix}}$ produces more Y_{CO2} compared to n-Dodecane and 1-Octanol with a concave shape.

On the other hand, the high stoichiometric mixture fraction of OME$_{\text{mix}}$ leads to significantly lower Y_{CO2} emissions in lean conditions. Comparing the values of Y_{CO2} at the stoichiometric mixture fraction of n-Dodecane at $Z_{\text{st}}{=}0.0460$ shows, that OME$_{\text{mix}}$ produces approximately half of Y_{CO2} than n-Dodecane and 1-Octanol.

Summarizing the most important findings:

- Aligning with the chemical ignition delay times in Sec. 6.2, n-Dodecane and 1-Octanol show a pronounced low-temperature chemistry behavior typical for Diesel fuels. OME$_{\text{mix}}$ also shows low-temperature chemistry, but first-stage ignition is short and less pronounced.

---

[2] In Mira et al. [112] it is mentioned that OME$_{\text{mix}}$ in contrast to n-Dodecane, combusts acetylene in the fuel-rich regions, which might explain the higher CO_2 values.

- Similar maximum temperatures are observed for all fuels at around T = 2200 K.
- OME$_{\mathrm{mix}}$ exhibits higher peak values of Y_{CH2O} in the stationary solution.
- 1-Octanol and OME$_{\mathrm{mix}}$ show faster thermal runaway than n-Dodecane, indicating higher reactivity during ignition.
- Similiar peak values of Y_{OH} are observed for all fuels. Besides OME$_{\mathrm{mix}}$ exhibiting slightly increased Y_{OH} due to more Y_{CH2O} and a higher mixture fraction at the peak position.
- At the prescribed χ profile, ignition delay times increase from OME$_{\mathrm{mix}}$ (fastest) to n-Dodecane and 1-Octanol (slowest).
- OME$_{\mathrm{mix}}$ exhibits almost doubled peak values of Y_{CO} than n-Dodecane and 1-Octanol.
- The peak values of Y_{CO2} and Y_{H2O} at the stoichiometric mixture fraction for OME$_{\mathrm{mix}}$ are slightly increased compared to the reference fuel n-Dodecane.
- The experimental findings of lower Y_{CO} and Y_{CO2} values compared to Diesel in engine experiments are elucidated. The increased stoichiometric mixture fraction of the oxygenated fuels OME$_{\mathrm{mix}}$ and 1-Octanol leads to lower emissions at the stoichiometric mixture fraction of the reference fuel n-Dodecane (respective lean conditions).

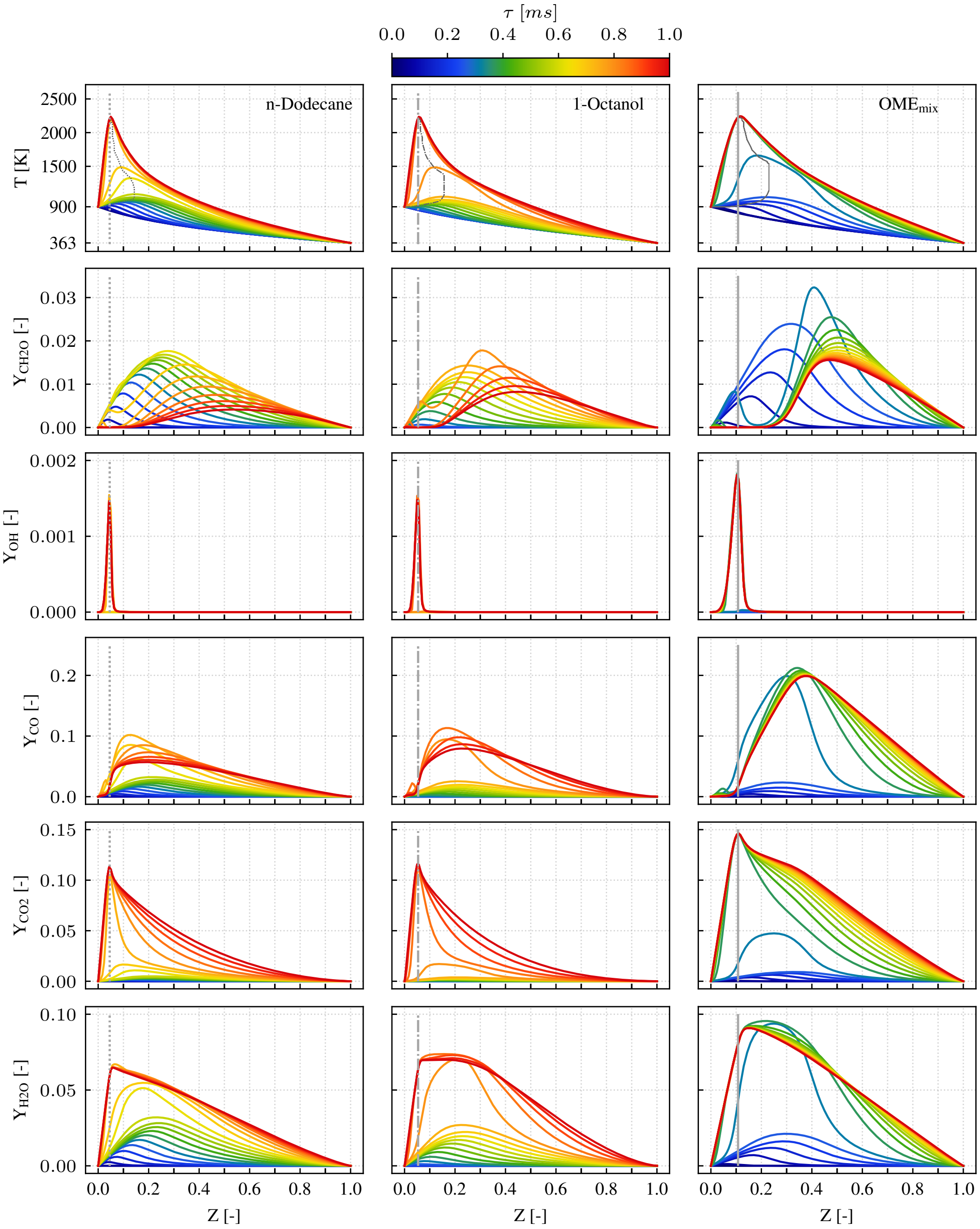

Figure 6.4: Comparison of laminar non-premixed flamelet simulations with the identical χ profile: n-Dodecane (left), 1-Octanol (center) and OME$_{\text{mix}}$ (right) at ECN baseline conditions (see Table 3.2). The simulations are conducted for scalar dissipation rates at stoichiometry of χ_{st}=$40.00\,1/\text{s}$ for n-Dodecane, χ_{st}=$51.32\,1/\text{s}$ for 1-Octanol and χ_{st}=$146.08\,1/\text{s}$ for OME$_{\text{mix}}$. The same temporal discretization is used for each line. Thus, the course of ignition can be compared based on the color code. In the top row, the temperature profile is shown. The following rows show the mass fractions of CH_2O, OH as flame markers for low and high-temperature chemistry. The next rows show the major species' mass fraction, used for the progress variable: CO, CO_2 and H_2O. The vertical lines represent the stoichiometric mixture fraction Z_{st} for each fuel.

6.3.2 Influence of strain on the ignition delay time

In Sec. 6.3.1, flame characteristics at identical profiles of the scalar dissipation rate are elucidated. But in spray flames, the auto-ignition is strongly influenced by different strain levels. In the following, the influence of strain on ignition delay time is examined for all fuels. This investigation provides deeper insight into the ignition behavior in the spray.

The main ignition delay time τ_{ign} in Figure 6.5 for different scalar dissipation rate profiles, has been evaluated as the maximum of the maximum temperature gradient ($\frac{\partial T_{\max}}{\partial \tau}$) for $T_{\max} > 1000\,\mathrm{K}$. The highest scalar dissipation rate at stoichiometry where auto-ignition occurs $\chi_{\mathrm{st,ign}}$ is represented by a vertical line.

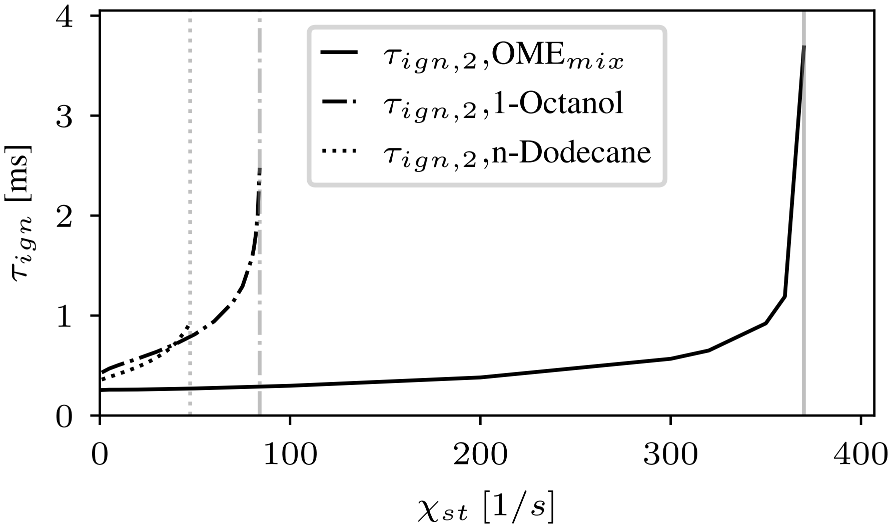

Figure 6.5: Investigation of the influence of strain on the ignition delay time in the 1-D flamelet for OME$_{\mathrm{mix}}$, 1-Octanol and n-Dodecane at ECN baseline conditions (see Table 3.2). The IDT of each fuel is plotted until their respective ignition limit $\chi_{\mathrm{st,ign}}$, which is highlighted as a vertical line.

Over the complete range of scalar dissipation rates at stoichiometry, OME$_{\mathrm{mix}}$ has the shortest ignition delay time. The sensitivity of OME$_{\mathrm{mix}}$ towards strain effects on ignition delay time is not pronounced. OME$_{\mathrm{mix}}$ also exhibits the highest ignition limit at $\chi_{\mathrm{st,ign}}=370\,1/\mathrm{s}$. This low sensitivity of the IDT towards the scalar dissipation rate is explained by the high reactivity of OME$_{\mathrm{mix}}$, reducing the chemical ignition delay time by a factor 3-6 compared to the other fuels (see Sec. 6.2). As expected from the chemical ignition delay times in Figure 6.3, the ignition delay time of n-Dodecane is shorter than 1-Octanol. In proximity to the ignition limit of n-Dodecane ($\chi_{\mathrm{st,ign}}$), the ignition delay time of 1-Octanol falls below the IDT of n-Dodecane. At first glance, this finding is counterintuitive. As seen in Figure 6.3, the chemical IDT of 1-Octanol is higher in the relevant temperature range for ignition. But at higher temperatures, the reactivity of 1-Octanol increases and the IDT falls below the IDT of n-Dodecane. The increasing IDT with increasing scalar dissipation rates in Figure 6.5, causes higher temperatures in the first-stage ignition process for 1-Octanol. As observed in the auto-ignition curves in Figure 6.3, the reactivity at higher temperatures is increased for 1-Octanol and leads to earlier main ignition. This behavior is also visible in the ignition limits. N-Dodecane shows the lowest value at $\chi_{\mathrm{st,ign}}=55.3\,1/\mathrm{s}$ and 1-Octanol has a slightly higher value of $\chi_{\mathrm{st,ign}}=84\,1/\mathrm{s}$.

It can be concluded that OME$_{\text{mix}}$ is more reactive than the other fuels and ignites earlier also under strained conditions. While 1-Octanol shows higher IDTs at lower scalar dissipation rates, the IDT decreases compared to n-Dodecane and also has a higher value of $\chi_{\text{st,ign}}$. The interested reader might object that the higher values of the stoichiometric mixture fraction of the oxygenated fuels may lead to higher $\chi_{\text{st,ign}}$ values, but the underlying χ profile does not exhibit higher values of the scalar dissipation rate (see Eq. 2.76). In Figure 6.6, the profiles of the scalar dissipation rate at ignition ($\chi_{\text{st,ign}}$) are presented for the investigated fuels in mixture fraction space. The horizontal lines in Figure 6.6 represent the ignition limit $\chi_{\text{st,ign}}$ and the vertical lines show the stoichiometric mixture fraction of each fuel. Figure 6.6 clearly shows that OME$_{\text{mix}}$ has the highest maximum value of the scalar dissipation rate, followed by 1-Octanol and n-Dodecane.

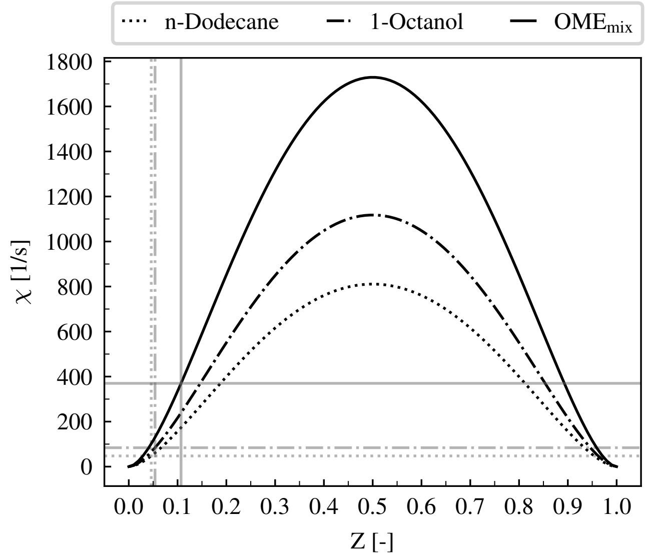

Figure 6.6: Comparison of χ profiles at the ignition limit for: n-Dodecane ($\chi_{\text{st,ign}}$=$55.3\,1/\text{s}$), , 1-Octanol ($\chi_{\text{st,ign}}$=$84\,1/\text{s}$) and OME$_{\text{mix}}$ ($\chi_{\text{st,ign}}$=$370\,1/\text{s}$) at ECN baseline conditions (see Table 3.2). Horizontal lines represent the corresponding $\chi_{\text{st,ign}}$ value, and vertical lines represent the mixture fraction at stoichiometry Z_{st}. The scalar dissipation rate profiles show that OME$_{\text{mix}}$ has the highest maximum of all profiles.

The most interesting findings are summarized below:

- OME$_{\text{mix}}$ has the highest scalar dissipation rate at stoichiometry where ignition occurs.
- OME$_{\text{mix}}$ has the lowest ignition delay time over the whole range of χ_{st}.
- The ignition delay time of OME$_{\text{mix}}$ is less sensitive to changes of the scalar dissipation rate.
- The ignition delay time of n-Dodecane is lower than 1-Octanol. Close before the ignition limit of n-Dodecane, the IDT of n-Dodecane exceeds the ignition delay time of 1-Octanol. The reactivity of 1-Octanol increases in the high-temperature region, which explains its higher ignition limit compared to n-Dodecane.
- The highest scalar dissipation rate where ignition occurs ($\chi_{\text{st,ign}}$) is associated with the stoichiometric mixture fraction of the fuel. It is shown that the higher Z_{st} of OME$_{\text{mix}}$ still means that OME$_{\text{mix}}$ ignites at the highest scalar dissipation rate profile.

6.4 Heat-loss corrected flamelet model derived from the mixture formation analysis

The mixture formation analysis presented in Sec. 5.4.2 revealed that especially 1-Octanol and $\mathrm{OME_{mix}}$, with a higher latent heat of evaporation than n-Dodecane, exhibit a significantly lower temperature distribution than it is assumed in the flamelet simulation. In addition, the lower heat capacities of 1-Octanol and $\mathrm{OME_{mix}}$ increase the sensitivity for the heat losses due to evaporation compared to n-Dodecane. Due to the respectively higher temperatures in the flamelet model than in the actual spray, the thermophysical state in the CFD is overpredicting the source term of the progress variable retrieved from the flamelet look-up table, and the ignition delay time in the CFD is underpredicted. As shown in the introduction in Sec. 1.1.5, incorporating spray cooling in flamelet models is an unresolved topic in the literature.

Some studies try to directly include evaporation in the one-dimensional flamelet model [219, 220]. This approach is well suited for investigating the effect of spray on the flame structure. In an UFPV approach, however, the high complexity and increased simulation time make this approach not suitable for a tabulated chemistry approach. In other studies, a lower fuel temperature is assumed, until an agreement between the temperature distribution in the spray and the adiabatic mixing line with the reduced fuel temperature is achieved [101, 221, 222]. However, the methodology results in fuel temperatures for the ECN Spray D down to $T_{\mathrm{Fuel}}=155\,\mathrm{K}$ [221] and is not standardized. The effect of very low fuel temperatures (e.g., $T_{\mathrm{Fuel}}=155\,\mathrm{K}$) on the flamelet manifold, described in [221, 222], remains open. This methodology is also limited to the absolute zero point for the fuel ($T_{\mathrm{Fuel}}=0\,\mathrm{K}$), which might be reached for increased nozzle sizes and fuels with a high latent heat of evaporation. Moreover, thermophysical properties for gas species (see Eq. 2.32-2.34) are usually defined only above $T=200\,\mathrm{K}$. The methodology of decreasing the fuel temperature significantly to incorporate heat loss due to evaporation does not represent the spray's temperature distribution properly, since ignition delay times show an offset of $10\text{-}20\,\%$ for n-Dodecane [101, 222]. Other studies for n-Dodecane in ECN Spray A without the correction of heat-loss due to evaporation sometimes even perform better [3, 90, 95, 112, 114]. In Zhang et al. [223], an enthalpy reduction-based method is presented, but no evaluation of the method compared to a standard model is provided.

As a novelty in this work, the investigation of the gas temperature distribution of the inert sprays revealed that n-Dodecane is less sensitive to heat loss due to evaporation, but in the context of renewable Diesel fuels with higher latent heat of formation and increasing nozzle sizes, the influence of heat loss due to evaporation on ignition increases. As shown in several studies for OMEs [59, 102, 112, 113], the ignition delay time in reactive sprays is underestimated by $10\text{-}50\,\%$. The unresolved issue of heat loss due to evaporation (*spray cooling*) on flamelet-based models remains unsolved [93]. In this thesis, a reproducible and physically consistent approach is introduced, incorporating spray cooling effects in the flamelet manifold.

The initial temperature profile of the novel heat-loss corrected flamelet model is reduced to two line segments instead of the adiabatic mixing line. This assumption has proven to be suitable in the coupled reactive spray simulation. The idea of the novel model is to obtain the optimal temperature profile that represents the average temperature of the spray for the flamelet simulation. The line segments must not intersect the adiabatic mixing line. Otherwise, higher temperatures would be assumed than in the original flamelet model, and the IDT in the spray would be further reduced. The midpoint of the line segments is determined by an optimization process. The marginal probability function of the mixture fraction P_Z is integrated until most scatters are incorporated ($x\%$ Confidence Interval (CI)), and the average temperature of the spray is evaluated at the position in mixture fraction space ($Z=Z_{x\mathrm{CI}\%}$). The process is repeated until a maximum of CI ($x\mathrm{CI}\%$) is found, and the line segment, defined by ($Z=0$, $T=T_{\mathrm{Oxidizer}}$), ($Z=Z_{x\mathrm{CI}\%}$, $T=\langle T|Z_{x\%\mathrm{CI}}\rangle$), is not intersecting the adiabatic mixing line. In Figure 6.7, the process to determine the initial temperature profile of the novel heat-loss corrected flamelet model (dash-dotted line) is visualized. The complete initial temperature profile is defined by the points (Z=0, T=T_{Oxidizer}), (Z=$Z_{x\mathrm{CI}\%}$, T=$\langle T|Z_{x\%\mathrm{CI}}\rangle$), and ($Z$=1, T=T_{Fuel}). The heat loss corrected initial temperature profile must not intersect the adiabatic mixing line, and $x\%$ CI must have its maximum (most scatters are incorporated). The heat loss corrected temperature profile is determined at t=0.1 ms, where all injectors have reached their maximum liquid penetration length.

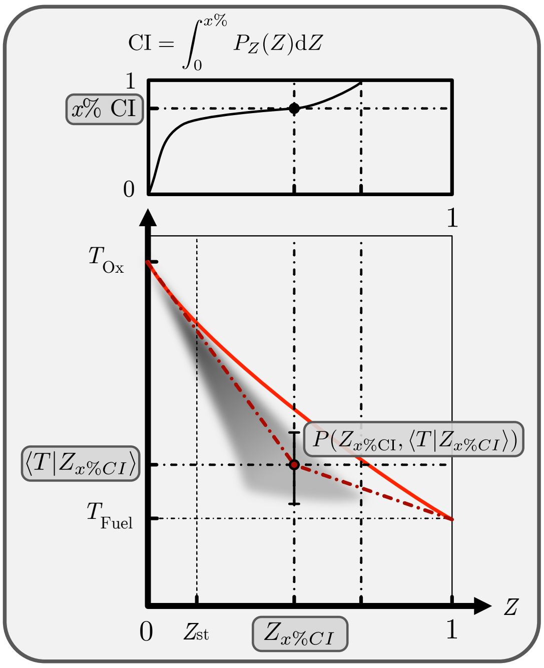

Figure 6.7: Illustration of the method determining the heat-loss corrected initial temperature profile from the inert spray simulation (gray distribution). The solid red line represents the adiabatic mixing line, and the dark red dash-dotted line represents the heat loss corrected temperature profile. At the top edge, the integration of the marginal PDF of the mixture fraction is visualized.

The procedure is applied to all sprays investigated in this thesis. In Figure 6.8 the heat-loss corrected temperature profiles are presented for the ECN Spray A3 and compared to the adiabatic mixing line assumed in the standard flamelet model. The highest difference between the adiabatic mixing line and the heat-loss corrected profile is observed for 1-Octanol (b). Also, $\mathrm{OME}_{\mathrm{mix}}$ (c) exhibits an undercooling effect, but not as pronounced as for 1-Octanol. On the other hand, for n-Dodecane (a) the difference between the heat-loss corrected profile and the original profile is negligible.

The difference between the novel method presented in this thesis and the method described in [221, 222], lowering the fuel temperature to T_{Fuel}= 155 K, is significant for n-Dodecane and $\mathrm{OME}_{\mathrm{mix}}$. The method from the literature underestimates the spray temperature and would underestimate the ignition delay time [221, 222].

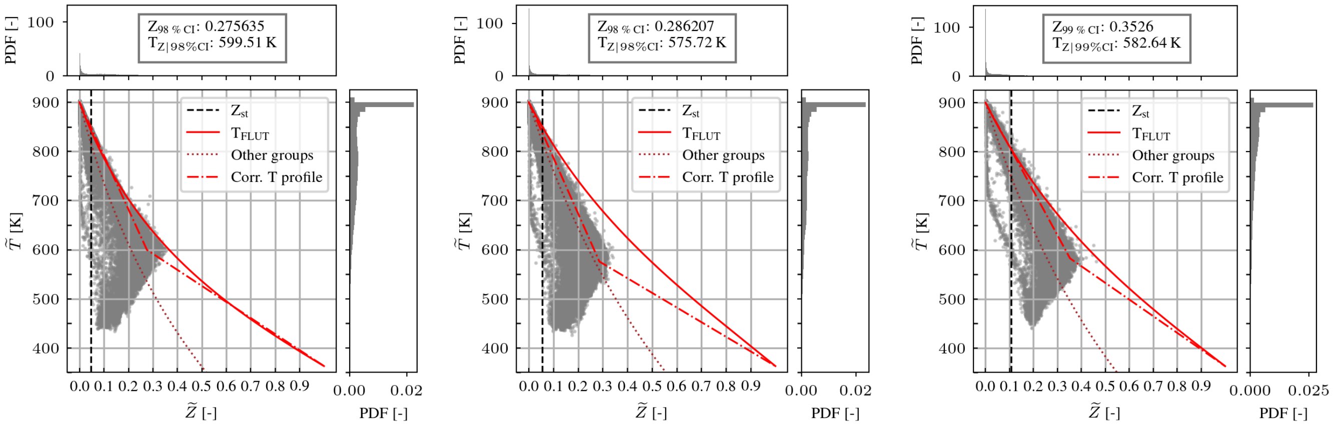

(a) n-Dodecane. (b) 1-Octanol. (c) OME$_{\text{mix}}$.

Figure 6.8: Temperature distribution extracted from the inert ECN Spray A3 simulation at tavSOI= $0.1\,\mathrm{ms}$ for n-Dodecane (a), 1-Octanol (b) and OME$_{\text{mix}}$ (c). The new initial profile for the flamelet simulations is shown as the dash-dotted line, the adiabatic mixing line is denoted as the solid line, and the methodology presented in [221, 222] is represented by the dotted line. Additionally, the marginal probability density functions of $\widetilde{Z}$ and $\widetilde{T}$ are shown at the respective edges.

With increasing nozzle size in ECN Spray D in Figure 6.9, n-Dodecane (a) exhibits more significant differences to the adiabatic mixing line. The temperature distribution for n-Dodecane is also shifted to lower temperatures due to a higher evaporated mass and hence, higher enthalpy loss. Also, the corrected profile of OME$_{\text{mix}}$ reveals a significant difference between the adiabatic mixing line and heat-loss corrected temperature profile.

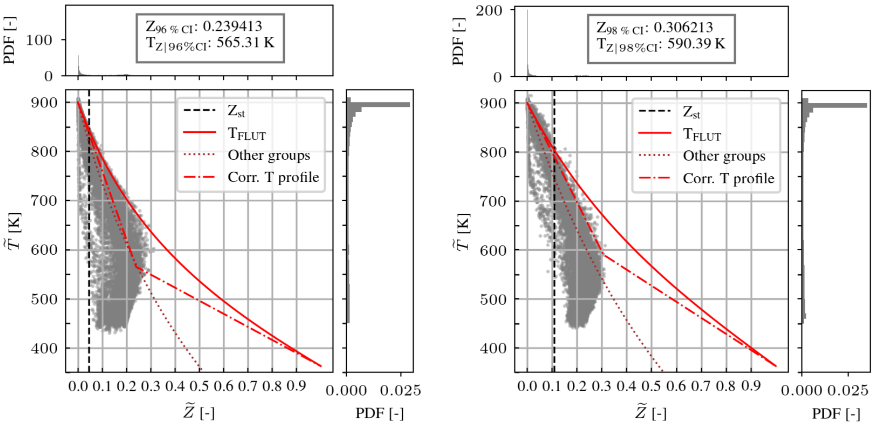

(a) n-Dodecane. (b) OME$_{\text{mix}}$.

Figure 6.9: Temperature distribution extracted from the inert ECN Spray D simulation at tavSOI= $0.1\,\mathrm{ms}$ for n-Dodecane (a) and OME$_{\text{mix}}$ (b). The new initial profile for the flamelet simulations is shown as the dash-dotted line, the adiabatic mixing line is denoted as the solid line, and the methodology presented in [221, 222] is represented by the dotted line. Additionally, the marginal probability density functions of $\widetilde{Z}$ and $\widetilde{T}$ are shown at the respective edges. Additionally, the marginal probability density functions of $\widetilde{Z}$ and $\widetilde{T}$ are shown at the respective edges.

For the marine injector from Woodward L'Orange in Figure 6.10 with the highest injection rates and injected masses, the heat-loss corrected temperature profile gets more important for 1-Octanol (b). The temperature distribution shifts towards lower temperatures. Moreover, the longer spray ignition delay time observed in the experiment shows a higher sensitivity in the temperature correction. For n-Dodecane (a), a lower sensitivity is observed, and the heat-loss corrected profile only shows small deviations compared to the adiabatic mixing line.

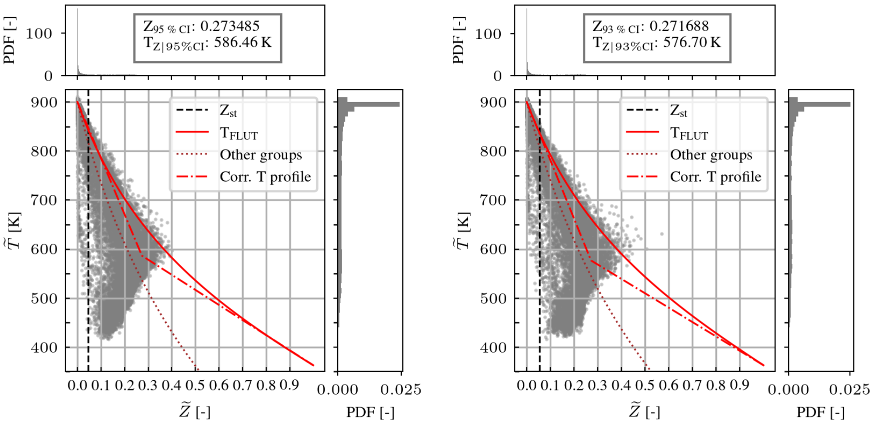

(a) n-Dodecane.

(b) 1-Octanol.

Figure 6.10: Temperature distribution extracted from the inert Woodward L'Orange single hole injector simulation at tavSOI= $0.1\,\mathrm{ms}$ for n-Dodecane (a) and 1-Octanol (b). The new initial profile for the flamelet simulations is shown as the dash-dotted line, the adiabatic mixing line is denoted as the solid line, and the methodology presented in [221, 222] is represented by the dotted line. Additionally, the marginal probability density functions of $\widetilde{Z}$ and $\widetilde{T}$ are shown at the respective edges.

The influence of the heat-loss corrected temperature profile is examined for 1-Octanol in the Woodward L'Orange injector (Figure 6.10 (b)) as it shows the highest sensitivity towards heat loss due to evaporation. The findings of this comparison are also valid for the other fuels. For the sake of brevity, only 1-Octanol is investigated in detail here.

In Figure 6.11, the side-by-side comparison of the adiabatic mixing line (left) and the heat-loss corrected temperature profile (right) in the flamelet simulation is shown. The connection point for the two line segments in the heat-loss corrected temperature profile is located at P(Z=0.27 |T=$576\,\mathrm{K}$), see Figure 6.10 (b). From the temperature profiles it can be observed, that as expected, the ignition of the heat-loss corrected flamelet is delayed. The path of the highest temperature (T at the most reactive mixture fraction Z_{MR}, denoted as the thin dash-dotted line in Figure 6.11) at each time step exhibits minor deviations, but overall very similar profiles are observed[3]. Also, the major species do not show significant differences. Besides the later ignition delay for the heat-loss corrected temperature profile, the stationary profiles for both modeling approaches are identical. Moreover, also the scalar dissipation rate where ignition occurs $\chi_{\mathrm{st,ign}}$ is not affected in the case of the heat-loss corrected temperature profile. It can be concluded, that all chemically dominated processes are not significantly affected in the stationary solution, but the expected shift in ignition delay is observed (see color code and Figure 6.12). An explanation is found in the Arrhenius equation (Eq. 2.64). The lower

---

[3] The most reactive mixture fraction has been introduced by [224] and has been used as a single point. However, Mastorakos [224] also states that Z_{MR} can shift over time. In recent spray studies, the term most reactive mixture fraction has been utilized as the point of highest temperature in the igniting flamelet manifold [102, 112, 178].

temperatures in fuel-rich regions reduce the reactivity of the formation of CH_2O. Through transport processes and low-temperature chemistry, the temperature rises, and the ignition follows the same processes as the standard modeling approach.

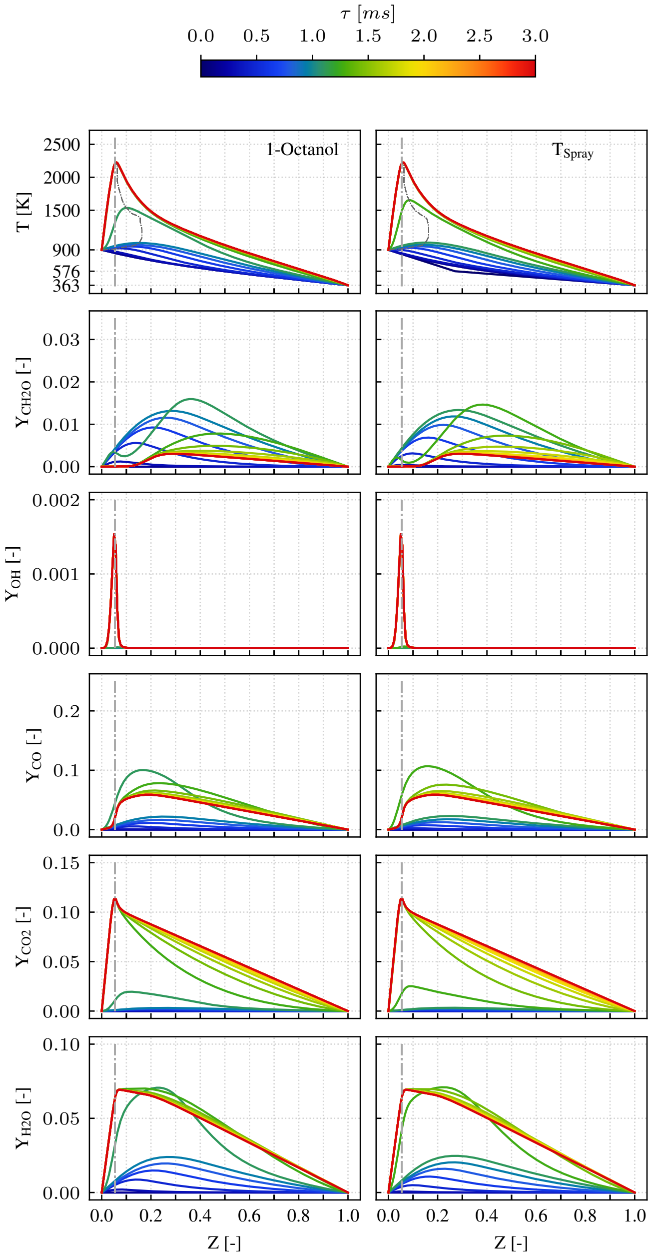

Figure 6.11: Comparison of flamelet simulations with adiabatic mixing (left) and the heat-loss corrected temperature profile (right) at $\chi_{\mathrm{st}}{=}70\,1/\mathrm{s}$ for 1-Octanol. The connection point for the two line segments in the heat-loss corrected temperature profile derived in Figure 6.10 (b) is located at P(Z=0.27 $|T$=$576\,\mathrm{K}$) and is used in the simulation of the marine injector. In the top row, the temperature profiles are presented for the course of ignition. In the rows below, the mass fractions of the low and high-temperature ignition markers (CH_2O and OH) and major species (CO, CO_2 and H_2O) are displayed. While the ignition delay time is delayed for the heat-loss corrected flamelet model, the stationary profiles are identical.

In Figure 6.12, the influence of the scalar dissipation rate on the ignition delay time is shown for adiabatic mixing and the heat-loss corrected temperature profile. The IDT of the heat-loss corrected profile exhibits a higher ignition delay time compared to the flamelet with adiabatic mixing. The offset between the two ignition delay curves remains nearly constant. Close to the ignition limit, both ignition delay curves align. The ignition limit $\chi_{\mathrm{st,ign}}$ is identical for both modeling approaches.

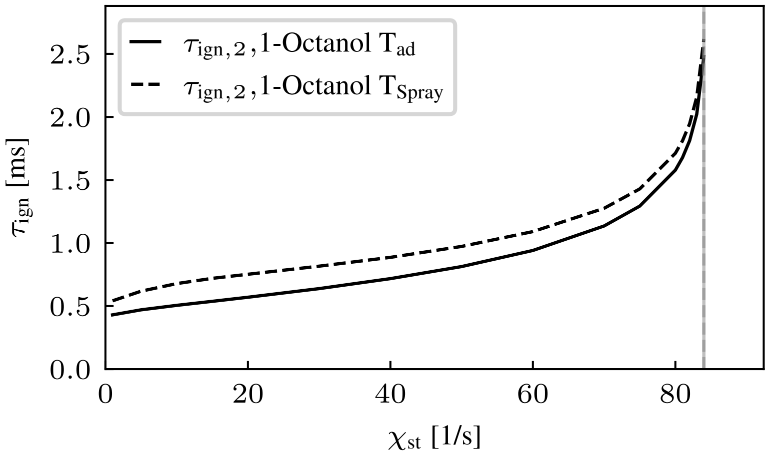

Figure 6.12: Influence of the scalar dissipation rate on the ignition delay time for 1-Octanol. The modeling approach with and without spray temperature correction is compared. The heat-loss corrected profile from Figure 6.10 (b) exhibits a nearly constant higher ignition delay time. The ignition limit $\chi_{\mathrm{st,ign}}$ for both modeling approaches is identical.

The findings from the analysis of a heat-loss corrected flamelet approach are summarized in bullet points:

- Based on the findings from the analysis of the temperature distribution, a novel method for heat-loss corrected initial temperature profiles due to latent heat of evaporation is proposed.
- The novel model is, in contrast to existing models, including heat losses due to evaporation, physically consistent, and the derivation of the initial temperature profile is a standardized and reproducible process.
- The novel model does not affect the stationary profiles of the flamelet simulation, only the course of ignition is different, leading to longer ignition delay times.
- Ignition at different values of the scalar dissipation rate at stoichiometry showed an almost constant offset on the ignition delay time until close proximity to the ignition limit.
- The ignition limit $\chi_{\mathrm{st,ign}}$ is identical for the standard and heat-loss corrected flamelet model.

6.5 Flamelet Lookup Table (FLUT) generation

The Flamelet Lookup Tables (FLUT) used within this thesis have been produced with the in-house C++ code "Universal Laminar Flame Solver" [185] and the in-house Python code "pyFLUT." According to Sec. 2.3.4, an ensemble of laminar non-premixed flamelets is solved before the LES. In this thesis, the resolution of Z in the flamelet simulations is 101 points. The flamelet simulations are simulated in the interval of τ=0-10 ms. The first step is to find the scalar dissipation rate at stoichiometric conditions where the flamelet simulation starts to ignite (ignition limit, $\chi_{\mathrm{st,ign}}$). The discretization of χ_{st} is evenly spaced in the table, only at the boundaries ($\chi_{\mathrm{st}} = 0$ and $\chi_{\mathrm{st}} = \chi_{\mathrm{st,ign}}$) a refinement is applied. Usually, two to three χ_{st} values above $\chi_{\mathrm{st,ign}}$ are added to discretize non-ignited thermophysical states above $\chi_{\mathrm{st,ign}}$. After a reasonable table layout is found in terms of accuracy and size, a suitable definition of the progress variable is determined. Further information about the optimization of the progress variable definition can be found in Sec. 2.3.4, and Sun et al. [77]. All flamelet solutions are mapped from the flamelet time τ to the progress variable C. The resolution of C is 151 within this thesis. Finally, all flamelet simulations are assembled into the FLUT, and the β-PDF integration is applied to get the filtered solution quantities needed in the LES for the TCI closure. The discretization in $\widetilde{Z''^2}^N$ direction is seven. Further information regarding the used FLUTs is found in Table 6.1. All tables have been assembled for the standard flamelet model and the heat loss corrected flamelet model.

6.6 Conclusions on the flame structure analysis

A detailed flame structure analysis has been conducted for n-Dodecane, 1-Octanol and OME$_{\mathrm{mix}}$. The analysis is based on models of increasing complexity.

First, chemical ignition delay times are investigated in the 0-D homogeneous reactor model. The chemical ignition delay time for OME$_{\mathrm{mix}}$ is three to six times lower than for n-Dodecane and 1-Octanol. This finding indicates high reactivity for OME$_{\mathrm{mix}}$. The chemical IDT of n-Dodecane is shorter than 1-Octanol in the temperature range relevant for ignition. In the high-temperature chemistry regime ($T > 1000\,\mathrm{K}$), 1-Octanol exhibits a higher reactivity, resulting in lower ignition delay times.

The ignition under strained conditions is investigated in the laminar non-premixed flamelet model. First, all fuels are compared in flamelet simulations with identical profiles of the scalar dissipation rate to elucidate differences in the flame structure. The increased share of bound oxygen in 1-Octanol and OME$_{\mathrm{mix}}$ increase the stoichiometric mixture fraction. The stoichiometric mixture fraction of OME$_{\mathrm{mix}}$ ($Z_{\mathrm{st}} = 0.1083$) is approximately twice as high as 1-Octanol and n-Dodecane at the ECN baseline conditions. This significantly influences the flame structure, shifting the diffusion flame to higher Z values. The oxygenated fuels exhibit the trend of higher mass fraction peaks of CO and CO_2 in the stationary solution. The peaks of Y_{CO} and Y_{CO2} shift to higher mixture fractions for oxygenated fuels, where higher amounts of carbon are present to form CO and CO_2. The higher maximum values of Y_{CO} and Y_{CO2} for oxygenated fuels compared to n-Dodecane in the flamelet do not agree with experimental results in engines, where lower CO emissions are reported. At stoichiometry, almost no CO but mainly CO_2 is produced. At the stoichiometric mixture fraction of n-Dodecane (Z_{st}=0.0460), 1-Octanol and OME$_{\mathrm{mix}}$ exhibit significantly lower values of CO (due to their higher stoichiometric mixture fraction). This explains why, at certain operating conditions, OME$_{\mathrm{mix}}$ and 1-Octanol show reduced levels of CO. As observed in the homogenous reactor model, OME$_{\mathrm{mix}}$ has the lowest ignition delay time over the whole range of scalar dissipation rates at stoichiometry. The high reactivity of OME$_{\mathrm{mix}}$ leads to a low sensitivity of strain on ignition delay and a high value of the scalar dissipation rate where ignition occurs ($\chi_{\mathrm{st,ign}}$).

In contrast, the influence on ignition delay by strain is significant for n-Dodecane and 1-Octanol. While at low scalar dissipation rates at stoichiometry, 1-Octanol shows a higher IDT, a turning point is observed close to the ignition limit of n-Dodecane where the IDT of 1-Octanol falls below the IDT of n-Dodecane. As observed in the ignition delay curve, the reactivity of 1-Octanol increases in the high-temperature chemistry regime, leading to a higher ignition limit $\chi_{\mathrm{st,ign}}$ compared to n-Dodecane.

The mixture formation analysis revealed significant differences in the temperature distribution between the fuels and the adiabatic mixing line assumed in the flamelet model. One important finding is that the lower heat capacities of 1-Octanol and $\mathrm{OME}_{\mathrm{mix}}$ increase the modeling error of neglecting the heat loss due to evaporation in the flamelet model. A novel methodology introducing a temperature correction for the spray cooling effect in the flamelet simulation is proposed. Compared to other approaches, the methodology is physically consistent and standardized. The heat loss corrected temperature profile is derived from the inert spray simulation in a post-processing step. The effects of the heat-loss corrected temperature profile have been shown in detail for 1-Octanol, the fuel with the highest latent heat of evaporation. While the ignition delay time is increased for the corrected temperature profile, no differences in the stationary solution are exhibited. Also, the ignition limits are identical since this is a reactivity-controlled process.

The detailed flame structure analysis provides detailed information for the reactive spray simulations. The novel heat-loss corrected flamelet manifold is compared to the state-of-the-art flamelet model. The performance of the new model will also be shown in the coupled reactive spray LES in the next chapter (Sec. 7).

7 Ignition of Turbulent Spray Flames

As a final step in this thesis, the results of the reactive spray simulations are presented. The simulations were conducted for n-Dodecane, 1-Octanol and $\mathrm{OME_{mix}}$ for the automotive ECN Spray A3 injector (Sec. 7.1), the heavy-duty ECN Spray D (Sec. 7.2) and the marine Woodward L'Orange single-hole injector (Sec. 7.3). The standard flamelet model and the heat-loss corrected flamelet model are compared based on the spray ignition delay time as a global characteristic. The aim of the spray flame analysis is threefold:

Influence of mixture formation First, the influence of mixture formation concerning different fuel thermophysical properties on ignition is elucidated.

Influence of latent heat of evaporation on ignition Second, the influence of heat loss due to evaporation on ignition is evaluated by comparison of the standard flamelet model with the temperature-corrected flamelet model.

Influence of nozzle size Third, the influence of increasing nozzle size on ignition is examined.

The structure of the ignition of turbulent spray flames investigation is based on that of the mixture formation analysis in Sec. 5. The fuels are compared side-by-side in one injector setup at a time, followed by the comparison of injectors with increasing nozzle sizes. An overview of the ignition delay times of all fuels and injectors is presented in Table 7.1.

7.1 Automotive injector: ECN Spray A3

In the following, the simulation results for the reactive ECN Spray A3 are presented. The comparison between n-Dodecane, 1-Octanol, and $\mathrm{OME_{mix}}$ is drawn based on different combustion metrics, e.g., ignition delay times, OH^* chemiluminescence imaging, different Favre-filtered fields extracted from the LES and the analysis of the flame structure in mixture fraction space.

7.1.1 Influence of latent heat of evaporation on ignition

The ignition delay time is a global spray flame characteristic crucial for engine design. The following analysis shows the different ignition delay times for all fuels in Spray A3. Furthermore, the influence of the heat-loss-corrected flamelet model is elucidated.

As described in the thesis of Rieß [191], the ignition delay in the experiment is determined as the $50\,\%$ probability of all ignition events. An ignition event in the experiment is detected when a threshold value is reached. The ignition delay time in the LES is determined by $2\,\%$ of the maximum of the volume-integrated $\widetilde{Y}_{\mathrm{OH}}$. The volume-integrated mass fraction of the Favre-filtered OH signal is considered to be most consistent with the experimental measurement technique. In Figure 7.1, the evolution of the volume-integrated Favre-filtered OH mass fraction is shown over time. The results for n-Dodecane (a) perfectly align with the IDT measured in the experiment. As described in Sec. 6.4, n-Dodecane in the Spray A3 configuration is not significantly affected by the heat loss due to evaporation. Hence, no heat-loss-corrected flamelet simulation is conducted.

Table 7.1: Overview of ignition delay times from the experiment and the reactive spray simulation. The ignition delay time $\tau_{\text{ign,Sim}_{T_{\text{ad}}}}$ of the standard flamelet model is compared with the solution of the heat loss corrected flamelet model $\tau_{\text{ign,Sim}_{T_{\text{Spray}}}}$. Excellent agreement of the ignition delay time has been achieved with the heat loss corrected flamelet model introduced in this thesis.

Injector	ECN Spray A3				
Fuel	$\tau_{\text{ign,Exp}}$	$\tau_{\text{ign,Sim}_{T_{\text{ad}}}}$	$\tau_{\text{ign,Sim}_{T_{\text{Spray}}}}$	$\epsilon_{\text{rel},T_{\text{ad}}}$ [%]	$\epsilon_{\text{rel},T_{\text{Spray}}}$ [%]
n-Dodecane	0.4726 $\pm$0.0185 ms	0.469 ms		-0.1	
1-Octanol	0.8065 $\pm$0.0286 ms	0.647 ms	0.7800 ms	-24.7	**-0.8**
OME$_{\text{mix}}$	0.3807 $\pm$0.0154 ms	0.348 ms	0.399 ms	-9.4	**4.6**
Injector	ECN Spray D				
Fuel	$\tau_{\text{ign,Exp}}$	$\tau_{\text{ign,Sim}_{T_{\text{ad}}}}$	$\tau_{\text{ign,Sim}_{T_{\text{Spray}}}}$	$\epsilon_{\text{rel},T_{\text{ad}}}$ [%]	$\epsilon_{\text{rel},T_{\text{Spray}}}$ [%]
n-Dodecane	0.628 $\pm$0.0280 ms	0.5520 ms	0.632 ms	-13.8	**0.6**
OME$_{\text{mix}}$	0.460 $\pm$0.029 ms	0.3800 ms	0.464 ms	-21.1	**0.9**
Injector	Woodward L'Orange				
Fuel	$\tau_{\text{ign,Exp}}$	$\tau_{\text{ign,Sim}_{T_{\text{ad}}}}$	$\tau_{\text{ign,Sim}_{T_{\text{Spray}}}}$	$\epsilon_{\text{rel},T_{\text{ad}}}$ [%]	$\epsilon_{\text{rel},T_{\text{Spray}}}$ [%]
n-Dodecane	0.5068 $\pm$0.0338 ms	0.5260 ms		3.6	
1-Octanol	0.8779 $\pm$0.0595 ms	0.7410 ms	0.851 ms	-18.5	**-3.2**

For 1-Octanol in subfigure (b) in Figure 7.1, the standard flamelet model fails to predict the correct ignition delay time. As shown in Table 7.1, the relative error in IDT for 1-Octanol with the standard flamelet model is around $-25\,\%$. From the analysis in Sec. 6.4, the high underestimation in IDT can be explained by the large deviations between the adiabatic mixing line and the temperature distribution in the spray. A high influence of heat loss due to evaporation is expected. The reactive spray simulation with the heat-loss corrected temperature profile achieves significantly improved results. The deviation to the experiment is reduced to around $-1\,\%$, perfect agreement is achieved.

For OME$_{\text{mix}}$ in subfigure (c), the ignition delay time as a global combustion metric shows reasonable agreement with the standard combustion model. However, the heat-loss corrected flamelet model for OME$_{\text{mix}}$ in Spray A3 halved the error to $5\,\%$. The heat-loss corrected flamelet model improved the results significantly and shows perfect alignment with the experiment.

The profile of the volume integrated $\widetilde{Y}_{\text{OH}}$ of OME$_{\text{mix}}$ in Figure 7.1 (c) reveals a significant difference to the profiles of n-Dodecane (a) and 1-Octanol (b). While the profiles of n-Dodecane and 1-Octanol show a steep increase of $\widetilde{Y}_{\text{OH}}$, OME$_{\text{mix}}$ shows a flatter slope until the maximum value is reached. In the ECN Spray A, also Mira et al. [112] observed lower values of $\widetilde{Y}_{\text{OH}}$ for OME$_{\text{mix}}$. The slope of OME$_{\text{mix}}$ suggests a high sensitivity toward experimental techniques utilizing a threshold for the determination of the IDT. A threshold technique might be inaccurate for fuels with a flat slope of the OH mass fraction.

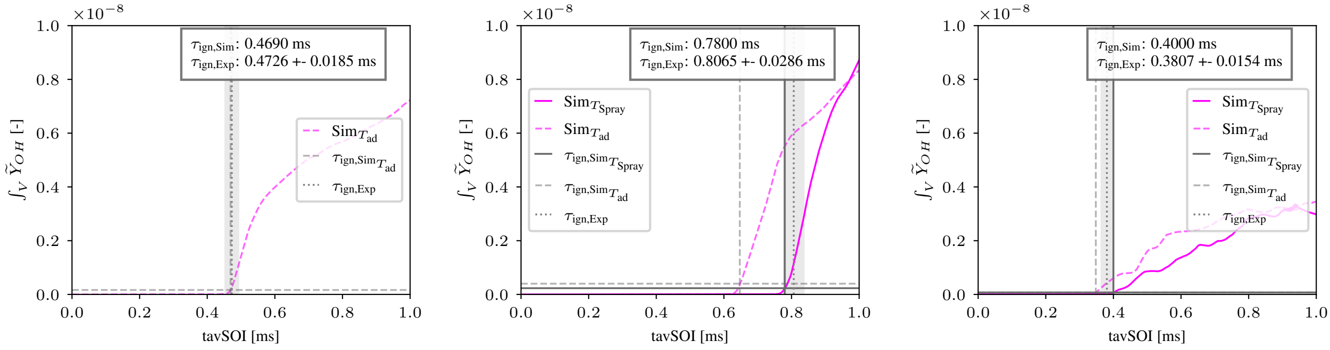

(a) n-Dodecane.

(b) 1-Octanol.

(c) $\mathrm{OME}_{\mathrm{mix}}$.

Figure 7.1: Comparison of the volume integrated $\widetilde{Y}_{\mathrm{OH}}$ signal for n-Dodecane (a), 1-Octanol (b) and $\mathrm{OME}_{\mathrm{mix}}$ (c) in ECN Spray A3. The spray ignition delay time is defined as $2\,\%(\int_V \widetilde{Y}_{\mathrm{OH}})_{\max}$. The comparison shows differences in the ignition delay time among the fuels for the standard flamelet model (dashed line) and the heat-loss corrected flamelet model (solid line). The heat-loss corrected flamelet model aligns excellently with the experimental ignition delay time.

7.1.2 Influence of the fuel on the ignition location

In spray flames, the formation of OH aligns with the flame front and is commonly used to compare experimental data and simulation results. The comparison of the ignition location based on the averaged OH^* chemiluminescence images and the line of sight integrated (LOSI) $\widetilde{Y}_{\mathrm{OH}}$ mixture fraction from the LES for Spray A3 in Figure 7.2 is used to validate the simulation framework. Further, the OH^* chemiluminescence distribution reveals more profound insight into the ignition location in the spray flame. In Figure 7.2, in each subfigure, the experimentally measured OH^* averaged and normalized signal intensity I is shown in the top row. The most consistent comparison in the LES is the line of sight integrated OH mass fraction, which is shown in the bottom row of each subfigure.

The comparison of n-Dodecane in Figure 7.2 (a) and 1-Octanol in Figure 7.2 (b) exhibit excellent agreement with the experimental data. The position and onset of the ignition is captured very well. The line of sight integrated $\widetilde{Y}_{\mathrm{OH}}$ is distributed slightly wider in the spray normal direction for n-Dodecane and 1-Octanol, which could be attributed to the kinetic mechanism used [91, 113, 225]. In contrast to n-Dodecane, the ignition location in spray direction, also known as lift-off length (LOL), for 1-Octanol is observed further downstream in the LES. The LOSI signal of $\mathrm{OME}_{\mathrm{mix}}$ exhibits good agreement with the experiment. Especially the onset of ignition is captured well. A slight shift downstream of the ignition position is observed. Experiments and simulations show a narrower distribution for $\mathrm{OME}_{\mathrm{mix}}$ compared to the other fuels. This finding is in line with experimental and numerical studies [82, 112].

All fuels investigated in Spray A3 exhibit the typical onset of ignition at the spray tip on the spray centerline. This finding aligns with the other studies in the literature and is an important characteristic for automotive injectors [59, 85, 90, 96, 101, 102, 112, 113]. Considering the strong influence of the used kinetic mechanism on the lift-off length [91, 113, 225], overall excellent agreement between experiment and simulation is achieved.

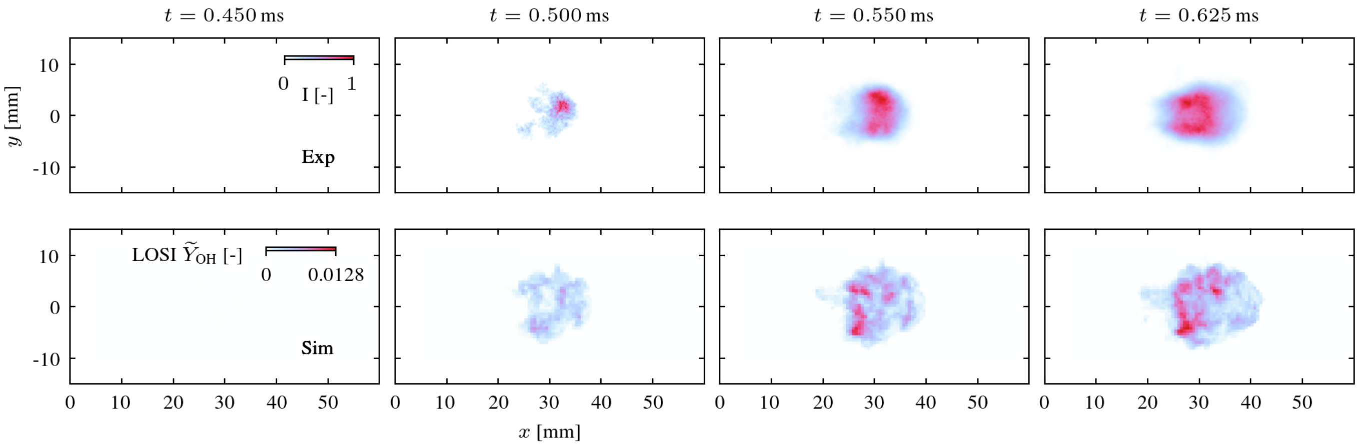

(a) n-Dodecane.

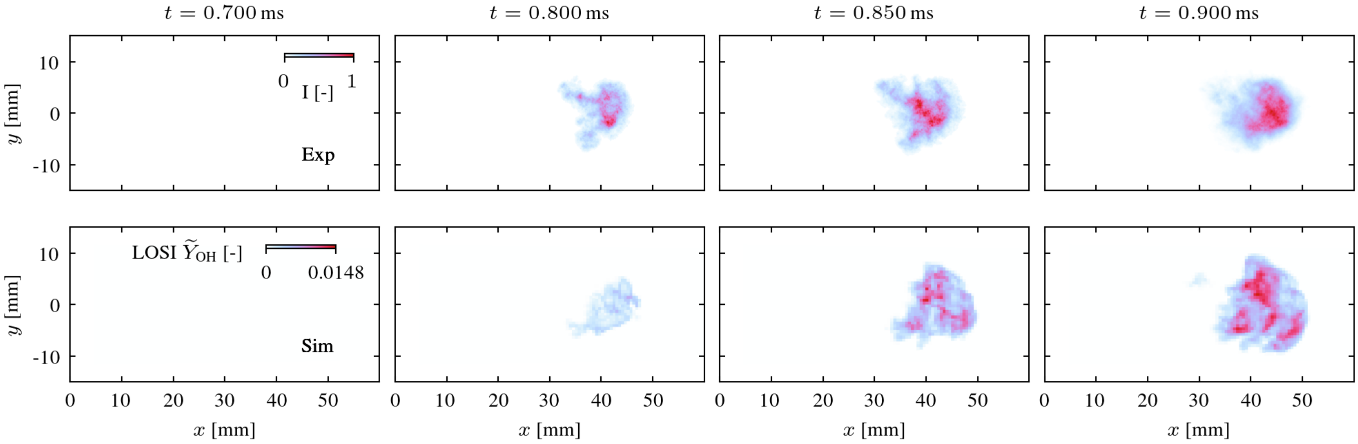

(b) 1-Octanol.

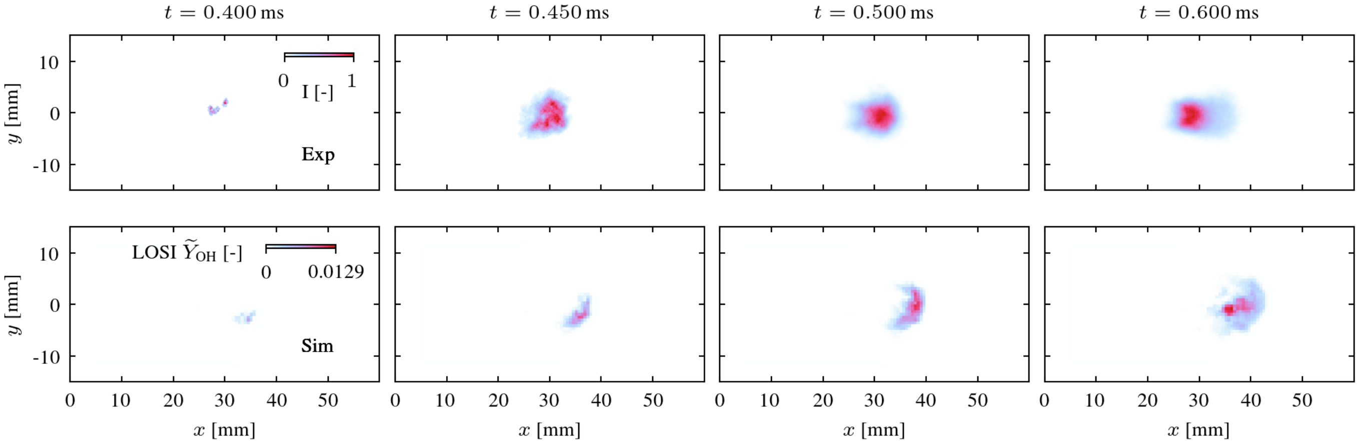

(c) OME$_{\mathrm{mix}}$.

Figure 7.2: Comparison of reactive Large Eddy Simulation results towards experimental data for n-Dodecane (a), 1-Octanol (b) and OME$_{\mathrm{mix}}$ (c) in ECN Spray A3. The top rows of each subfigure show the averaged normalized signal intensity of OH* chemiluminescence. In the bottom rows, the instantaneous line-of-sight integrated Favre-filtered OH mass fraction $\widetilde{Y}_{\mathrm{OH}}$ is shown for comparison. The spatial structure of ignition is captured very well by the LES for n-Dodecane, 1-Octanol and OME$_{\mathrm{mix}}$.

7.1.3 Spray flame structure in physical space

The ignition process of the different fuels is now elucidated based on the Favre-filtered fields of the temperature, CH_2O and OH mass fractions, the mixture fraction and the scalar dissipation rate at stoichiometry on the center plane of the spray. In Fig. 7.3-Figure 7.5, the first row is the Favre-filtered temperature field $\widetilde{T}$ (a) close before and after the onset of ignition. In the second row, the mass fraction of CH_2O ($\widetilde{Y}_{\mathrm{CH2O}}$) as the low-temperature ignition marker and the mass fraction of the high-temperature ignition marker OH ($\widetilde{Y}_{\mathrm{OH}}$) (b) are shown. The third row shows the Favre-filtered mixture fraction field $\widetilde{Z}$ (c) and the fourth row the scalar dissipation rate at stoichiometry $\widetilde{\chi}_{\mathrm{st}}$ (d). In all subfigures, the iso-line of the stoichiometric mixture fraction is shown as a gray line. This analysis delivers a comprehensive insight into the ignition process, which is not accessible by the experimental data available.

The ignition process of n-Dodecane is elucidated using the LES results in Figure 7.3. As described in Dahms et al. [210], the cool flame marked by the formation of $\widetilde{Y}_{\mathrm{CH2O}}$ (b) starts in the fuel-rich parts of the spray at $t{=}0.4\,\mathrm{ms}$. At the corresponding mixture fraction, an increase in the temperature field (a) is observed. At $t{=}0.450\,\mathrm{ms}$, the onset of main ignition is exhibited with the consumption of CH_2O (b) (opaque region at the tip). In the subsequent time step at $t{=}0.500\,\mathrm{ms}$, the formation of OH (b) is observed at the spray head, which is accompanied by high temperatures (a). The ignition over the spray head aligns with regions with a very homogenous mixture fraction field, and low scalar dissipation rates at stoichiometry.

Compared to n-Dodecane, the ignition of 1-Octanol in Figure 7.4 is shifted towards later times ($t{=}0.78\,\mathrm{ms}$). In Figure 5.2, the outline ($\widetilde{Z}_{\mathrm{iso}} = 0.001$) of the spray was comparable to that of n-Dodecane, while the Z_{st} iso-line in Figure 7.4 exhibits a slightly narrower spray due to the higher stoichiometric mixture fraction. As also observed in the mixture formation analysis in Sec. 5, the spray of 1-Octanol shows significantly lower temperatures (a) than n-Dodecane. The scalar dissipation rate (d) at the spray tip shows higher values than n-Dodecane at the same time steps, inhibiting the ignition process. At $t{=}0.75\,\mathrm{ms}$, first ignition kernels are observed at the spray tip.

The spray of $\mathrm{OME_{mix}}$ in Figure 7.5, shows a significantly different shape compared to n-Dodecane and 1-Octanol. The contour formed by the Z_{st} iso-line is notably narrower due to the high mixture fraction at stoichiometry ($Z_{\mathrm{st}}{=}0.1083$) and the slightly narrower spray outline observed in Figure 5.2. Higher values of the mixture fraction and the scalar dissipation rate at stoichiometry (d) are found, which aligns with the results in Figure 5.16. The iso-line of Z_{st} is not closed, as exhibited for the other sprays. At $t{=}0.35\,\mathrm{ms}$, a detached cloud of small fuel-rich isles is shown, which is also reported in Mira et al. [112]. Despite the higher scalar dissipation rates, the onset of ignition is located at the position of the detached isle of fuel-rich mixture. Hence, the typical ignition over the spray head is also observed for $\mathrm{OME_{mix}}$. All fuels show the typical cool flame propagation behavior.

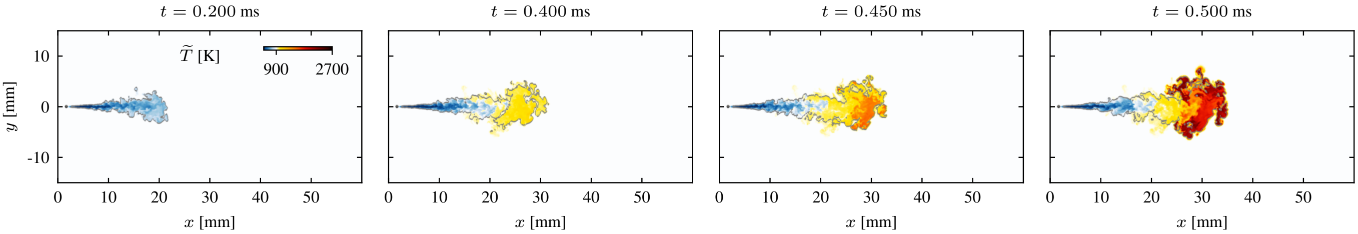

(a) Favre-filtered temperature: $\widetilde{T}$.

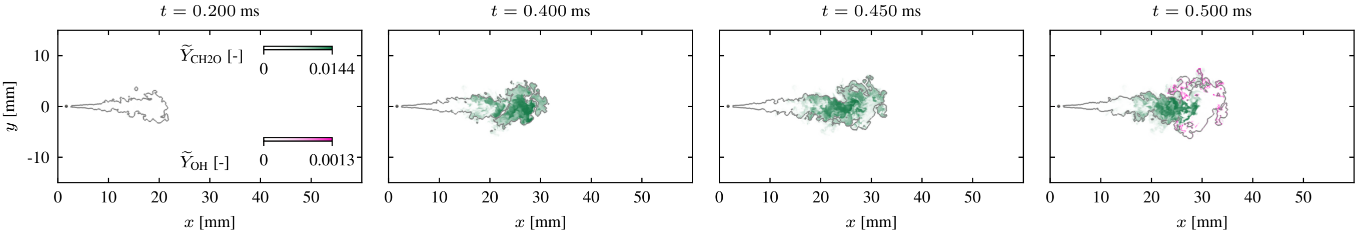

(b) Favre-filtered mass fractions of CH_2O and OH: $\widetilde{Y}_{\mathrm{CH2O}}$ & $\widetilde{Y}_{\mathrm{OH}}$.

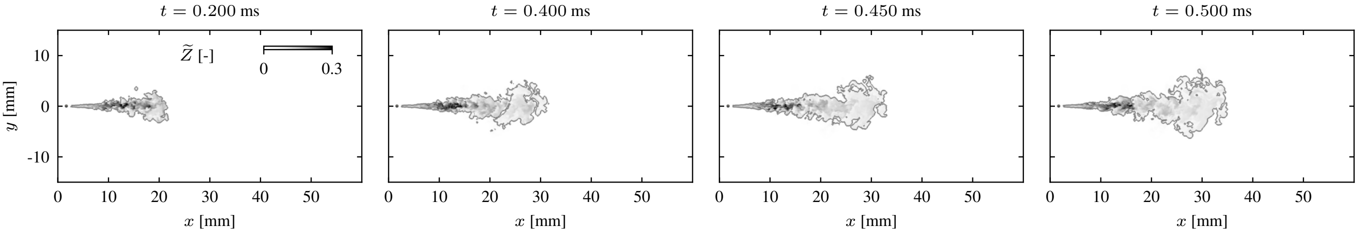

(c) Favre-filtered mixture fraction: $\widetilde{Z}$.

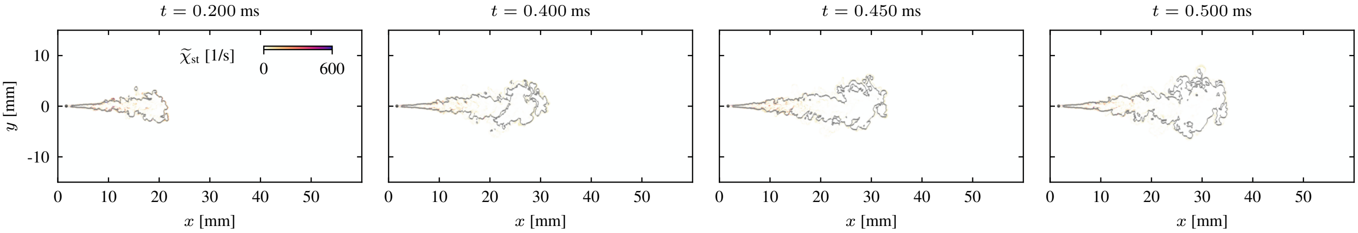

(d) Favre-filtered scalar dissipation rate at stoichiometry: $\widetilde{\chi}_{\mathrm{st}}$.

Figure 7.3: Comparison of $\widetilde{T}$ (a), $\widetilde{Y}_{\mathrm{CH2O}}$ & $\widetilde{Y}_{\mathrm{OH}}$ (b), $\widetilde{Z}$ (c) and $\widetilde{\chi}_{\mathrm{st}}$ (d) fields of the reactive n-Dodecane Spray A3 simulation. The gray line represents the iso-line of Z_{st}. The comparison gives deeper insight into the ignition process. The ignition over the spray head, typical for ECN Spray A is shown in the temperature and $\widetilde{Y}_{\mathrm{OH}}$ fields.

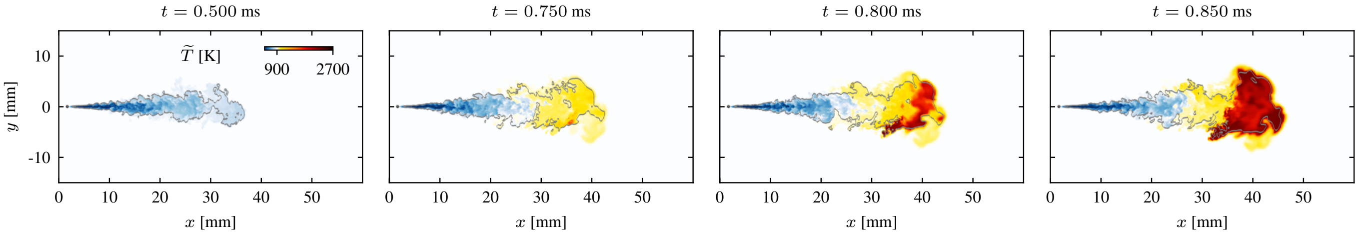

(a) Favre-filtered temperature: $\widetilde{T}$.

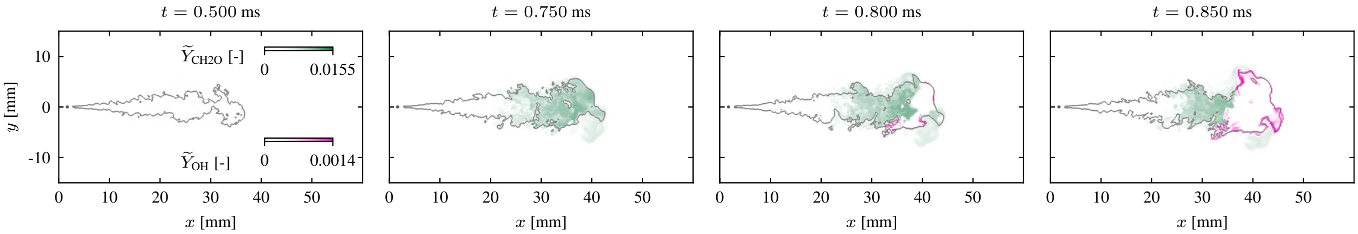

(b) Favre-filtered mass fractions of CH_2O and OH: $\widetilde{Y}_{\mathrm{CH2O}}$ & $\widetilde{Y}_{\mathrm{OH}}$.

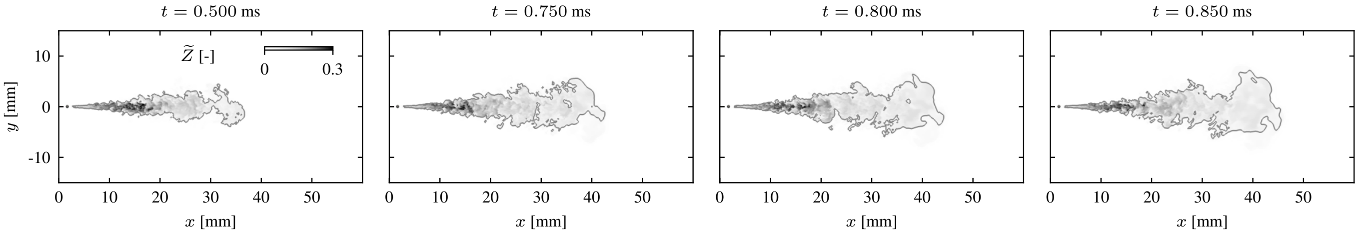

(c) Favre-filtered mixture fraction: $\widetilde{Z}$.

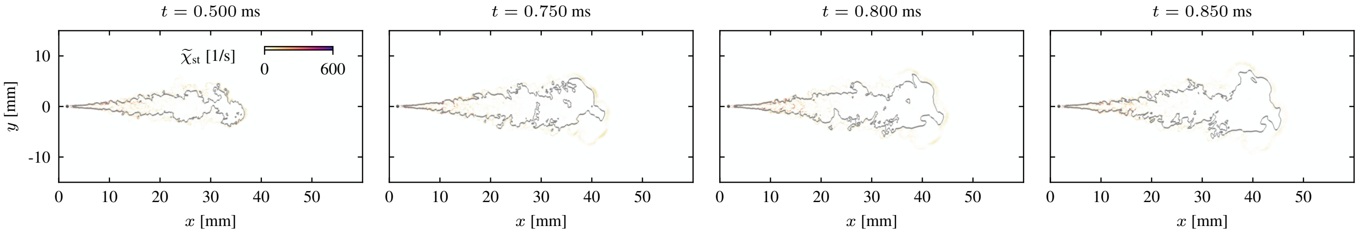

(d) Favre-filtered scalar dissipation rate at stoichiometry: $\widetilde{\chi}_{\mathrm{st}}$.

Figure 7.4: Comparison of $\widetilde{T}$ (a), $\widetilde{Y}_{\mathrm{CH2O}}$ & $\widetilde{Y}_{\mathrm{OH}}$ (b), $\widetilde{Z}$ (c) and $\widetilde{\chi}_{\mathrm{st}}$ (d) fields of the reactive 1-Octanol Spray A3 simulation. The gray line represents the iso-line of Z_{st}. The comparison gives deeper insight into the ignition process. The ignition over the spray head, typical for ECN Spray A is shown in the temperature and $\widetilde{Y}_{\mathrm{OH}}$ fields.

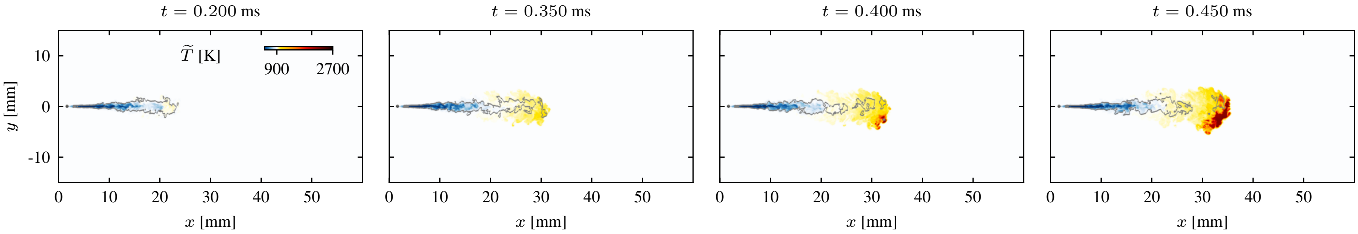

(a) Favre-filtered temperature: $\widetilde{T}$.

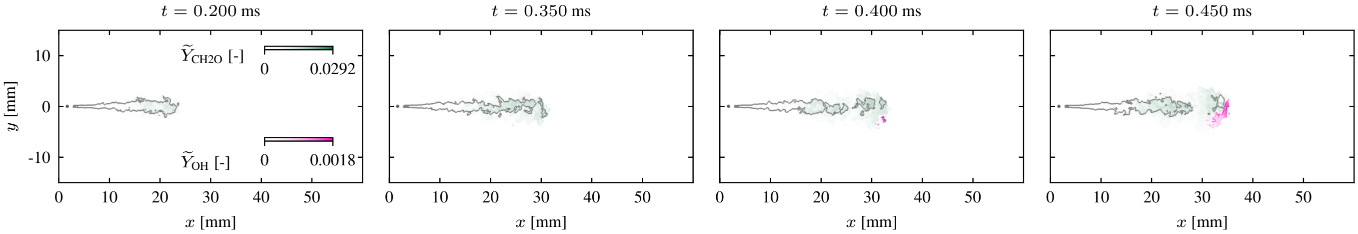

(b) Favre-filtered mass fractions of CH_2O and OH: $\widetilde{Y}_{\mathrm{CH2O}}$ & $\widetilde{Y}_{\mathrm{OH}}$.

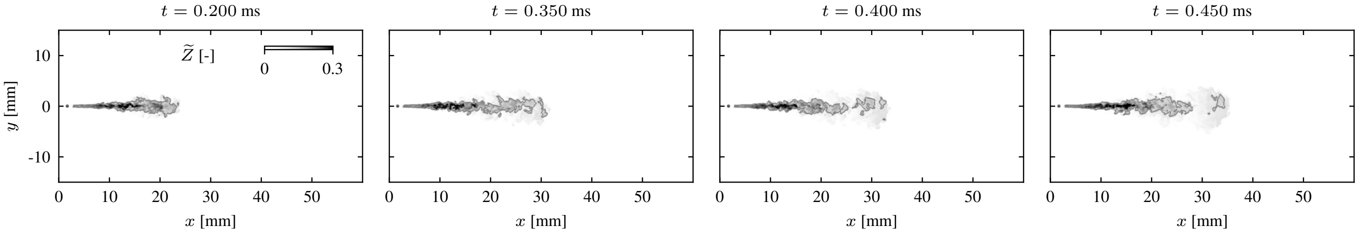

(c) Favre-filtered mixture fraction: $\widetilde{Z}$.

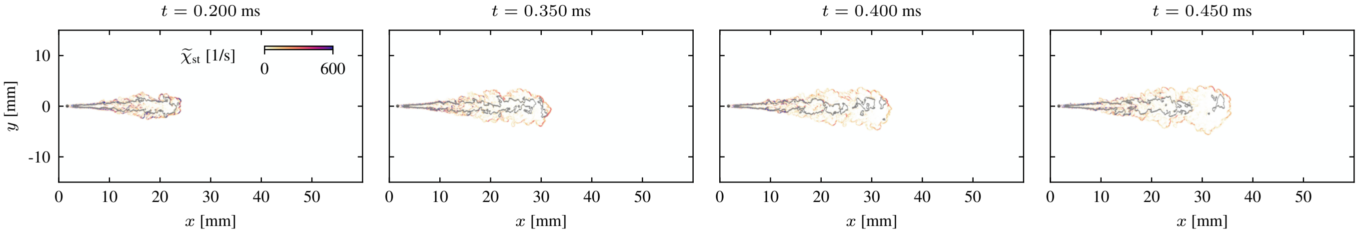

(d) Favre-filtered scalar dissipation rate at stoichiometry: $\widetilde{\chi}_{\mathrm{st}}$.

Figure 7.5: Comparison of $\widetilde{T}$ (a), $\widetilde{Y}_{\mathrm{CH2O}}$ & $\widetilde{Y}_{\mathrm{OH}}$ (b), $\widetilde{Z}$ (c) and $\widetilde{\chi}_{\mathrm{st}}$ (d) fields of the reactive $\mathrm{OME}_{\mathrm{mix}}$ Spray A3 simulation. The gray line represents the iso-line of Z_{st}. The comparison gives deeper insight into the ignition process. The ignition over the spray head, typical for ECN Spray A is shown in the temperature and $\widetilde{Y}_{\mathrm{OH}}$ fields.

7.1.4 Spray flame structure in mixture fraction space

The flame structure analysis is now conducted in mixture fraction space. In Figure 7.6-Figure 7.8, the subfigures (a) show the Favre-filtered temperature $\widetilde{T}$ in physical coordinates for a better understanding of the results in mixture fraction space. The analysis in mixture fraction space is shown in subfigures (b). The temperature scatters are colored in their respective distance to the nozzle in the spray direction (y-direction) in the first row and as the distance from the spray centerline (x-direction) in the second row. This method allows visualizing the location of ignition in mixture fraction space. The Favre-filtered mass fractions of $\widetilde{Y}_{\mathrm{CH2O}}$ and $\widetilde{Y}_{\mathrm{OH}}$ as the marker for low and high-temperature ignition are colored by the distance to the nozzle (y-direction) and are plotted in the third and fourth row in subfigures (b).

The temperature distribution of the reactive n-Dodecane Spray A3 is shown in Figure 7.6. The distribution in mixture fraction space in subfigure (b) reveals that the ignition of n-Dodecane starts in fuel-rich mixtures with the formation of CH_2O. At $t = 0.450\,\mathrm{ms}$, the formation of hydroxyl radicals is visible close to stoichiometry in the fuel-rich part. The production of OH aligns with the consumption of CH_2O and the onset of main ignition. The highest temperatures are now observed at the stoichiometric mixture fraction. The temperature scatters show that ignition starts at the spray tip and near the spray centerline. The analysis of the spray flame structure in mixture fraction space reflects the flame structure observed in the flamelet simulation.

The spray flame analysis for 1-Octanol in mixture fraction space is presented in Figure 7.7. Compared to n-Dodecane, more scatters are observed at lower temperatures in the fuel-rich region in Figure 7.7 (b). The onset of a significant temperature increase is observed at $t = 0.6\,\mathrm{ms}$, approximately $0.2\,\mathrm{ms}$ later than n-Dodecane. In contrast to n-Dodecane, more high-temperature scatters are located further away from the spray axis (second row in Figure 7.7 (b)). But the main ignition occurs at the spray head on the spray center line. The broader ignition distribution for 1-Octanol is also visible in the OH^* chemiluminescence signal, discussed in Sec. 7.1.2.

The analysis of $\mathrm{OME_{mix}}$ in mixture fraction space in Figure 7.8, reveals a significantly different spray flame structure. The contour formed by the Z_{st} iso-line in Figure 7.8 (a) is notably narrower due to the high stoichiometric mixture fraction of $Z_{\mathrm{st}} = 0.1083$. In contrast to the other fuels, the iso-line of Z_{st} is not enclosed.

In Figure 7.8 (b), scatters are found at higher values of the mixture fraction for $\mathrm{OME_{mix}}$ (up to $\widetilde{Z} = 0.4$), which aligns with the results in Figure 5.16. At $t = 0.35\,\mathrm{ms}$, a detached cloud of small fuel-rich isles is shown in Figure 7.8 (a), which is also reported in Mira et al. [112]. Despite the higher scalar dissipation rates observed in Figure 7.5 (d), the onset of ignition is located at the position of the detached isles of the fuel-rich mixtures, which confirms the typical ignition over the spray head for $\mathrm{OME_{mix}}$ (see also first row of Figure 7.8 (b)).

After the ignition at $t = 0.45\,\mathrm{ms}$ in Figure 7.8 (b), the flame structure of $\mathrm{OME_{mix}}$ in mixture fraction space exhibits only high temperatures in lean mixtures, which is unique for $\mathrm{OME_{mix}}$ in Spray A3. The high temperatures in lean mixtures are also confirmed in Figure 7.8 (a) at $t = 1.0\,\mathrm{ms}$. In contrast to the other fuels, this reduces the formation of $\widetilde{Y}_{\mathrm{OH}}$ in Figure 7.7 (b) significantly. This finding explains the results from Figure 7.1 (c), where also lower values of the volume integrated OH mass fraction were found. A similar flame structure in mixture fraction space shown in this work has also been reported for Spray A in Mira et al. [112].

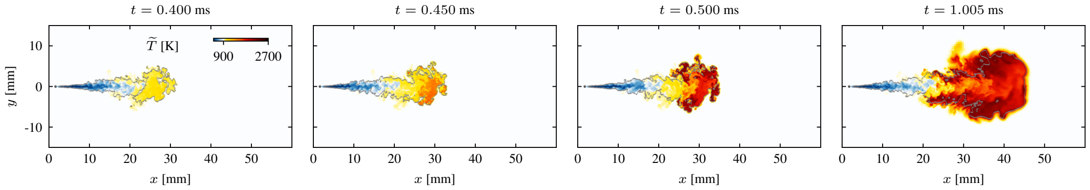

(a) Favre-filtered temperature field in physical space: $\widetilde{T}$.

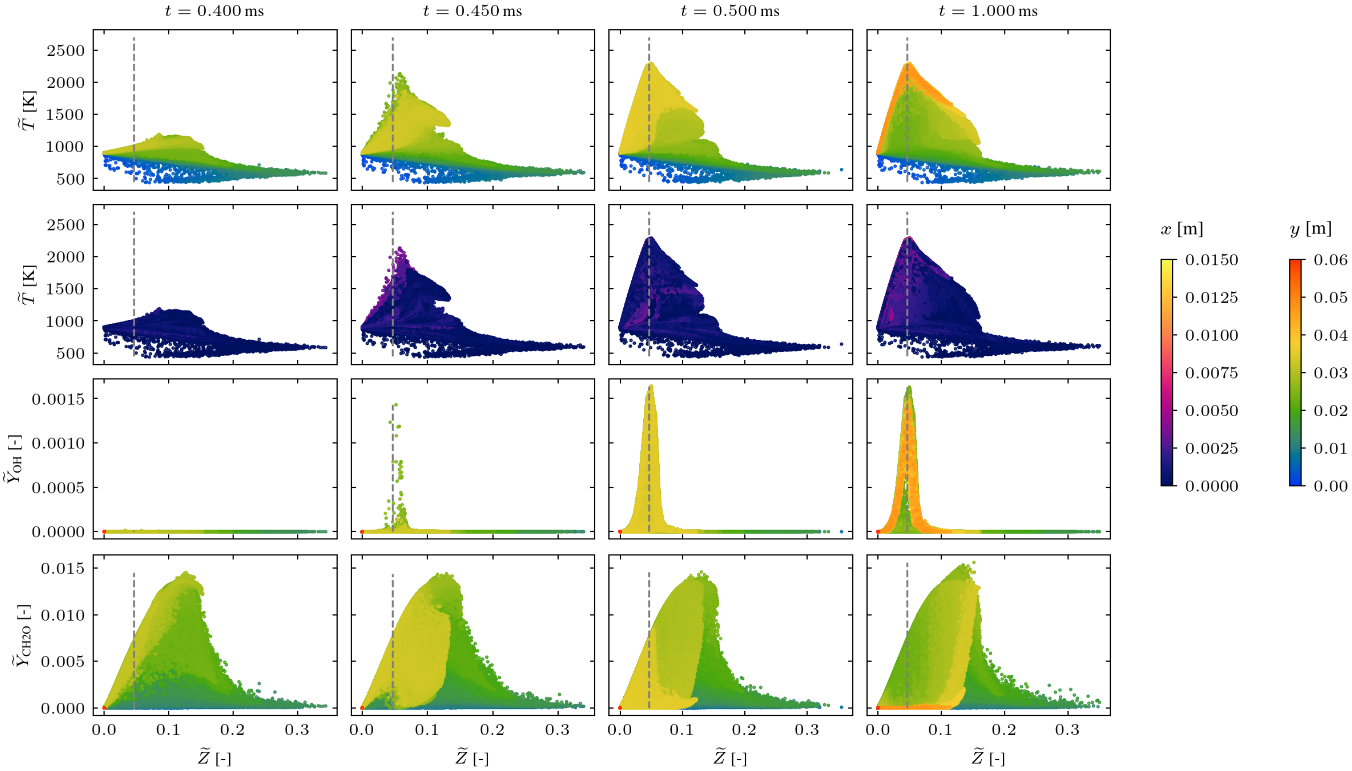

(b) Spray flame structure in mixture fraction space.

Figure 7.6: Spray flame structure analysis of n-Dodecane for the ECN Spray A3 injector. In subfigure (a), the filtered temperature field in physical space is shown for comparison. The top row in (b) shows the Favre-filtered temperature $\widetilde{T}$ colored as the distance in y-direction from the nozzle, and the second row is colored as the distance in x-direction. The third and fourth rows are the Favre-filtred mass fractions of OH and CH_2O colored as the distance from the nozzle in y-direction.

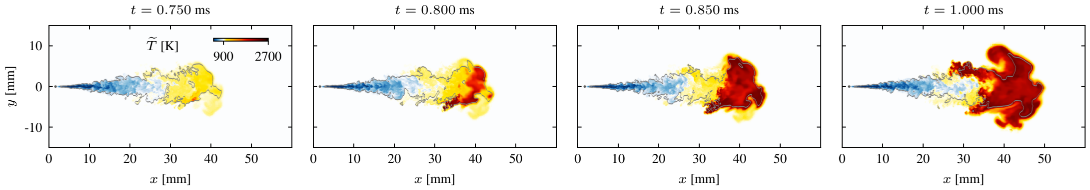

(a) Favre-filtered temperature field in physical space: $\widetilde{T}$.

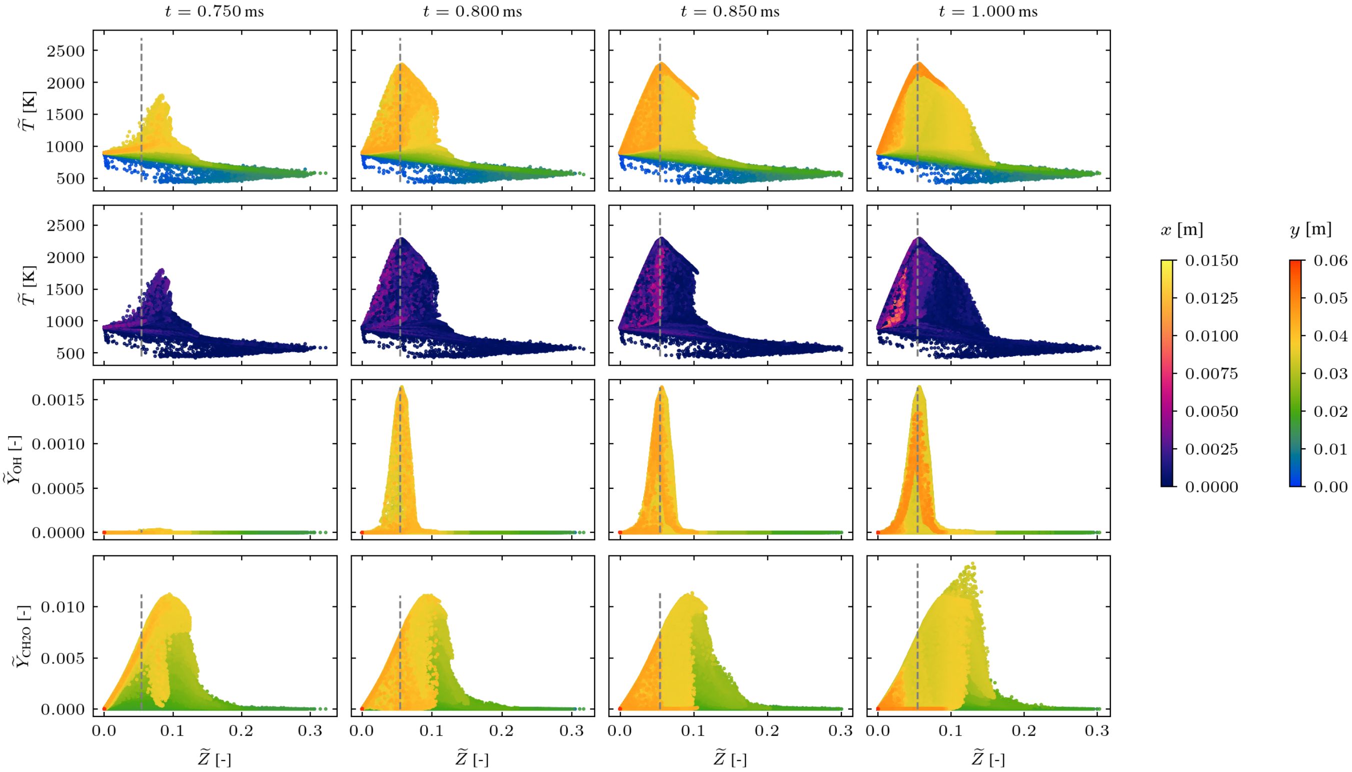

(b) Spray flame structure in mixture fraction space.

Figure 7.7: Spray flame structure analysis of 1-Octanol for the ECN Spray A3 injector. In subfigure (a), the filtered temperature field in physical space is shown for comparison. The top row in (b) shows the Favre-filtered temperature $\widetilde{T}$ colored as the distance in y-direction from the nozzle, and the second row is colored as the distance in x-direction. The third and fourth rows are the Favre-filtred mass fractions of OH and CH_2O colored as the distance from the nozzle in y-direction.

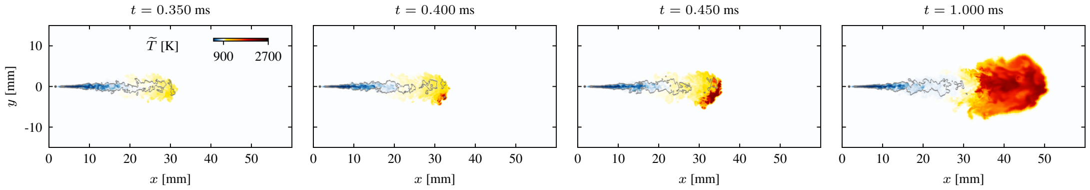

(a) Favre-filtered temperature field in physical space: $\widetilde{T}$.

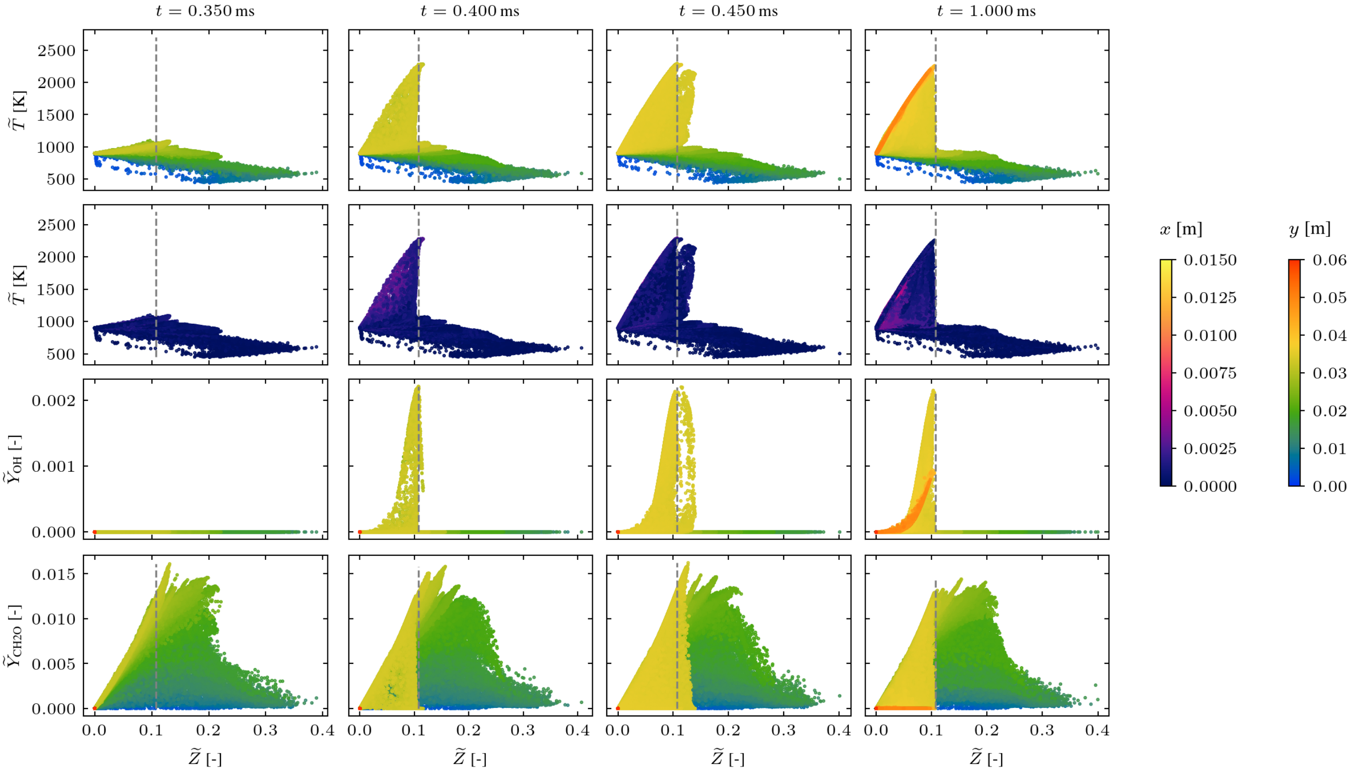

(b) Spray flame structure in mixture fraction space.

Figure 7.8: Spray flame structure analysis of $\mathrm{OME_{mix}}$ for the ECN Spray A3 injector. In subfigure (a), the filtered temperature field in physical space is shown for comparison. The top row in (b) shows the Favre-filtered temperature $\widetilde{T}$ colored as the distance in y-direction from the nozzle, and the second row is colored as the distance in x-direction. The third and fourth rows are the Favre-filtred mass fractions of OH and CH_2O colored as the distance from the nozzle in y-direction.

7.2 Heavy-duty injector: ECN Spray D

In the following, the simulation results for the reactive ECN Spray D simulation are presented. The comparison between n-Dodecane and $\mathrm{OME_{mix}}$ is drawn based on different combustion metrics.

7.2.1 Influence of latent heat of evaporation on ignition

The comparison of the experimental ignition delay time and the volume integrated OH mass fraction for the ECN Spray D in Figure 7.9 reveals significant differences to Spray A3. The experimental ignition delay time for n-Dodecane in subfigure (a) is approximately $30\,\%$ later compared to the IDT in Spray A3. As shown in the mixture formation analysis in Figure 5.14, the evaporation process is delayed. Consecutive, the mixture formation process takes longer until ignitable mixtures are present. Furthermore, the higher injected mass in Spray D also leads to a lower temperature distribution (see Figure 6.9), and ignitable fluid particles need more time for ignition.

The simulation incorporating the heat-loss corrected flamelet model for n-Dodecane shows excellent agreement with the experimental IDT. However, the standard flamelet model underestimates the IDT by roughly $10\,\%$. This finding suggests that the later IDT in Spray D for n-Dodecane is mostly attributed to a different mixture formation process than in Spray A3.

For OME$_{\text{mix}}$ in subfigure (b) of Figure 7.9, the experimental IDT is only approximately $20\,\%$ longer than in Spray A3. The reactive spray simulation with the standard flamelet model exhibits an IDT of approximately $0.38\,\text{ms}$, which is identical to the IDT discovered in Spray A3 conditions. The temperature-corrected flamelet model for OME$_{\text{mix}}$ aligns perfectly with the experimental IDT of $0.46\,\text{ms}$. It can be concluded that the later ignition delay for OME$_{\text{mix}}$ in Spray D is, in contrast to n-Dodecane, mainly attributed to heat loss due to evaporation. This finding is supported by the analysis of the influence of the scalar dissipation rate on ignition in Figure 6.5, showing that OME$_{\text{mix}}$ does not exhibit a high sensitivity towards the scalar dissipation rate.

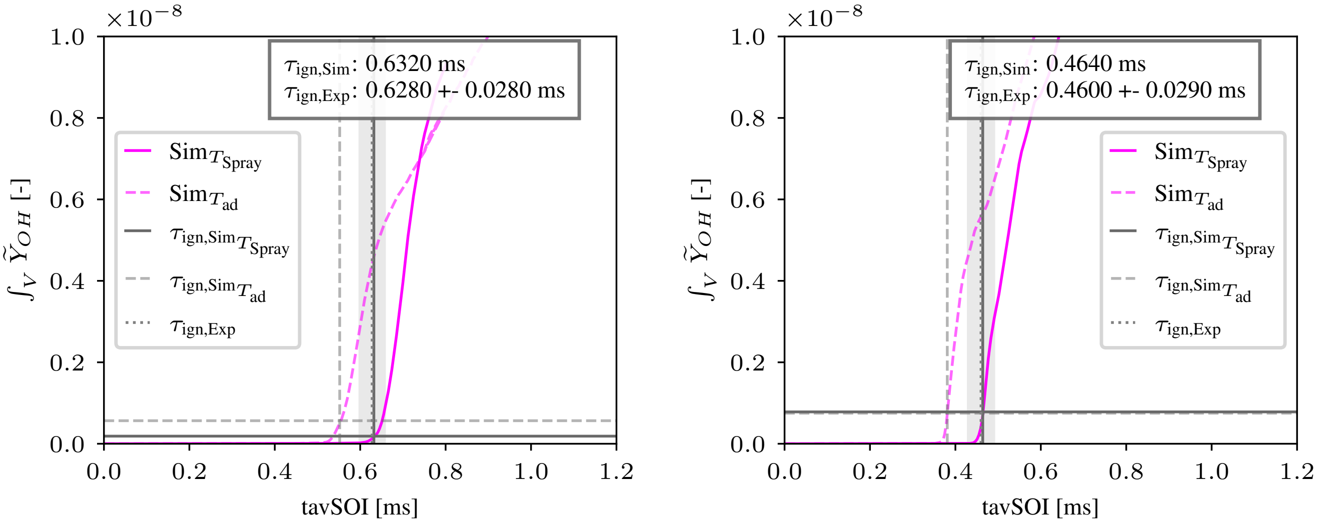

(a) n-Dodecane.

(b) OME$_{\text{mix}}$.

Figure 7.9: Comparison of the volume integrated $\widetilde{Y}_{\text{OH}}$ signal for n-Dodecane (a), and OME$_{\text{mix}}$ (b) in ECN Spray D. The spray ignition delay time is defined as $2\,\%(\int_V \widetilde{Y}_{\text{OH}})_{\text{max}}$. The comparison shows differences in the ignition delay time among the fuels for the standard flamelet model (dashed line) and the heat-loss corrected flamelet model (solid line). The heat-loss corrected flamelet model aligns excellently with the experimental ignition delay time.

7.2.2 Influence of the fuel on ignition location

The comparison of the experimental OH^* signal and the line of sight integrated Favre-filtered OH mass fraction in Figure 7.10 reveals insight into the ignition location for Spray D. The experimental data in Figure 7.10 has been provided by personal communication by one of the co-authors (José Maria Garcia) of Pastor et al. [82]. In Figure 7.10, the top row in each subfigure shows the experimental averaged and normalized OH^* signal intensity I and the bottom row shows the line of sight integrated $\widetilde{Y}_{\mathrm{OH}}$. For $\mathrm{OME}_{\mathrm{mix}}$, the normalization process at $t{=}0.45\,\mathrm{ms}$ causes a noisy image in subfigure (b).

In Figure 7.10 (a), the results for n-Dodecane are shown. The onset of ignition is captured excellently by the LES. Further, in line with experimental and simulation results in the literature [82, 93–95, 97, 140], the ignition of n-Dodecane in Spray D is observed at the spray flanks. The peaks of the LOSI $\widetilde{Y}_{\mathrm{OH}}$ are located at around $8\,\mathrm{mm}$ in the radial direction, which aligns well with the experimental OH^* signal. Also, the lift-off lengths of the experiment and simulation align very well.

In contrast, the results for $\mathrm{OME}_{\mathrm{mix}}$ in Figure 7.10 (b) show a significantly different distribution. The peaks of the OH^* signal and the LOSI $\widetilde{Y}_{\mathrm{OH}}$ are closer together in the radial direction than for n-Dodecane. Also, in the spray direction, the distribution of $\mathrm{OME}_{\mathrm{mix}}$ is more compact than for n-Dodecane. The experimental OH^* images in the top row also show a narrow distribution of the intensity for $\mathrm{OME}_{\mathrm{mix}}$ with ignition over the spray flanks. In the instantaneous LES in the bottom row, a distinction between the peaks at the flanks can be identified too, but the signals are very close together. The onset of ignition and lift-off length of the LES for $\mathrm{OME}_{\mathrm{mix}}$ align perfectly with the experimental data.

In contrast to the findings in Pastor et al. [82] (at $t{=}3.015\,\mathrm{ms}$), ignition over the spray flanks is also observed for $\mathrm{OME}_{\mathrm{mix}}$. The narrower distribution and ignition closer to the spray center axis for $\mathrm{OME}_{\mathrm{mix}}$ is explained with the doubled stoichiometric mixture fraction compared to the n-Dodecane of $Z_{\mathrm{st}}{=}0.1083$ and will be further discussed in Sec. 7.2.3. This finding is a novelty in this work and extends the understanding of spray flames with oxygenated fuels. Overall, perfect agreement of ignition location and the onset of ignition is observed for the reactive spray simulation.

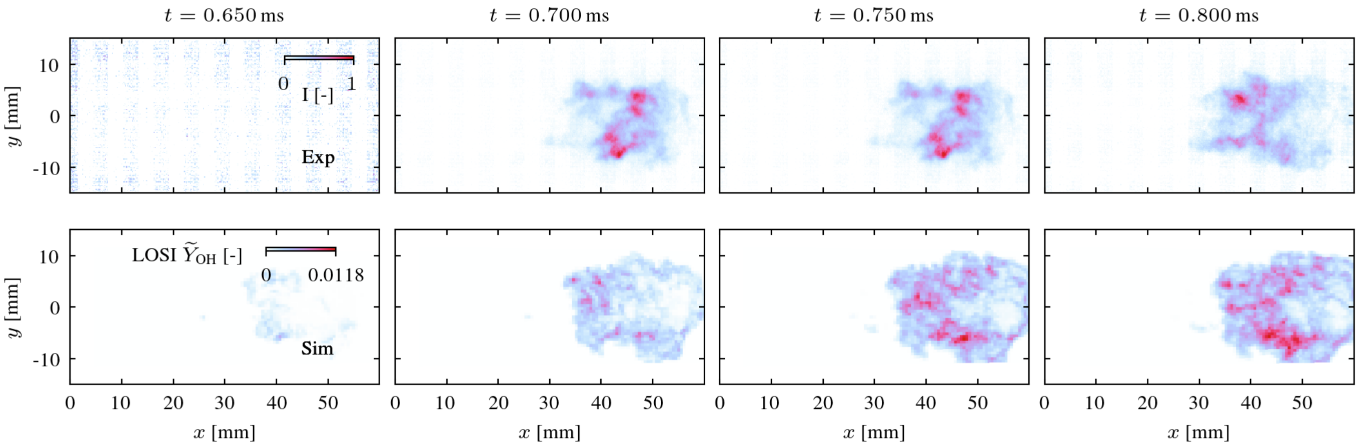

(a) n-Dodecane.

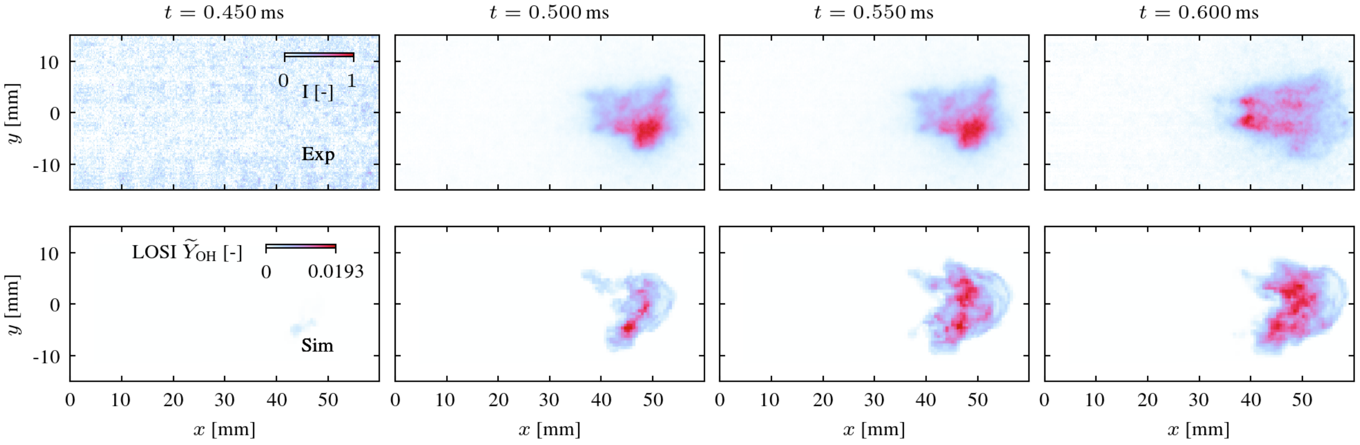

(b) $\mathrm{OME_{mix}}$.

Figure 7.10: Comparison of reactive Large Eddy Simulation results towards experimental data for n-Dodecane (a) and $\mathrm{OME_{mix}}$ (b) in the ECN Spray D [82]. The top rows of each subfigure, show the averaged normalized signal intensity of OH^* chemiluminescence. In the bottom rows, the instantaneous line-of-sight integrated Favre-filtered OH mass fraction $\widetilde{Y}_{\mathrm{OH}}$ is shown for comparison. The spatial structure of ignition is captured very well by the LES. The LOSI $\widetilde{Y}_{\mathrm{OH}}$ highlights the ignition over the spray flanks for n-Dodecane in (a). For $\mathrm{OME_{mix}}$ in (b), the high-intensity regions are closer together, which has also been observed in [82].

7.2.3 Spray flame structure in physical space

The spray flames of n-Dodecane and $\mathrm{OME_{mix}}$ in Spray D are now analyzed in physical space. In Figure 7.11, the ignition process of n-Dodecane is shown. The characteristic ignition over the spray flanks is clearly visible in the Favre-filtered temperature field (Figure 7.11 (a)) and the Favre-filtered mass fraction of OH (Figure 7.11 (b)). The mixture fraction field in subfigure (c) reveals that the ignition location at the spray flank exhibits significantly lower values of the mixture fraction compared to the spray tip. As shown in a flame regime analysis by Popp et al. [94], the same locations exhibit the low-temperature chemistry regime and successively high-temperature ignition in Spray D. The findings from Figure 5.6 show that, in comparison to Spray A3, the liquid penetration and vapor penetration align for a longer time. This mixing phenomenon leads to high mixture fractions and low temperatures on the spray center axis. In contrast, in Spray A3 (see Figure 5.2), the liquid and vapor penetration lengths separate faster. As a direct effect, in Spray A3, a fuel vapor cloud is pushed in front of the liquid spray that mixes with the hot ambient and creates an ignitable mixture at the spray head. In Spray D, however, air entrainment is found at the spray flanks.

The mixture formation of $\mathrm{OME}_{\mathrm{mix}}$ in Figure 7.12 exhibits a narrower spray due to the high stoichiometric mixture fraction. The ignition over the spray flanks, which has been observed in Figure 7.10 is clearly visible in the temperature (Figure 7.12 (a)) and $\widetilde{Y}_{\mathrm{OH}}$ (Figure 7.12 (b)) fields. The observation of lower scalar dissipation rates $\widetilde{\chi}_{\mathrm{st}}$ (d) at the spray flanks compared to the spray head for n-Dodecane is also found for $\mathrm{OME}_{\mathrm{mix}}$. However, for $\mathrm{OME}_{\mathrm{mix}}$ higher values of the mixture fraction (Figure 7.12 (c)) are observed at the spray flanks than for n-Dodecane. In contrast to Spray A3, in Spray D, the iso-line for $\mathrm{OME}_{\mathrm{mix}}$ of Z_{st} is enclosed, and no detached clouds of fuel-rich mixtures are observed.

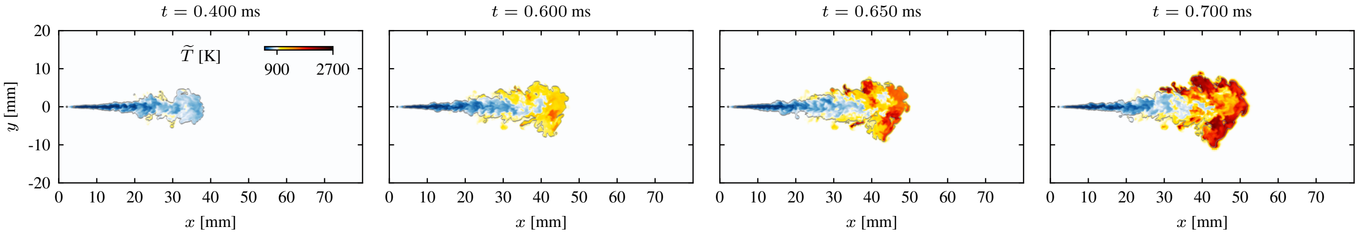

(a) Favre-filtered temperature: $\widetilde{T}$.

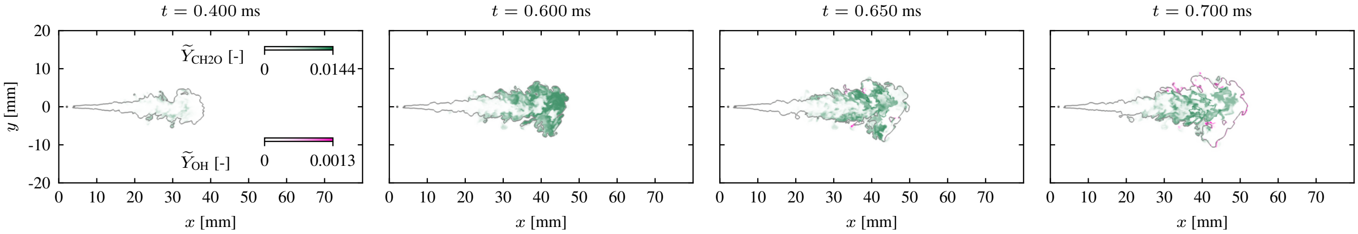

(b) Favre-filtered mass fractions of CH_2O and OH: $\widetilde{Y}_{\mathrm{CH2O}}$ & $\widetilde{Y}_{\mathrm{OH}}$.

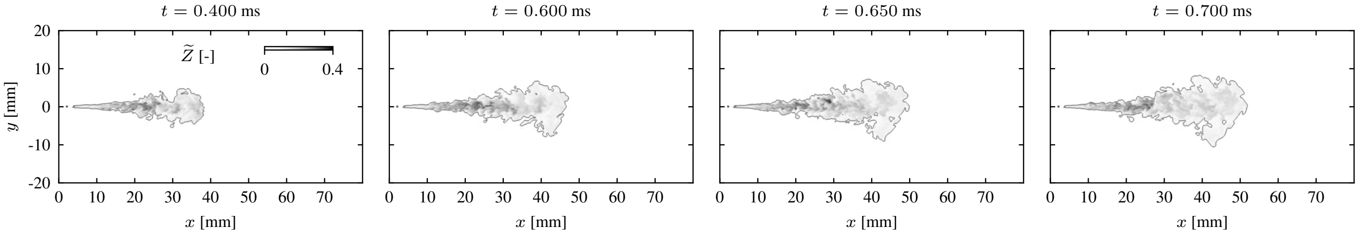

(c) Favre-filtered mixture fraction: $\widetilde{Z}$.

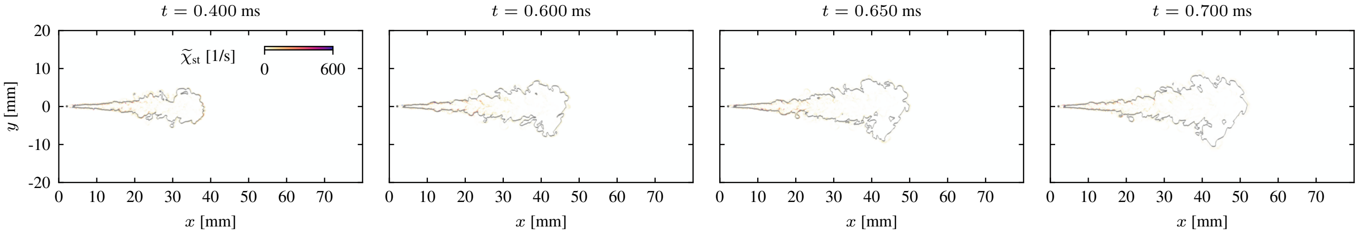

(d) Favre-filtered scalar dissipation rate at stoichiometry: $\widetilde{\chi}_{\mathrm{st}}$.

Figure 7.11: Comparison of $\widetilde{T}$ (a), $\widetilde{Y}_{\mathrm{CH2O}}$ & $\widetilde{Y}_{\mathrm{OH}}$ (b), $\widetilde{Z}$ (c) and $\widetilde{\chi}_{\mathrm{st}}$ (d) fields of the reactive n-Dodecane Spray D simulation. The gray line represents the iso-line of Z_{st}. The comparison gives deeper insight into the ignition process. The ignition over the spray flanks, typical for ECN Spray D, is shown in the temperature and the $\widetilde{Y}_{\mathrm{OH}}$ fields.

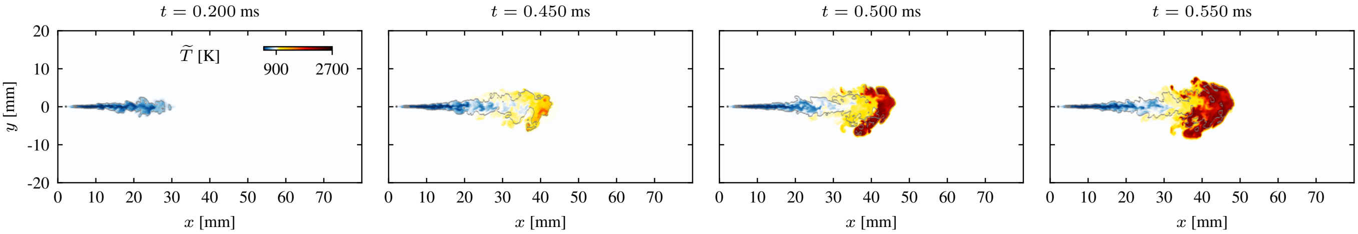

(a) Favre-filtered temperature: $\widetilde{T}$.

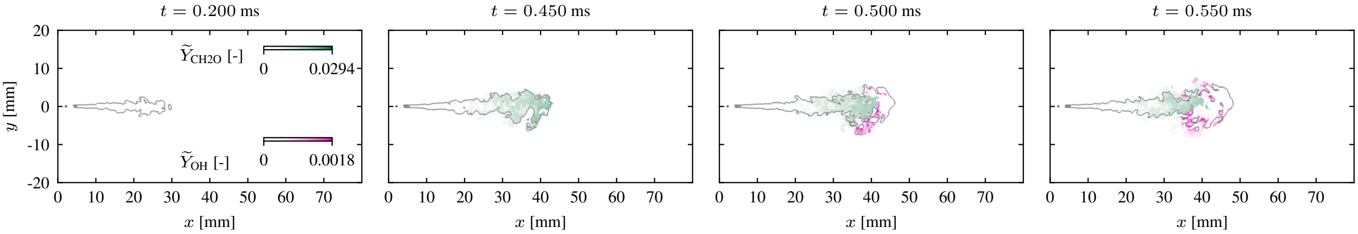

(b) Favre-filtered mass fractions of CH_2O and OH: $\widetilde{Y}_{\mathrm{CH2O}}$ & $\widetilde{Y}_{\mathrm{OH}}$.

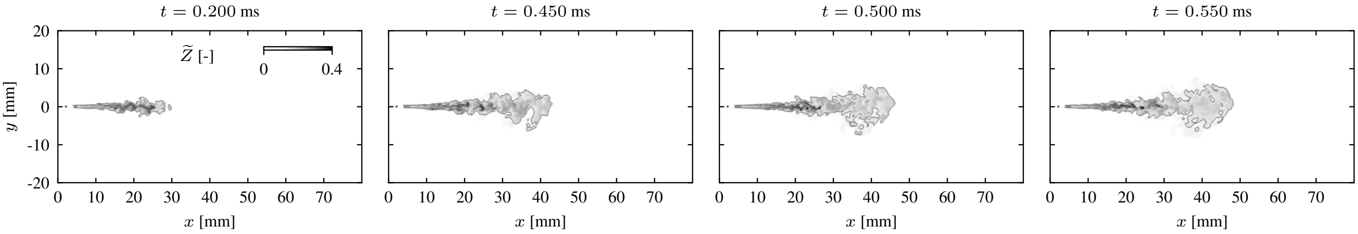

(c) Favre-filtered mixture fraction: $\widetilde{Z}$.

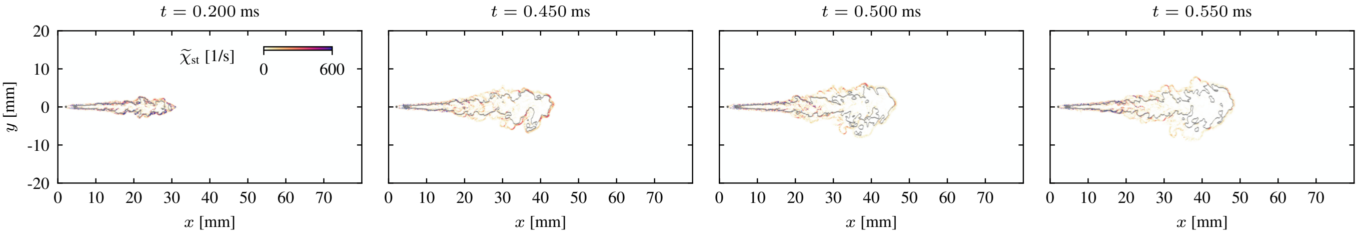

(d) Favre-filtered scalar dissipation rate at stoichiometry: $\widetilde{\chi}_{\mathrm{st}}$.

Figure 7.12: Comparison of $\widetilde{T}$ (a), $\widetilde{Y}_{\mathrm{CH2O}}$ & $\widetilde{Y}_{\mathrm{OH}}$ (b), $\widetilde{Z}$ (c) and $\widetilde{\chi}_{\mathrm{st}}$ (d) fields of the reactive $\mathrm{OME}_{\mathrm{mix}}$ Spray D simulation. The gray line represents the iso-line of Z_{st}. The comparison gives deeper insight into the ignition process. The ignition over the spray flanks, typical for ECN Spray D, is shown in the temperature and the $\widetilde{Y}_{\mathrm{OH}}$ fields.

7.2.4 Spray flame structure in mixture fraction space

The flame structure analysis in mixture fraction space in Figure 7.13 and Figure 7.14 provides a comprehensive insight into the ignition process of Spray D. In subfigures (a), the temperature distribution in physical coordinates is shown for a better understanding of the results in mixture fraction space. The ignition is examined with the temperature distribution colored in the spray direction (y) in the first row, and spray normal direction (x) in the second row in subfigures (b).

For n-Dodecane, the onset of ignition at t=0.65 ms in Figure 7.13 (b) clearly shows that the hottest scatters are not at the spray tip, but at the spray flanks. This aligns with the findings made in the previous sections

(Sec. 7.2.2 and Sec. 7.2.3). The analysis in mixture fraction space reveals that the onset of ignition is approximately at the same mixture fraction $\widetilde{Z}=0.1$ as observed in Spray A3, while in Spray A3 the ignition starts at the spray head and in Spray D at the spray flanks. It can be concluded that the mixture formation process in Spray D is significantly different than in Spray A3. This finding is supported by the results made in Popp et al. [94].

After ignition has occurred at $t=0.65\,\mathrm{ms}$, the spray head of n-Dodecane is also ignited. At $t=1.0\,\mathrm{ms}$ ignited scatters are found distributed in y and x direction in Figure 7.13 (b). The ignited spray head is also visible in Figure 7.13 (a). At $t=1.0\,\mathrm{ms}$, the cool flame propagation becomes visible. In the region where $\widetilde{Y}_{\mathrm{OH}}$ is produced, formaldehyde $\widetilde{Y}_{\mathrm{CH2O}}$ is consumed.

The analysis for $\mathrm{OME}_{\mathrm{mix}}$ in Figure 7.14 confirms the findings from the analysis in physical space in Sec. 7.2.3. The ignition occurs in a smaller area around the spray center line. The separation between ignition over the spray head or spray flanks in the first and second row of Figure 7.14 (b) is not pronounced in mixture fraction space. Hot scatters in the x direction (second row) in Figure 7.14 (b) reveal that the ignition over the spray flanks is mainly present in fuel-lean conditions. However, the onset of ignition at $t=0.4\,\mathrm{ms}$ is found at fuel-rich conditions at $\widetilde{Z}=0.2$. This finding contrasts the classical cool flame propagation [210] observed in Spray A3. The scatters in fuel-lean conditions during ignition suggest that in Spray D with $\mathrm{OME}_{\mathrm{mix}}$, the influence of the premixed combustion regime is more pronounced [226].

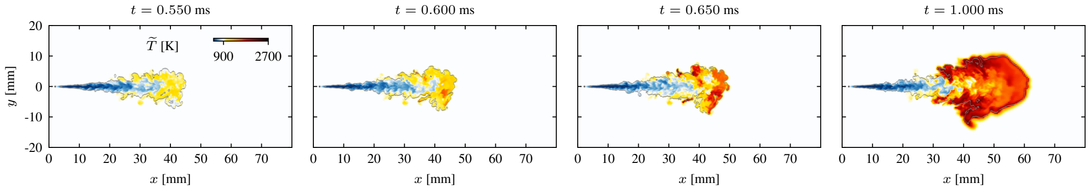

(a) Favre-filtered temperature field in physical space: $\widetilde{T}$.

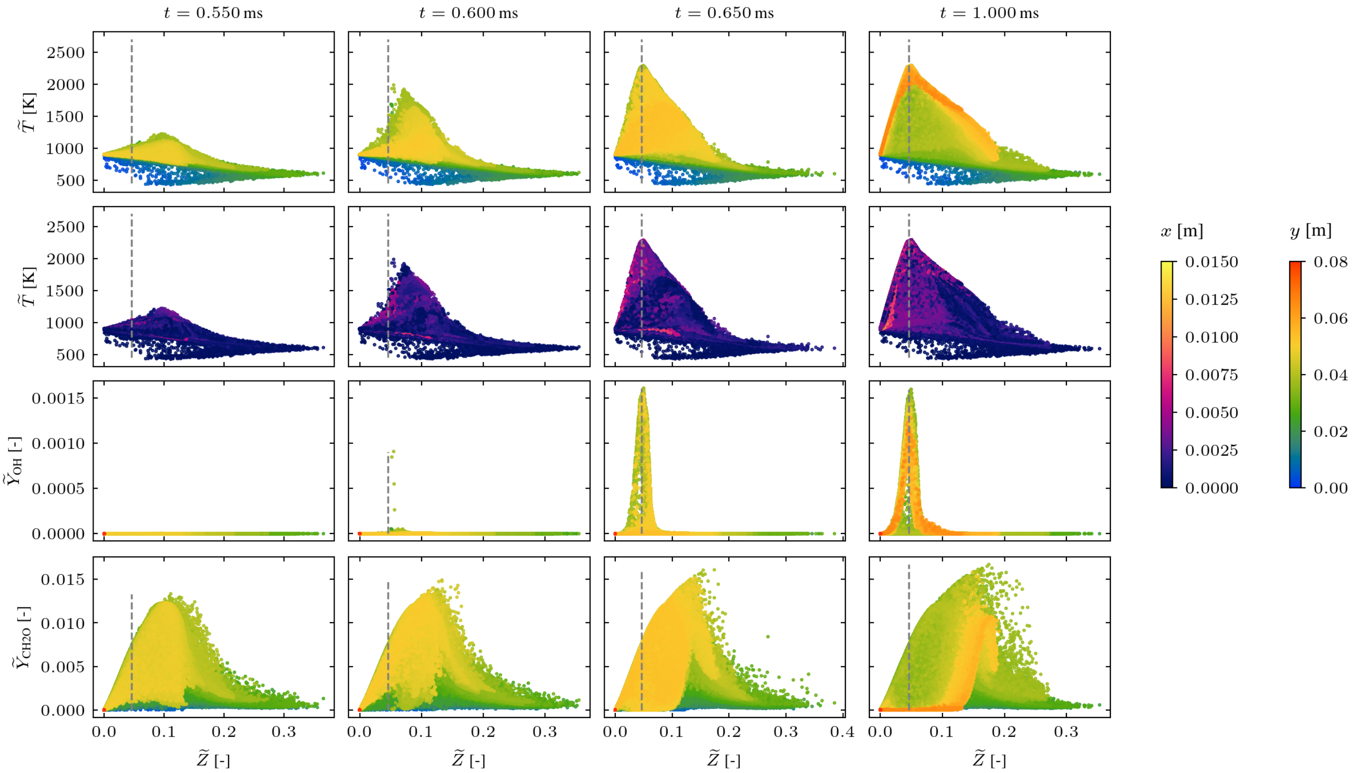

(b) Spray flame structure in mixture fraction space.

Figure 7.13: Spray flame structure analysis of n-Dodecane for the ECN Spray D injector. In subfigure (a), the filtered temperature field in physical space is shown for comparison. The top row in (b) shows the Favre-filtered temperature $\widetilde{T}$ colored as the distance in y-direction from the nozzle, and the second row is colored as the distance in x-direction. The third and fourth rows are the Favre-filtred mass fractions of OH and CH_2O colored as the distance from the nozzle in y-direction.

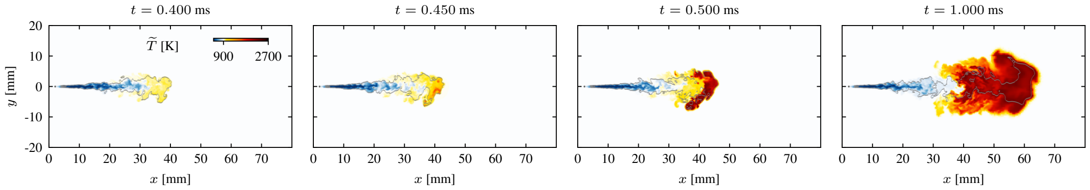

(a) Favre-filtered temperature field in physical space: $\widetilde{T}$.

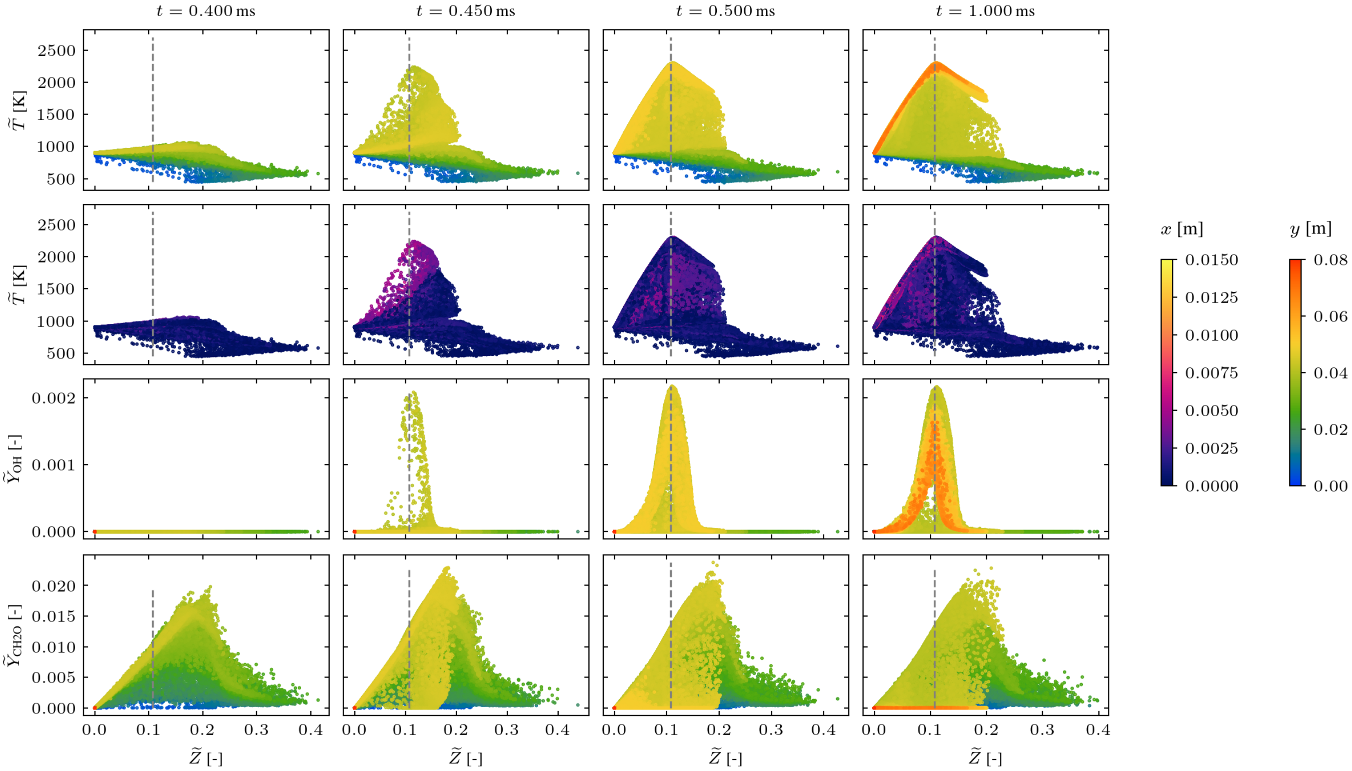

(b) Spray flame structure in mixture fraction space.

Figure 7.14: Spray flame structure analysis of OME_{mix} for the ECN Spray D injector. In subfigure (a), the filtered temperature field in physical space is shown for comparison. The top row in (b) shows the Favre-filtered temperature $\widetilde{T}$ colored as the distance in y-direction from the nozzle, and the second row is colored as the distance in x-direction. The third and fourth rows are the Favre-filtred mass fractions of OH and CH_2O colored as the distance from the nozzle in y-direction.

7.3 Marine injector: Woodward L'Orange single hole

In the following, the simulation results for the reactive Woodward L'Orange injector are presented. The comparison between n-Dodecane and 1-Octanol is drawn based on different combustion metrics.

7.3.1 Influence of latent heat of evaporation on ignition

In Figure 7.15, the profiles of the volume integrated $\widetilde{Y}_{\mathrm{OH}}$ are shown together with the experimentally determined ignition delay time for n-Dodecane (a) and 1-Octanol (b) in the Woodward L'Orange injector. The experimentally measured ignition delay times for the marine injector for n-Dodecane ($\tau_{\mathrm{ign,Exp}}=0.5068\,\mathrm{ms}$) and 1-Octanol ($\tau_{\mathrm{ign,Exp}}=0.8779\,\mathrm{ms}$) are only slightly higher compared to ECN Spray A3 (see Table 7.1). For comparison, the IDT of n-Dodecane and 1-Octanol in the marine injector is increased by only approximately $10\,\%$ than in Spray A3, while in Spray D, the IDT was increased by approximately $30\,\%$ for n-Dodecane. Hence, the IDT of n-Dodecane in the marine injector is shorter than in Spray D. The mixture formation analysis in Sec. 5.4 revealed very similar profiles of the averaged mixture fraction and scalar dissipation rate for n-Dodecane in Spray D and the marine injector. The lower ignition delay time for n-Dodecane in the marine injector than in Spray D is explained by the higher averaged temperature distribution in the marine injector in Figure 6.10 (a).

The ignition delay time of n-Dodecane of $\tau_{\mathrm{ign,Sim}}=0.526\,\mathrm{ms}$ in 7.15 (a) shows excellent agreement with the experimental IDT. As already observed in Spray A3, no heat-loss correction is needed for n-Dodecane. The temperature distribution of n-Dodecane in the marine injector in Figure 6.10 (a) is shifted towards fuel-rich conditions and higher temperatures, which explains that no temperature correction is needed.

In contrast to n-Dodecane, the influence of heat loss due to evaporation is significant in the IDT of 1-Octanol. The simulation with the standard flamelet model underestimates the IDT by approximately $20\,\%$ (see Table 7.1). As shown in Figure 7.15 (b), the heat-loss corrected flamelet model delivers excellent agreement with the experiment for 1-Octanol ($\tau_{\mathrm{ign,Sim}}=0.851\,\mathrm{ms}$). The later ignition of 1-Octanol in the marine injector compared to Spray A3 can be explained by the delayed mixture formation process shown in Figure 5.15 (b). Further, lower chemical reactivity has been shown in Figure 6.3.

Overall, a perfect agreement has been shown in the ignition delay times of the marine injector for n-Dodecane and 1-Octanol. While n-Dodecane did not exhibit a sensitivity toward the heat-loss corrected flamelet model, the influence for 1-Octanol was very significant.

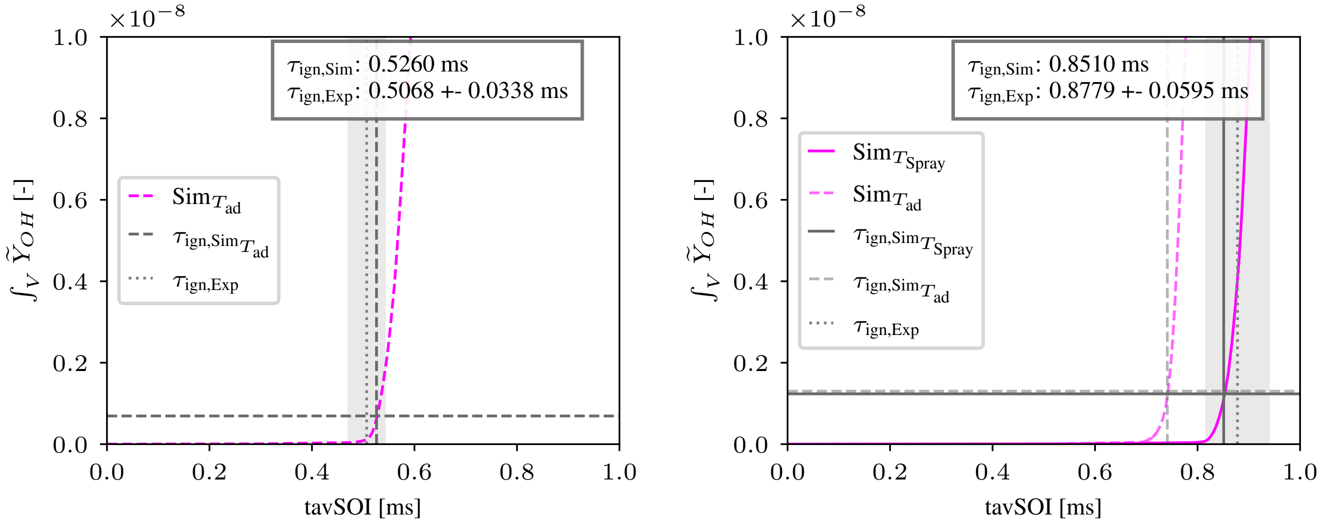

(a) n-Dodecane.

(b) 1-Octanol.

Figure 7.15: Comparison of the volume integrated $\widetilde{Y}_{\mathrm{OH}}$ signal for n-Dodecane (a), and 1-Octanol (b) in the marine Woodward L'Orange injector. The spray ignition delay time is defined as $2\,\%(\int_V \widetilde{Y}_{\mathrm{OH}})_{\mathrm{max}}$. The comparison shows differences in the ignition delay time among the fuels for the standard flamelet model (dashed line) and the heat-loss corrected flamelet model (solid line). The heat-loss corrected flamelet model aligns perfectly with the experimental ignition delay time.

7.3.2 Influence of the fuel on ignition location

The comparison of the OH* signal with the line of sight integrated mass fraction of OH in Figure 7.16 reveals significant differences in the ignition process of n-Dodecane (a) and 1-Octanol (b).

The lift-off length of n-Dodecane in Figure 7.16 (a) is slightly overestimated in the LES. Most high-intensity regions in the LOSI $\widetilde{Y}_{\mathrm{OH}}$ signal are located at the spray flanks, which is also observed in the experiment. In contrast to the averaged experimental data, the instantaneous LES results exhibit scattered peaks of $\widetilde{Y}_{\mathrm{OH}}$, while the experiment predicts a more continuous ignition front at the flanks. The strong dependency of the used chemical kinetic mechanism on the OH formation explains differences to the experiment.

Also, the LES results of 1-Octanol in Figure 7.16 (b) show ignition at the spray flanks, which aligns well with the experiment. The lift-off length of 1-Octanol is slightly underestimated in the simulation. The shape of the LOSI $\widetilde{Y}_{\mathrm{OH}}$ in Figure 7.16 (b) for 1-Octanol is narrower than the experiment. While the experiment shows distinct high-intensity regions, the LES exhibits smaller scattered regions. Overall, good agreement in the ignition location and onset of ignition is achieved for n-Dodecane and 1-Octanol.

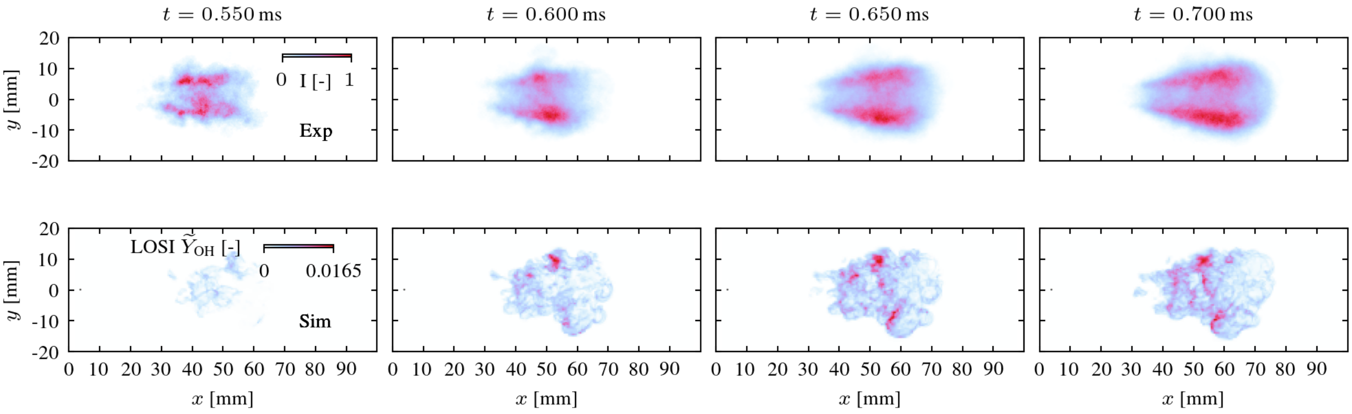

(a) n-Dodecane.

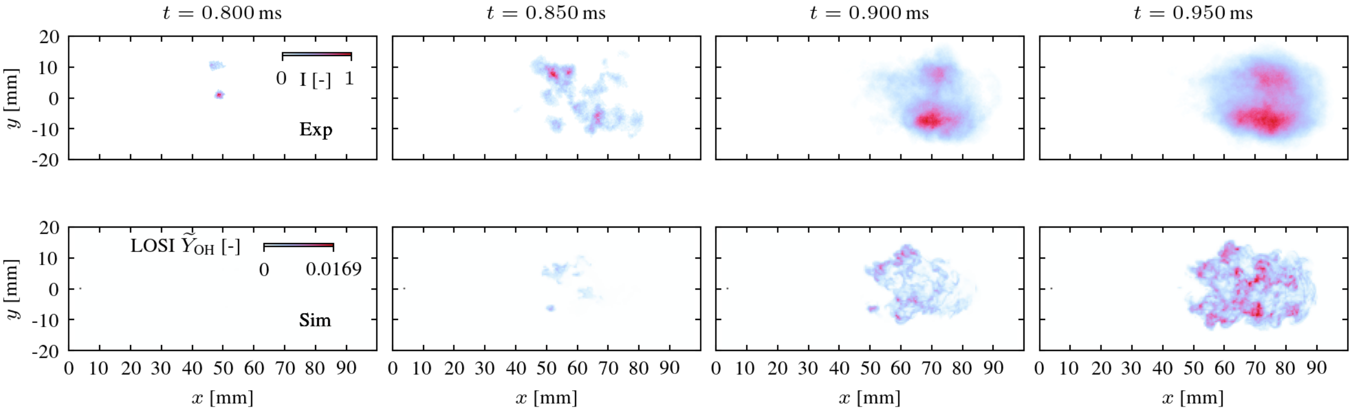

(b) 1-Octanol.

Figure 7.16: Comparison of reactive Large Eddy Simulation results for the Woodward L'Orange single hole injector towards experimental data for n-Dodecane (a) and 1-Octanol (b). In the top rows of each subfigure, the averaged normalized signal intensity of OH^* chemiluminescence is shown. In the bottom rows, the instantaneous line-of-sight integrated Favre-filtered OH mass fraction $\widetilde{Y}_{\mathrm{OH}}$ is shown for comparison. The spatial structure of ignition is captured very well by the LES.

7.3.3 Spray flame structure in physical space

The spray flame structure of the marine injector for n-Dodecane and 1-Octanol is now examined in physical space in Figure 7.17 and Figure 7.18. In general, n-Dodecane and 1-Octanol show very similar mixing behavior in the Woodward L'Orange injector, while the ignition delay times are different.

The nozzle diameter of the marine injector compared to Spray D is increased by a factor of 1.6, and the resulting spray pattern for both fuels is broader in the spray normal direction. However, both fuels in the Woodward L'Orange injector exhibit the same characteristic distribution of the mixture fraction reported for Spray D. High values of the mixture fraction are present on the spray center axis from the spray base until the spray head, visible in the subfigures (c) in Figure 7.17 and Figure 7.18. Still fuel-rich, but leaner mixtures are observed at the spray flanks where also lower scalar dissipation rates $\widetilde{\chi}_{\mathrm{st}}$ are observed (subfigures (d) in Figure 7.17 and Figure 7.18). It can be concluded, that more hot air has been entrained at the spray flanks, and the ignition process is initiated. This assumption is supported by the flame regime analysis of Spray D in Popp et al. [94], where similar spray structures are found. As shown in the line of sight integrated

$\widetilde{Y}_{\mathrm{OH}}$ in Figure 7.16, the onset of ignition is observed at the spray flanks visible by high-temperature regions in subfigure (a) and the formation of $\widetilde{Y}_{\mathrm{OH}}$ in subfigures (b) of Figure 7.17 and Figure 7.18. This effect is very prominent for n-Dodecane, in Figure 7.17 (a). At $t{=}0.50\,\mathrm{ms}$, a pocket is formed for n-Dodecane at the lower flank of the spray where first formaldehyde (Figure 7.17 (b)) is produced and subsequently consumed, denoting the onset of high-temperature ignition.

However, the same mixture formation process leading to ignition over the spray flanks is observed for 1-Octanol. The onset of ignition for 1-Octanol is also observed at the spray flanks (see Figure 7.18 (a)). The significantly higher IDT of 1-Octanol in the spray flame is explained by the lower temperatures due to the high latent heat of evaporation observed in the mixture formation analysis in Figure 5.19 (b) and the higher chemical ignition delay in Figure 6.3.

The spray flame of n-Dodecane shows a higher spray cone angle after ignition. The thermal expansion due to hot products at ignition occurs at approximately $t{=}0.5\,\mathrm{ms}$ for n-Dodecane and spreads the spray. Due to the later ignition of 1-Octanol and slightly higher stoichiometric mixture fraction, the spray structure in Figure 7.18 is narrower compared to n-Dodecane until ignition. After ignition at $t{=}0.9\,\mathrm{ms}$, also the spray flame of 1-Octanol spreads out.

Overall, n-Dodecane and 1-Octanol show a very similar mixture formation process in the Woodward L'Orange injector. Both fuels show the onset of ignition over the spray flanks, as observed in the heavy-duty ECN Spray D injector in Sec. 7.2. The later ignition of 1-Octanol is explained by the lower temperature distribution due to the high latent heat of evaporation and its high chemical ignition delay time. The spray flame shape of 1-Octanol exhibits a more elongated shape than n-Dodecane, due to the later onset of ignition.

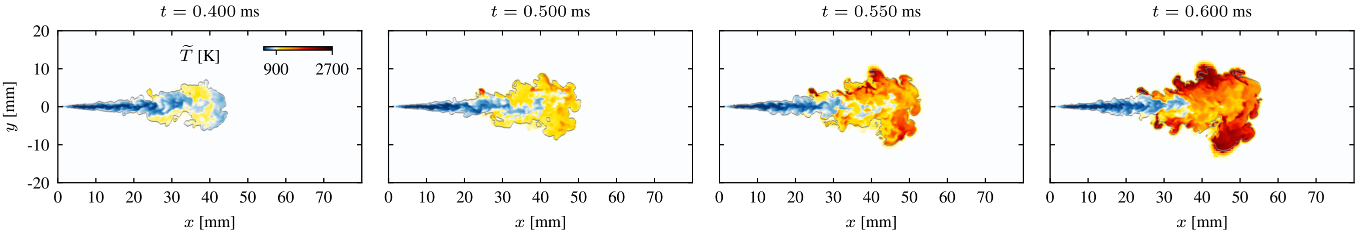

(a) Favre-filtered temperature: $\widetilde{T}$.

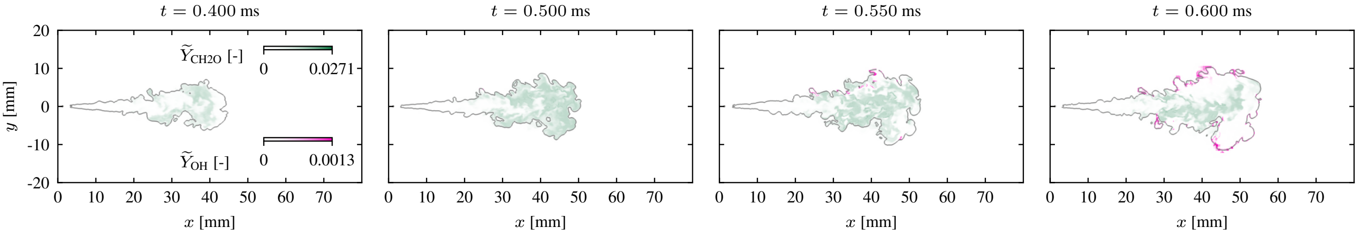

(b) Favre-filtered mass fractions of CH_2O and OH: $\widetilde{Y}_{\mathrm{CH2O}}$ & $\widetilde{Y}_{\mathrm{OH}}$.

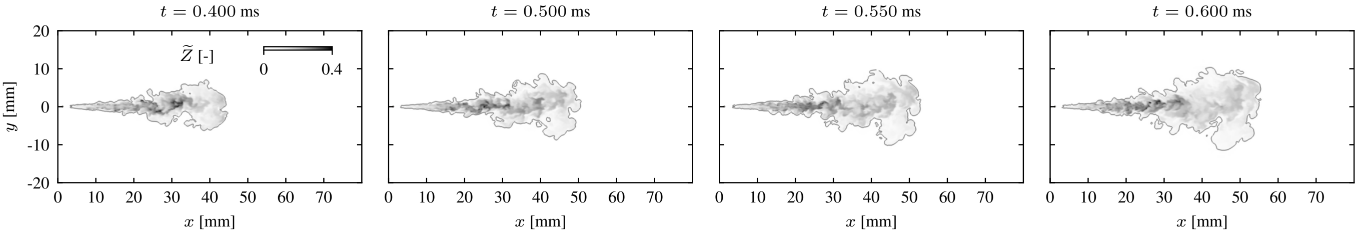

(c) Favre-filtered mixture fraction: $\widetilde{Z}$.

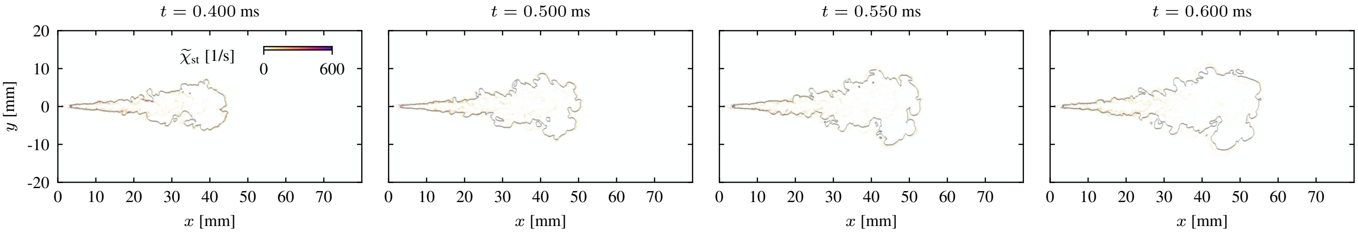

(d) Favre-filtered scalar dissipation rate at stoichiometry: $\widetilde{\chi}_{\mathrm{st}}$.

Figure 7.17: Comparison of $\widetilde{T}$ (a), $\widetilde{Y}_{\mathrm{CH2O}}$ & $\widetilde{Y}_{\mathrm{OH}}$ (b), $\widetilde{Z}$ (c) and $\widetilde{\chi}_{\mathrm{st}}$ (d) fields of the reactive n-Dodecane Woodward L'Orange single hole injector simulation. The gray line represents the iso-line of Z_{st}. The comparison gives deeper insight into the ignition process. The ignition over the spray flanks, typical for heavy-duty injectors, is shown in the temperature and $\widetilde{Y}_{\mathrm{OH}}$ fields.

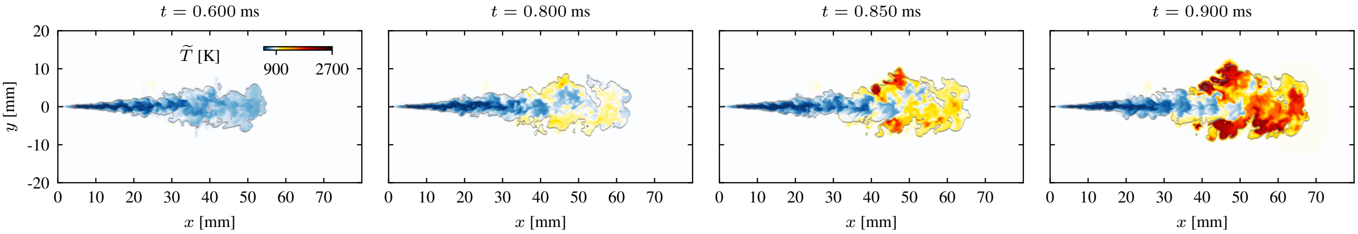

(a) Favre-filtered temperature: $\widetilde{Z}$.

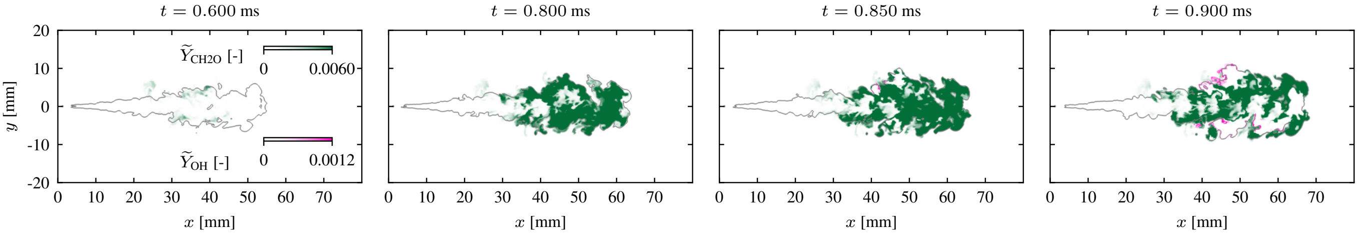

(b) Favre-filtered mass fractions of CH_2O and OH: $\widetilde{Y}_{\mathrm{CH2O}}$ & $\widetilde{Y}_{\mathrm{OH}}$.

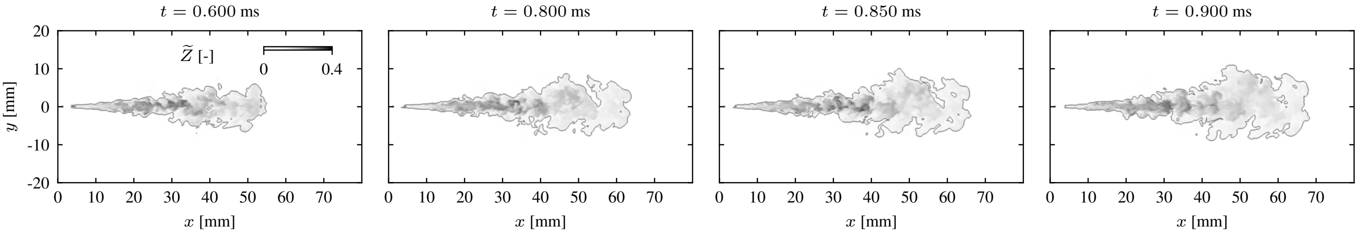

(c) Favre-filtered mixture fraction: $\widetilde{Z}$.

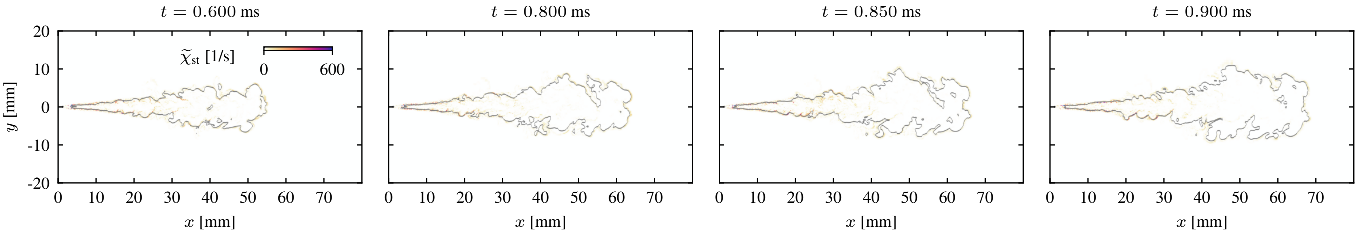

(d) Favre-filtered scalar dissipation rate at stoichiometry: $\widetilde{\chi}_{\mathrm{st}}$.

Figure 7.18: Comparison of $\widetilde{T}$ (a), $\widetilde{Y}_{\mathrm{CH2O}}$ & $\widetilde{Y}_{\mathrm{OH}}$ (b), $\widetilde{Z}$ (c) and $\widetilde{\chi}_{\mathrm{st}}$ (d) fields of the reactive 1-Octanol Woodward L'Orange single hole injector simulation. The gray line represents the iso-line of Z_{st}. The comparison gives deeper insight into the ignition process. The ignition over the spray flanks, typical for heavy-duty injectors, is shown in the temperature and the $\widetilde{Y}_{\mathrm{OH}}$ fields.

7.3.4 Spray flame structure in mixture fraction space

In the following, the spray flame structure of the marine injector is analyzed in mixture fraction space in Figure 7.19 and Figure 7.20. In particular, the ignition location in mixture fraction space is investigated. For an easier interpretation of the results in mixture fraction space, the corresponding temperature field in physical space is shown in subfigures (a). The temperature scatters in Figure 7.19 (b) and Figure 7.20 (b) are colored according to the distance from the nozzle in the spray direction (y-direction, first row) and as the distance in the spray normal direction (x-direction, second row).

The spray flame structure of n-Dodecane in Figure 7.19 (b) exhibits the highest mixture fractions among all injectors. In the marine injector, values up to $\widetilde{Z}=0.4$ are observed for n-Dodecane. The onset of ignition for n-Dodecane is observed at $\widetilde{Z}\approx0.1$ in Figure 7.19 (b). The same value has also been observed for Spray A3 (Sec. 7.1.4) and Spray D (Sec. 7.2.4). The temperature distribution in Figure 7.19 (b) clearly shows, that the onset of ignition is located at the spray flanks. At $t=1.000\,\mathrm{ms}$, the spray flame is fully developed, and the cool flame propagation process is clearly visible in 7.19 (b) for $\widetilde{Y}_{\mathrm{OH}}$ and $\widetilde{Y}_{\mathrm{CH2O}}$. The red scatters of $\widetilde{Y}_{\mathrm{OH}}$ in Figure 7.19 (b) represent the flame at the spray head. At the location of the peak of $\widetilde{Y}_{\mathrm{OH}}$, $\widetilde{Y}_{\mathrm{CH2O}}$ is almost completely consumed.

The flame structure of 1-Octanol in Figure 7.20 (b) is similar to n-Dodecane. The onset of ignition is observed in the second row of Figure 7.20 (b) at $\widetilde{Z}\approx0.1$ at the spray flanks. Due to the longer ignition delay time of 1-Octanol, the ignition is observed further downstream compared to the other sprays (see first and second row of Figure 7.20 (b)). The lower chemical IDT and the lower temperatures observed in Figure 6.10 lead to the later ignition. The fully developed spray flame at $t=1.000\,\mathrm{ms}$ in Figure 7.20 (a) is narrower than n-Dodecane and exhibits a cylindrical shape, while n-Dodecane shows a conical shape. The scatters colored in the spray's normal direction in the second row of Figure 7.20 (b) are homogenously distributed over fuel-lean and fuel-rich mixtures, which is reflected in the temperature field in Figure 7.20 (a).

The analysis in mixture space of the marine Woodward L'Orange injector confirms the observations made in Spray A3 and Spray D. The ignition location in mixture fraction space is determined by a fuel-dependent mixture fraction of ignition, but the ignition in physical space is dominated by mixture formation. For 1-Octanol and n-Dodecane the ignition starts at $\widetilde{Z}\approx0.1$ in all injector sizes. As shown in Figure 7.17 (c) and Figure 7.18 (c), the mixture fraction of ignition in the marine injector is observed at the spray flanks, where subsequently ignition is initiated.

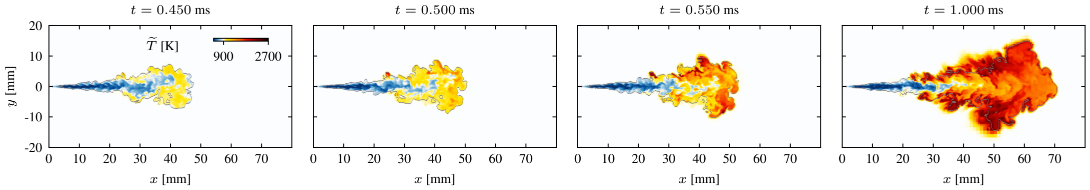

(a) Favre-filtered temperature field in physical space: $\widetilde{T}$.

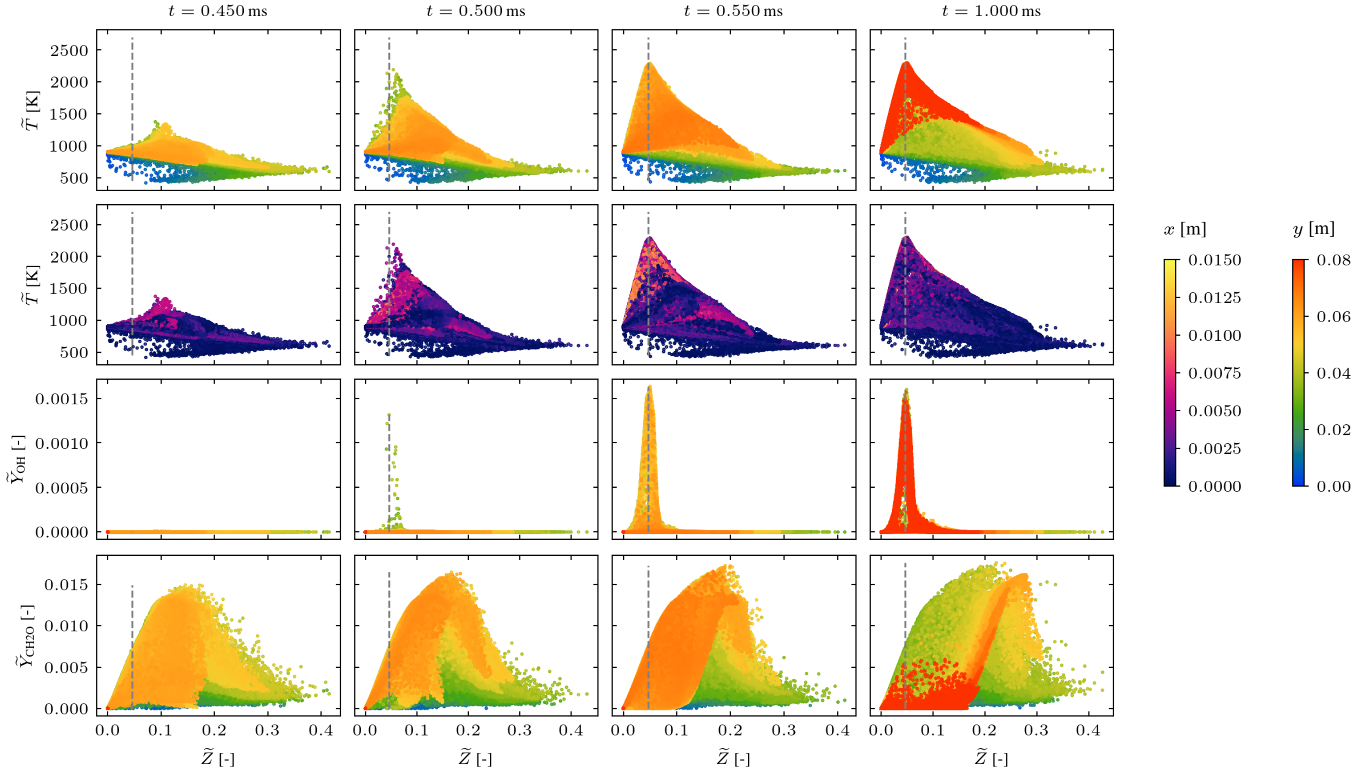

(b) Spray flame structure in mixture fraction space.

Figure 7.19: Spray flame structure analysis of n-Dodecane for the Woodward L'Orange single hole injector. In subfigure (a), the filtered temperature field in physical space is shown for comparison. The top row in (b) shows the Favre-filtered temperature $\widetilde{T}$ colored as the distance in y-direction from the nozzle, and the second row is colored as the distance in x-direction. The third and fourth rows are the Favre-filtred mass fractions of OH and CH_2O colored as the distance from the nozzle in y-direction.

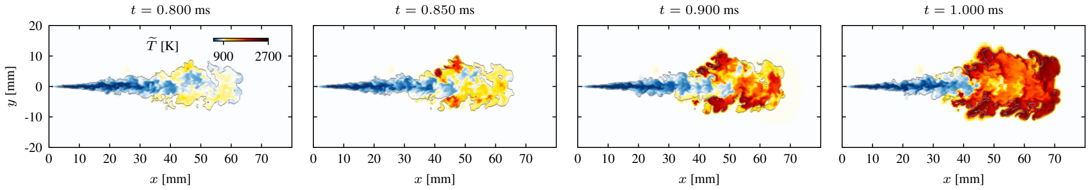

(a) Favre-filtered temperature field in physical space: $\widetilde{T}$.

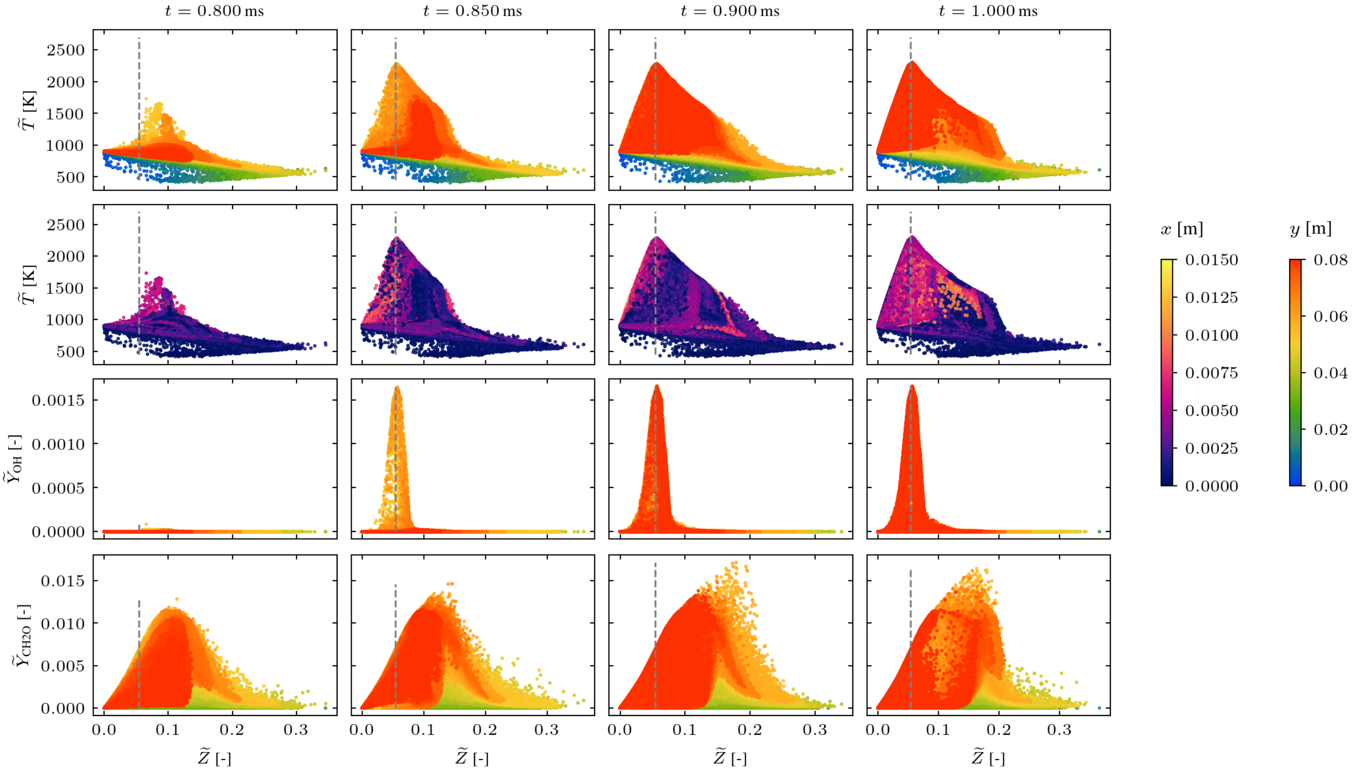

(b) Spray flame structure in mixture fraction space.

Figure 7.20: Spray flame structure analysis of 1-Octanol for the Woodward L'Orange single hole injector. In subfigure (a), the filtered temperature field in physical space is shown for comparison. The top row in (b) shows the Favre-filtered temperature $\widetilde{T}$ colored as the distance in y-direction from the nozzle, and the second row is colored as the distance in x-direction. The third and fourth rows are the Favre-filtred mass fractions of OH and CH_2O colored as the distance from the nozzle in y-direction.

7.4 Conclusions on ignition in turbulent spray flames

In this chapter, the reference fuel n-Dodecane, the biogenic oxygenated fuel 1-Octanol and the synthetic oxygenated fuel $\mathrm{OME}_{\mathrm{mix}}$ have been investigated under reactive conditions in different injectors with increasing nozzle sizes. In the following, the findings and results of this examination are discussed. First, the influence of the nozzle size on the spray flame structure is discussed. Second, the differences in spray flame combustion among the fuels are elucidated in detail.

The analysis of the automotive Spray A3, the heavy-duty injector Spray D and the marine Woodward L'Orange injector revealed significant differences in the mixture formation and ignition process among the injectors.

A characteristic feature of the automotive injector Spray A3 is the ignition over the spray head. The small nozzle size leads to smaller droplets that can exchange momentum very fast. The momentum exchange leads to air entrainment that enhances the evaporation process significantly. An ignitible, slightly fuel-rich mixture is formed in the spray head. Through the mixing process in the spray head, lower scalar dissipation rates at stoichiometry are observed, while the spray base exhibits higher scalar dissipation rates. In contrast to the automotive injector Spray A3, the mixture formation process of the heavy-duty and marine injector is significantly different. The larger nozzle sizes of the Spray D and Woodward L'Orange injectors exhibit delayed evaporation, which is shown in the averaged mixture fraction analysis in Sec. 5.4. It is assumed, that the higher injected mass and the initially larger blobs exhibit reduced momentum exchange due to reduced drag (Figure 5.10). Also, the visual inspection of the Spray D and Woodward L'Orange injectors shows that the liquid penetration is on the same level as the vapor penetration until approximately $t{=}0.2\,\mathrm{ms}$. The high liquid penetration depths lead to a cool area and high values of the mixture fraction on the spray center line. The visual inspection of the mixture fraction field for Spray D and the Woodward L'Orange injector reveals (subfigures (c) in Figure 7.11, Figure 7.12, Figure 7.17 and Figure 7.18) that lower values of the mixture fraction are observed at the spray flanks, compared to the spray head. The mixing in large nozzles is assumed to be located at the spray flank, while the smaller nozzle of Spray A3 shows the main mixing at the spray head. This finding aligns with the results of Popp et al. [94], where a regime identification method for n-Dodecane in Spray A and Spray D was conducted. In Spray A, the low-temperature chemistry regime was observed at the spray head and for Spray D at the spray flanks [94]. The spray flame characterization in mixture fraction space shows that ignition for small and large nozzle occurs at the same respective mixture fraction. It can be concluded, that the differences in the spatial ignition location at the ECN baseline conditions investigated in this study are mainly attributed to the mixture formation process. This finding is a novelty discovered in this work.

Besides the different mixture formation behavior due to the size of the nozzle, also significant differences in the ignition behavior among the fuels: n-Dodecane, 1-Octanol and $\mathrm{OME_{mix}}$ are observed. In the following, the most significant differences are elucidated.

N-Dodecane is used in this thesis as a reference fuel since it is the most common surrogate fuel for Diesel. The chemical ignition delay time of n-Dodecane is between that of 1-Octanol (highest IDT) and $\mathrm{OME_{mix}}$ (lowest IDT) in this thesis. The ignition delay time of n-Dodecane is increasing with the size of the nozzle. A trend of increasing IDT with the nozzle size from Spray A3 (smallest) to Woodward L'Orange (higher IDT) and Spray D (highest IDT) is observed for n-Dodecane. The gaseous heat capacity at constant pressure of n-Dodecane is significantly higher compared to the other fuels. The higher heat capacity leads to a more concave shape of the adiabatic mixing line assumed in the combustion model, which fits better with the spray's temperature distribution. The sensitivity towards heat loss due to evaporation for n-Dodecane is less significant compared to 1-Octanol and $\mathrm{OME_{mix}}$.

The lowest reactivity has been observed for 1-Octanol, which also has the longest chemical ignition delay time among the fuels. Especially in the low-temperature chemistry regime, the lowest reactivity is observed. At higher temperatures, a higher reactivity for 1-Octanol is observed than for n-Dodecane. 1-Octanol exhibits the highest latent heat of evaporation among the fuels (Figure 2.4), which leads to high heat losses due to evaporation in the spray (see Sec. 5.4.2). Consecutively, high ignition delay times are observed in the spray. 1-Octanol exhibits the highest sensitivity towards the heat-loss corrected flamelet model. The ignition delay times without the corrected model underestimate the ignition delay time by up to $25\,\%$. Even though the latent heat of evaporation is significantly higher compared to n-Dodecane, the mixture formation process is similar to n-Dodecane.

In contrast to the other fuels considered, $\mathrm{OME_{mix}}$ exhibits a significantly different mixture formation process.

The high vapor pressure of OME_{mix} (Figure 2.4) leads to higher maximum values of the mixture fraction. The stoichiometric mixture fraction of OME_{mix} is approximately doubled compared to n-Dodecane and 1-Octanol at ECN baseline conditions. The high value of the stoichiometric mixture fraction results in less fuel-rich mixtures in Spray A3, where a detached cloud of small isles with fuel-rich mixtures is observed. The unique mixture formation process leads to an overall leaner mixture that could be utilized for CO reduction since CO is mainly produced in the fuel-rich regions of the flame. Further, the chemical and thermophysical properties of OME_{mix} are significantly different. The chemical ignition delay time and ignition delay time under strained conditions are significantly lower than for n-Dodecane and 1-Octanol. Furthermore, the low sensitivity of strain on ignition delay and the high ignition limit of OME_{mix} results in a lower sensitivity of the ignition delay time with increasing nozzle sizes. The influence of heat-loss correction is evaluated as moderate for OME_{mix} in Spray A3 but significant in Spray D[1].

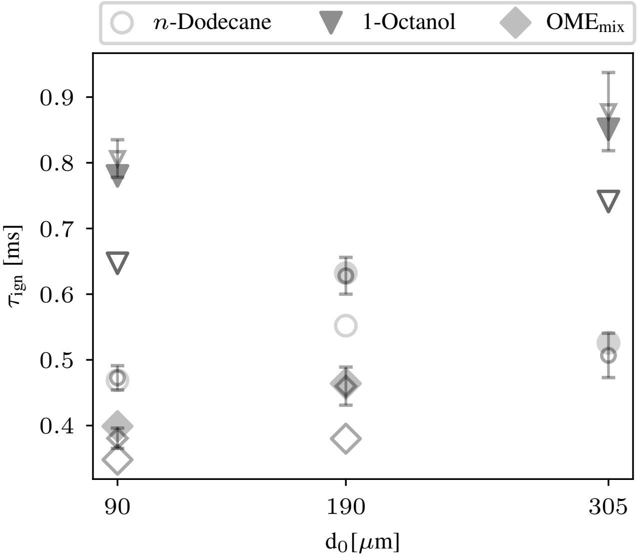

Figure 7.21: Overview of the ignition delay times for all fuels and injectors. The circles represent n-Dodecane, the downright triangles represent 1-Octanol, and the diamonds represent OME_{mix}. Filled markers denote the ignition delay times utilizing the heat loss corrected flamelet model, non-filled markers show the IDT of the standard flamelet model, and the smaller non-filled markers with error bars represent the experimental IDTs.

As shown in Figure 7.21, excellent agreement has been achieved among all fuels and injectors utilizing the novel heat-loss corrected flamelet model developed in this thesis. The developed LES spray framework has been adapted and validated for the simulation of fuels with significantly different thermophysical properties in small and very large injector setups. The LES reveals new insights into the mixture formation and ignition process of turbulent spray flames. The combined mixture formation analysis in inert conditions and the spray flame analysis in mixture fraction space revealed the cause-effect chain of different ignition locations in the spray. Finally, the critical parameters and sensitivities among n-Dodecane, 1-Octanol, and OME_{mix} have been identified and discussed.

---

[1] Note that the smaller influence of the heat-loss corrected flamelet model for OME_{mix} only holds for the investigated injectors and boundary conditions. In Haspel et al. [1], the ignition delay time was underestimated more significantly for neat OME_3 and OME_4 in a heavy-duty injector at reduced ambient temperatures and an increased rate of injection. It is assumed that the underestimated IDTs are due to the high enthalpy loss due to the latent heat of evaporation.

8 Summary, Conclusion and Outlook

The transport sector contributes significantly to the emission of greenhouse gases due to the combustion of fossil fuels. The increasing threats of global warming accelerate the development of renewable technologies reducing the carbon dioxide footprint. The preferred route in the transport sector is defossilation using fuels from renewable resources. Novel Diesel fuels from biogenic sources and renewable electricity (E-Fuels) are promising candidates due to their carbon-neutral production and backstop ability. In this thesis, the biogenic fatty alcohol 1-Octanol and the synthetic group of oligomers (Poly-)oxymethylene ethers are investigated. Due to their oxygenated molecular structure, both fuels exhibit changed thermophysical and chemical kinetic properties. This thesis aims to elucidate the influence of the changed thermophysical properties on mixture formation in high-pressure, high-temperature sprays. Furthermore, the question of how the fuels from renewable resources are changing the ignition behavior is addressed. Influences of mixture formation and changed chemical kinetic behavior are elucidated. The influence of the latent heat of evaporation on the spray flame structure is examined in this thesis. Finally, the question of how the increasing nozzle size for automotive (ECN Spray A3), heavy-duty (ECN Spray D) and marine (Woodward L'Orange) injectors influences the ignition in spray flames is investigated. The scientific questions are answered utilizing a high-fidelity Large Eddy Simulation framework coupled with a tabulated chemistry approach. For the first time, OME_{mix} has been studied in the ECN Spray D configuration using an LES framework. Further, to the author's best knowledge, this thesis is the first to investigate 1-Octanol in spray flames, and the first study of its kind of a marine injector in LES.

First, the numerical framework for the LES of spray simulations is validated under inert conditions. Excellent agreement with experimental Schlieren and Mie scattering data was achieved in terms of liquid and vapor penetration, as well as spray morphology for all fuels and injectors. The subsequent mixture formation analysis revealed significant differences to the reference Diesel surrogate n-Dodecane. Spray experiments in Spray A3 showed longer liquid penetration lengths of the more volatile 1-Octanol and OME_{mix} compared to n-Dodecane. In this thesis, a non-dimensional number is derived that suggests that due to the higher vapor pressure and latent heat of evaporation, more enthalpy is withdrawn during evaporation, reducing the gas temperature significantly. Hence, the evaporation limiting heat transfer is reduced, and longer liquid penetration lengths are exhibited. While 1-Octanol shows similar mixing behavior to n-Dodecane, OME_{mix} shows narrower spray shapes and different mixing characteristics.

Next, the influence of the nozzle size on mixture formation is examined based on volume averaged mixture fraction and scalar dissipation rate profiles. Distinct differences between the smaller automotive and the large heavy-duty and marine injectors are identified. The mixture formation process in Spray A3 is significantly faster than in Spray D and the Woodward L'Orange injector. In Spray A3, higher values of the scalar dissipation rate are observed than in the larger nozzles. While the profiles of n-Dodecane and 1-Octanol align in all injector sizes, OME_{mix} exhibits higher values of the scalar dissipation rate. In this thesis, an explanation for the delayed mixture formation is presented. The similar liquid and vapor penetration lengths in the initial injection phase for Spray D and the Woodward L'Orange injectors and the delayed mixing process suggest that the large particles show reduced momentum exchange and less air entrainment. This finding is important for the explanation of different ignition locations. Further, the influence of increased latent heat of evaporation of 1-Octanol and $\mathrm{OME_{mix}}$ is investigated in mixture fraction space. The comparison of the spray's gas temperature distribution and the adiabatic mixing line, which is prescribed as an initial condition in many combustion models, reveals, that the gas phase is significantly cooled by 1-Octanol, which has the highest latent heat of evaporation. The influence of heat-loss due to evaporation scales with the latent heat of evaporation (low to high: n-Dodecane, $\mathrm{OME_{mix}}$, 1-Octanol). For the first time, it has been shown that n-Dodecane exhibits a higher gas heat capacity, which inherently compensates for the effect of heat loss due to latent heat of evaporation, meaning that n-Dodecane is less sensitive towards spray cooling effects on ignition. Among all fuels and injectors, lower scalar dissipation rates have been observed for fuel-rich mixtures contributing significantly to ignition in spray flames.

The influence of the changed chemical properties has been examined in 0D and 1D canonical combustion models. The analysis of the chemical ignition delay times in the 0D homogeneous reactor model revealed distinct differences among the fuels. While n-Dodecane and 1-Octanol show a Diesel typical Negative Temperature Coefficient (NTC) behavior, the NTC regime of $\mathrm{OME_{mix}}$ is not pronounced. The highest chemical ignition delay time is observed for 1-Octanol, followed by n-Dodecane. Despite the higher IDT in the low-temperature chemistry regime, at higher temperatures, the ignition delay time of 1-Octanol falls below n-Dodecane. The IDT of $\mathrm{OME_{mix}}$ is three to six times shorter than the other fuels, suggesting a high reactivity.

Subsequently, the ignition under strained conditions is analyzed in 1D laminar non-premixed flamelet simulations. At identical scalar dissipation rate profiles, all fuels show similar maximum temperature values of $T{\approx}2200\,\mathrm{K}$. Higher peak values of Y_{CO} and Y_{CO2} are found for 1-Octanol and $\mathrm{OME_{mix}}$, while the peaks are shifted toward higher mixture fractions due to the increased stoichiometric mixture fraction of the oxygenated fuels. A comparison at the position of the stoichiometric mixture fraction of n-Dodecane reveals that less CO is produced for 1-Octanol and $\mathrm{OME_{mix}}$, which aligns with experimental observations. Within the ignition limits, $\mathrm{OME_{mix}}$ shows the lowest ignition delay time among all fuels. The ignition delay profile over the scalar dissipation rate for $\mathrm{OME_{mix}}$ reveals low sensitivity toward strain effects. Furthermore, $\mathrm{OME_{mix}}$ shows the highest ignition limit $\chi_{\mathrm{st,ign}}$ of all fuels. Even though 1-Octanol showed a lower reactivity in the 0D model, the ignition limit is higher than for n-Dodecane. For low scalar dissipation rates, the IDT of n-Dodecane is lower, but at higher scalar dissipation rates and longer ignition delay times, the higher reactivity of 1-Octanol at higher temperatures becomes apparent, and the IDT of 1-Octanol falls below the IDT of n-Dodecane.

A novel flamelet model is derived that accounts for the effect of latent heat of evaporation on the flame structure, which is based on the mixture formation analysis. In the model, the initial temperature profile is modeled by line segments that are derived from inert spray simulations, including the distinct temperature distribution of the spray. A new methodology to determine the shape of the initial temperature profile is presented that, in contrast to other methods in the literature, is physically consistent, flexible for all fuel and injector combinations and is standardized. The investigation for 1-Octanol showed that the solution between the standard model (adiabatic mixing line) and the heat-loss corrected model does not change integral combustion properties (stationary solution and ignition limits). Only the transient ignition process and, consecutively, the ignition delay times are prolonged.

The heat-loss corrected flamelet model has been utilized in reactive Large Eddy Spray Simulations. First, the influence of increasing nozzle sizes on the ignition is discussed. For all fuels, the typical onset of ignition over the spray head has been observed in Spray A3. In the larger heavy-duty Spray D and marine injector from Woodward L'Orange, the onset of ignition has been observed at the spray flanks. The ignition delay time in the spray increases with the nozzle size. The later ignition of larger nozzles is explained by the delayed evaporation observed in the mixture formation analysis and lower temperatures due to more enthalpy loss. In this work, it has been shown for the first time that the ignition starts at a fuel-specific mixture fraction among all injectors, while the spatial point of ignition is determined by mixture formation. The highly evaporative Spray A3 shows the mixing and air entrainment at the spray head. In injectors with larger nozzles, the large particles experience less drag and momentum exchange. This leads to higher values of the mixture fraction at the spray center line up to the vapor penetration length. Air entrainment of hot gases occurs at the spray flanks, leading to ignition. This cause-effect mechanism of mixture formation has been reported for the first time in Spray D and a marine injector in LES and is a novelty of this work.

Further, the influence of the changed thermophysical properties and different chemical properties have been investigated among all fuels. 1-Octanol exhibits the longest ignition delay time in all injectors examined. The influence of the heat loss due to evaporation has been most significant for 1-Octanol. The flamelet model without heat-loss correction underestimated the IDT by about $25\,\%$. The novel heat-loss corrected model achieved perfect agreement for all fuels. All ignition delay times are within the experimental uncertainty. Even though 1-Octanol has a significantly higher latent heat of evaporation and slightly higher vapor pressure, the mixture formation and spray shape are very similar to n-Dodecane, which is also reported in the literature. In contrast, the mixture formation of OME_{mix} differs from the other fuels. In Spray A3, OME_{mix} shows detached fuel-rich clouds in contrast to the other fuels. Due to the doubled stoichiometric mixture fraction compared to the other fuels, the cross area of fuel-rich mixtures is reduced significantly, which can be clearly shown in the mixture fraction space. OME_{mix} exhibits the narrowest spray shape among all fuels. Due to the high stoichiometric mixture fraction, ignition and the diffusion flame are closer to the spray center axis. In contrast to n-Dodecane, the increase of the ignition delay time from Spray A3 to Spray D is significantly lower for OME_{mix}. As shown in the flamelet simulations, OME_{mix} is highly reactive and less sensitive toward changes in the scalar dissipation rate. Hence, the IDT of OME_{mix} is not particularly sensitive to different nozzle sizes.

It can be summarized that the influence of changed thermophysical and chemical kinetic properties of the renewable fuels 1-Octanol and OME_{mix} have been successfully investigated in a high-fidelity Large Eddy Simulation framework. The influence of higher latent heat of evaporation and vapor pressure has been elucidated and compared to the reference fuel n-Dodecane. Based on the mixture formation analysis, a novel method to incorporate the effects of heat loss due to evaporation in the combustion model has been developed in this thesis and has been successfully applied in reactive spray simulations. Effects of increasing nozzle sizes have been identified and could be explained with the help of the detailed mixture formation analysis under inert and reactive conditions. Perfect agreement has been achieved for all LES spray simulations under inert and reactive conditions. This thesis revealed relevant cause-effect chains in the ignition process for renewable Diesel fuels and the effects of the nozzle size. A comprehensive insight to spray flame ignition and the influence of heat loss due to evaporation is presented and extends the existing understanding of spray flames.

In future works, the next steps toward predictive LES spray simulations could be incorporating inner nozzle flow simulations into the spray simulation framework used in this thesis. The spray simulations with the Particle-In-Cell approach still heavily rely on experimental measurements for the rate of injection profiles, penetration lengths and spray angles that are input to the breakup models. With the help of inner nozzle flow simulations, complex effects, e.g., cavitation can be captured, and LES could become a predictive tool in engine pre-development. The results from this thesis should be incorporated into the combustion method development process. In particular, the heat-loss corrected flamelet model should be utilized for 1-Octanol in engine simulations. With the help of the novel flamelet model, the ignition delay times could be optimized for 1-Octanol by increasing the compression ratio and increasing the ambient temperature at ignition. The presented LES framework could also be utilized to optimize nozzle designs for OME_{mix} to reduce greenhouse gas emissions. Furthermore, OME_{mix} as a highly reactive fuel could be utilized in dual fuel combustion methods as a pilot fuel, compensating for the influence of the low reactivity of gaseous fuels. The presented work contributes significantly to reducing emissions in the transport sector.

Nomenclature

Abbreviations

BEV	Battery Electric Vehicle
BTE	Brake Thermal Efficiency
CFD	Computational Fluid Dynamics
CI	Compression Ignition
CI	Confidence Interval
CMT	Instituto Universitario de Motores Térmicos
DBI	Diffuse Backlight Illumination
DNS	Direct Numerical Simulations
ECN	Engine Combustion Network
EN 590	European Norm 590
ETAB	Enhanced Taylor Analogy Breakup Model
FDF	Filtered Density Function
FPV	Flamelet Progress Variable
FST	Fluidsystemtechnik
FVM	Finite Volume Method
HDA	Hydraulischer Druckanstiegs-Analysator
HRM	Homogeneous Reactor Model
HRR	Heat Release Rate
ICE	Internal Combustion Engine
KH-RT	Kelvin-Helmholtz Rayleigh-Taylor

LCA	Life cycle analysis
LES	Large Eddy Simulation
LHS	Left hand side
LHV	Lower Heating Value
LOL	Lift Off Length
LOSI	Line Of Sight Integration
MILES	Monotonically Integrated LES
NDF	Number Density Function
NTC	Negative Temperature Coefficient
PDA	Phase-Doppler-Anemometry
PDF	Probability Density Function
PIC	Particle-In-Cell
PLIF	Planar Laser Induced Fluorescence
PM	Particulate Matter
RANS	Reynolds-Averaged Navier-Stokes
RCM	Rapid Compression Machine
RDE	Real Driving Emission
RHS	Right hand side
ROI	Rate of injection
RUFPV	Reduced Unsteady Flamelet Progress Variable
SDR	Scalar dissipation rate
SNL	Sandia National Laboratories
TAB	Taylor Analogy Breakup Model
tavSOI	Time after the visible start of the injection
TCI	Turbulence Chemistry Interaction
UFPV	Unsteady Flamelet Progress Variable

ULF	Universal Laminar Flame Solver
VLE	Vapor-Liquid Equilibria
VOF	Volume of Fluid

Physical Symbols and Constants

α	Weight for Y_{CO} in the progress variable
$\bar{c}_{p,i}$	Molar heat capacity at constant pressure
$\bar{h}_i$	Molar enthalpy
β	Weight for Y_{CO2} in the progress variable
β_1	Parameter of the β function
β_2	Parameter of the β function
χ	Scalar dissipation rate
ΔH_j^0	Entropy changes
$\Delta h_{f,k}^0$	Standard enthalpy of formation for species k
ΔS_j^0	Entropy changes
δ	Weight for Y_{CH2O} in the progress variable
$\dot{\omega}_k$	Production rate
$\dot{m}$	Mass flow
$\dot{Q}$	Heat flux
$\dot{q}_s$	Heat flux to the droplet
$\dot{S}_k$	Species evaporation source term for species k
ϵ	Weight for Y_{H2} in the progress variable
Γ	Gamma function
γ	Weight for Y_{H2O} in the progress variable
λ	Air-fuel equivalence ratio
λ	Thermal conductivity
λ_k	Thermal conductivity of species k

$[X_k]$	Molar concentration
$\mathcal{D}_m$	σ model differential operator
$\mathcal{M}_k$	Molecule
$\mathcal{Q}_j$	Rate of progress of reaction j
Da	Damköhler number
$\mathrm{Pr}_{\mathrm{SGS}}$	Sub-grid scale Prandtl number
$\mathrm{Sc}_{\mathrm{SGS}}$	Sub-grid scale Schmidt number
μ	Viscosity of mixture
μ_k	Viscosity of species k
ν'_{kj}	Stoichiometric coefficient for reactant for species k and reaction j
ν''_{kj}	Stoichiometric coefficient for product for species k and reaction j
$\Omega_{kk}^{(2,2)*}$	Collision integral
$\overrightarrow{v}$	Velocity vector of blob parcel
Φ_{kj}	Auxiliary variable to compute viscosity of mixture
Π	Independent non-dimensional variable
π	Pi
ρ	Density
σ	Singular value of the velocity gradient tensor
σ_k^2	Collision diameter of the "$k-k$" interaction potential
τ	Flamelet time
τ_{f}	Characteristic flow time
$\widetilde{\dot{\omega}}_{Y_C}$	Favre filtered progress variable source term
$\widetilde{\dot{S}}_k$	Favre filtered species mass fraction source term due to evaporation
$\widetilde{\dot{S}}_m$	Favre filtered fuel mass source term due to evaporation
$\widetilde{\dot{S}}_{h_t}$	Favre filtered spray cooling enthalpy source term

$\widetilde{\dot{S}}_{u,i}$	Favre filtered spray momentum source term
$\widetilde{Z''^2}$	Variance of the mixture fraction
a	Strain rate
a	Thermal conductivity
a_i	Coefficient for the NASA polynomials
a_k	Thermal conductivity of species k
A_{fj}	Preexponential constant
$a_{n,k}$	Coefficient to compute species viscosity
B_0	KH-RT parameter
B_1	KH-RT parameter
$b_{n,k}$	Coefficient to compute species thermal conductivity
C_m	σ model constant
c_p	Heat capacity of at constant pressure
C_v	Heat capacity at constant volume
$c_{p,k}$	Heat capacity at constant pressure for species k
D	Diffusion coefficient
D_k	Diffusion coefficient for species k
E_j	Activation energy
$h_{a,k}$	Absolute enthalpy for species k
h_{vap}	Heat of vaporization
K	Conicity factor
k_B	Boltzmann constant
K_{fj}	Forward reaction rate
K_{rj}	Reverse reaction rate
m_k	Mass of species k
$N_{d,q}$	Number of particles in parcel

p	Pressure
p_a	Ambient pressure at $1\,\mathrm{bar}$
p_{crit}	Critical pressure
$p_{\mathrm{vap},i}$	Vapor pressure of species i
R	Universal gas constant
T	Temperature
t	Time
T_{crit}	Critical temperature
u_i	Velocity in direction i
u_{gas}	Gas velocity in cell
u_{parcel}	Parcel velocity in cell
u_{slip}	Parcel slip velocity
V	Volume
V_{crit}	Critical volume
$V_{k,j}$	Diffusion velocity of species k in direction j
W_k	Molecular mass of species k
W_k	Molecular mass
x_i	Spatial coordinate in direction i
X_k	Mole fraction of species k
$X^l_{f,i}$	Mole fraction of species i in the liquid phase
Y_k	Species mass fraction for species k
Z	Mixture fraction
Z_{crit}	Critical compressibility factor
$\widetilde{Z''^2}^N$	Normalized variance of the mixture fraction
A	Avogadro number
Le	Lewis number

Le_k	Lewis number of species k
PH	Parcel Heat index
Re	Reynolds number

Super- and Subscripts

α	Index variable
β_j	Temperature coefficient
st	Stoichiometry
erfc	Error function compliment
σ	σ model
^{m}	Mass based evaluation
$cell$	Cell
d	Droplet
F	Fuel
f	Forward
g	Gas
Ox	Oxidizer
q	Parcel index
r	Reverse
V	Constant volume
ign	Ignition
l	Liquid
s	Surface
SGS	Sub-grid scale

Bibliography

[1] Philip Michael Haspel, Sandro Gierth, Sebastian Popp, Sebastian Rieß, Michael Wensing, and Christian Hasse. “Combined experimental and numerical study of OME3 and OME4 spray combustion under heavy-duty conditions - under revision”. In: *Fuel* (2023).

[2] Michael H. H. Fechter, Philip Haspel, Christian Hasse, and Andreas S. Braeuer. “Vapor pressures and latent heats of vaporization of Poly(oxymethylene) Dimethyl Ethers (OME3 and OME4) up to the vicinity of the critical temperature”. In: *Fuel* 303.May (2021).

[3] Sandro Gierth, Philip Haspel, Arne Scholtissek, Zhen Sun, and Sebastian Popp. “Evaluation of the Unsteady Flamelet Progress Variable Approach in Large Eddy Simulations of the ECN Spray A”. In: *Science and Technology for Energy Transition* (2021).

[4] J D Hunter. “Matplotlib: A 2D graphics environment”. In: *Computing in Science & Engineering* 9.3 (2007), pp. 90–95.

[5] Intergovernmental Panel on Climate Change. *AR6 Synthesis Report: Climate Change 2023*. Tech. rep. 2023.

[6] Andrew Sullivan, Elaine Baker, and Tiina Kurvits. *Spreading like wildfire*. Tech. rep. 2022.

[7] *Paris Agreement to the United Nations Framework Convention on Climate Change*. Tech. rep. T.I.A.S. No. 16-1104. 2016.

[8] EEA. *Annual European Union greenhouse gas inventory 1990–2013 and inventory report 2015, submission to the UNFCCC*. Tech. rep. April. 2023, http://unfccc.int/national_reports/items/1408.php.

[9] Shell. *Shell LKW-Studie: Fakten, Trends und Perspektiven im Straßengüterverkehr bis 2030*. Tech. rep. 2010, p. 37.

[10] EXXON Mobil. *World Energy Outlook 2022 - Outlook for electricity*. Tech. rep. 2022, pp. 1–5.

[11] U.S. Energy Information Administration. *Annual Energy Outlook*. Tech. rep. 2023.

[12] John W. Brennan and Timothy E. Barder. *Battery Electric Vehicles vs . Internal Combustion Engine Vehicles : A United States-Based Comprehensive Assessment*. Tech. rep. 2016, p. 48.

[13] Gautam Kalghatgi. “Is it really the end of internal combustion engines and petroleum in transport?” In: *Applied Energy* 225.February (2018), pp. 965–974.

[14] R. D. Reitz, H. Ogawa, R. Payri, T. Fansler, S. Kokjohn, Y. Moriyoshi, A. K. Agarwal, D. Arcoumanis, D. Assanis, C. Bae, K. Boulouchos, M. Canakci, S. Curran, I. Denbratt, M. Gavaises, M. Guenthner, C. Hasse, Z. Huang, T. Ishiyama, B. Johansson, T. V. Johnson, G. Kalghatgi, M. Koike, S. C. Kong, A. Leipertz, P. Miles, R. Novella, A. Onorati, M. Richter, S. Shuai, D. Siebers, W. Su, M. Trujillo, N. Uchida, B. M. Vaglieco, R. M. Wagner, and H. Zhao. “IJER editorial: The future of the internal combustion engine”. In: *International Journal of Engine Research* 21.1 (2020), pp. 3–10.

[15] Kasper T. Møller, Torben R. Jensen, Etsuo Akiba, and Hai Wen Li. “Hydrogen - A sustainable energy carrier”. In: *Progress in Natural Science: Materials International* 27.1 (2017), pp. 34–40.

[16] Michael Fischer, Mathew Werber, and Peter V Schwartz. “Batteries: Higher energy density than gasoline?” In: *Energy Policy* 37.7 (2009), pp. 2639–2641.

[17] Jürgen Kern, Energy Systems Analysis, and Engineering Thermodynamics. “Decarbonisation or Defossilisation ? Innovative Alternative Fuels for the Aviation in Brazil . An international reference model . Sustainable Aviation Fuels in Practice”. In: *UNFCCC: Eleventh Meeting of the SBSTA Research Dialogue*. June 2019. 2020.

[18] Fraunhofer ISE. *Aktuelle Fakten zur Photovoltaik in Deutschland*. Tech. rep. 2023.

[19] Christoph Hank, Lukas Lazar, Franz Mantei, Mohamed Ouda, Robin J. White, Tom Smolinka, Achim Schaadt, Christopher Hebling, and Hans Martin Henning. “Comparative well-to-wheel life cycle assessment of OME3-5 synfuel production via the power-to-liquid pathway”. In: *Sustainable Energy and Fuels* 3.11 (2019), pp. 3219–3233.

[20] Daniel F. Rodríguez-Vallejo, Antonio Valente, Gonzalo Guillén-Gosálbez, and Benoît Chachuat. “Economic and life-cycle assessment of OME3-5as transport fuel: A comparison of production pathways”. In: *Sustainable Energy and Fuels* 5.9 (2021), pp. 2504–2516.

[21] Lukas Strauß, Sebastian Rieß, Michael Wensing, and Jonathan Martin. “Mixture formation of OME 3-5 and 1-Octanol in comparison with diesel-like Dodecane under ECN Spray A conditions”. In: 2023.January (2023), pp. 1–13.

[22] Tim Beutler, Niklas Prchal, and Michael Günthner. “Numerical Modeling of Diesel and Polyoxymethylene Dimethyl Ether Spray in a High Pressure Chamber Using the Fischer Primary Breakup Model”. In: *Automot. Engine Technol.* (2022).

[23] J V Pastor, A García, C Micó, F Lewiski, A Vassallo, and F C Pesce. “An optical investigation of combustion and soot formation in a single cylinder optical diesel engine for different e-fuels and piston bowl geometries”. In: *THIESEL 2020 Conference on Thermo- and Fluid Dynamic Processes in Direct Injection Engines High-pressure*. 2020, pp. 27–45.

[24] Liming Cai, S Jacob, F Lehn, R Langer, K A Heufer, and H Pitsch. “Automatic mechanism generation for auto-ignition of the promising e-fuels oxymethylene ethers (OMEn , n = 2-4)”. In: *1st International Conference on Smart Energy Carriers*. 2019, pp. 4–7.

[25] Liming Cai, Yasar Uygun, Casimir Togbé, Heinz Pitsch, Herbert Olivier, Philippe Dagaut, and S Mani Sarathy. “An experimental and modeling study of n-octanol combustion”. In: *Proceedings of the Combustion Institute* 35.1 (2015), pp. 419–427.

[26] M. Pelucchi, S. Namysl, E. Ranzi, A. Rodriguez, C. Rizzo, K. P. Somers, Y. Zhang, O. Herbinet, H. J. Curran, F. Battin-Leclerc, and T. Faravelli. “Combustion of n-C3-C6Linear Alcohols: An Experimental and Kinetic Modeling Study. Part II: Speciation Measurements in a Jet-Stirred Reactor, Ignition Delay Time Measurements in a Rapid Compression Machine, Model Validation, and Kinetic Analysis”. In: *Energy and Fuels* 34.11 (2020), pp. 14708–14725.

[27] Michael H.H. Fechter, Jessica Koschack, and Andreas S. Braeuer. “Vapor-Liquid equilibria of the systems 1-octanol/nitrogen and 1-octanol/oxygen at pressures from 3 to 9 MPa and temperatures up to 613 K – Measured in a microcapillary with Raman spectroscopy”. In: *Fuel* 323.March (2022).

[28] Andreas Peter, B Siewert, S Riess, L Strauss, C Pastoetter, and M M Wensing. “Mixture formation analysis of polyoxymethylenether injection”. In: *Atomization and Sprays* 30.11 (2020), pp. 843–859.

[29] Ian Sofian Yunus, Zhixuan Wang, Pachara Sattayawat, Jonathan Muller, Fessehaye W. Zemichael, Klaus Hellgardt, and Patrik R. Jones. “Improved Bioproduction of 1-Octanol Using Engineered Synechocystis sp. PCC 6803”. In: *ACS Synthetic Biology* 10.6 (2021), pp. 1417–1428.

[30] Deepak S. Desai and Ganapati D. Yadav. “Green Synthesis of Furfural Acetone by Solvent-Free Aldol Condensation of Furfural with Acetone over La2O3-MgO Mixed Oxide Catalyst”. In: *Industrial and Engineering Chemistry Research* 58.35 (2019), pp. 16096–16105.

[31] Jennifer Julis and Walter Leitner. “Synthesis of 1-octanol and 1,1-dioctyl ether from biomass-derived platform chemicals”. In: *Angewandte Chemie - International Edition* 51.34 (2012), pp. 8615–8619.

[32] M. Kalim Akhtar, Hariharan Dandapani, Kati Thiel, and Patrik R. Jones. “Microbial production of 1-octanol: A naturally excreted biofuel with diesel-like properties”. In: *Metabolic Engineering Communications* 2 (2015), pp. 1–5.

[33] Qineng Xia, Yinjiang Xia, Jinxu Xi, Xiaohui Liu, and Yanqin Wang. “Energy-efficient production of 1-octanol from biomass-derived furfural-acetone in water”. In: *Green Chemistry* 17.8 (2015), pp. 4411–4417.

[34] Florian Kremer, Lars M. Blank, Patrik R. Jones, and M. Kalim Akhtar. “A comparison of the microbial production and combustion characteristics of three alcohol biofuels: Ethanol, 1-butanol, and 1-octanol”. In: *Frontiers in Bioengineering and Biotechnology* 3.AUG (2015), pp. 1–7.

[35] María Santos-Merino, M. Pilar Garcillán-Barcia, and Fernando De La Cruz. “Engineering the fatty acid synthesis pathway in Synechococcus elongatus PCC 7942 improves omega-3 fatty acid production”. In: *Biotechnology for Biofuels* 11.1 (2018), pp. 1–13.

[36] Christian Henning Gierlich, Kassem Beydoun, Jürgen Klankermayer, and Regina Palkovits. “Challenges and Opportunities in the Production of Oxymethylene Dimethylether”. In: *Chemie-Ingenieur-Technik* 92.1-2 (2020), pp. 116–124.

[37] Niklas Schmitz, Jakob Burger, Eckhard Ströfer, and Hans Hasse. “From methanol to the oxygenated diesel fuel poly(oxymethylene) dimethyl ether: An assessment of the production costs”. In: *Fuel* 185 (2016), pp. 67–72.

[38] Aleksandar Damyanov, Peter Hofmann, Bernhard Geringer, Nikolaus Schwaiger, Thomas Pichler, and Matthäus Siebenhofer. “Biogenous ethers: production and operation in a diesel engine”. In: *Automotive and Engine Technology* 3.1-2 (2018), pp. 69–82.

[39] Jakob Burger, Eckhard Ströfer, and Hans Hasse. “Production process for diesel fuel components poly(oxymethylene) dimethyl ethers from methane-based products by hierarchical optimization with varying model depth”. In: *Chemical Engineering Research and Design* 91.12 (2013), pp. 2648–2662.

[40] Mei Rong Kang, He Yuan Song, Fu Xiang Jin, and Jing Chen. “Synthesis and physicochemical characterization of polyoxymethylene dimethyl ethers”. In: *Ranliao Huaxue Xuebao/Journal of Fuel Chemistry and Technology* 45.7 (2017), pp. 837–845.

[41] Yannic Tönges, Vincent Dieterich, Sebastian Fendt, Hartmut Spliethoff, and Jakob Burger. “Techno-Economic Analysis of Large Scale Production of Poly(oxymethylene) Dimethyl Ether Fuels from Methanol in Water-Tolerant Processes”. In: *Fuels* 4.1 (2023), pp. 1–18.

[42] Falko Ueckerdt, Christian Bauer, Alois Dirnaichner, Jordan Everall, Romain Sacchi, and Gunnar Luderer. “Potential and risks of hydrogen-based e-fuels in climate change mitigation”. In: *Nature Climate Change* 11.5 (2021), pp. 384–393.

[43] Barbara (FEV) Graziano, Sascha (FEV) Schönfeld, Heuser (FEV) Benedikt, and Dominik (Daimler Truck AG) Pelerin. “1-Octanol as CO 2 -neutral Fuel for Commercial Vehicle Applications”. In: *atzelectronics-magazine* 04|2020.DEVELOPMEheavyduty worldwide (2020), pp. 36–41.

[44] Tankai Zhang, Karin Munch, and Ingemar Denbratt. “An Experimental Study on the Use of Butanol or Octanol Blends in a Heavy Duty Diesel Engine”. In: *SAE International Journal of Fuels and Lubricants* 8.3 (2015), pp. 610–621.

[45] B. Rajesh Kumar, S. Saravanan, D. Rana, V. Anish, and A. Nagendran. “Effect of a sustainable biofuel - N-octanol - on the combustion, performance and emissions of a di diesel engine under naturally aspirated and exhaust gas recirculation (EGR) modes”. In: *Energy Conversion and Management* 118 (2016), pp. 275–286.

[46] Melvin Victor De Poures, Sathiyagnanam A.P, Dipak Rana, Rajesh Kumar Babu, Saravanan Subramani, Balaji Sethuramasamyraja, and D. Damodharan. “Using renewable n-octanol in a non-road diesel engine with some modifications”. In: *Energy Sources, Part A: Recovery, Utilization and Environmental Effects* 41.10 (2019), pp. 1194–1208.

[47] Daniel Klein and Stefan Pischinger. “Laser-Induced Incandescence Measurements of Tailor-Made Fuels in an Optical Single-Cylinder Diesel Engine”. In: *SAE International Journal of Engines* 10.3 (2017), pp. 1143–1154.

[48] Qiwei Wang, Rong Huang, Jimin Ni, and Qinqing Chen. “Potential improvement in PM-NOx trade-off in a compression ignition engine by N-octanol addition and injection pressure”. In: *Processes* 9.2 (2021), pp. 1–17.

[49] Irene Ruiz-Rodriguez, Roger Cracknell, Michael Parkes, Thanos Megaritis, and Lionel Ganippa. “Experimental study of the effect of C8 oxygenates on sooting processes in high pressure spray flames”. In: *Combustion and Flame* 220 (2020), pp. 235–246.

[50] Mingzhang Pan, Zeyuan Zheng, Rong Huang, Xiaorong Zhou, Haozhong Huang, Jiaying Pan, and Zhaohui Chen. “Reduction in PM and NOX of a diesel engine integrated with n-octanol fuel addition and exhaust gas recirculation”. In: *Energy* 187.X (2019).

[51] Irene Ruiz-Rodriguez, Roger Cracknell, Michael Parkes, Thanos Megaritis, and Lionel Ganippa. “Evaluating the potential of a long carbon chain oxygenate (octanol) on soot reduction in diesel engines”. In: *Proceedings of the International Conference on Internal Combustion Engines and Powertrain Systems for Future Transport.* (2019), pp. 227–238.

[52] Haoye Liu, Zhi Wang, Jianxin Wang, Xin He, Yanyan Zheng, Qiang Tang, and Jinfu Wang. “Performance, combustion and emission characteristics of a diesel engine fueled with polyoxymethylene dimethyl ethers (PODE3-4)/ diesel blends”. In: *Energy* 88 (2015), pp. 793–800.

[53] Florian Zacherl, Christoph Wopper, Peter Schwanzer, and Hans-Peter Rabl. “Potential of the Synthetic Fuel Oxymethylene Ether (OME) for the Usage in a Single-Cylinder Non-Road Diesel Engine: Thermodynamics and Emissions”. In: *Energies* 15.21 (2022).

[54] Christophe Barro, Matteo Parravicini, Konstantinos Boulouchos, and Anthi Liati. “Neat polyoxymethylene dimethyl ether in a diesel engine; part 2: Exhaust emission analysis”. In: *Fuel* 234.July (2018), pp. 1414–1421.

[55] Ricardo Novella, Gabriela Bracho, Josep Gomez-Soriano, Cássio S. Fernandes, and Tommaso Lucchini. “Combustion system optimization for the integration of e-fuels (Oxymethylene Ether) in compression ignition engines”. In: *Fuel* 305.July (2021).

[56] Jialin Liu, Lei Feng, Hu Wang, Zunqing Zheng, Beiling Chen, Diping Zhang, and Mingfa Yao. “Spray characteristics of gasoline/PODE and diesel/PODE blends in a constant volume chamber”. In: *Applied Thermal Engineering* 159 (2019).

[57] Qinjie Lin, Kun Lin Tay, Wenbin Yu, Wenming Yang, and Zhi Wang. “Effects of polyoxymethylene dimethyl ether 3 (PODE3) addition and injection pressure on combustion performance and particle size distributions in a diesel engine”. In: *Fuel* 283 (Jan. 2021).

[58] Björn Lumpp, Dieter Rothe, Christian Pastötter, Reinhard Lämmermann, and Eberhard Jacob. “Oxymethylenether als Dieselkraftstoffzusätze der Zukunft”. In: *MTZ - Motortechnische Zeitschrift* 72.3 (2011), pp. 198–203.

[59] D Goeb, M Bode, M Davidovic, L Cai, T Ottenwälder, S Jacobs, S Pischinger, K A Heufer, and H Pitsch. “High-fidelity simulations and experiments of oxymethylene ether spray ignition.” In: *Proceedings of the European Combustion Meeting 2019*. Portugal, 2019.

[60] Donghua Li, Yuxin Gao, Shenghua Liu, Zhijie Ma, and Yanju Wei. “Effect of polyoxymethylene dimethyl ethers addition on spray and atomization characteristics using a common rail diesel injection system”. In: *Fuel* 186 (2016), pp. 235–247.

[61] Stefano Emanuele Iannuzzi, Christophe Barro, Konstantinos Boulouchos, and Jakob Burger. “Combustion behavior and soot formation/oxidation of oxygenated fuels in a cylindrical constant volume chamber”. In: *Fuel* 167 (2016), pp. 49–59.

[62] Robert Schmitz, Mariano Sirignano, Christian Hasse, and Federica Ferraro. “Numerical Investigation on the Effect of the Oxymethylene Ether-3 (OME3) Blending Ratio in Premixed Sooting Ethylene Flames”. In: *Frontiers in Mechanical Engineering* 7 (2021).

[63] Yong Ren Tan, Maria L. Botero, Yuan Sheng, Jochen A.H. Dreyer, Rong Xu, Wenming Yang, and Markus Kraft. “Sooting characteristics of polyoxymethylene dimethyl ether blends with diesel in a diffusion flame”. In: *Fuel* 224.November 2017 (2018), pp. 499–506.

[64] Simon LeBlanc, Xiao Yu, Gared Pisciotto, Xiaoye Han, Jimi Tjong, and Ming Zheng. “Impact of fuel injection pressure on spray and combustion characteristics of OME and diesel blends”. In: *Proceedings of ASME 2021 Internal Combustion Engine Division Fall Technical Conference, ICEF 2021* Ic (2021), pp. 1–12.

[65] Jingjing He, Xin Su, Hao Chen, Yisong Chen, Xinfeng Zhang, Yanfang Liu, Zhilin Tian, and Hongming Xu. “Spray and combustion characteristics of polyoxymethylene dimethyl ethers and diesel blends in a constant volume chamber”. In: *Energy Reports* 8 (2022), pp. 1056–1066.

[66] Yue Ma, Longxi Cui, Xiao Ma, and Jianxin Wang. “Optical study on spray combustion characteristics of PODE/diesel blends in different ambient conditions”. In: *Fuel* 272.November 2019 (2020).

[67] Yong Ren Tan, Maurin Salamanca, Laura Pascazio, Jethro Akroyd, and Markus Kraft. “The effect of poly(oxymethylene) dimethyl ethers (PODE3) on soot formation in ethylene/PODE3 laminar coflow diffusion flames”. In: *Fuel* 283.July 2020 (2021).

[68] Giovanni Avolio, Oliver Kastner, Gerd Rösel, and Rolf Brück. “Der Einfluss synthetischer Kraftstoffe auf die Dieselmotor-Emissionen”. In: *MTZ- Motortechnische Zeitschrift* 79.7-8 (June 2018), pp. 16–23.

[69] Markus Münz, Alexander Mokros, David Töpfer, and Christian Beidl. “OME- Partikelbewertung unter Realfahrbedingungen”. In: *MTZ - Motortechnische Zeitschrift* 79.3 (Feb. 2018), pp. 16–21.

[70] Stephan Kabelac, Matthias Kind, Holger Martin, Dieter Mewes, Karlheinz Schaber, and Peter Stephan. *VDI-Wärmeatlas, 11. Auflage*. 2013.

[71] D. Ambrose, C. H.S. Sprake, and R. Townsend. “Thermodynamic properties of organic oxygen compounds XXXVII. Vapour pressures of methanol, ethanol, pentan-1-ol, and octan-1-ol from the normal boiling temperature to the critical temperature”. In: *The Journal of Chemical Thermodynamics* 7.2 (1975), pp. 185–190.

[72] Richard H Boyd. “Some physical properties of polyoxymethylene dimethyl ethers”. In: *Journal of Polymer Science* 50.153 (1961), pp. 133–141.

[73] Aditya Kulkarni, Edder J Garcia, Angelo Damone, Michael Schappals, Simon Stephan, Maximilian Kohns, and Hans Hasse. “A Force Field for Poly(oxymethylene) Dimethyl Ethers OMEn”. In: *Journal of Chemical Theory and Computation* 16.4 (Mar. 2020), pp. 2517–2528.

[74] Haoran Li and Ming Jia. “Measurements and Derivation of the Spray Simulation Required Physical Properties of Polyoxymethylene Dimethyl Ethers (PODEn)”. In: *International Journal of Thermophysics* 44.3 (Mar. 2023).

[75] Jing Li, Dezhi Zhou, and Wenming Yang. “A multi-component reaction mechanism of n-butanol, n-octanol, and di-n-buthylether for engine combustion”. In: *Fuel* 275 (2020).

[76] M. Pelucchi, S. Namysl, E. Ranzi, A. Rodriguez, C. Rizzo, K. P. Somers, Y. Zhang, O. Herbinet, H. J. Curran, F. Battin-Leclerc, and T. Faravelli. “Combustion of n-C3-C6Linear Alcohols: An Experimental and Kinetic Modeling Study. Part II: Speciation Measurements in a Jet-Stirred Reactor, Ignition Delay Time Measurements in a Rapid Compression Machine, Model Validation, and Kinetic Analysis”. In: *Energy and Fuels* 34.11 (2020), pp. 14708–14725.

[77] Wenyu Sun, Guoqing Wang, Shuang Li, Ruzheng Zhang, Bin Yang, Jiuzhong Yang, Yuyang Li, Charles K Westbrook, and Chung K Law. “Speciation and the laminar burning velocities of poly(oxymethylene) dimethyl ether 3 (POMDME3) flames: An experimental and modeling study”. In: *Proceedings of the Combustion Institute* 36.1 (2017), pp. 1269–1278.

[78] Tanjin He, Zhi Wang, Xiaoqing You, Haoye Liu, Yingdi Wang, Xiaoyu Li, and Xin He. “A chemical kinetic mechanism for the low- and intermediate-temperature combustion of Polyoxymethylene Dimethyl Ether 3 (PODE3)”. In: *Fuel* 212.May 2017 (2018), pp. 223–235.

[79] Bo Niu, Ming Jia, Yachao Chang, Huiquan Duan, Xue Dong, and Pengzhi Wang. “Construction of reduced oxidation mechanisms of polyoxymethylene dimethyl ethers (PODE1–6) with consistent structure using decoupling methodology and reaction rate rule”. In: *Combustion and Flame* 232 (Oct. 2021).

[80] Dorian Oestreich. “Prozessentwicklung zur Gewinnung von Oxymethylenethern (OME) aus Methanol und Formaldehyd”. PhD thesis. 2017.

[81] *Engine Combustion Network*.

[82] José V. Pastor, José M. García-Oliver, Carlos Micó, and Alba A. García-Carrero. “An experimental study with renewable fuels using ECN Spray A and D nozzles”. In: *International Journal of Engine Research* 23.10 (2022), pp. 1748–1759.

[83] Jaime Gimeno, Gabriela Bracho, Pedro Martí-Aldaraví, and Jesús E Peraza. “Experimental study of the injection conditions influence over n-dodecane and diesel sprays with two ECN single-hole nozzles. Part I: Inert atmosphere”. In: *Energy Conversion and Management* 126 (2016), pp. 1146–1156.

[84] Maarten Meijer, Bart Somers, Jaclyn Johnson, Jeffrey Naber, Seong Young Lee, Louis Marie Malbec, Gilles Bruneaux, Lyle M Pickett, Michele Bardi, Raul Payri, and Tim Bazyn. “Engine Combustion Network (ECN): Characterization and comparison of boundary conditions for different combustion vessels”. In: *Atomization and Sprays* 22.9 (2012), pp. 777–806.

[85] Scott A. Skeen, Julien Manin, Kristine Dalen, and Lyle M. Pickett. “Extinction-based imaging of soot processes over a range of diesel operating conditions”. In: *8th US National Combustion Meeting 2013* 3 (2013), pp. 1981–1993.

[86] Zachary Falgout, Mattias Rahm, Zhenkan Wang, and Mark Linne. “Evidence for supercritical mixing layers in the ECN Spray A”. In: *Proceedings of the Combustion Institute* 35.2 (2015), pp. 1579–1586.

[87] Michele Bardi, Raul Payri, Louis Marie Malbec, Gilles Bruneaux, Lyle M. Pickett, Julien Manin, Tim Bazyn, and Caroline Genzale. “Engine combustion network: Comparison of spray development, vaporization, and combustion in different combustion vessels”. In: *Atomization and Sprays* 22.10 (2012), pp. 807–842.

[88] Noud Maes, Maarten Meijer, Nico Dam, Bart Somers, Hubert Baya Toda, Gilles Bruneaux, Scott A. Skeen, Lyle M. Pickett, and Julien Manin. “Characterization of Spray A flame structure for parametric variations in ECN constant-volume vessels using chemiluminescence and laser-induced fluorescence”. In: *Combustion and Flame* 174 (2016), pp. 138–151.

[89] S. Ayyapureddi, U. Egüz, C. Bekdemir, L. M.T. Somers, and L. P.H. De Goey. “Application of the FGM method to spray a conditions of the ECN database”. In: *ICLASS 2012 - 12th International Conference on Liquid Atomization and Spray Systems* 2012 (2012).

[90] Armin Wehrfritz, Ossi Kaario, Ville Vuorinen, and Bart Somers. “Large Eddy Simulation of n-dodecane spray flames using Flamelet Generated Manifolds”. In: *Combustion and Flame* 167 (2016), pp. 113–131.

[91] Armin Wehrfritz. “Large Eddy Simulation of Fuel Spray Combustion”. PhD thesis. Aalto University, 2016.

[92] Leonardo Pachano, Chao Xu, Jose M. García-Oliver, Jose M. Pastor, Ricardo Novella, and Prithwish Kundu. “A two-equation soot-in-flamelet modeling approach applied under Spray A conditions”. In: *Combustion and Flame* 231 (2021), pp. 1–4.

[93] Sandro Gierth. “Advanced flamelet tabulation strategies for Large Eddy Simulations of single- and multi-phase turbulent jet flames”. PhD thesis. Darmstadt: Technische Universität, 2022.

[94] Sebastian Popp, Sandro Gierth, Christian Hasse, and Sandra Hartl. “Flame regimes in DI diesel combustion: LES study for light-and heavy-duty injectors”. In: *Combustion and Flame* 252 (2023).

[95] J M García-Oliver, R Novella, J M Pastor, and L Pachano. “Computational study of ECN Spray A and Spray D combustion at different ambient temperature conditions”. In: *Transportation Engineering* 2.August (2020).

[96] Jiun Cai Ong, Kar Mun Pang, Xue Song Bai, Mehdi Jangi, and Jens Honore Walther. “Large-eddy simulation of n-dodecane spray flame: Effects of nozzle diameters on autoignition at varying ambient temperatures”. In: *Proceedings of the Combustion Institute* 38.2 (2021), pp. 3427–3434.

[97] Min Zhang, Jiun Cai Ong, Kar Mun Pang, Xue Song Bai, and Jens H. Walther. “Large eddy simulation of transient combustion and soot recession in the ECN Spray A and D flames”. In: *Fuel* 329.May (2022).

[98] Jan Matheis and Stefan Hickel. “Multi-component vapor-liquid equilibrium model for LES of high-pressure fuel injection and application to ECN Spray A”. In: *International Journal of Multiphase Flow* 99 (2018), pp. 294–311.

[99] Mahmoud Gadalla, Jeevananthan Kannan, Bulut Tekgül, Shervin Karimkashi, Ossi Kaario, and Ville Vuorinen. “Large-eddy simulation of ECN spray a: Sensitivity study on modeling assumptions”. In: *Energies* 13.13 (2020), pp. 1–24.

[100] Wai Tong Chung, Peter C. Ma, and Matthias Ihme. “Examination of diesel spray combustion in supercritical ambient fluid using large-eddy simulations”. In: *International Journal of Engine Research* 21.1 (2020), pp. 122–133.

[101] Marco Davidovic, Tobias Falkenstein, Mathis Bode, Liming Cai, Seongwon Kang, Jörn Hinrichs, and Heinz Pitsch. “LES of n -Dodecane Spray Combustion Using a Multiple Representative Interactive Flamelets Model”. In: *Oil and Gas Science and Technology* 72.5 (2017).

[102] Dominik Goeb, Marco Davidovic, Liming Cai, Pankaj Pancharia, Mathis Bode, Sascha Jacobs, Joachim Beeckmann, Werner Willems, Karl Alexander Heufer, and Heinz Pitsch. “Oxymethylene ether – n-dodecane blend spray combustion: Experimental study and large-eddy simulations”. In: *Proceedings of the Combustion Institute* 38.2 (2021), pp. 3417–3425.

[103] Tuan M. Nguyen, Rainer N. Dahms, Lyle M. Pickett, and Fabien Tagliante. “The Corrected Distortion model for Lagrangian spray simulation of transcritical fuel injection”. In: *International Journal of Multiphase Flow* 148.June 2021 (2022).

[104] Andrea Di Matteo, Hesheng Bao, and Bart Somers. “Modeling Spray C and Spray D with FGM within the framework of RANS and LES”. In: *Frontiers in Mechanical Engineering* 8.November (2022), pp. 1–17.

[105] Jiun Cai Ong, Kar Mun Pang, Xue Song Bai, Mehdi Jangi, and Jens Honore Walther. “Large-eddy simulation of n-dodecane spray flame: Effects of nozzle diameters on autoignition at varying ambient temperatures”. In: *Proceedings of the Combustion Institute* 38.2 (2021), pp. 3427–3434.

[106] Johannes Palmer, Mogan Ramesh, Valeri Kirsch, Manuel Reddemann, and Reinhold Kneer. “Spray Analysis of C8H18O Fuel Blends Using High-Speed Schlieren Imaging and Mie Scattering”. In: *SAE Technical Papers* 2015-Septe.September (2015).

[107] Junjian Tian, Yu Liu, Fengyu Li, Kai Han, Wenliang Zhou, Qizhao Lin, and Kesheng Meng. “Experimental study on spray characteristics of octanol biodiesel and modification of spray tip penetration model”. In: *Physics of Fluids* 33.9 (2021).

[108] Toni Dageförde, Karsten Gröger, Noritsune Kawaharada, and Friedrich Dinkelacker. “Velocity Field Measurements with High Speed Structural Image Velocimetry in the Primary Atomization Region of Future Diesel Fuels”. In: *SAE Technical Papers* 2020 (2020).

[109] Srijna Singh, Akhil Ailaboina, Michele Battistoni, and Mohammad Danish. “Numerical Investigation of Cavitation Behaviour for Dodecane and OME3 Fuel in ECN Spray C Injector Nozzle Numerical Investigation of Cavitation Behaviour for Dodecane and OME 3 Fuel in ECN Spray C Injector Nozzle”. In: July (2022).

[110] José V. Pastor, José M. García-Oliver, Carlos Micó, Alba A. García-Carrero, and Arantzazu Gómez. “Experimental study of the effect of hydrotreated vegetable oil and oxymethylene ethers on main spray and combustion characteristics under engine combustion network spray A conditions”. In: *Applied Sciences (Switzerland)* 10.16 (2020).

[111] Jose V. Pastor, Jose M. García-Oliver, Carlos Micó, and Francisco J. Tejada. “Characterization of the oxymethylene ether fuels flame structure for ECN Spray A and Spray D nozzles”. In: *Applied Energy* 332 (Feb. 2023).

[112] Daniel Mira, Eduardo J. Pérez-Sánchez, Anurag Surapaneni, Jesús Benajes, José M. García-Oliver, José M. Pastor, and Daiana De León. “LES study on spray combustion with renewable fuels under ECN spray-a conditions”. In: *Proceedings of ASME 2021 Internal Combustion Engine Division Fall Technical Conference, ICEF 2021*. American Society of Mechanical Engineers, Oct. 2021, pp. 1–11.

[113] Frederik Wiesmann, Lukas Strauß, Sebastian Rieß, Julien Manin, Kevin Wan, and Thomas Lauer. “Numerical and Experimental Investigations on the Ignition Behavior of OME”. In: *Energies* 15.18 (Sept. 2022).

[114] Jesus Benajes, Jose M. Garcia-Oliver, Jose M. Pastor, and Daiana De Leon-Ceriani. “Unsteady Flamelet modeling study on OMEx-type fuels under Engine Combustion Network Spray A conditions”. In: *Fuel* 331.April (2023).

[115] Thierry Poinsot and Denis Veynante. *Theoretical and numerical combustion*. 2012.

[116] J. Boussinesq. “Theorie de l’ecoulement tourbillant”. In: *Memoires presentes par divers savants a l’Academie des Sciences* 23 (1877), pp. 46–50.

[117] Osborne Reynolds. “XXIX. An experimental investigation of the circumstances which determine whether the motion of water shall be direct or sinuous, and of the law of resistance in parallel channels”. In: *Philosophical Transactions of the Royal Society of London* 174 (Dec. 1883), pp. 935–982.

[118] Jochen Fröhlich. *Large Eddy Simulation turbulenter Strömungen*. Wiesbaden: Teubner, 2006.

[119] Stephen B. Pope. *Turbulent Flows*. Cambridge University Press, Aug. 2000.

[120] J. SMAGORINSKY. “GENERAL CIRCULATION EXPERIMENTS WITH THE PRIMITIVE EQUATIONS”. In: *Monthly Weather Review* 91.3 (Mar. 1963), pp. 99–164.

[121] A. Leonard. “Energy Cascade in Large-Eddy Simulations of Turbulent Fluid Flows”. In: 1975, pp. 237–248.

[122] U. Schumann. “Subgrid scale model for finite difference simulations of turbulent flows in plane channels and annuli”. In: *Journal of Computational Physics* 18.4 (Aug. 1975), pp. 376–404.

[123] A. Wehrfritz, V. Vuorinen, O. Kaario, and M. Larmi. “Large eddy simulation of high-velocity fuel sprays: Studying mesh resolution and breakup model effects for spray A”. In: *Atomization and Sprays* 23.5 (2013), pp. 419–442.

[124] Q Xue, S Som, P K Senecal, and E Pomraning. “A Study of Grid Resolution and SGS Models for LES under Non-reacting Spray Conditions”. In: *ILASS Americas* 25.May (2013).

[125] Carlos Härtel. “Turbulent flows”. In: *Handbook of Computational Fluid Mechanics*. Elsevier, 1996, pp. 283–338.

[126] J. P. Boris, F. F. Grinstein, E. S. Oran, and R. L. Kolbe. “New insights into large eddy simulation”. In: *Fluid Dynamics Research* 10.4-6 (1992), pp. 199–228.

[127] Franck Nicoud, Hubert Baya Toda, Olivier Cabrit, Sanjeeb Bose, and Jungil Lee. “Using singular values to build a subgrid-scale model for large eddy simulations”. In: *Physics of Fluids (1994-present)* 23.8 (2011).

[128] M. Rieth, F. Proch, O. T. Stein, M. W.A. Pettit, and A. M. Kempf. “Comparison of the Sigma and Smagorinsky LES models for grid generated turbulence and a channel flow”. In: *Computers and Fluids* 99 (2014), pp. 172–181.

[129] Bonnie J. McBride, Sandford Gordon, and Martin A. Reno. *Coefficents for Calculating Thermodynamic and Transport Properties of Individual Species*. Tech. rep. 1993.

[130] *CHEMKIN 10112 Reaction Design: San Diego, 2011*. 2011.

[131] David G Goodwin, Harry K Moffat, Ingmar Schoegl, Raymond L Speth, and Bryan W Weber. *Cantera: An Object-oriented Software Toolkit for Chemical Kinetics, Thermodynamics, and Transport Processes*. 2022.

[132] R B Bird, W E Stewart, and E N Lightfoot. *Transport Phenomena*. J. Wiley, 2002.

[133] Robert J Kee. *Chemically reacting flow: theory and practice*. Vol. 41. 01. 2003.

[134] Pauli Virtanen, Ralf Gommers, Travis E Oliphant, Matt Haberland, Tyler Reddy, David Cournapeau, Evgeni Burovski, Pearu Peterson, Warren Weckesser, Jonathan Bright, Stéfan J van der Walt, Matthew Brett, Joshua Wilson, K Jarrod Millman, Nikolay Mayorov, Andrew R J Nelson, Eric Jones, Robert Kern, Eric Larson, C J Carey, İlhan Polat, Yu Feng, Eric W Moore, Jake VanderPlas, Denis Laxalde, Josef Perktold, Robert Cimrman, Ian Henriksen, E A Quintero, Charles R Harris, Anne M Archibald, Antônio H Ribeiro, Fabian Pedregosa, Paul van Mulbregt, and SciPy 1.0 Contributors. “{SciPy} 1.0: Fundamental Algorithms for Scientific Computing in Python”. In: *Nature Methods* 17 (2020), pp. 261–272.

[135] C. R. Wilke. “A viscosity equation for gas mixtures”. In: *The Journal of Chemical Physics* 18.4 (1950), pp. 517–519.

[136] S. Mathur and S. C. Saxena. “Viscosity of polar gas mixtures: Wilke’s method”. In: *Applied Scientific Research* 15.1 (1965), pp. 404–410.

[137] Daniel Rettenmaier. “Numerical Simulation of Shear Driven Wetting”. PhD thesis. Darmstadt: Technische Universität, Jan. 2019.

[138] M Blume and Shaker Verlag. *3D Flow Simulation for the Investigation of Cavitation and Its Relationship To Erosion, Turbulence and Primary Breakup in Hydraulic Components by Single-Fluid Multi-Phase Methods*. Berichte aus der Strömungstechnik. Shaker Verlag, 2021.

[139] A. Vallet, A. A. Burluka, and R. Borghi. “Development of a Eulerian model for the "Atomization" of a liquid jet”. In: *Atomization and Sprays* 11.6 (2001), pp. 619–642.

[140] Jose M Desantes, Jose M Garcia-Oliver, Ricardo Novella, and Leonardo Pachano. “A numerical study of the effect of nozzle diameter on diesel combustion ignition and flame stabilization”. In: *International Journal of Engine Research* 21.1 (2020), pp. 101–121.

[141] Peter C. Ma, Hao Wu, Thomas Jaravel, Luis Bravo, and Matthias Ihme. “Large-eddy simulations of transcritical injection and auto-ignition using diffuse-interface method and finite-rate chemistry”. In: *Proceedings of the Combustion Institute* 37.3 (2019), pp. 3303–3310.

[142] F. A. Williams. “Spray combustion and atomization”. In: *Physics of Fluids* 1.6 (1958), pp. 541–545.

[143] Rolf D. Reitz. *Reitz - 1978 - Atomization and other Breakup Reigmes of a Liquid Jet.pdf*. 1978.

[144] F H Harlow, M Evans, and R D Richtmyer. *A Machine Calculation Method for Hydrodynamic Problems*. LAMS (Los Alamos Scientific Laboratory). Los Alamos Scientific Laboratory of the University of California, 1955.

[145] John K. Dukowicz. “A particle-fluid numerical model for liquid sprays”. In: *Journal of Computational Physics* 35.2 (1980), pp. 229–253.

[146] Peter J. O’rourke, J. U. Brackbill, and Bernard Larrouturou. “On particle-grid interpolation and calculating chemistry in particle-in-cell methods”. In: *Journal of Computational Physics* 109.1 (1993), pp. 37–52.

[147] Alex B. Liu, Daniel Mather, and Rolf D. Reitz. “Modeling the effects of drop drag and breakup on fuel sprays”. In: *SAE Technical Papers* 412 (1993).

[148] B. Abramzon and W.A. Sirignano. “Droplet vaporization model for spray combustion calculations”. In: *International Journal of Heat and Mass Transfer* 32.9 (Sept. 1989), pp. 1605–1618.

[149] By D B Spalding. “COMBUSTION OF LIQUID FUELS 847 Symbol a B b THE COMBUSTION OF LIQUID FUELS”. In: *Symposium (international) on combustion* 4 (1953), pp. 847–864.

[150] W.R. Ranz W.E. Marshall. “Evaporation from Drops: Part 1-2”. In: *Chemical Engineering Progress* 48 (1952), pp. 141–146.

[151] G.L. Hubbard, V.E. Denny, and A.F. Mills. “Droplet evaporation: Effects of transients and variable properties”. In: *International Journal of Heat and Mass Transfer* 18.9 (Sept. 1975), pp. 1003–1008.

[152] M. C. YUEN and L. W. CHEN. “On Drag of Evaporating Liquid Droplets”. In: *Combustion Science and Technology* 14.4-6 (Oct. 1976), pp. 147–154.

[153] Peter Keller. “Numerical Simulation of Multicomponent Fuel Evaporation”. PhD thesis. 2015.

[154] P. Rosin and E. Rammler. “The Laws Governing the Fineness of Powdered Coal”. In: *Journal of the Institute of Fuel* 7 (1933), pp. 29–36.

[155] Tobias Knorsch, Markus Heldmann, Lars Zigan, Michael Wensing, and Alfred Leipertz. “On the role of physiochemical properties on evaporation behavior of DISI biofuel sprays”. In: *Experiments in Fluids* 54.6 (June 2013).

[156] Matthias Koegl, Yogeshwar Nath Mishra, Kevin Baderschneider, Chris Conrad, Bastian Lehnert, Stefan Will, and Lars Zigan. “Planar droplet sizing for studying the influence of ethanol admixture on the spray structure of gasoline sprays”. In: *Experiments in Fluids* 61.10 (2020), pp. 1–20.

[157] Peter J. O’Rourke and Anthony A. Amsden. “The Tab Method for Numerical Calculation of Spray Droplet Breakup”. In: Nov. 1987.

[158] F. X. Tanner. “Liquid jet atomization and droplet breakup modeling of non-evaporating diesel fuel sprays”. In: *SAE Technical Papers* 106 (1997), pp. 127–140.

[159] Rolf D Reitz. “Modeling atomization processes in high-pressure vaporizing sprays”. In: *Atomisation Spray Technology* 3.4 (Jan. 1987), pp. 309–337.

[160] R. D. Reitz and R. Diwakar. “Structure of high-pressure fuel sprays”. In: *SAE Technical Papers* 96 (1987), pp. 492–509.

[161] Rolf D Reitz and Jennifer C Beale. “Modeling spray atomization with the Kelvin-Helmholtz/Rayleigh-Taylor hybrid model”. In: *Atomization and Sprays* 9.6 (1999), pp. 623–650.

[162] Jeffrey D Naber and Dennis L Siebers. “Effects of gas density and vaporization on penetration and dispersion of diesel sprays”. In: *SAE Technical Papers* 412 (1996).

[163] Sibendu Som and Suresh K Aggarwal. “Modeling diesel spray flame lift-off using detailed chemistry and a new primary breakup model”. In: *47th AIAA Aerospace Sciences Meeting including the New Horizons Forum and Aerospace Exposition* January (2009), pp. 1–14.

[164] S Som and S K Aggarwal. “Effects of primary breakup modeling on spray and combustion characteristics of compression ignition engines”. In: *Combustion and Flame* 157.6 (2010), pp. 1179–1193.

[165] Fabian Fischer, B Heine, and C Tropea. “Primary Breakup Model Considering Spray Core Development”. In: *Ilasseurope2010.Org* September (2010), pp. 1–9.

[166] Fabian Fischer. “Primary Breakup Model Considering the Spray Core Development”. PhD thesis. 2011, p. 138.

[167] OpenFOAM. *OpenFOAM v2012, https://www.openfoam.com/news/main-news/openfoam-v20-12/*. 2020.

[168] Ludger Lautenschütz, Dorian Oestreich, Philipp Seidenspinner, Ulrich Arnold, Eckhard Dinjus, and Jörg Sauer. “Physico-chemical properties and fuel characteristics of oxymethylene dialkyl ethers”. In: *Fuel* 173 (June 2016), pp. 129–137.

[169] Haoran Li and Ming Jia. “Measurements and Derivation of the Spray Simulation Required Physical Properties of Polyoxymethylene Dimethyl Ethers (PODEn)”. In: *International Journal of Thermophysics* 44.3 (Mar. 2023).

[170] S R Turns. *An Introduction to Combustion: Concepts and Applications*. McGraw-Hill series in mechanical engineering. McGraw-Hill, 2000.

[171] Norbert Peters. “Laminar diffusion flamelet models in non-premixed turbulent combustion”. In: *Progress in Energy and Combustion Science* 10.3 (Jan. 1984), pp. 319–339.

[172] Norbert Peters. “Laminar flamelet concepts in turbulent combustion”. In: *Symposium (International) on Combustion*. Vol. 21. 1. Elsevier. 1986, pp. 1231–1250.

[173] Arne Scholtissek. “Flamelet modeling in composition space for premixed and non-premixed combustion”. In: (2018), p. 198.

[174] Heinz Günter Pitsch. “Modellierung der Zündung und Schadstoffbildung bei der dieselmotorischen Verbrennung mit Hilfe eines interaktiven Flamelet-Modells”. In: 82 (1998), VI, 148 S. : Ill., graph. Darst.

[175] Christian Hasse. “A Two-Dimensional Flamelet Model for Multiple Injections in Diesel Engines”. PhD thesis. 2004.

[176] Charles D. Pierce. “PROGRESS-VARIABLE APPROACH FOR LARGE-EDDY SIMULATION OF TURBULENT COMBUSTION”. PhD thesis. 2001.

[177] Charles D. Pierce and Parviz Moin. “Progress-variable approach for large-eddy simulation of non-premixed turbulent combustion”. In: *Journal of Fluid Mechanics* 504 (Apr. 2004), pp. 73–97.

[178] Z. Sun, S. Gierth, M. Pollack, C. Hasse, and A. Scholtissek. “Ignition under strained conditions: Unsteady flamelet progress variable modeling for diesel engine conditions in the transient counterflow configuration”. In: *Combustion and Flame* 240 (2022).

[179] Matthias Ihme, Lee Shunn, and Jian Zhang. “Regularization of reaction progress variable for application to flamelet-based combustion models”. In: *Journal of Computational Physics* 231.23 (2012), pp. 7715–7721.

[180] H. Pitsch and H. Steiner. “Large-eddy simulation of a turbulent piloted methane/air diffusion flame (Sandia flame D)”. In: *Physics of Fluids* 12.10 (2000), pp. 2541–2554.

[181] Heinz Pitsch and Matthias Ihme. “An unsteady/flamelet progress variable method for les of non-premixed turbulent combustion”. In: *43rd AIAA Aerospace Sciences Meeting and Exhibit - Meeting Papers* (2005), pp. 2593–2606.

[182] Matthias Ihme and Yee Chee See. “Prediction of autoignition in a lifted methane/air flame using an unsteady flamelet/progress variable model”. In: *Combustion and Flame* 157.10 (2010), pp. 1850–1862.

[183] Andrew W. Cook and James J. Riley. “A subgrid model for equilibrium chemistry in turbulent flows”. In: *Physics of Fluids* 6.8 (1994), pp. 2868–2870.

[184] Qing Wang, Thomas Jaravel, and Matthias Ihme. “Assessment of spray combustion models in large-eddy simulations of a polydispersed acetone spray flame”. In: *Proceedings of the Combustion Institute* 37.3 (2019), pp. 3335–3344.

[185] Axel Zschutschke, Danny Messig, Arne Scholtissek, and Christian Hasse. *Universal Laminar Flame Solver (ULF)*. Tech. rep. 2017.

[186] Helfried Steiner and Heinz Pitsch. “Scalar Mixing and Dissipation Rate in Large-Eddy Simulations of Non-Premixed Turbulent Combustion”. In: *Proceedings of the Combustion Institute* 28 (2000), pp. 1–9.

[187] Sharath S. Girimaji and Ye Zhou. “Analysis and modeling of subgrid scalar mixing using numerical data”. In: *Physics of Fluids* 8.5 (1996), pp. 1224–1236.

[188] Thomas Hellström. *RIF Implementation and Testing*. Tech. rep. 1997, Task 9, DIESEL.

[189] Fredrik R. Westlye, Keith Penney, Anders Ivarsson, Lyle M. Pickett, Julien Manin, and Scott A. Skeen. "Diffuse back-illumination setup for high temporally resolved extinction imaging". In: *Applied Optics* 56.17 (2017).

[190] Noud Maes, Scott A. Skeen, Michele Bardi, Russell P. Fitzgerald, Louis Marie Malbec, Gilles Bruneaux, Lyle M. Pickett, Koji Yasutomi, and Glen Martin. "Spray penetration, combustion, and soot formation characteristics of the ECN Spray C and Spray D injectors in multiple combustion facilities". In: *Applied Thermal Engineering* 172.January (2020).

[191] Sebastian Riess. "Einfluss von Kraftstoff und Abgasrückführung auf Gemischbildung und Verbrennung von dieselmotorischen Sprays". PhD thesis. 2017.

[192] Julien Manin, Lyle M. Pickett, Scott A. Skeen, and Jonathan H. Frank. "Image processing methods for Rayleigh scattering measurements of diesel spray mixing at high repetition rate". In: *Applied Physics B: Lasers and Optics* 127.5 (2021).

[193] F. Poschen, D. Notheis, U. Wagner, A. Velji, T. Koch, and M. Olzmann. "Formation of NOx and Formaldehyde in Oxymethylene Ether / n -Heptane Combustion : Engine Studies and Kinetic Modeling". In: *10th European Combustion Meeting*. 2021.

[194] Universitat Politechnica de Valencia. *CMT-Motores Termicos, https://www.cmt.upv.es/#/ecn/download/-Enerxicodata/Enerxicodata*.

[195] S. V. Apte, K. Mahesh, and T. Lundgren. "Accounting for finite-size effects in simulations of disperse particle-laden flows". In: *International Journal of Multiphase Flow* 34.3 (2008), pp. 260–271.

[196] Fabien Evrard, Fabian Denner, and Berend van Wachem. "Euler-Lagrange modelling of dilute particle-laden flows with arbitrary particle-size to mesh-spacing ratio". In: *Journal of Computational Physics: X* 8 (2020).

[197] S. Weise and C. Hasse. "Reducing the memory footprint in Large Eddy Simulations of reactive flows". In: *Parallel Computing* 49 (2015), pp. 50–65.

[198] Michael Schäfer. *Numerik im Maschinenbau*. Springer-Lehrbuch. Berlin, Heidelberg: Springer Berlin Heidelberg, 1999.

[199] J.H. Ferziger and M. Peric. *Numerische Strömungsmechanik*. Vol. 53. 9. 2017, pp. 1689–1699.

[200] Lyle M. Pickett, Julien Manin, Raul Payri, Michele Bardi, and Jaime Gimeno. "Transient rate of injection effects on spray development". In: *SAE Technical Papers* 6 (2013), pp. 15–16.

[201] Helmut Tschöke. "9.Tagung Diesel- und Benzindirekteinspritzung". In: *9.Tagung Diesel- und Benzindirekteinspritzung*. 2014.

[202] Mahmoud Gadalla, Jeevananthan Kannan, Bulut Tekgül, Shervin Karimkashi, Ossi Kaario, and Ville Vuorinen. "Large-eddy simulation of ECN spray a: Sensitivity study on modeling assumptions". In: *Energies* 13.13 (2020), pp. 1–24.

[203] E. Buckingham. "On Physically Similar Systems; Illustrations of the Use of Dimensional Equations". In: *Physical Review* 4.4 (Oct. 1914), pp. 345–376.

[204] Michele Battistoni, Gina M. Magnotti, Caroline L. Genzale, Marco Arienti, Katarzyna E. Matusik, Daniel J. Duke, Jhoan Giraldo, Jan Ilavsky, Alan L. Kastengren, Christopher F. Powell, and Pedro Marti-Aldaravi. "Experimental and Computational Investigation of Subcritical Near-Nozzle Spray Structure and Primary Atomization in the Engine Combustion Network Spray D". In: *SAE International Journal of Fuels and Lubricants* 11.4 (Apr. 2018).

[205] Wai Tong Chung, Peter C. Ma, and Matthias Ihme. “Examination of diesel spray combustion in supercritical ambient fluid using large-eddy simulations”. In: *International Journal of Engine Research* 21.1 (2020), pp. 122–133.

[206] Andrea Pati. “Numerical investigation of the in-cylinder flow-spray-wall interactions in direct injection engines”. PhD thesis. 2022.

[207] Mark P.B. Musculus and Kyle Kattke. “Entrainment waves in diesel jets”. In: *SAE Technical Papers* 2.1 (2009), pp. 1170–1193.

[208] Lyle M. Pickett, Julien Manin, Caroline L. Genzale, Dennis L. Siebers, Mark P.B. Musculus, and Cherian A. Idicheria. “Relationship Between Diesel Fuel Spray Vapor Penetration/Dispersion and Local Fuel Mixture Fraction”. In: *SAE International Journal of Engines* 4.1 (2011), pp. 764–799.

[209] Haohan Li, Roel Verschaeren, Gilles Decan, Tarek Beji, and Sebastian Verhelst. “Evaluation of breakup models for marine diesel spray simulations”. In: September (2019), pp. 2–4.

[210] Rainer N Dahms, Günter A Paczko, Scott A Skeen, and Lyle M Pickett. “Understanding the ignition mechanism of high-pressure spray flames”. In: *Proceedings of the Combustion Institute* 36.2 (Jan. 2017), pp. 2615–2623.

[211] Herman Bergwerf. “MolView : an attempt to get the cloud into chemistry classrooms”. In: *ACS CHED CCCE Newsletter* 9 (2015), pp. 1–9.

[212] Tong Yao, Yuanjiang Pei, Bei Jing Zhong, Sibendu Som, Tianfeng Lu, and Kai Hong Luo. “A compact skeletal mechanism for n-dodecane with optimized semi-global low-temperature chemistry for diesel engine simulations”. In: *Fuel* 191 (2017), pp. 339–349.

[213] G.P: Smith, Y. Tao, and H. Wang. *Foundational Fuel Chemistry Model Version 1.0 (FFCM-1)*. 2016.

[214] Eliseo Ranzi, Carlo Cavallotti, Alberto Cuoci, Alessio Frassoldati, Matteo Pelucchi, and Tiziano Faravelli. “New reaction classes in the kinetic modeling of low temperature oxidation of n-alkanes”. In: *Combustion and Flame* 162.5 (May 2015), pp. 1679–1691.

[215] Alessandro Stagni. *Personal Communication*.

[216] M. Pelucchi, S. Namysl, E. Ranzi, A. Rodriguez, C. Rizzo, K. P. Somers, Y. Zhang, O. Herbinet, H. J. Curran, F. Battin-Leclerc, and T. Faravelli. “Combustion of n-C3-C6Linear Alcohols: An Experimental and Kinetic Modeling Study. Part I: Reaction Classes, Rate Rules, Model Lumping, and Validation”. In: *Energy and Fuels* 34.11 (2020), pp. 14688–14707.

[217] Alessandro Stagni, Alberto Cuoci, Alessio Frassoldati, Tiziano Faravelli, and Eliseo Ranzi. “Lumping and reduction of detailed kinetic schemes: An effective coupling”. In: *Industrial and Engineering Chemistry Research* 53.22 (2014), pp. 9004–9016.

[218] Benedikt Heuser, Florian Kremer, Stefan Pischinger, Jennifer Julis, and Walter Leitner. “Optimization of diesel combustion and emissions with newly derived biogenic alcohols”. In: *SAE Technical Papers* 11 (2013).

[219] Hernan Olguin and Eva Gutheil. “Influence of evaporation on spray flamelet structures”. In: *Combustion and Flame* 161.4 (2014), pp. 987–996.

[220] Hernan Olguin and Eva Gutheil. “Derivation and evaluation of a multi-regime spray flamelet model”. In: *Zeitschrift fur Physikalische Chemie* 229.4 (2015), pp. 461–482.

[221] Hesheng Bao, Noud Maes, Hayri Yigit Akargun, and Bart Somers. “Large Eeddy Simulation of cavitation effects on reacting spray flames using FGM and a new dispersion model with multiple realizations”. In: *Combustion and Flame* 236 (2022).

[222] B Akkurt. “Modelling multi-pulse diesel injection with flamelet generated manifolds”. PhD thesis. 2019, p. 232.

[223] Yan Zhang, Hu Wang, Ambrus Both, Likun Ma, and Mingfa Yao. “Effects of turbulence-chemistry interactions on auto-ignition and flame structure for n-dodecane spray combustion”. In: *Combustion Theory and Modelling* 23.5 (2019), pp. 907–934.

[224] Epaminondas Mastorakos. “Ignition of turbulent non-premixed flames”. In: *Progress in Energy and Combustion Science* 35.1 (2009), pp. 57–97.

[225] C. Bekdemir, L. M.T. Somers, L. P.H. De Goey, J. Tillou, and C. Angelberger. “Predicting diesel combustion characteristics with Large-Eddy Simulations including tabulated chemical kinetics”. In: *Proceedings of the Combustion Institute* 34.2 (2013), pp. 3067–3074.

[226] John E. Dec. *A Conceptual Model of DI Diesel Combustion Based on Laser-Sheet Imaging**. Tech. rep. 1997.

List of Figures

List of Tables